The Nature of Fast Radio Bursts and Their Potential as Probes of the Universe

Dissertation
zur
Erlangung des Doktorgrades (Dr. rer. nat.)
der
Mathematisch-Naturwissenschaftlichen Fakultät
der
Rheinischen Friedrich-Wilhelms-Universität Bonn

von
Joscha Nicolai Jahns-Schindler
aus
Berlin

Bonn, September 2023

Angefertigt mit Genehmigung der Mathematisch-Naturwissenschaftlichen Fakultät der Rheinischen Friedrich-Wilhelms-Universität Bonn

Gutachter / Betreuer:	Prof. Dr. Michael Kramer
Gutachter:	Prof. Dr. Cristiano Porciani
Tag der Promotion:	26.08.2024
Erscheinungsjahr:	2024

Contents

CHAPTER 1

Fast Radio Bursts

1.1 Introduction

Fast radio bursts (FRBs) are bright flashes of radio waves coming from far-away galaxies and occurring all over the sky. Their duration of < 0.1–$200\,\mathrm{ms}$[1] (CHIME/FRB Collaboration et al., 2021) is similar to the duration of a camera flash. Yet, the wavelength of the light that constitutes an FRB is very different from visible light; visible light has a wavelength of 400–780 nm ($1\,\mathrm{nm} = 10^{-9}\,\mathrm{m}$), while FRBs have been observed at wavelengths between 4 cm and 3 m (Gajjar et al., 2018; Pleunis et al., 2021). Equivalently, expressed in terms of their frequency, FRBs are observed between 110 MHz and 8 GHz. These wavelengths are close to the longest wavelengths that can penetrate Earth's atmosphere and are therefore observable by astronomers on Earth. Fig. 1.1 shows an FRB, as we observe them with radio telescopes.

I described FRBs as bright, but then why were they only discovered around 16 years ago by Lorimer et al. (2007)? First, for the split second of their duration, some FRBs are among the brightest sources in the sky sometimes exceeding 200 Jy[2]. However, most radio observations sum their data up over at least several minutes, burying the FRB in noise. Second, to detect weak radio sources, we need radio telescopes with large collecting areas. A side effect of this is that the field of view is very small because the observed solid angle $\Omega \propto \lambda^2/A$, where λ is the observed wavelength and A is the collecting area of the telescope. The 100-m telescope in Effelsberg, for example, observes a solid angle of $\Omega = 0.02\,\mathrm{deg}^2$ at $\lambda = 21\,\mathrm{cm}$, which is only $\frac{1}{2\,140\,000}$ of the whole sky. Third and maybe most importantly, people were not searching for single pulses. Pulsars, a class of strictly periodic Galactic transients, had originally been found by their individual pulses (Hewish et al., 1968). Yet, the high time-resolution searches for weaker and weaker pulsars had evolved to a search, specifically for signals that are strictly periodic over longer times. Additionally, they were typically limited (via the searched dispersion measure) to distances not much outside the Milky Way. These specific searches made it almost impossible to find FRBs. Only the discovery of rotating radio transients (McLaughlin et al., 2006), a sporadically emitting type of Galactic neutron stars, sparked a new popularity of single pulse searches and made the discovery of FRBs possible.

While they appear about as bright on the sky as other transient sources, like pulsars, their luminosities (or equivalently energies) are truly outstanding. The difference comes from FRBs' much larger distances. Pulsars are only observable nearby, mostly in our own Galaxy. FRBs on the other hand come from $\sim 10^5$

[1] A list of discovered FRBs can be found at https://www.wis-tns.org/ or at https://www.herta-experiment.org/frbstats/

[2] Radio astronomers express the spectral flux density of a source in 'Jansky', where $1\,\mathrm{Jy} = 10^{-26}\,\mathrm{W\,m^{-2}\,Hz^{-1}}$.

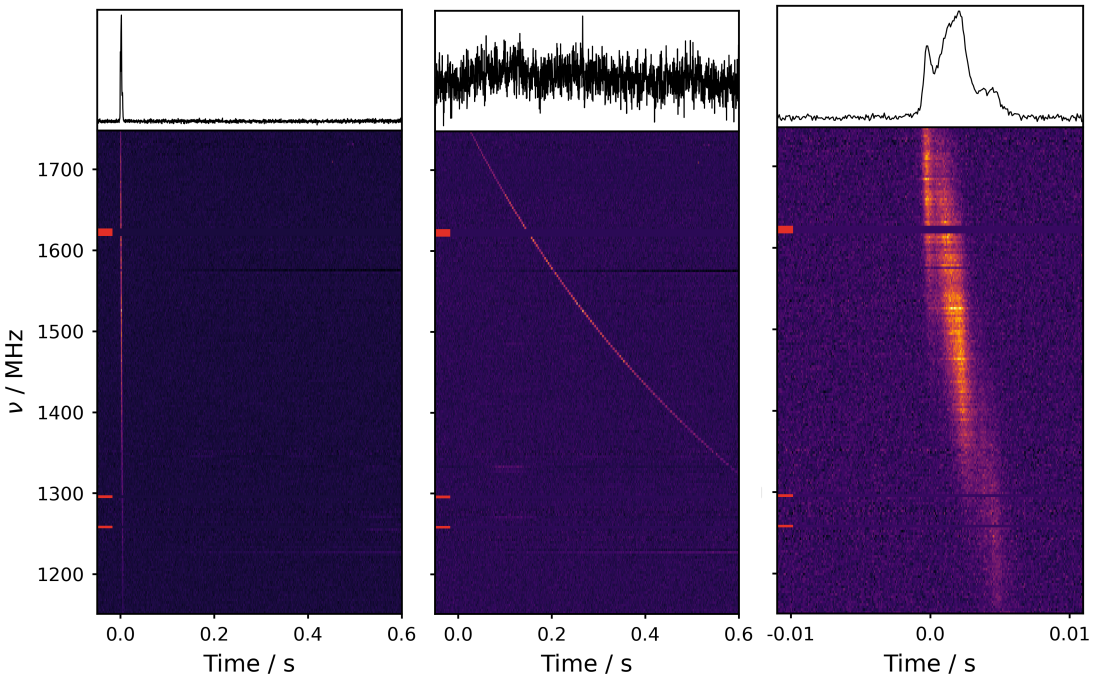

(a) Emitted burst (b) Dispersed burst (c) Zoom in

Figure 1.1: An FRB that my collaborators and I observed with the Arecibo Telescope. In each figure, the bottom panel shows the *dynamic spectrum*, while the top panel shows the same data, after summing over frequencies. Fig. (a) shows the FRB, as it is emitted by its source. It is only a few milliseconds long. Fig. (b) shows how it arrives at our telescope, with the characteristic sweep across frequencies. This dispersive delay of lower frequencies with respect to higher frequencies occurs while it travels toward us through the thin medium between stars and galaxies. Fig. (c) shows a zoom in after dedispersion. The structure reveals that the emission already drifts in frequency before becoming dispersed. This observation is referred to as the sad-trombone effect.

times larger distances, of order 100 Mpc to several Gpc (1 pc $\approx$ 3.3 ly $\approx 3 \times 10^{16}$ m). This results in energies of order $\sim 10^{31}$ J (Petroff, Hessels, and Lorimer, 2019) comparable to the energy that the Sun emits over one to several days.

Most FRBs have only been observed as one-off events, despite many hours of follow-up, targeted at FRB positions. Only about 4 % have been seen to repeat and therefore labeled as *repeaters* (CHIME/FRB Collaboration et al., 2021). We can never rule out that a single burst will repeat eventually, but in the large sample of CHIME/FRB Collaboration et al. (2021) repeaters also appeared different in their statistical analysis. Repeaters typically have longer durations and limited frequency bandwidth, while non-repeaters are shorter duration but very broad in frequency, usually extending beyond both edges of the observing band. Whether the two burst classes stem from the same objects or if one-off FRBs originate from cataclysmic events is still an open question.

After initial doubts, evidence for the extragalactic nature of FRBs came in two ways. Statistically, the FRB population does not depend on the Galactic latitude, i.e. they do not preferentially occur in the Milky Way plane like for example pulsars (see e.g. Josephy et al., 2021). Direct evidence is available for a few FRBs from their positions on the Sky. The exact position can be compared with optical images to associate the FRB with a host galaxy. Identification with a galaxy gives evidence for the extragalactic

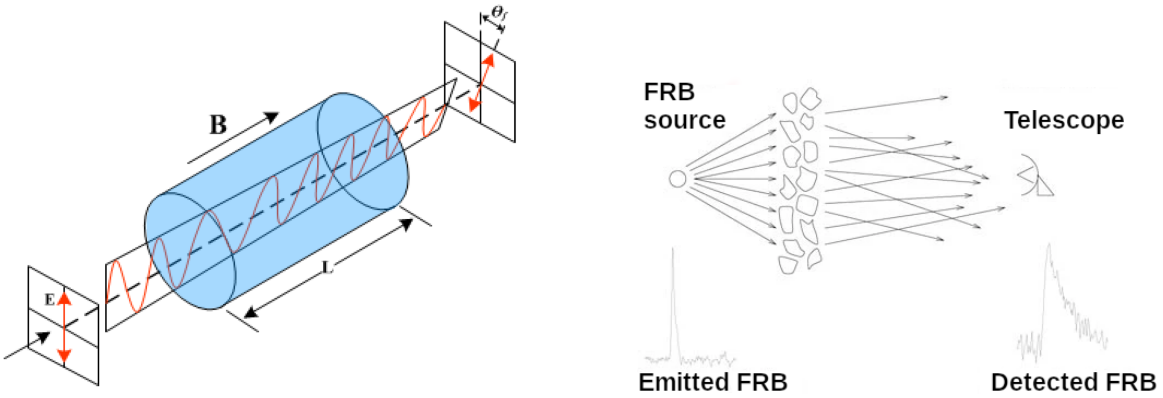

(a) Faraday rotation

(b) Scattering

Figure 1.2: Illustrations of propagation effects. The left-hand panel shows how Faraday rotation changes the polarization angle of a monochromatic linearly polarized wave. $\vec{\mathbf{B}}$ denotes the magnetic field, L the propagation path length, $\vec{\mathbf{E}}$ the electric field, and θ_f the difference in the polarization angle. The right-hand panel shows how a sharp emitted pulse gets scattered and how different paths end up in our telescope. The multi-path propagation 'washes out' the burst causing an exponential scattering tail. Fig. (a) from Silva et al. (2012), licensed under CC BY 3.0. Fig. (b) adapted from Lorimer (2008), licensed under CC BY 4.0.

origin. A difficulty is that most positions are very imprecise, often exceeding measurement uncertainties of 0.1 deg (CHIME/FRB Collaboration et al., 2021). Yet, some telescope arrays can do interferometry upon discovery (see e.g. Bannister et al., 2019) to localize one-off FRBs on the Sky at ~1 arcsec precision. Further localizations are possible for repeaters by doing interferometric follow-up observations (Tendulkar et al., 2017). Both ways allow the identification of host galaxies in optical images, confirming their extragalactic origin. The identification of host galaxies has great value beyond this application and we will discuss these at several points throughout this thesis.

The names of FRBs are derived from the date of the observation in the form FRB YYMMDD (introduced by Thornton et al., 2013). FRB 010724 for example, was discovered in data from July 24, 2001. Newer FRBs also have a letter at the end to allow for several FRBs per day[3]. Repeaters are named after the first detected burst.

1.2 Propagation effects

Several effects act on FRBs and modify them during their path from their source to our telescopes. The most prominent and arguably most important is the dispersion. FRBs, like all radio waves, interact with the non-relativistic free electrons that are omnipresent in the plasmas along their path. As a result, FRBs are delayed by up to several seconds with respect to a signal traveling at the speed of light and, moreover, lower frequencies are delayed more than higher frequencies. This results in the sweep across frequencies that is illustrated in Fig. 1.1. This sweep follows an inverse-square law, where the time delay Δt at a frequency ν,

[3] Oftentimes, FRBs are reported with a 20 in front of their name, which is superfluous for another 77 years but follows the format of the Transient Name Server. In this work, I am omitting it.

with respect to a non-dispersed signal, is given in Gaussian units by

$$\Delta t = \frac{e^2}{2\pi m_e c}\frac{DM}{\nu^2} \equiv K\frac{DM}{\nu^2}\,, \quad \text{with the } \textit{dispersion measure} \quad DM = \int_{\text{source}}^{\text{observer}} n_e(\ell)\,\mathrm{d}\ell\,. \tag{1.1}$$

In words, it is the integrated column density of electrons (n_e) between the source and observer. The physical constants e, m_e, and c are the elementary charge, electron mass, and speed of light, respectively, and have been collected in the constant K which takes the value $K = 4.1488064239(11)\,\mathrm{GHz}^2\,\mathrm{cm}^3\,\mathrm{pc}^{-1}\,\mathrm{ms}$ (Kulkarni, 2020). The dispersion of bursts has, both, advantages and disadvantages when searching for bursts. The disadvantage is that the signal is stretched out in time and not visible anymore in the time series. To still find FRBs, we must *dedisperse* the data at many trial *DM*s, which is computationally expensive and still leaves intra-channel smearing. On the other hand, dispersion has the advantage that it allows us to tell FRBs apart from human-made *radio frequency interference* (RFI), which does not travel through space and therefore typically arrives simultaneously in all frequencies. Aside from this, the *DM* is also the main observable for many cosmological applications of FRBs. We will discuss those in Chapter 2.

Other propagation effects, which are less relevant to this thesis, are *Faraday rotation*, *scattering*, and *scintillation*. The first two are illustrated in Fig. 1.2. Faraday rotation is caused by magnetic fields parallel to the line of sight in the presence of plasma. Free electrons oscillate in the electric field of the electromagnetic radio wave. Any movement in a magnetic field also results in a perpendicular acceleration due to the Lorentz force $\vec{\mathbf{F}} = e(\vec{\mathbf{E}} + \vec{\mathbf{v}} \times \vec{\mathbf{B}})$, where $\vec{\mathbf{E}}$, $\vec{\mathbf{v}}$, and $\vec{\mathbf{B}}$ denote the three-dimensional electric field, electron velocity, and magnetic field, respectively. Due to this force, electrons oscillate with a very small inclination with respect to the wave's electric field. In return, the electromagnetic wave also slightly changes its orientation when traveling in the medium of free electrons. This change in the orientation due to Faraday rotation is only measurable if the wave is linearly polarized. Like dispersion, this polarization angle Ψ depends on $1/\nu^2$ and on the integral along the line of sight, but this time also involving the magnetic field component $B_\parallel$ that is parallel to the line of sight,

$$\Psi = \frac{e^3}{2\pi m_e^2 c^2}\frac{1}{\nu^2}\int_{\text{source}}^{\text{observer}} n_e(\ell) B_\parallel(\ell)\,\mathrm{d}\ell \equiv RM\frac{1}{\nu^2}\,, \tag{1.2}$$

where we defined the *rotation measure*, *RM* in the second step. In FRBs and other sources, the polarization fraction itself can tell us about the emission mechanism (D. Li and Zanazzi, 2021; Bethapudi et al., 2023). The *RM* can tell us about the immediate environment of the source, the host galaxy, the magnetic fields in the intergalactic medium (IGM), and the Milky Way.

Radio waves, e.g. an FRB, that travel through an inhomogeneous medium get refracted. As a result they propagate along multiple paths which introduces two effects: *scattering* and *scintillation*. Scattering broadens the pulse in time by the scattering time τ_s. Scintillation causes a frequency modulation in the spectrum with the characteristic scintillation bandwidth ν_s. The scales of the two effects, if caused by the same screen, are related as $\tau_\mathrm{s} = 1/2\pi\nu_\mathrm{s}$ (see e.g. Main et al., 2022). Additionally, both effects are strongly frequency dependent usually with $\nu_\mathrm{s} \propto \nu^4$.

Scattering usually happens in the interstellar medium (ISM) of the galaxy where the FRB originated or in the ISM of the Milky Way, because these are denser and clumpier than the thin IGM. As a result, scattering can be used to probe these ISM regions (Ocker et al., 2022). In many cases, scattering could also be so strong that the FRB gets completely washed out and can no longer be detected. For example, there might be many FRBs originating around the centers of galaxies that we are missing due to scattering (Seebeck et al., 2021).

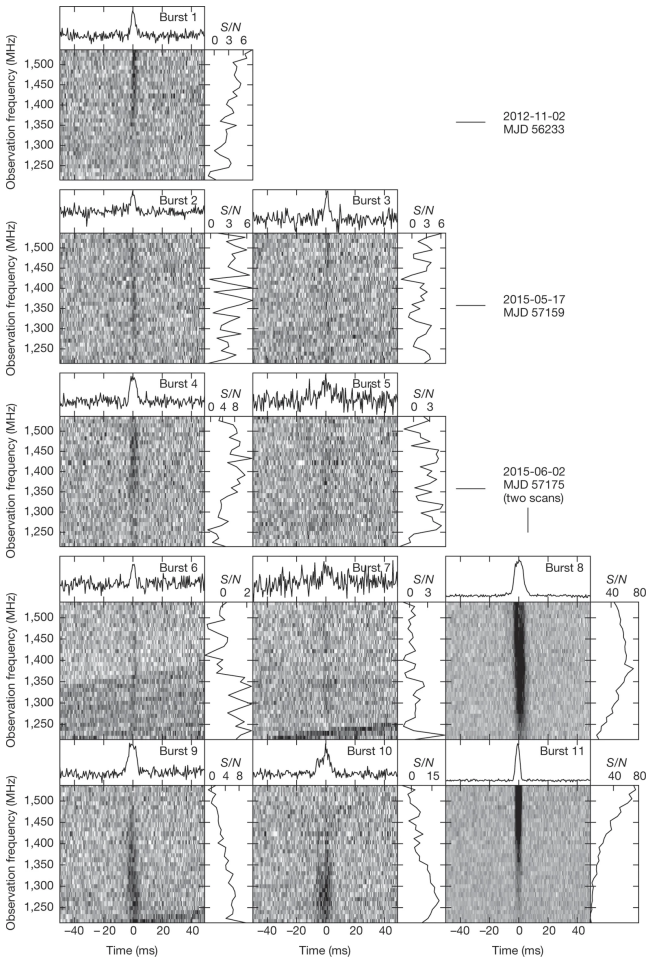

(a) Repeater bursts

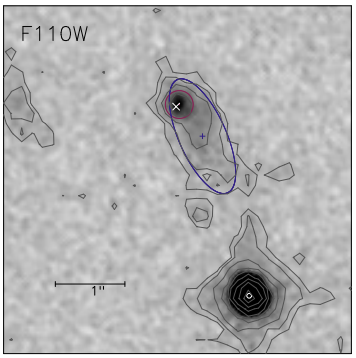

(b) The host galaxy of FRB 121102

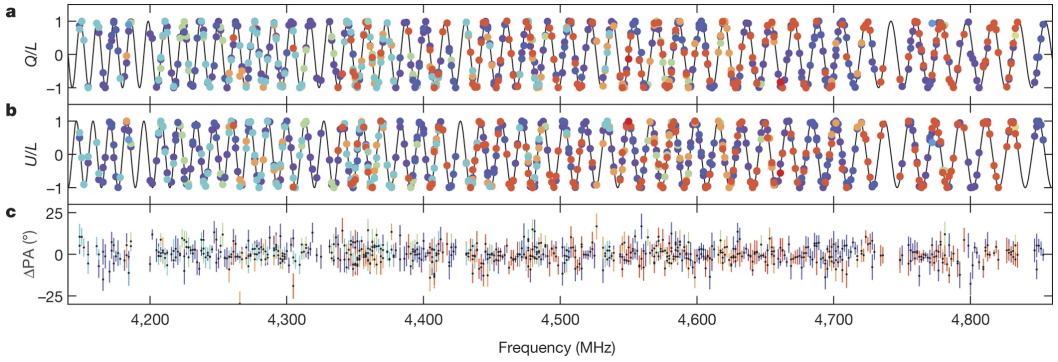

(c) The *RM* of FRB 121102

Figure 1.3: Key figures of FRB 121102. Panel (a) shows the first repetitions discovered of FRB 121102. Panel (b) shows the host galaxy, observed with the Hubble space telescope. The white cross marks the FRB position as measured with the European VLBI Network (Marcote et al., 2017). A red circle and a blue ellipse mark the half-light radii of a star-forming region and extended emission from the galaxy, respectively. Panel (c) shows the *RM* measurement. Q/L and U/L parameterize the direction of the linear polarization. It wraps around many times over the measured frequency range. Fig. (a) from Spitler et al. (2016), reproduced with permission from SNCSC. Fig. (b) from Bassa et al. (2017), ©AAS. Reproduced with kind permission from the author and the AAS. Fig. (c) Michilli et al. (2018), reproduced with permission from SNCSC.

1.3 Specific FRBs

Since the discovery of the first FRB (Lorimer et al., 2007) – FRB 010724 or *Lorimer burst* – several bursts have shaped our understanding more than others. It took another five years until Keane et al. (2012) discovered the second FRB. Yet, its DM of 746 cm^{-3} pc did not greatly exceed the estimated Milky Way DM of 533 cm^{-3} pc in this direction, and therefore its extragalactic interpretation is not secure (Bannister and Madsen, 2014). Only the four bursts found by (Thornton et al., 2013) could convince the community that the phenomenon FRB indeed had its origin in the Sky rather than being human-made and that they stem from outside the Milky Way.

1.3.1 FRB 121102

FRB 121102 is truly remarkable in many ways. It was the first FRB that was not discovered in data from the Parkes telescope, Murriyang, in Australia but instead in data from the Arecibo Telescope in Puerto Rico by Spitler et al. (2014). This way it silenced the last doubts regarding the celestial origin of FRBs. We show the first discovered repeat bursts in Fig. 1.3 along with some other essential discoveries of this source. Even more outstanding was that Spitler et al. (2016) found additional bursts from the same source, making

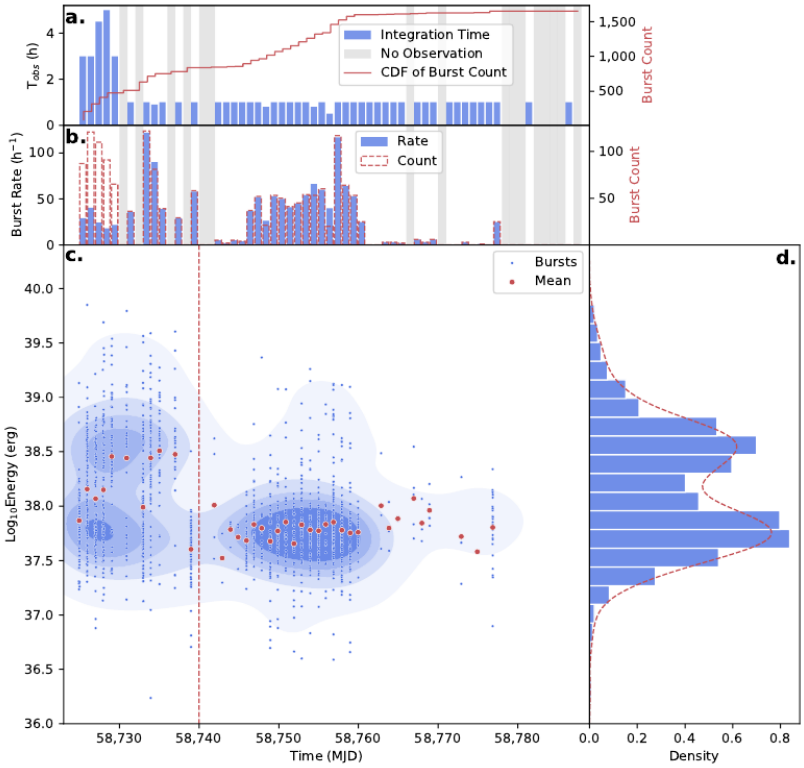

Figure 1.4: Bimodality in the energy distribution of FRB 121102, as measured with the FAST telescope. The bursts before MJD 58740 are summarized into a histogram in panel (d), which shows two peaks. Afterward, the energy distribution changes its form to a single peak. Figure from D. Li et al. (2021), reproduced with permission from SNCSC.

it the first repeater (it is therefore sometimes also referred to as R1). Even though the repetition was very irregular, with sometimes weeks without observed bursts, the repeating nature allowed observations with various telescopes at different observing frequencies. Using the Very Large Array VLA, which consists of several telescopes combined in an array, to do interferometry, Chatterjee et al. (2017) localized the source to a small dwarf galaxy at a redshift of $z = 0.193$ (Tendulkar et al., 2017), and found that it is co-located with a compact persistent radio source. Marcote et al. (2017) used the European VLBI Network to constrain the projected separation to within $\lesssim 40$ pc, strongly suggesting a physical link between the two sources. They derive it to be either an accreting supermassive black hole or a supernova remnant energized by a young neutron star. However, if the source of persistent emission is also the source of FRBs remains unclear.

In the original data at 1.4 GHz, the bursts seemed unpolarized, but at higher frequencies around 4 GHz Michilli et al. (2018) found that it is 100 % linearly polarized with an *RM* of 1.4×10^5 rad cm^{-2}. Such a high *RM* has previously only been observed around the central super massive black holes of galaxies (see e.g. Eatough et al., 2013) and requires very high magnetic fields in the environment of the source. A set of high signal-to-noise bursts, *coherently dedispersed*, i.e., before channelization, revealed fascinating substructure in some bursts (Hessels et al., 2019).In particular, the substructure often seemed to drift towards lower frequencies and never to higher frequencies. This is now called the *sad-trombone effect* and has since been observed in several other repeaters. After another repeater – FRB 180916B – showed periodic activity (CHIME/FRB Collaboration et al., 2020b), such periodic activity was also found for bursts of FRB 121102 (Rajwade et al., 2020; Cruces et al., 2021). Yet, the active window is very wide, with ~60 % of the 160-day cycle. Within this cycle, bursts still arrive randomly, i.e. no strict periodicity on ms to minute time scales has been found (Cruces et al., 2021; D. Li et al., 2021). Monitoring of the source for several years has shown small changes in the *DM* with a small upward trend. The *RM* on the other hand, has dropped significantly in the same period of time (Hilmarsson et al., 2021).

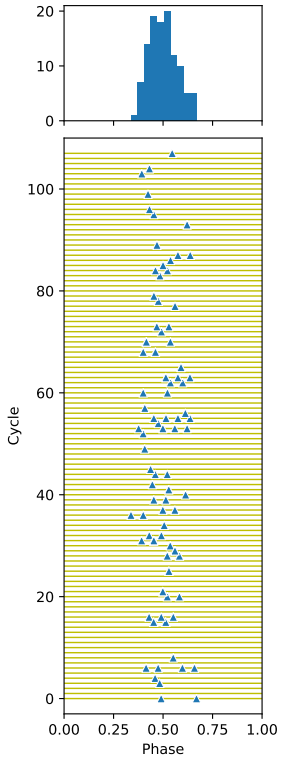

Figure 1.5: Periodicity in the activity of FRB 180916B. One phase spans 16.3 days. Activity is only seen within about 4 days even though CHIME observes the source daily. Figure made after a figure from Dongzi Li with data from Chime/Frb Collaboration et al. (2023).

The energy distribution of FRB 121102 can sometimes be bimodal and changes with time (D. Li et al., 2021), as shown in Fig. 1.4. This finding explained the differences in power-law indices that had previously been found (Gourdji et al., 2019; Cruces et al., 2021). However, there is no straightforward interpretation within the emission models.

1.3.2 FRB 180916B

The repeater FRB 180916B was one of the first and most active repeaters found by CHIME/FRB Collaboration et al. (2019). It is one of two repeaters so far that has an activity cycle, in this case of only 16 days with a 4-day active window (Z. Li et al., 2020), which is shown in Fig. 1.5. It is located in a spiral galaxy at $z = 0.0337 \pm 0.0002$ slightly offset by 250 pc from the center of an active star-forming region (Marcote et al., 2020). However, this projected offset is enough to exclude some progenitor models. For example, it cannot be an isolated magnetar, a neutron star type that is young and highly magnetized, because the travel time of 800 kyr to 7 Myr

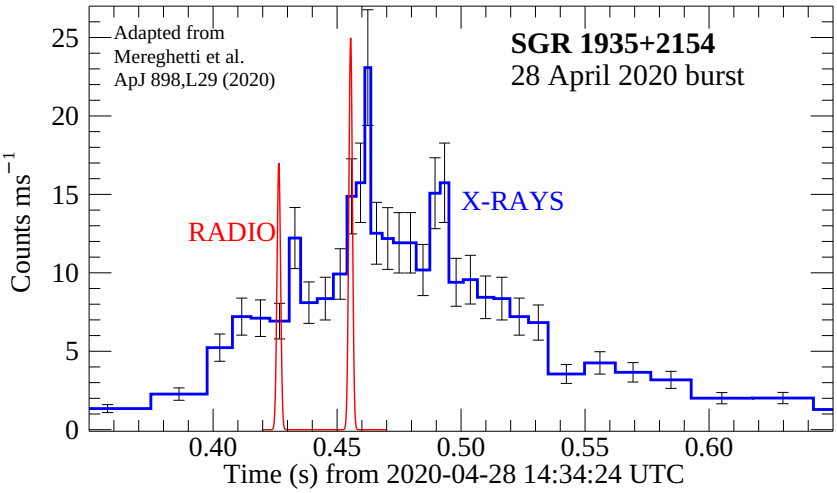

Figure 1.6: The two bursts of SGR 1935+2154 almost simultaneously observed at the two ends of the electromagnetic spectrum. Figure from Mereghetti (2023), licensed under CC BY 4.0, adapted from Mereghetti et al. (2020), ©AAS. Reproduced with kind permission by the author and the AAS.

is already much longer than the active lifetime of $\lesssim 10\,\mathrm{kyr}$ of a magnetar (Tendulkar et al., 2021). The favored theory for FRB 180916B is therefore a magnetar in a binary system with a heavy star, called a high-mass X-ray binary.

1.3.3 SGR 1935+2154

In 2020, SGR 1935+2154 emitted a burst that is often regarded as the first Galactic FRB. It was already known as a magnetar, specifically a soft gamma repeater (hence the name) that was detected in X-rays and γ-rays. On April 28, the two radio telescopes CHIME and STARE2 detected a bright burst at the same time whose position was coincident with this source (CHIME/FRB Collaboration et al., 2020a; Bochenek et al., 2020). CHIME detected it outside its primary field of view, in a far sidelobe, where only very bright sources can be detected. STARE2 was specifically built to observe very bright nearby sources in the whole sky, but this quick success was a big surprise.

The burst from SGR 1935+2154 was so bright that it would have been detectable with our current telescopes even if it came from a nearby galaxy. In fact, it is more luminous than some detected bursts from the repeater FRB 200120E (Kirsten et al., 2021). It is therefore regarded as the first galactic FRB. At the time of the burst, there was also a burst detected in X-rays (C. K. Li et al., 2021; Ridnaia et al., 2021; Tavani et al., 2021), and in γ-rays (Mereghetti et al., 2020), which was delayed by $(6.5 \pm 1.0)\,\mathrm{ms}$ with respect to the radio signal, as Fig. 1.6 is showing. As a result, it is the first source of FRBs to be detected at another part of the electromagnetic spectrum than radio and the first identified object with a definite association with an FRB. The association was a strong confirmation that magnetars are capable of emitting FRBs and shows that at least some FRBs originate from these objects.

1.4 Telescopes

The first six FRBs were detected with Murriyang, starting and establishing the field of FRBs. Murriyang is a telescope located in Parkes, Australia, with a diameter of 64 m. Fig. 1.7 shows it among other important radio telescopes, which we describe in the following.

The 305-m Arecibo Telescope was very influential for FRB science and the telescope that I used in my first publication. It was the second telescope to find an FRB and the telescope that found the first repeater, FRB 121102 (Spitler et al., 2014). Built into a valley near Arecibo, Puerto Rico, it was the world's largest telescope for 53 years, until the completion of the Chinese Five-hundred-meter Aperture Spherical Telescope (FAST) in 2016. It collapsed unexpectedly in December 2020.

The Australian SKA Pathfinder (ASKAP) is a very influential telescope for the field because it was the first that was capable of localizing FRBs upon discovery to within sub-arcseconds (Bannister et al., 2019). Classical single-dish telescopes like Murriyang or the Arecibo Telescope have no information on where a detected FRB originated within a beam. ASKAP is an interferometer with 36 dishes (Hotan et al., 2021) and can therefore be used to localize FRBs with high enough precision to identify their host galaxy, the importance of which we will expand upon later. At the same time, it is equipped with phased array feeds, a newly developed receiver type that is used to form 36 beams simultaneously (instead of typically 1–13), giving it a large field of view and therefore a high rate of FRB detections.

The telescope that currently finds most FRBs is the Canadian Hydrogen Intensity Mapping Experiment (CHIME, CHIME Collaboration et al., 2022). As the name suggests, it was not designed for the search of FRBs, but its potential was recognized during its planning phase when FRBs got widely accepted to be astrophysical. At the time of writing, May 2023, 561 out of 670 known FRBs were discovered by CHIME (CHIME/FRB Collaboration et al., 2021) and 43 out of 50 repeaters (CHIME/FRB Collaboration et al., 2019; Chime/Frb Collaboration et al., 2023). CHIME is not steerable, hence it can not target known sources, a fortunate case for studying the statistical properties of FRBs, because it observes any given point in the sky for the same time every day. Its four cylindrical dishes give it a large collecting area, a very budget-efficient way of building a telescope.

The FRB field has grown so much that science done with FRBs is considered when new telescopes are designed. Some planned telescopes, e.g. DSA-110, are even specifically designed to detect FRBs. The one that we considered in our forecast in my second project is the Square Kilometer Array (SKA, Dewdney et al., 2009). The SKA is a large international project with two planned telescopes. SKA-Mid will be located in South Africa, with the first phase consisting of 133 15-m dishes and 64 13.5-m dishes, distributed with baselines up to 150 km. SKA-Low will be placed in Australia and observe at frequencies of 50–350 MHz. The telescopes will make groundbreaking discoveries in many fields of radio astronomy, and also discover high numbers of FRBs out to very far distances.

1.5 The origin of FRBs

Since the discovery of FRBs, one aspect that has generated a lot of excitement is the uncertain origin of FRBs. It sparked many creative model ideas among physicists and astronomers, which exceeded the number of detected FRBs for several years (see Platts et al., 2019, for a summary). Here, I will focus on a few models that the community favors, and I will approach them from an observational perspective.

There are two ways of asking for the origins of FRBs. The first question is: which objects emit FRBs, under which circumstances, and how do these objects or circumstances come to be? The second question

(a) Murriyang

(b) The Arecibo Telescope

(c) ASKAP

(d) CHIME

Figure 1.7: Some of the most important telescopes for FRBs. (a) The telescope that discovered the first FRB. (b) The Arecibo Telescope in Puerto Rico, used in this thesis. (c) The first telescope that could localize FRBs to their host galaxy upon discovery. (d) The telescopes that has by now discovered most FRBs by a large margin. Figures (a) and (d) from Petroff, Hessels, and Lorimer (2019), licensed under CC BY 4.0. Fig. (b) credit: Credit: Author H. Schweiker/WIYN and NOAO/AURA/NSF, licensed under CC BY 2.0. Fig. (c) by CSIRO.

is: which physical mechanism is responsible for the emission of the radio waves that we see?

1.5.1 Source models

The progenitors of FRBs that are now strongly favored are neutron stars. Neutron stars are very dense compact objects, with masses of about 1–2 $M_\odot$ and radii of only 10 km (Lorimer and Kramer, 2004). They are the remnants of heavy stars above ~8 $M_\odot$ that explode in a supernova. They can be detected because of their strong magnetic fields, which have two possible origins (see e.g. the recent review by Igoshev, Popov, and Hollerbach, 2021): (I) The neutron stars inherit the magnetic flux of their progenitor stars, and the field gets highly compressed when the core collapses to a neutron star. (II) A dynamo effect amplifies magnetic fields at the proto neutron star stage. Their emission was first observed at radio frequencies in 1967 from pulsars (Hewish et al., 1968), which emit beamed radio waves from their magnetic poles. An even more extreme class of neutron stars are magnetars, whose magnetic field strengths exceed 10^{14} G (e.g. Kaspi and Beloborodov, 2017), which is more than 10^8 times stronger than any human-made magnet.

Both, pulsars and magnetars sometimes emit pulses that are from their duration and appearance similar to FRBs, although missing the sad-trombone effect. Hence, they were one of the main culprits from the

beginning. However, the gap between the emitted energies of pulsars and FRBs is large. FRBs are about 10^7 times more energetic than even the giant pulses from the Crab pulsar (see e.g. Karuppusamy, Stappers, and van Straten, 2010). Direct observational evidence for the connection between FRBs and magnetars came from SGR 1935+2154, as we already discussed in Section 1.3.3. Since there is some morphological differences between most FRBs and SGR 1935+2154, we will discuss some other possibilities and observational clues.

One other interesting and much-discussed class of FRB candidates can be summarized as violent cataclysmic events that set free a lot of energy. These events include for example supernovae and the mergers of two neutron stars. These cataclysmic events can naturally be excluded for repeaters, as they could only emit a single FRB. For one-off FRBs, the rate of FRBs can give us a clue, because it is higher than most rates of other cataclysmic events. The FRB volumetric event rate inferred from CHIME is about $8.7 \times 10^4\,\mathrm{Gpc^{-3}\,yr^{-1}}$, above an energy of 10^{39} erg (James et al., 2022; Shin et al., 2023). The merger rate of neutron stars, on the other hand, is typically estimated to be below $1 \times 10^3\,\mathrm{Gpc^{-3}\,yr^{-1}}$ in the local universe (Mandel and Broekgaarden, 2022). As a result, they could make up, at most, a fraction of the FRBs population.

A promising route to constrain FRB sources is through their host galaxies and immediate environments. One can, for example, compare galaxy properties, like the star formation history, with the host galaxy of other transients or the locations within these galaxies. In this way, several studies could exclude that all FRBs originate from long gamma-ray bursts or super luminous supernovae (Heintz et al., 2020; Bhandari et al., 2022; Gordon et al., 2023). Assuming most FRBs originate from neutron stars, studying their host galaxies could reveal differences from Galactic neutron stars or possibly a specific formation channel.

1.5.2 Emission models

Together with the high energy, one of the most constraining quantities of FRBs is their duration. The duration of the shortest features in a burst sets a limit on the size of the emission region because it can not be larger than the distance, light can travel during this time. If the material is moving close to the speed of light, the size may be larger by the Lorentz factor γ. The shortest observed structures were found in FRB 200120E and had a minimal duration of about $t = 60\,\mathrm{ns}$ (Nimmo et al., 2022). This results in an emission region size of only $d \leq c \cdot t \cdot \gamma = 18\,\mathrm{m} \cdot \gamma$. Typical durations of 1 ms imply a maximum size of $300\,\mathrm{km} \cdot \gamma$.

This tiny dimension is another hint towards neutron stars, because of their compact, highly energetic magnetic fields. There are two concurrent classes of emission models, near-field and far-field models (see Lyubarsky, 2021, for a review). In near-field models, the emission occurs within the magnetosphere. One possibility is curvature radiation emitted by bunches of electrons that move along the magnetic field lines. They might but are not required to be induced by starquakes in the neutron star crust or magnetic reconnections of the field lines in the magnetosphere.

Far-field models create the bursts outside the magnetosphere. One way of still reaching the high energies is through a synchrotron maser mechanism. The required large population inversions are reached via highly relativistic shocks, e.g., due to the wind of a young neutron star going into the supernova ejecta surrounding it (Metzger, Margalit, and Sironi, 2019).

1.6 Gravitational waves

The merger of two neutron stars as the origin of FRBs was one of the earliest proposed scenarios. FRBs have been suggested to arise in at least four different ways (see e.g. Rowlinson and Anderson, 2019). The interactions of magnetic fields before the merger might result in an FRB (Lipunov and Panchenko, 1996; Metzger and Zivancev, 2016). A jet that is launched during the merger could interact with the surrounding medium and produce an FRB (Usov and Katz, 2000). The neutron star resulting from the merger might emit FRBs in any way that has been suggested for neutron stars. Finally, the newly formed neutron star can collapse into a black hole if its mass exceeds a certain threshold. When this happens, its whole magnetic field snaps and recombines, which might result in an FRB (Falcke and Rezzolla, 2014). Although the expected merger rate is too low to produce all the FRBs that we observe, the synergies with other multi-messenger signals make this an interesting possibility. An FRB detection simultaneous with another signal from the merger would provide evidence for this model and open up interesting possibilities.

The first and most iconic sign of a neutron star merger is the gravitational wave (GW) that it produces. GWs come from the time variable gravitational field as the two neutron stars orbit each other. In general relativity, accelerations produce ripples in space-time that travel at the speed of light. The first GW from a double neutron star merger was GW170817, detected with the two GW experiments LIGO and Virgo (Abbott et al., 2017c). GW experiments are not very sensitive to the direction that a GW came from, but for this event, a multi-messenger effort could pin down the origin (Abbott et al., 2017d). Independently of the GW detection, a short gamma-ray burst (a type of < 2 s long transient in gamma-rays) was detected 1.7 s after the merger by the Fermi Gamma-ray Burst Monitor (Meegan et al., 2009). These two detections triggered a follow-up campaign across the electromagnetic spectrum. The location of the merger was constrained from the combination of the three GW detectors to within 31 deg^2 and to a distance of (40 ± 8) Mpc. In this big volume, a large number of teams and optical telescopes took part in the search for an optical counterpart, looking for changes compared to previous images of galaxies. The One-Meter Two-Hemispheres Collaboration was the first to find and report the kilonova counterpart (named SSS17a or AT 2017gfo), which they associated with the GW event. Kilonovae appear similar to supernovae but one to two orders of magnitude dimmer. They were previously associated with short gamma-ray bursts, which were theorized to come from a neutron star merger. The source of GW170817 was the first event where GW, gamma-ray burst, and kilonova were observed from the same source.

Subsequent follow-up yielded detections throughout the whole electromagnetic spectrum from X-rays, over ultraviolet and infrared, down to radio waves, which enabled countless scientific studies. The multi-messenger effort around GW170817 provided the strongest observational link between short gamma-ray bursts, kilonovae, and neutron star mergers. It provided 14 orders of magnitude better constraints on the speed of GWs to previous studies (Abbott et al., 2017b), constraining the difference from the speed of light to -3×10^{-15} and 7×10^{-16} times the speed of light. Comparison of the GW distance with the galaxy redshift enabled the first, still very imprecise, measurement of the local expansion of the universe with gravitational waves (Abbott et al., 2017a). These important findings showcase the importance and potential of electromagnetic counterparts to GWs.

1.6.1 A tentative FRB-GW association

The second double neutron star merger was GW190425 (Abbott et al., 2020). Unfortunately, this time, one of the LIGO detectors was temporarily offline, and the GW was so weak that Virgo detected it with a signal-to-noise ratio of only 2.5. This essential single detector discovery results in a very large 90 %

credible sky region of 8 284 deg^2, about a fifth of the sky. Consequently, no electromagnetic counterpart to the event could be found.

Later comparisons between catalogs have yielded a tentative association between GW190425 and FRB 190425A. Moroianu et al. (2023) searched for FRBs in the CHIME catalog (CHIME/FRB Collaboration et al., 2021) between 2 hours before and 24 hours after all GWs and found FRB 190425A 2.5 hours after the only double neutron star merger, GW190425, in the overlap between the CHIME and GW catalogs. The chances of getting such an association by chance are quite high when searching over 26 hours and considering CHIME's detection rate of 1.93 FRBs per day around the FRB 190425A. Yet, the sky location and distance can be used to lower the probability of a coincidence. The sky location does not significantly reduce the coincidence probability given the large GW localization region, which yields a chance probability to be in the region of $P_{\mathrm{S}} = 0.265$. The GW's inferred distance of $z = 0.03^{+0.01}_{-0.02}$, on the other hand, is low compared to the distances of most CHIME FRBs. The low DM of FRB 190425A of only 128.2 cm^{-3} pc implies a redshift of $z < 0.0394$. Combining these three factors, Moroianu et al. (2023) report a total chance coincidence probability of 0.0052 (2.8σ). They favor the collapse of the neutron star as the FRB model. Owing to the small distance, Panther et al. (2023) could also identify the most probable host of FRB 190425A to be the galaxy UGC10667 with 80 % confidence.

Some criticism can be passed on the method of the FRB-GW association. The above probability calculation does not account for the look-else-where effect. For example, it ignores that there is a non-negligible chance for CHIME to detect more than one FRB within the searched 26-hour window. Moreover, Bhardwaj et al. (2023) reestimate the GW parameters under the assumption that UGC10667 is the host. They argue that an FRB could not pass through the ejecta of a merger after only 2.5 hours without noticeable attenuation. They further infer a viewing angle of $> 30°$ on the system, disfavoring the FRB emission in our direction. In summary, the association between GW190425 and FRB 190425A is uncertain, but the possibility of neutron star mergers being the origin of a subpopulation of FRBs remains appealing.

1.7 Scientific goals of the thesis

This thesis broadly addresses two scientific questions:

- What are the origins of FRBs?
- How can we use these unique signals as tools to study the universe?

Chapter 2 gives a detailed overview of all applications of FRBs to astrophysical and cosmological problems. It is the result of an extensive literature review, intending to summarize the state of the field and assess the feasibility of applications in front of the background of our updated knowledge of, e.g., the FRB population.

Chapter 3 addresses the question of the origin of FRBs through an observational study of FRB 121102 with the Arecibo Telescope. With our detected burst population, we specifically address the following questions:

- What are the statistical burst properties?
- Do burst arrival times follow a pattern, or are they even periodic?
- What distributions do the burst energies follow, and are these always the same?

- What can the burst spectro-temporal structure tell us about the FRB origins?

This work has been published in Monthly Notices of the Royal Astronomical Society.

While Chapter 2 gives an overview of FRB applications, Chapter 4 addresses an aspect that was neglected in these studies. Many applications assume the distance to FRBs to be measured via their redshifts, but at the same time obtaining these through optical observations is regarded as the bottleneck of many applications. The work summarized in Chapter 4, which was likewise published in Monthly Notices of the Royal Astronomical Society, addresses the following questions:

- For how many FRBs, at which distances, can we measure the redshifts?
- How much are FRB applications affected by this limitation?
- Which applications are still possible in a realistic scenario?
- What are strategies to maximize the scientific output in case of limited optical follow-up time?

Motivated by the tentative GW-FRB association that we discussed in Section 1.6, Chapter 5 addresses the question:

- How can we use associated GW-FRB events like FRB 190425A in the absence of a localization?

Finally, Chapter 6 summarizes and recapitulates the achievements of this thesis.

References

Abbott, B. P. et al. (2017a), *A gravitational-wave standard siren measurement of the Hubble constant*, Nature **551** 85, arXiv: 1710.05835 [astro-ph.CO] (cit. on p. 12).

– (2017b), *Gravitational Waves and Gamma-Rays from a Binary Neutron Star Merger: GW170817 and GRB 170817A*, ApJ **848**, L13 L13, arXiv: 1710.05834 [astro-ph.HE] (cit. on p. 12).

– (2017c), *GW170817: Observation of Gravitational Waves from a Binary Neutron Star Inspiral*, Phys. Rev. Lett. **119**, 161101 161101, arXiv: 1710.05832 [gr-qc] (cit. on p. 12).

– (2017d), *Multi-messenger Observations of a Binary Neutron Star Merger*, ApJ **848**, L12 L12, arXiv: 1710.05833 [astro-ph.HE] (cit. on p. 12).

Abbott, B. P. et al. (2020), *GW190425: Observation of a Compact Binary Coalescence with Total Mass ~ 3.4 $M_\odot$*, ApJ **892**, L3 L3, arXiv: 2001.01761 [astro-ph.HE] (cit. on p. 12).

Bannister, K. W. and G. J. Madsen (2014), *A Galactic origin for the fast radio burst FRB010621*, MNRAS **440** 353, arXiv: 1402.0268 [astro-ph.GA] (cit. on p. 6).

Bannister, K. W. et al. (2019), *A single fast radio burst localized to a massive galaxy at cosmological distance*, Science **365** 565, ADS Bibcode: 2019Sci...365..565B, ISSN: 0036-8075, arXiv: 1906.11476 [astro-ph.HE], (visited on 04/20/2022) (cit. on pp. 3, 9).

Bassa, C. G. et al. (2017), *FRB 121102 Is Coincident with a Star-forming Region in Its Host Galaxy*, ApJ **843**, L8 L8, arXiv: 1705.07698 [astro-ph.HE] (cit. on p. 5).

Bethapudi, S. et al. (2023), *High frequency study of FRB 20180916B using the 100-m Effelsberg radio telescope*, MNRAS **524** 3303, arXiv: 2207.13669 [astro-ph.HE] (cit. on p. 4).

Bhandari, S. et al. (2022), *Characterizing the Fast Radio Burst Host Galaxy Population and its Connection to Transients in the Local and Extragalactic Universe*, AJ **163**, 69 69, arXiv: 2108.01282 [astro-ph.HE] (cit. on p. 11).

Bhardwaj, M. et al. (2023), *GW190425 and FRB20190425A: Challenges for Fast Radio Bursts as Multi-Messenger Sources from Binary Neutron Star Mergers*, arXiv e-prints, arXiv:2306.00948 arXiv:2306.00948, arXiv: 2306.00948 [astro-ph.HE] (cit. on p. 13).

Bochenek, C. D. et al. (2020), *A fast radio burst associated with a Galactic magnetar*, Nature **587** 59, arXiv: 2005.10828 [astro-ph.HE] (cit. on p. 8).

Chatterjee, S. et al. (2017), *A direct localization of a fast radio burst and its host*, Nature **541** 58, arXiv: 1701.01098 [astro-ph.HE] (cit. on p. 7).

CHIME Collaboration et al. (2022), *An Overview of CHIME, the Canadian Hydrogen Intensity Mapping Experiment*, ApJS **261**, 29 29, arXiv: 2201.07869 [astro-ph.IM] (cit. on p. 9).

CHIME/FRB Collaboration et al. (2019), *CHIME/FRB Discovery of Eight New Repeating Fast Radio Burst Sources*, ApJ **885**, L24 L24, arXiv: 1908.03507 [astro-ph.HE] (cit. on pp. 7, 9).

CHIME/FRB Collaboration et al. (2020a), *A bright millisecond-duration radio burst from a Galactic magnetar*, Nature **587** 54, arXiv: 2005.10324 [astro-ph.HE] (cit. on p. 8).

CHIME/FRB Collaboration et al. (2020b), *Periodic activity from a fast radio burst source*, Nature **582** 351, arXiv: 2001.10275 [astro-ph.HE] (cit. on p. 7).

CHIME/FRB Collaboration et al. (2021), *The First CHIME/FRB Fast Radio Burst Catalog*, ApJS **257**, 59 59, arXiv: 2106.04352 [astro-ph.HE] (cit. on pp. 1–3, 9, 13).

Chime/Frb Collaboration et al. (2023), *CHIME/FRB Discovery of 25 Repeating Fast Radio Burst Sources*, ApJ **947**, 83 83, arXiv: 2301.08762 [astro-ph.HE] (cit. on pp. 7, 9).

Cruces, M. et al. (2021), *Repeating behaviour of FRB 121102: periodicity, waiting times, and energy distribution*, MNRAS **500** 448, arXiv: 2008.03461 [astro-ph.HE] (cit. on p. 7).

Dewdney, P. E. et al. (2009), *The Square Kilometre Array*, IEEE Proceedings **97** 1482 (cit. on p. 9).

Eatough, R. P. et al. (2013), *A strong magnetic field around the supermassive black hole at the centre of the Galaxy*, Nature **501** 391, arXiv: 1308.3147 [astro-ph.GA] (cit. on p. 7).

Falcke, H. and L. Rezzolla (2014), *Fast radio bursts: the last sign of supramassive neutron stars*, A&A **562**, A137 A137, arXiv: 1307.1409 [astro-ph.HE] (cit. on p. 12).

Gajjar, V. et al. (2018), *Highest Frequency Detection of FRB 121102 at 4-8 GHz Using the Breakthrough Listen Digital Backend at the Green Bank Telescope*, ApJ **863**, 2 2, arXiv: 1804.04101 [astro-ph.HE] (cit. on p. 1).

Gordon, A. C. et al. (2023), *The Demographics, Stellar Populations, and Star Formation Histories of Fast Radio Burst Host Galaxies: Implications for the Progenitors*, ApJ **954**, 80 80, arXiv: 2302.05465 [astro-ph.GA] (cit. on p. 11).

Gourdji, K. et al. (2019), *A Sample of Low-energy Bursts from FRB 121102*, ApJ **877**, L19 L19, arXiv: 1903.02249 [astro-ph.HE] (cit. on p. 7).

Heintz, K. E. et al. (2020), *Host Galaxy Properties and Offset Distributions of Fast Radio Bursts: Implications for Their Progenitors*, ApJ **903**, 152 152, arXiv: 2009.10747 [astro-ph.GA] (cit. on p. 11).

Hessels, J. W. T. et al. (2019), *FRB 121102 Bursts Show Complex Time-Frequency Structure*, ApJ **876**, L23 L23, arXiv: 1811.10748 [astro-ph.HE] (cit. on p. 7).

Hewish, A. et al. (1968), *Observation of a Rapidly Pulsating Radio Source*, Nature **217** 709 (cit. on pp. 1, 10).

Hilmarsson, G. H. et al. (2021), *Rotation Measure Evolution of the Repeating Fast Radio Burst Source FRB 121102*, ApJ **908**, L10 L10, arXiv: 2009.12135 [astro-ph.HE] (cit. on p. 7).

Hotan, A. W. et al. (2021), *Australian square kilometre array pathfinder: I. system description*, PASA **38**, e009 e009, arXiv: 2102.01870 [astro-ph.IM] (cit. on p. 9).

Igoshev, A. P., S. B. Popov, and R. Hollerbach (2021), *Evolution of Neutron Star Magnetic Fields*, Universe **7** 351, arXiv: 2109.05584 [astro-ph.HE] (cit. on p. 10).
James, C. W. et al. (2022), *The z-DM distribution of fast radio bursts*, MNRAS **509** 4775, arXiv: 2101.08005 [astro-ph.HE] (cit. on p. 11).
Josephy, A. et al. (2021), *No Evidence for Galactic Latitude Dependence of the Fast Radio Burst Sky Distribution*, ApJ **923**, 2 2, arXiv: 2106.04353 [astro-ph.HE] (cit. on p. 2).
Karuppusamy, R., B. W. Stappers, and W. van Straten (2010), *Giant pulses from the Crab pulsar. A wide-band study*, A&A **515**, A36 A36, arXiv: 1004.2803 [astro-ph.GA] (cit. on p. 11).
Kaspi, V. M. and A. M. Beloborodov (2017), *Magnetars*, ARA&A **55** 261, arXiv: 1703.00068 [astro-ph.HE] (cit. on p. 10).
Keane, E. F. et al. (2012), *On the origin of a highly dispersed coherent radio burst*, MNRAS **425** L71, arXiv: 1206.4135 [astro-ph.SR] (cit. on p. 6).
Kirsten, F. et al. (2021), *Detection of two bright radio bursts from magnetar SGR 1935 + 2154*, Nature Astronomy **5** 414, arXiv: 2007.05101 [astro-ph.HE] (cit. on p. 8).
Kulkarni, S. R. (2020), *Dispersion measure: Confusion, Constants & Clarity*, arXiv e-prints, arXiv:2007.02886 arXiv:2007.02886, arXiv: 2007.02886 [astro-ph.HE] (cit. on p. 4).
Li, C. K. et al. (2021), *HXMT identification of a non-thermal X-ray burst from SGR J1935+2154 and with FRB 200428.*, Nature Astronomy **5** 378, arXiv: 2005.11071 [astro-ph.HE] (cit. on p. 8).
Li, D. et al. (2021), *A bimodal burst energy distribution of a repeating fast radio burst source*, Nature **598** 267, arXiv: 2107.08205 [astro-ph.HE] (cit. on pp. 6, 7).
Li, D. and J. J. Zanazzi (2021), *Emission Properties of Periodic Fast Radio Bursts from the Motion of Magnetars: Testing Dynamical Models*, ApJ **909**, L25 L25, arXiv: 2101.05836 [astro-ph.HE] (cit. on p. 4).
Li, Z. et al. (2020), *Cosmology-insensitive estimate of IGM baryon mass fraction from five localized fast radio bursts*, MNRAS **496** L28, arXiv: 2004.08393 [astro-ph.HE] (cit. on p. 7).
Lipunov, V. M. and I. E. Panchenko (1996), *Pulsars revived by gravitational waves.*, A&A **312** 937, arXiv: astro-ph/9608155 [astro-ph] (cit. on p. 12).
Lorimer, D. R. and M. Kramer (2004), *Handbook of Pulsar Astronomy*, 4, Cambridge University Press (cit. on p. 10).
Lorimer, D. R. et al. (2007), *A Bright Millisecond Radio Burst of Extragalactic Origin*, Science **318** 777, arXiv: 0709.4301 [astro-ph] (cit. on pp. 1, 6).
Lorimer, D. R. (2008), *Binary and Millisecond Pulsars*, Living Reviews in Relativity **11**, 8 8, arXiv: 0811.0762 [astro-ph] (cit. on p. 3).
Lyubarsky, Y. (2021), *Emission Mechanisms of Fast Radio Bursts*, Universe **7** 56, arXiv: 2103.00470 [astro-ph.HE] (cit. on p. 11).
Main, R. A. et al. (2022), *Scintillation time-scale measurement of the highly active FRB20201124A*, MNRAS **509** 3172, arXiv: 2108.00052 [astro-ph.HE] (cit. on p. 4).
Mandel, I. and F. S. Broekgaarden (2022), *Rates of compact object coalescences*, Living Reviews in Relativity **25**, 1 1, arXiv: 2107.14239 [astro-ph.HE] (cit. on p. 11).
Marcote, B. et al. (2017), *The Repeating Fast Radio Burst FRB 121102 as Seen on Milliarcsecond Angular Scales*, ApJ **834**, L8 L8, arXiv: 1701.01099 [astro-ph.HE] (cit. on pp. 5, 7).
Marcote, B. et al. (2020), *A repeating fast radio burst source localized to a nearby spiral galaxy*, Nature **577** 190, arXiv: 2001.02222 [astro-ph.HE] (cit. on p. 7).

McLaughlin, M. A. et al. (2006), *Transient radio bursts from rotating neutron stars*, Nature **439** 817, arXiv: astro-ph/0511587 [astro-ph] (cit. on p. 1).
Meegan, C. et al. (2009), *The Fermi Gamma-ray Burst Monitor*, ApJ **702** 791, arXiv: 0908.0450 [astro-ph.IM] (cit. on p. 12).
Mereghetti, S. et al. (2020), *INTEGRAL Discovery of a Burst with Associated Radio Emission from the Magnetar SGR 1935+2154*, ApJ **898**, L29 L29, arXiv: 2005.06335 [astro-ph.HE] (cit. on p. 8).
Mereghetti, S. (2023), *INTEGRAL contributions to magnetars and multimessenger astrophysics*, IAU Symposium **363** 259 (cit. on p. 8).
Metzger, B. D., B. Margalit, and L. Sironi (2019), *Fast radio bursts as synchrotron maser emission from decelerating relativistic blast waves*, MNRAS **485** 4091, arXiv: 1902.01866 [astro-ph.HE] (cit. on p. 11).
Metzger, B. D. and C. Zivancev (2016), *Pair fireball precursors of neutron star mergers*, MNRAS **461** 4435, arXiv: 1605.01060 [astro-ph.HE] (cit. on p. 12).
Michilli, D. et al. (2018), *An extreme magneto-ionic environment associated with the fast radio burst source FRB 121102*, Nature **553** 182, arXiv: 1801.03965 [astro-ph.HE] (cit. on pp. 5, 7).
Moroianu, A. et al. (2023), *An assessment of the association between a fast radio burst and binary neutron star merger*, Nature Astronomy **7** 579, arXiv: 2212.00201 [astro-ph.HE] (cit. on p. 13).
Nimmo, K. et al. (2022), *Burst timescales and luminosities as links between young pulsars and fast radio bursts*, Nature Astronomy **6** 393, arXiv: 2105.11446 [astro-ph.HE] (cit. on p. 11).
Ocker, S. K. et al. (2022), *The Large Dispersion and Scattering of FRB 20190520B Are Dominated by the Host Galaxy*, ApJ **931**, 87 87, arXiv: 2202.13458 [astro-ph.HE] (cit. on p. 4).
Panther, F. H. et al. (2023), *The most probable host of CHIME FRB 190425A, associated with binary neutron star merger GW190425, and a late-time transient search*, MNRAS **519** 2235, arXiv: 2212.00954 [astro-ph.HE] (cit. on p. 13).
Petroff, E., J. W. T. Hessels, and D. R. Lorimer (2019), *Fast radio bursts*, A&A Rev. **27**, 4 4, arXiv: 1904.07947 [astro-ph.HE] (cit. on pp. 2, 10).
Platts, E. et al. (2019), *A living theory catalogue for fast radio bursts*, Phys. Rep. **821** 1, arXiv: 1810.05836 [astro-ph.HE] (cit. on p. 9).
Pleunis, Z. et al. (2021), *LOFAR Detection of 110-188 MHz Emission and Frequency-dependent Activity from FRB 20180916B*, ApJ **911**, L3 L3, arXiv: 2012.08372 [astro-ph.HE] (cit. on p. 1).
Rajwade, K. M. et al. (2020), *Possible periodic activity in the repeating FRB 121102*, MNRAS **495** 3551, arXiv: 2003.03596 [astro-ph.HE] (cit. on p. 7).
Ridnaia, A. et al. (2021), *A peculiar hard X-ray counterpart of a Galactic fast radio burst*, Nature Astronomy **5** 372, arXiv: 2005.11178 [astro-ph.HE] (cit. on p. 8).
Rowlinson, A. and G. E. Anderson (2019), *Constraining coherent low-frequency radio flares from compact binary mergers*, MNRAS **489** 3316, arXiv: 1905.02509 [astro-ph.HE] (cit. on p. 12).
Seebeck, J. et al. (2021), *The Effects of Selection Biases on the Analysis of Localised Fast Radio Bursts*, arXiv e-prints, arXiv:2112.07639 arXiv:2112.07639, arXiv: 2112.07639 [astro-ph.HE] (cit. on p. 4).
Shin, K. et al. (2023), *Inferring the Energy and Distance Distributions of Fast Radio Bursts Using the First CHIME/FRB Catalog*, ApJ **944**, 105 105, arXiv: 2207.14316 [astro-ph.HE] (cit. on p. 11).

Silva, R. M. et al. (2012), *Optical Current Sensors for High Power Systems: A Review*, Applied Sciences **2** 602, ISSN: 2076-3417 (cit. on p. 3).
Spitler, L. G. et al. (2014), *Fast Radio Burst Discovered in the Arecibo Pulsar ALFA Survey*, ApJ **790**, 101 101, arXiv: 1404.2934 [astro-ph.HE] (cit. on pp. 6, 9).
Spitler, L. G. et al. (2016), *A repeating fast radio burst*, Nature **531** 202, arXiv: 1603.00581 [astro-ph.HE] (cit. on pp. 5, 6).
Tavani, M. et al. (2021), *An X-ray burst from a magnetar enlightening the mechanism of fast radio bursts*, Nature Astronomy **5** 401, arXiv: 2005.12164 [astro-ph.HE] (cit. on p. 8).
Tendulkar, S. P. et al. (2017), *The Host Galaxy and Redshift of the Repeating Fast Radio Burst FRB 121102*, ApJ **834**, L7 L7, arXiv: 1701.01100 [astro-ph.HE] (cit. on pp. 3, 7).
Tendulkar, S. P. et al. (2021), *The 60 pc Environment of FRB 20180916B*, ApJ **908**, L12 L12, arXiv: 2011.03257 [astro-ph.HE] (cit. on p. 8).
Thornton, D. et al. (2013), *A Population of Fast Radio Bursts at Cosmological Distances*, Science **341** 53, arXiv: 1307.1628 [astro-ph.HE] (cit. on pp. 3, 6).
Usov, V. V. and J. I. Katz (2000), *Low frequency radio pulses from gamma-ray bursts?* A&A **364** 655, arXiv: astro-ph/0002278 [astro-ph] (cit. on p. 12).

CHAPTER 2

FRBs as tools

FRBs are the first class of radio sources varying on sub-second timescales and detectable at cosmological distances. The potential of such sources was anticipated long ago. When the quasar CTA-102 showed variations on a timescale of 100 days (Sholomitsky, 1965), Haddock and Sciama (1965) proposed the search for variations on shorter time scales to measure their dispersion. The goal was to distinguish between cosmological models that predicted an ionized intergalactic gas and those that did not, as well as to distinguish between an Einstein–de Sitter model and a steady-state model for the universe. After the discovery of pulsars, Weinberg (1972) added the idea of using hypothetical pulsars in nearby galaxies to study the ionized medium in between. The discovery of gamma-ray bursts (GRBs) sparked new hope that a small fraction of the energy could be observable as a radio flare to probe the intergalactic gas density (Ginzburg, 1973). The idea was later picked up again as a way to study GRBs (Palmer, 1993; Lipunova, Panchenko, and Lipunov, 1997) and to study the reionization history of the Universe (Ioka, 2003; Inoue, 2004). However, quasars never showed variations that were short enough to measure a *DM*, and no fast radio counterparts to GRBs could be found. Even though some of the models that were suggested have been falsified in the meantime, the principles are still the same as the ones behind many proposed FRB applications. Chiefly, the discovery of FRBs represents a realization of astronomers' long-held aspirations.

The main measurement quantity of interest is the *DM*. In Eq. (1.1), we introduced *DM* as the integral over all the free (non-relativistic) electrons along the FRB path. Since they are of different use to us, we split the *DM* into three components coming from the FRB host galaxy $DM_{\rm host}$, the ionized IGM $DM_{\rm IGM}$, and the ionized component of the inter-stellar medium of the Milky Way $DM_{\rm MW}$ such that (Deng and B. Zhang, 2014)

$$DM = DM_{\rm MW} + DM_{\rm IGM} + DM_{\rm host,obs}\,. \tag{2.1}$$

$DM_{\rm IGM}$ is the most interesting component because we can use it for astrophysical and cosmological studies. According to cosmological hydrodynamic simulations, the IGM is filled with a warm-to-hot plasma at temperatures of $T = 10^5$–10^7 K (Davé et al., 2001). It is very sparse with densities of 0.3 atoms m^{-3}, but if FRBs are far enough away, $DM_{\rm IGM}$ can dominate over the denser but shorter paths in the Milky Way and the host galaxy.

To calculate the expected $DM_{\rm IGM}$ from known quantities, we need to carry out four steps and consider the effects of an expanding Universe: (1) how it stretches an emitted radio wave, (2) how the length of the light-path changes, (3) how the expansion changes the average electron density, and lastly (4) we need to express the electron number density in terms of the better known mass density of the Universe. Because of

its importance for FRBs, we will carry out the full derivation here.

In the expanding Universe which we live in, an integration over the electron density needs to account for the expansion. The scale factor $a(t)$ describes the fraction of a length at time t after the Big Bang to the length it would have today; since today is the reference, it fixes $a(0) = 1$. The scale factor is related to the redshift as $a = 1/(1+z)$. Let us assume a host galaxy at redshift z, which imposes a dispersion of DM_{host} on the FRB in its rest frame. Following Eq. (1.1), in the rest frame, it will cause a delay of $\Delta t_0 = K\,DM_{\mathrm{host}}/\nu_0^2$ at frequency ν_0. Today, the distance between very high frequencies and the retarded wave at ν_0 has grown with the Universe and the delay increased to $\Delta t = \Delta t_0/a$. At the same time, the wavelength λ_0 has increased by the same factor, and we observe $\lambda = \lambda_0/a$ and therefore $\nu = a\,\nu_0$. It follows that

$$DM_{\mathrm{host,obs}} = \frac{\Delta t\,\nu^2}{K} = \frac{\Delta t_0\,a\,\nu_0}{K} = \frac{DM_{\mathrm{host}}}{1+z}\,. \tag{2.2}$$

Accordingly, every infinitesimal $\mathrm{d}DM'$ that originates at redshift z is observed as $\mathrm{d}DM = \frac{\mathrm{d}DM'}{1+z}$.

The change of the light-path (2) is contained in the line element $\mathrm{d}\ell$ in Eq. (1.1). We want to express it in terms of the redshift, which is the most precise distance we can measure at large distances. The proper distance $\mathrm{d}\ell$ that light travels in a time $\mathrm{d}t$ is $c\,\mathrm{d}t$ (formally this is described by the Friedmann–Lemaître–Robertson–Walker metric). Because we define distances away from us, the path element is $\mathrm{d}\ell = -c\,\mathrm{d}t$. To further express $\mathrm{d}t$, we use the Hubble parameter $H(t)$, which is defined as the relative change of the scale factor, i.e., $H(t) \equiv \dot{a}/a = a^{-1}\,\frac{\mathrm{d}a}{\mathrm{d}t}$. Since $a = \frac{1}{1+z}$, the derivative is $\frac{\mathrm{d}a}{\mathrm{d}z} = -a^2$. Sequentially replacing the differentials (see e.g. Schneider, 2006) yields

$$\mathrm{d}\ell = -c\,\mathrm{d}t = -\frac{c\,\mathrm{d}a}{aH} = \frac{c\,\mathrm{d}z}{(1+z)\,H(z)}\,. \tag{2.3}$$

Now we consider (3) the effects of the expanding Universe on the electron density n_e. The average density shrinks with advancing expansion as the volume increases. Using the comoving number density $n_{e,0}(z)$, the density becomes

$$n_e(z) = (1+z)^3 n_{e,0}(z)\,. \tag{2.4}$$

Lastly, (4) we want to express $n_{e,0}$ in terms of the mass density of baryons, since that is measured by other experiments. The baryon density ρ_{b} is typically written as the dimensionless quantity

$$\Omega_{\mathrm{b}} = \frac{\rho_{\mathrm{b}}}{\rho_{\mathrm{c}}}\,, \quad \text{relative to the } \textit{critical density} \quad \rho_{\mathrm{c}} = \frac{3H_0^2}{8\pi G}\,, \tag{2.5}$$

defined as the present-day density at which the Universe would be flat, here G is the gravitational constant $G = (6.67430 \pm 0.00015) \times 10^{-8}\,\mathrm{cm^3\,g^{-1}\,s^{-2}}$ and H_0 is the *Hubble constant*, which describes the present-day expansion rate. The baryonic mass of the Universe consists of $3/4$ of hydrogen and $1/4$ of helium (Coc and Vangioni, 2017). A hydrogen atom weighs about the mass of a proton $m_{\mathrm{p}} = 1.67262192369(51) \times 10^{-24}\,\mathrm{g}$ (Workman et al., 2022), and a helium atom weighs about $4m_{\mathrm{p}}$, thus their average number density today is

$$n_{\mathrm{H},0} = \frac{3}{4}\frac{\rho_{\mathrm{b}}}{m_{\mathrm{p}}} = \frac{3}{4}\frac{\Omega_{\mathrm{b}}\rho_{\mathrm{c}}}{m_{\mathrm{p}}} \quad \text{and} \quad n_{\mathrm{He},0} = \frac{1}{4}\frac{\rho_{\mathrm{b}}}{4m_{\mathrm{p}}} = \frac{1}{16}\frac{\Omega_{\mathrm{b}}\rho_{\mathrm{c}}}{m_{\mathrm{p}}}\,, \tag{2.6}$$

respectively. To get the electron density, a factor 2 considers that helium can contribute two electrons per atom. The ionization fractions $\chi_{\mathrm{H}}(z)$ and $\chi_{\mathrm{He}}(z)$ ensure that only the free electrons that contribute to the dispersion are counted. Finally, some mass is bound in galaxies, which we account for by multiplying

with the fraction of diffuse baryons in the IGM $f_{\rm IGM}(z)$. The ionized electron number density in the IGM follows with Eqs. (2.5) and (2.6) as (Deng and B. Zhang, 2014)

$$n_{e,0}(z) = f_{\rm IGM}(z)\left[n_{\rm H,0}\,\chi_{\rm H}(z) + 2\,n_{\rm He,0}\,\chi_{\rm He}(z)\right] = \frac{\Omega_{\rm b}\rho_{\rm c}}{m_{\rm p}} f_{\rm IGM}(z)\left[\frac{3}{4}\chi_{\rm H}(z) + \frac{1}{8}\chi_{\rm He}(z)\right] \tag{2.7}$$

$$= \frac{3\Omega_{\rm b}H_0^2}{8\pi G m_{\rm p}} f_{\rm IGM}(z)\left[\frac{3}{4}\chi_{\rm H}(z) + \frac{1}{8}\chi_{\rm He}(z)\right] \tag{2.8}$$

Collecting all the ingredients from Eqs. (2.2) to (2.4) and (2.8) yields the sight line averaged (Ioka, 2003; Inoue, 2004; Deng and B. Zhang, 2014)

$$\langle DM_{\rm IGM}\rangle(z) = \int \frac{n_e(z)}{1+z}\,{\rm d}\ell = \int_0^z \frac{(1+z)^3 n_{e,0}(z)}{(1+z)^2}\frac{c\,{\rm d}z}{H(z)} \tag{2.9}$$

$$= \frac{3c}{8\pi G m_{\rm p}}\Omega_{\rm b}H_0^2\int_0^z \frac{(1+z) f_{\rm IGM}(z)\left[\frac{3}{4}\chi_{\rm H}(z) + \frac{1}{8}\chi_{\rm He}(z)\right]}{H(z)}\,{\rm d}z\,. \tag{2.10}$$

The Hubble parameter encompasses the cosmological model. In the standard cosmological model – the Lambda cold dark matter model (ΛCDM) – it can be expressed in terms of $\Omega_{\rm m}$ and Ω_Λ, the matter and dark energy densities, respectively, in units of the critical density. Further assuming a flat Universe, the Hubble parameter takes the form $H(z) = H_0\sqrt{\Omega_{\rm m}(1+z)^3 + \Omega_\Lambda}$, where $\Omega_\Lambda = 1 - \Omega_{\rm m}$ because of the flatness assumption (see e.g. Peacock, 1999).

Several approximations to Eq. (2.10) can be useful under certain circumstances. The reionization epochs of H and He II are expected at $z \sim 7$ and 3, respectively. Therefore, $\chi_{\rm H} = 1$ and $\chi_{\rm He} = 1$ can be assumed below $z \sim 2$ (McQuinn et al., 2009). At low redshifts, $f_{\rm IGM}$ does not change much and can be approximated as a constant. Further, the integral can be simplified by its Taylor approximation as z. Depending on the use case, one might therefore write Eq. (2.10) as

$$\langle DM_{\rm IGM}\rangle(z) \approx \frac{3c}{8\pi G m_{\rm p}}\frac{7}{8}\Omega_{\rm b}f_{\rm IGM}H_0\int_0^z \frac{1+z}{\sqrt{\Omega_{\rm m}(1+z)^3 + \Omega_\Lambda}}\,{\rm d}z \approx \frac{3c}{8\pi G m_{\rm p}}\frac{7}{8}\Omega_{\rm b}f_{\rm IGM}H_0\,z\,. \tag{2.11}$$

For back of the envelope estimates $\langle DM_{\rm IGM}\rangle(z) \sim 1000\,z\,{\rm cm^{-3}}$ pc is easy to remember.

All the quantities in Eq. (2.10) influence DM and can conversely in principle be probed with FRBs. This includes the baryons in the IGM ($\Omega_{\rm b}f_{\rm IGM}$), the Hubble constant, the ionization history of the universe in $\chi_{\rm H}$ and $\chi_{\rm He}$, and the cosmological parameters in $H(z)$, $\Omega_{\rm m}$ and Ω_Λ. However, two main difficulties challenge all applications of FRBs. The contribution from $DM_{\rm host}$ can dominate DM, particularly at low redshifts (the estimated $DM_{\rm host} = 903^{+72}_{-111}$ cm^{-3} pc of FRB 190520B is one extreme example, see Niu et al., 2022), and it can principally not be well determined because of the unknown line of sight through the host galaxy. Furthermore, $DM_{\rm IGM}$ has a large variance because the matter in the IGM is not homogeneous but forms a large-scale structure – the cosmic web – made of sheets, filaments, and clusters. Both of these scatters cause large uncertainties in $DM_{\rm IGM}$ and any parameters inferred from the measurements. The third variation in DM, coming from $DM_{\rm MW}$, is usually small compared to host and cosmic variations but can be relevant for FRBs close to the Galactic disc, i.e., at galactic latitudes below $|b| \sim 15°$ (Price, Flynn, and Deller, 2021). Uncertainties can only be confined by observing a large number of FRBs, with the value depending on the application and desired precision.

The most important additional measurement quantity is the FRB redshift, which cannot be obtained

from the radio signal. This uncloaks the importance of arcsecond-precision localizations, because the redshift can only be obtained through the identification of the host galaxy and a subsequent spectroscopic measurement. This optical or infrared follow-up will be the bottleneck for many future FRB applications, as we will investigate in Chapter 4. FRBs without a redshift can still be used for the same purposes using statistical methods. However, this requires good knowledge of telescope beam shape and the FRB population, which previously needs to be studied with localized FRBs. If these prerequisites are fulfilled, the number of unlocalized FRBs required to reach a given uncertainty remains at least an order of magnitude higher than the number of localized FRBs; the exact factor depends on the application and the FRB redshift distribution.

In the following, we will discuss the various proposed usages of FRBs. Table 2.1 summarizes some key properties of these applications including, if available, the number of FRBs that is required to reach a specified goal.

2.1 Baryons in the IGM

2.1.1 The missing baryon problem

Interest in the search for ionized gas in the IGM got renewed when a census of all the observed present-day baryonic matter revealed a deficit of about 50 % (Persic and Salucci, 1992; Fukugita, Hogan, and Peebles, 1998). The total baryon density was well constrained by $z > 2$ hydrogen absorption lines (Rauch, 1998) and independently from measured deuterium to hydrogen ratios combined with Big Bang nucleosynthesis theory (Tytler, Fan, and Burles, 1996). Yet, only half of the known density was detectable in the nearby Universe in the form of stars, dust, and gas within galaxies as well as in galaxy groups and galaxy clusters. Cosmological hydrodynamic simulations, assuming the ΛCDM model, confirmed conjectures that the baryons should reside in the IGM in the form of an ionized warm-to-hot medium (Cen and Ostriker, 1999; Davé et al., 2001). However, this thin plasma is very difficult to detect. This became known as the *missing baryon problem*. Notably, the missing baryons have been observed at earlier stages of the Universe and are therefore not related to dark matter, which does not interact electromagnetically.

Various studies have since tried to find the missing baryons and detected some phases. Methods include X-ray observations of their emission (Eckert et al., 2015), stacking of the thermal Sunyaev-Zeldovich (SZ) effect of filaments (de Graaff et al., 2019), and quasar absorption line studies of H I, O VI, and O VII (Nicastro et al., 2018). FRBs offer the first probe of the missing baryons that is completely independent of their temperature and can account for every electron along the way (as long as the electrons are non-relativistic).

In Eq. (2.10), the baryons are contained in $\Omega_\mathrm{b} f_\mathrm{IGM}$ (Deng and B. Zhang, 2014). We can therefore directly measure them when we apply external constraints on H_0, e.g., from cosmic microwave background (CMB), type Ia supernova, or baryonic acoustic oscillation measurements. Staying agnostic about the value of H_0, J. .-. Macquart et al. (2020) used the first five localized ASKAP FRBs and (fixing $f_\mathrm{IGM} = 0.85$) obtained $\Omega_\mathrm{b} = 0.051^{+0.021}_{-0.025}\, h_{70}$, where $h_{70} = H_0/(70\,\mathrm{km\,s^{-1}\,Mpc^{-1}})$. This result agrees with CMB measurements, which yield $\Omega_\mathrm{b} = (0.0454 \pm 0.0003)\, h_{70}^2$ (Planck Collaboration et al., 2016).

2.1.2 Locating the baryons

Beyond detecting the missing baryons, it is especially interesting where in the ISM the baryons reside (McQuinn, 2014). This is not contained in the average DM_IGM but in the full probability density function (PDF) $p(DM_\mathrm{IGM} \mid z)$. It is determined by the inhomogeneous matter distribution. Homogeneously

Table 2.1: Summary of some FRB applications discussed in this Chapter.

Application	Quantity of interest	Condition	Redshift[a]	Goal	Number[b]	Reference
Currently available					690	FRB Newsletter 2023-08
With redshift		measured redshift	$z \leq 0.66$		39	FRB Newsletter 2023-08
Detect Baryons	$\Omega_{\rm b}, f_{\rm IGM}$	measured redshift	high	$\Omega_{\rm b} f_{\rm IGM}$ to 10 %	500	Jahns-Schindler et al. (2023)
Locate Baryons	F, halo profile	measured redshift	high	$F \sim \pm 0.15$	100	Baptista et al. (2023)
Milky Way halo	$DM_{\rm MW,halo}$	very nearby	low		–	
Hubble parameter	H_0	measured redshift	high	$\pm 2.5\,{\rm km\,s^{-1}\,Mpc^{-1}}$	100	James et al. (2022)
Other parameters	$\Omega_{\rm m}$, Ω_Λ, w	measured redshift	high		–	
H0 via lensing	H_0	lensed repeater			–	
Microlensing	10–100 $\rm M_\odot$	halo intersected		existing 35 % constraints	170	Sammons et al. (2020)
Diffractive lensing	10^{-4}–10^{-1} $\rm M_\odot$	halo intersected			–	
H EoR	$DM_{\rm max}$, $z_{\rm H}$, $\chi_{\rm H}$		$z \sim 7$	$\sigma(DM_{\rm max}) < 500\,{\rm cm^{-3}\,pc}$	5×10^3	Beniamini et al. (2021)
He EoR	$z_{\rm He}$, $\chi_{\rm He}$	measured redshift	$z \sim 3$	5σ detection	500	Linder (2020)
IGM magnetic fields	RM	measured redshift	high	Discriminate origins	$> 10^3$	Hackstein et al. (2019)
Photon mass	m_γ	measured redshift	$z \lesssim 1$	$m_\gamma < 4.8 \times 10^{48}$ kg	17	Lin, Tang, and Zou (2023)
CMB optical depths	τ		$z \gtrsim 8$		–	

[a] "high" means the higher the better, "low" means the lower the better.

[b] The number is always related to the goal. No number means that no suitable forecast exists, possibly because a trustworthy forecast is not possible with our current knowledge.

distributed matter would give a PDF sharply concentrated around the mean, while strongly concentrated matter yields very stochastic values of $DM_{\rm IGM}$ and hence a broad PDF with a long tail (McQuinn, 2014; J. P. Macquart et al., 2015). Galaxies themselves are intersected very rarely (Prochaska and Neeleman, 2018, estimate an average of 0.01 cm^{-3} pc for $z = 2$ FRBs). The PDF is rather defined by the shapes and extents of the large halos around galaxies, galaxy groups, and galaxy clusters (Jaroszynski, 2019; Batten et al., 2021). Furthermore, the distribution of baryons in the large scale structure influences the PDF; an FRB intersecting a filament or a cluster will have a much higher *DM* than one that travels mostly through voids. The baryon content of these structures will again influence the shape of the PDF.

It may surprise that the baryon distribution is not completely understood. Surely, it is mostly described by the gravitational wells of the underlying dark matter and the laws of magnetohydrodynamics. Hence, large magnetohydrodynamic simulations can mostly describe the resulting baryon distribution. However, the feedback from stars, supernovae, and the jets of active galactic nuclei (AGN) is difficult to model but plays an important role in galaxy evolution through modulating the star formation rate and the inflow of gas from the IGM (Davé, Oppenheimer, and Finlator, 2011; Davé, Finlator, and Oppenheimer, 2011). Feedback also throws baryons out of their galaxies into the circumgalactic medium and back into the IGM, producing shocks and heating it up. Additional to galaxy evolution, the resulting distribution is important in future observational cosmology (Chisari et al., 2019). FRBs can take up the role of distinguishing different distributions from the form of the PDF. The distribution would allow drawing conclusion on the feedback mechanisms at play (Batten et al., 2022; Baptista et al., 2023).

Simulations show that $p(DM_{\rm IGM} \mid z)$ is in all cases expected to have a long tail (McQuinn, 2014), quite different from the frequently used normal distribution. One such distribution that is frequently used is (Miralda-Escudé, Haehnelt, and Rees, 2000; J. .-. Macquart et al., 2020)

$$p_{\rm cosmic}(DM_{\rm IGM} \mid z) = A\Delta^{-3} \exp\left(-\frac{(\Delta^{-3} - C_0)^2}{18\,\sigma^2}\right), \quad \sigma = \frac{F}{\sqrt{z}}, \tag{2.12}$$

with parameters $\alpha = 3$, $\beta = 3$, and the *fluctuation parameter* F. One open question is how the connection between F and the matter distribution, as well as the cosmological parameter σ_8, can be modeled and what the relative contributions are.

Since the fluctuation parameter is influenced by both, the LSS and smaller (galaxy) halos, one future challenge is how to disentangle the two. A promising route is to do additional optical follow-up observations around the FRB location, which can be used in three main ways. (I) The general underlying LSS can be mapped extrapolating the galaxy distribution and cross-matched with the FRB positions (Lee et al., 2022). (II) Impact parameters between FRB and galaxies can be measured and together with galaxy properties lead to much better measurements of galaxy halo profiles (Ravi et al., 2019; Prochaska and Y. Zheng, 2019; Simha et al., 2020). (III) Intersected galaxy clusters can be identified, which can explain large *DM*s (Simha et al., 2023; Lee et al., 2023).

When redshifts are not obtainable because of large location uncertainties, FRBs can still be used in a statistical way, yet with less constraining power. Cross-correlating the coarse FRB locations with galaxy catalogs optical measurements can improve constraints on baryons (Rafiei-Ravandi, Smith, and Masui, 2020; Rafiei-Ravandi et al., 2021).

2.1.3 Milky Way halo

The Milky Way halo is of special interest because it is representative for other galaxies, and its dispersion is a systematic uncertainty for almost all other FRB probes. Very close FRBs from nearby galaxies are

most sensitive to the halo *DM* as they have only the host contribution but close to no $DM_{\rm IGM}$ (Chapter 15.4 of Weinberg, 1972, already considers this idea).

The Milky Way halo was very weakly constrained prior to FRB measurements. Hydrodynamic simulations disagree by a factor of two in the predicted baryon content (Kelly et al., 2022). Observational estimates from O VII absorption lines ranged from <10–80 $\mathrm{cm^{-3}}$ pc (Prochaska and Y. Zheng, 2019; Keating and U.-L. Pen, 2020).

FRB 200120E and FRB 220319D were two close FRBs that set upper limits on the Milky Way *DM*. The *DM*s of 88 $\mathrm{cm^{-3}}$ pc and 111 $\mathrm{cm^{-3}}$ pc set limits of $DM_{\rm MW,halo} < 53\,\mathrm{cm^{-3}}$ pc, and 28.7–47.3 $\mathrm{cm^{-3}}$ pc, respectively, with the uncertainties dominated by the Galactic *DM* models (Bhardwaj et al., 2021; Ravi et al., 2023). Future measurements will allow further constraints, as well as measurements of the anisotropy or clumpiness of the Galactic halo (Yamasaki and Totani, 2020; Kaaret et al., 2020; Cook et al., 2023). FRBs from the right directions can further reveal the halos of nearby galaxies and the group medium between the Milky Way and Andromeda (Prochaska and Y. Zheng, 2019).

2.2 The Hubble tension

The Hubble tension is one of the mayor problems of contemporary cosmology (see Hu and F.-Y. Wang, 2023, for a review). It represents the disagreement on the measured value of H_0 between probes in the early and late Universe. In the beginning, systematic uncertainties in type Ia supernova measurements were the main culprit for the discrepancy, but several probes have signified the difference to 5σ, or equivalently less than 5.7×10^{-5} % probability to measure the difference by chance (Riess et al., 2022). Additional independent probes from different redshifts and with independent systematic uncertainties are valuable to gauge different modifications of the ΛCDM model (Di Valentino et al., 2021).

FRBs measure H_0 via the dependency in $\langle DM_{\rm IGM}\rangle$. Like in the case of the missing baryons, the degeneracy with $\Omega_{\rm b} f_{\rm IGM}$ needs to be broken by external means. Possible constraints come from CMB measurements or Big Bang nucleosynthesis with the measured deuterium to hydrogen fraction, which both constrain $\Omega_{\rm b} h^2$. Independently, $f_{\rm IGM}$ has to be constrained by observing $1 - f_{\rm IGM}$, i.e., the mass in galaxies. This can be done by counting the matter in stars from their luminosity and applying mass to luminosity scaling relations, obtained from simulations.

The current constraints of $H_0 = 73^{+12}_{-8}\,\mathrm{km\,s^{-1}\,Mpc^{-1}}$ from FRBs come from the combination of localized ASKAP and unlocalized Parkes FRBs (James et al., 2022). The localized FRBs are inferred to jointly constrain H_0 with FRB population parameters. The population parameters together with the unlocalized FRBs give additional constraints on H_0.

2.3 Other cosmological parameters

Constraints on cosmological parameters beyond H_0 have also been proposed. The parameters include $\Omega_{\rm m}$, Ω_Λ, and parameters of models beyond the standard model, in particular the wCDM model with w the equation of state parameter of dark energy.

These parameters have the advantage over H_0 of influencing $DM_{\rm IGM}$ with a certain redshift dependence. However, needing larger FRB numbers to mitigate the large uncertainties in $DM_{\rm IGM}$ is not their only problem. The biggest difficulty will be discerning their redshift dependence from other still uncertain redshift evolutions, primarily of $f_{\rm IGM}(z)$ and $DM_{\rm host}(z)$.

2.4 FRBs lensed by galaxies or galaxy clusters

Gravitationally lensed FRBs would be of special interest, regardless whether they are lensed by galaxies (Z.-X. Li et al., 2018) or galaxy clusters (Zitrin and Eichler, 2018; Wagner, Liesenborgs, and Eichler, 2019). In certain configurations, these lenses can produce multiple images of background objects with time delay differences of $\mathcal{O}(10)$ and $\mathcal{O}(100)$ days, respectively.

The delays can be used to measure cosmological parameters (Z.-X. Li et al., 2018; Liu et al., 2019; Wucknitz, Spitler, and U. .-. Pen, 2021), cluster growth (Wagner, Liesenborgs, and Eichler, 2019), differences in the densities along paths (Connor and Ravi, 2023), and differences in magnetic fields (Mao et al., 2017). Especially, lensed repeaters would allow measuring the changes in time delays. The changes are dominated by the relative motions of source and lens (Zitrin and Eichler, 2018). Yet, the combination of delay changes with delay times would allow disentangling the motion from the effects of cosmological parameters (Wucknitz, Spitler, and U. .-. Pen, 2021).

Other lensed transients, foremost variable AGN, are already used for some of these purposes (Oguri, 2019). FRBs are suited best because they are more abundant than supernovae or GRBs, give orders of magnitudes better precision on the time delay than AGN (Wagner, Liesenborgs, and Eichler, 2019), and do not complicate the lens reconstruction in the optical galaxy images like bright quasars (Ding et al., 2021).

The difficulty is finding and associating multiply imaged FRBs. The different images have different fluxes, but very similar dynamic spectra, slightly altered by changing ISM properties along the line-of-sight. Most telescopes do not visit the same part of the Sky very often or, in the case of CHIME, only spend a short amount of times every day. Ultra wide-field monitors might therefore be needed to find lensed FRBs (Connor and Ravi, 2023). However, there are two other possibilities for targeted searches: Crosschecking each FRB with catalogs of lensed galaxies can yield candidate lensed FRBs, which can be followed up. Alternatively, known lens system can be searched for FRBs.

2.5 Microlensed FRBs to constrain compact dark matter

A fraction of dark matter could be in the form of compact objects with masses 20–100 $M_\odot$, like primordial black holes (Bird et al., 2016). GW experiments have indeed detected black hole mergers with ~30 $M_\odot$ (Abbott et al., 2019), although, their formation channels are uncertain (Abbott et al., 2016). By searching for FRB copies with time differences below a few milliseconds, this compact dark matter could be observed or the fraction constrained (Zhou et al., 2014; Muñoz et al., 2016). The highest chance of lensing is by objects in the middle between source and observer, while objects in the Milky Way and host galaxy have vanishing cross-sections (see e.g. Y. K. Wang and F. Y. Wang, 2018; Laha, 2020). FRBs with sharp features generally allow better constraints (Sammons et al., 2020).

2.5.1 Diffractive lensing

Diffractive gravitational lensing describes the special case where the time delay is too short to have distinct bursts, but could be observed as interference within bursts (Eichler, 2017; Katz et al., 2020). This can especially be the case for lens masses below 0.1 $M_\odot$. One peculiarity of FRBs is that the assumption of geometric optics $\nu \gg \Delta t$ can break down, which is generally used in gravitational lensing. This makes the method less sensitive but allows for better mass constraints on lensed objects (Jow et al., 2020). 172 CHIME FRBs yielded no significant detection and allowed first constraints (Kader et al., 2022; Leung et al., 2022). A difficulty is that sight line variations can make the bursts incoherent (Leung et al., 2022).

2.6 Epochs of reionization

At the recombination epoch at $z = 1100$, or 400 000 years after the Big Bang, electrons and atoms combined, and the Universe became neutral. Today, most of the matter in the Universe is ionized, but the reionization history is fairly unknown (see e.g. Greig and Mesinger, 2017). Hydrogen has the peak of its epoch of reionization (EoR) at about $z \sim 7$, and the peak of He II to He III is expected to be at $z \sim 3$.

FRBs can measure the shape of hydrogen EoR assuming different models for $\chi_{\rm H}(z)$ (Deng and B. Zhang, 2014; Fialkov and Loeb, 2016; Pagano and Fronenberg, 2021; Z. J. Zhang et al., 2021; Heimersheim et al., 2022), probe ionization bubble size during the EoR (Yoshiura and Takahashi, 2018), and with different statistical methods (Hashimoto et al., 2021; Beniamini et al., 2021). The FRBs have to be in the redshift range of interest ($z = 6$–8), which requires a very sensitive future telescope like SKA2 (the proposed extension of SKA1 that might become 10 times more sensitive Dewdney et al., 2009). Furthermore, most methods require measured redshifts, which we will further address in Chapter 4.

The He II EoR is closer but affects a smaller number of electrons, therefore producing a weaker effect in *DM*. The number of FRBs required to detect the He II EoR is estimated to be of the order 10^3–10^4 (Z. Zheng et al., 2014; Caleb, Flynn, and Stappers, 2019; Linder, 2020; Bhattacharya, Kumar, and Linder, 2021).

2.7 Magnetic fields in the IGM

The origins of cosmic magnetic fields are not well understood, and the fields in the IGM are particularly difficult to observe (Vazza et al., 2017). FRBs with measured *RM*s could probe the magnetic fields in the IGM (Z. Zheng et al., 2014; Akahori, Ryu, and Gaensler, 2016). The difficulty is to overcome the *RM* contributions from host galaxies and the Milky Way. Simulations indicate that > 1000 FRBs at $z > 3$ are required to discriminate between a primordial and an astrophysical origin of the magnetic seed fields (Vazza et al., 2018; Hackstein et al., 2019). Yet, the same number of unlocalized FRBs can already improve current limits on the strength of intergalactic magnetic fields (Hackstein et al., 2020).

2.8 Constraining the hypothetical photon mass

The search for a non-zero photon rest mass is a test of the fundamental assumption of electromagnetism and special relativity that all electromagnetic waves travel with the speed of light (J.-J. Wei and Wu, 2021). If photons had a rest mass different from zero, the speed of light would be frequency dependent (Wu et al., 2016; Bonetti et al., 2016). Searching for this frequency dependence is the most direct and most robust test. The arrival times of FRBs would be frequency dependent as $\Delta t \propto m_\gamma^2/\nu^2$, which implies that it is indistinguishable from dispersion in a single FRB. A set of FRBs still provides a unique probe over the different redshift dependence, and (2σ) upper limits of $m_\gamma \lesssim 7 \times 10^{-48}$ g or equivalently $m_\gamma \lesssim 4 \times 10^{-15}$ eV c^{-2} have been derived (Lin, Tang, and Zou, 2023). However, future FRB measurements cannot significantly lower the limits. The constraints do not scale well with the number of FRBs but rather depend on low-*DM* FRBs at $z \lesssim 1$. Furthermore the redshift evolution is similar to the one from $DM_{\rm host}$ (Lin, Tang, and Zou, 2023).

2.9 The CMB optical depth

Synergies between FRBs and other measurements are of special interest. Among them is the CMB optical depth, which is relevant to several usages of the CMB. The optical depth describes scattering of CMB photons by free electrons and is poorly constrained by other probes. This affects the accuracy of cosmic parameters obtained by CMB measurements.

Since dispersion is caused by the same electrons, FRBs at very high redshifts ($z \sim 14$) provide the means of measuring the optical depth, supposed they exist and can be detected (Fialkov and Loeb, 2016). Some CMB photons gain energy by scattering of energetic electrons in hot clusters, i.e., through inverse Compton scattering, observable as a small change in the CMB spectrum. This SZ effect can yield a pressure profile of a cluster, which could be combined with a density profile obtained from FRBs to yield a temperature profile of the cluster (Fujita et al., 2017). However, this would require many FRBs behind individual clusters. Alternatively, cross correlations of *DM* and SZ maps were proposed to characterize the IGM (Muñoz and Loeb, 2018). The *kinematic* SZ effect is a variation of the SZ coming from motions of galaxies or clusters. The optical depth is the leading systematic uncertainty in future measurements and could be lifted with FRB *DM*s (Madhavacheril et al., 2019).

All of these require large FRB numbers at large redshifts, which could be obtained by phase 2 of the SKA.

2.10 Other applications

Further applications have been proposed but have not received much attention yet. These include probing the turbulent properties of the IGM (J.-P. Macquart and Koay, 2013; Xu and B. Zhang, 2020), the weak equivalence principle (Reischke, Hagstotz, and Lilow, 2022; Reischke and Hagstotz, 2023), cosmic proper distances (Yu and F. Y. Wang, 2017), the cosmic anisotropy (Cai et al., 2019; Qiang and H. Wei, 2020; Lin and Sang, 2021), effects of a swampland constant (D. Wang, Z. Li, and J. Zhang, 2020), primordial non-Gaussianity (Reischke, Hagstotz, and Lilow, 2021), extragalactic ISMs (Simard and Ravi, 2021), gravitational waves (Pearson, Trendafilova, and Meyers, 2021), gravitational slip (Abadi and Kovetz, 2021), and cosmic strings (Xiao, Dai, and McQuinn, 2022).

References

Abadi, T. and E. D. Kovetz (2021), *Probing gravitational slip with strongly lensed fast radio bursts*, Phys. Rev. D **104**, 103515 103515, arXiv: 2109.00403 [astro-ph.CO] (cit. on p. 28).

Abbott, B. P. et al. (2016), *Astrophysical Implications of the Binary Black-hole Merger GW150914*, ApJ **818**, L22 L22, arXiv: 1602.03846 [astro-ph.HE] (cit. on p. 26).

Abbott, B. P. et al. (2019), *GWTC-1: A Gravitational-Wave Transient Catalog of Compact Binary Mergers Observed by LIGO and Virgo during the First and Second Observing Runs*, Physical Review X **9**, 031040 031040, arXiv: 1811.12907 [astro-ph.HE] (cit. on p. 26).

Akahori, T., D. Ryu, and B. M. Gaensler (2016), *Fast Radio Bursts as Probes of Magnetic Fields in the Intergalactic Medium*, ApJ **824**, 105 105, arXiv: 1602.03235 [astro-ph.CO] (cit. on p. 27).

Baptista, J. et al. (2023), *Measuring the Variance of the Macquart Relation in z-DM Modeling*, arXiv e-prints, arXiv:2305.07022 arXiv:2305.07022, arXiv: 2305.07022 [astro-ph.CO] (cit. on pp. 23, 24).

Batten, A. J. et al. (2021), *The cosmic dispersion measure in the EAGLE simulations*, MNRAS **505** 5356, arXiv: 2011.14547 [astro-ph.CO] (cit. on p. 24).

Batten, A. J. et al. (2022), *Fast radio bursts as probes of feedback from active galactic nuclei*, MNRAS **512** L49, arXiv: 2109.13472 [astro-ph.GA] (cit. on p. 24).

Beniamini, P. et al. (2021), *Exploring the epoch of hydrogen reionization using FRBs*, MNRAS **502** 5134, arXiv: 2011.11643 [astro-ph.CO] (cit. on pp. 23, 27).

Bhardwaj, M. et al. (2021), *A Nearby Repeating Fast Radio Burst in the Direction of M81*, ApJ **910**, L18 L18, arXiv: 2103.01295 [astro-ph.HE] (cit. on p. 25).

Bhattacharya, M., P. Kumar, and E. V. Linder (2021), *Fast radio burst dispersion measure distribution as a probe of helium reionization*, Phys. Rev. D **103**, 103526 103526, arXiv: 2010.14530 [astro-ph.CO] (cit. on p. 27).

Bird, S. et al. (2016), *Did LIGO Detect Dark Matter?* Phys. Rev. Lett. **116**, 201301 201301, arXiv: 1603.00464 [astro-ph.CO] (cit. on p. 26).

Bonetti, L. et al. (2016), *Photon mass limits from fast radio bursts*, Physics Letters B **757** 548, arXiv: 1602.09135 [astro-ph.HE] (cit. on p. 27).

Cai, R.-G. et al. (2019), *Probing cosmic anisotropy with GW/FRB as upgraded standard sirens*, J. Cosmology Astropart. Phys. **2019**, 016 016, arXiv: 1905.01803 [astro-ph.CO] (cit. on p. 28).

Caleb, M., C. Flynn, and B. W. Stappers (2019), *Constraining the era of helium reionization using fast radio bursts*, MNRAS **485** 2281, arXiv: 1902.06981 [astro-ph.HE] (cit. on p. 27).

Cen, R. and J. P. Ostriker (1999), *Where Are the Baryons?* ApJ **514** 1, arXiv: astro-ph/9806281 [astro-ph] (cit. on p. 22).

Chisari, N. E. et al. (2019), *Modelling baryonic feedback for survey cosmology*, The Open Journal of Astrophysics **2**, 4 4, arXiv: 1905.06082 [astro-ph.CO] (cit. on p. 24).

Coc, A. and E. Vangioni (2017), *Primordial nucleosynthesis*, International Journal of Modern Physics E **26**, 1741002 1741002, arXiv: 1707.01004 [astro-ph.CO] (cit. on p. 20).

Connor, L. and V. Ravi (2023), *Stellar prospects for FRB gravitational lensing*, MNRAS **521** 4024, arXiv: 2206.14310 [astro-ph.CO] (cit. on p. 26).

Cook, A. M. et al. (2023), *An FRB Sent Me a DM: Constraining the Electron Column of the Milky Way Halo with Fast Radio Burst Dispersion Measures from CHIME/FRB*, ApJ **946**, 58 58, arXiv: 2301.03502 [astro-ph.GA] (cit. on p. 25).

Davé, R., K. Finlator, and B. D. Oppenheimer (2011), *Galaxy evolution in cosmological simulations with outflows - II. Metallicities and gas fractions*, MNRAS **416** 1354, arXiv: 1104.3156 [astro-ph.CO] (cit. on p. 24).

Davé, R., B. D. Oppenheimer, and K. Finlator (2011), *Galaxy evolution in cosmological simulations with outflows - I. Stellar masses and star formation rates*, MNRAS **415** 11, arXiv: 1103.3528 [astro-ph.CO] (cit. on p. 24).

Davé, R. et al. (2001), *Baryons in the Warm-Hot Intergalactic Medium*, ApJ **552** 473, arXiv: astro-ph/0007217 [astro-ph] (cit. on pp. 19, 22).

de Graaff, A. et al. (2019), *Probing the missing baryons with the Sunyaev-Zel'dovich effect from filaments*, A&A **624**, A48 A48, arXiv: 1709.10378 [astro-ph.CO] (cit. on p. 22).

Deng, W. and B. Zhang (2014), *Cosmological Implications of Fast Radio Burst/Gamma-Ray Burst Associations*, ApJ **783**, L35 L35, arXiv: 1401.0059 [astro-ph.HE] (cit. on pp. 19, 21, 22, 27).

Dewdney, P. E. et al. (2009), *The Square Kilometre Array*, IEEE Proceedings **97** 1482 (cit. on p. 27).

Di Valentino, E. et al. (2021), *In the realm of the Hubble tension-a review of solutions*, Classical and Quantum Gravity **38**, 153001 153001, arXiv: 2103.01183 [astro-ph.CO] (cit. on p. 25).
Ding, X. et al. (2021), *Improved time-delay lens modelling and H_0 inference with transient sources*, MNRAS **504** 5621, arXiv: 2103.08609 [astro-ph.CO] (cit. on p. 26).
Eckert, D. et al. (2015), *Warm-hot baryons comprise 5-10 per cent of filaments in the cosmic web*, Nature **528** 105, arXiv: 1512.00454 [astro-ph.CO] (cit. on p. 22).
Eichler, D. (2017), *Nanolensed Fast Radio Bursts*, ApJ **850**, 159 159, arXiv: 1711.04764 [astro-ph.HE] (cit. on p. 26).
Fialkov, A. and A. Loeb (2016), *Constraining the CMB optical depth through the dispersion measure of cosmological radio transients*, J. Cosmology Astropart. Phys. **2016**, 004 004, arXiv: 1602.08130 [astro-ph.CO] (cit. on pp. 27, 28).
Fujita, Y. et al. (2017), *Probing WHIM around Galaxy Clusters with Fast Radio Bursts and the Sunyaev-Zel'dovich effect*, ApJ **834**, 13 13, arXiv: 1609.03566 [astro-ph.GA] (cit. on p. 28).
Fukugita, M., C. J. Hogan, and P. J. E. Peebles (1998), *The Cosmic Baryon Budget*, ApJ **503** 518, arXiv: astro-ph/9712020 [astro-ph] (cit. on p. 22).
Ginzburg, V. L. (1973), *Possibility of Determining Intergalactic Gas Density by Radio Observations of Flares of Remote Sources*, Nature **246** 415 (cit. on p. 19).
Greig, B. and A. Mesinger (2017), *The global history of reionization*, MNRAS **465** 4838, arXiv: 1605.05374 [astro-ph.CO] (cit. on p. 27).
Hackstein, S. et al. (2019), *Fast radio burst dispersion measures and rotation measures and the origin of intergalactic magnetic fields*, MNRAS **488** 4220, arXiv: 1907.09650 [astro-ph.CO] (cit. on pp. 23, 27).
Hackstein, S. et al. (2020), *Redshift estimates for fast radio bursts and implications on intergalactic magnetic fields*, MNRAS **498** 4811, arXiv: 2008.10536 [astro-ph.CO] (cit. on p. 27).
Haddock, F. T. and D. W. Sciama (1965), *Proposal for the Detection of Dispersion in Radio-Wave Propagation Through Intergalactic Space*, Phys. Rev. Lett. **14** 1007 (cit. on p. 19).
Hashimoto, T. et al. (2021), *Revealing the cosmic reionization history with fast radio bursts in the era of Square Kilometre Array*, MNRAS **502** 2346, arXiv: 2101.08798 [astro-ph.CO] (cit. on p. 27).
Heimersheim, S. et al. (2022), *What It Takes to Measure Reionization with Fast Radio Bursts*, ApJ **933**, 57 57, arXiv: 2107.14242 [astro-ph.CO] (cit. on p. 27).
Hu, J.-P. and F.-Y. Wang (2023), *Hubble Tension: The Evidence of New Physics*, Universe **9** 94, arXiv: 2302.05709 [astro-ph.CO] (cit. on p. 25).
Inoue, S. (2004), *Probing the cosmic reionization history and local environment of gamma-ray bursts through radio dispersion*, MNRAS **348** 999, arXiv: astro-ph/0309364 [astro-ph] (cit. on pp. 19, 21).
Ioka, K. (2003), *The Cosmic Dispersion Measure from Gamma-Ray Burst Afterglows: Probing the Reionization History and the Burst Environment*, ApJ **598** L79, arXiv: astro-ph/0309200 [astro-ph] (cit. on pp. 19, 21).
Jahns-Schindler, J. N. et al. (2023), *How limiting is optical follow-up for fast radio burst applications? Forecasts for radio and optical surveys*, MNRAS **523** 5006, arXiv: 2306.00084 [astro-ph.HE] (cit. on p. 23).
James, C. W. et al. (2022), *A measurement of Hubble's Constant using Fast Radio Bursts*, MNRAS **516** 4862, arXiv: 2208.00819 [astro-ph.CO] (cit. on pp. 23, 25).

Jaroszynski, M. (2019), *Fast radio bursts and cosmological tests*, MNRAS **484** 1637, arXiv: 1812.11936 [astro-ph.CO] (cit. on p. 24).

Jow, D. L. et al. (2020), *Wave effects in the microlensing of pulsars and FRBs by point masses*, MNRAS **497** 4956, arXiv: 2002.01570 [astro-ph.HE] (cit. on p. 26).

Kaaret, P. et al. (2020), *A disk-dominated and clumpy circumgalactic medium of the Milky Way seen in X-ray emission*, Nature Astronomy **4** 1072, arXiv: 2011.00126 [astro-ph.GA] (cit. on p. 25).

Kader, Z. et al. (2022), *High-time resolution search for compact objects using fast radio burst gravitational lens interferometry with CHIME/FRB*, Phys. Rev. D **106**, 043016 043016, arXiv: 2204.06014 [astro-ph.HE] (cit. on p. 26).

Katz, A. et al. (2020), *Looking for MACHOs in the spectra of fast radio bursts*, MNRAS **496** 564, arXiv: 1912.07620 [astro-ph.CO] (cit. on p. 26).

Keating, L. C. and U.-L. Pen (2020), *Exploring the dispersion measure of the Milky Way halo*, MNRAS **496** L106, arXiv: 2001.11105 [astro-ph.GA] (cit. on p. 25).

Kelly, A. J. et al. (2022), *Apostle-Auriga: effects of different subgrid models on the baryon cycle around Milky Way-mass galaxies*, MNRAS **514** 3113, arXiv: 2106.08618 [astro-ph.GA] (cit. on p. 25).

Laha, R. (2020), *Lensing of fast radio bursts: Future constraints on primordial black hole density with an extended mass function and a new probe of exotic compact fermion and boson stars*, Phys. Rev. D **102**, 023016 023016 (cit. on p. 26).

Lee, K.-G. et al. (2022), *Constraining the Cosmic Baryon Distribution with Fast Radio Burst Foreground Mapping*, ApJ **928**, 9 9, arXiv: 2109.00386 [astro-ph.CO] (cit. on p. 24).

Lee, K.-G. et al. (2023), *The FRB 20190520B Sight Line Intersects Foreground Galaxy Clusters*, ApJ **954**, L7 L7, arXiv: 2306.05403 [astro-ph.GA] (cit. on p. 24).

Leung, C. et al. (2022), *Constraining primordial black holes using fast radio burst gravitational-lens interferometry with CHIME/FRB*, Phys. Rev. D **106**, 043017 043017, arXiv: 2204.06001 [astro-ph.HE] (cit. on p. 26).

Li, Z.-X. et al. (2018), *Strongly lensed repeating fast radio bursts as precision probes of the universe*, Nature Communications **9**, 3833 3833, arXiv: 1708.06357 [astro-ph.CO] (cit. on p. 26).

Lin, H.-N. and Y. Sang (2021), *Probing the anisotropic distribution of baryon matter in the Universe using fast radio bursts*, Chinese Physics C **45**, 125101 125101, arXiv: 2111.12934 [astro-ph.CO] (cit. on p. 28).

Lin, H.-N., L. Tang, and R. Zou (2023), *Revised constraints on the photon mass from well-localized fast radio bursts*, MNRAS **520** 1324, arXiv: 2301.12103 [gr-qc] (cit. on pp. 23, 27).

Linder, E. V. (2020), *Detecting helium reionization with fast radio bursts*, Phys. Rev. D **101**, 103019 103019, arXiv: 2001.11517 [astro-ph.CO] (cit. on pp. 23, 27).

Lipunova, G. V., I. E. Panchenko, and V. M. Lipunov (1997), *The radioastronomical "time machine" effect can help the solution of the gamma ray bursts mystery*, New A **2** 555, arXiv: astro-ph/9706074 [astro-ph] (cit. on p. 19).

Liu, B. et al. (2019), *Prospects of strongly lensed repeating fast radio bursts: Complementary constraints on dark energy evolution*, Phys. Rev. D **99**, 123517 123517, arXiv: 1907.10488 [astro-ph.CO] (cit. on p. 26).

Macquart, J. .-. et al. (2020), *A census of baryons in the Universe from localized fast radio bursts*, Nature **581** 391, arXiv: 2005.13161 [astro-ph.CO] (cit. on pp. 22, 24).

Macquart, J. P. et al. (2015), "Fast Transients at Cosmological Distances with the SKA," *Advancing Astrophysics with the Square Kilometre Array (AASKA14)* 55 55, arXiv: 1501.07535 [astro-ph.HE] (cit. on p. 24).
Macquart, J.-P. and J. Y. Koay (2013), *Temporal Smearing of Transient Radio Sources by the Intergalactic Medium*, ApJ **776**, 125 125, arXiv: 1308.4459 [astro-ph.CO] (cit. on p. 28).
Madhavacheril, M. S. et al. (2019), *Cosmology with the kinematic Sunyaev-Zeldovich effect: Breaking the optical depth degeneracy with fast radio bursts*, Phys. Rev. D **100**, 103532 103532 (cit. on p. 28).
Mao, S. A. et al. (2017), *Detection of microgauss coherent magnetic fields in a galaxy five billion years ago*, Nature Astronomy **1** 621, arXiv: 1708.07844 [astro-ph.GA] (cit. on p. 26).
McQuinn, M. (2014), *Locating the "Missing" Baryons with Extragalactic Dispersion Measure Estimates*, ApJ **780**, L33 L33, arXiv: 1309.4451 [astro-ph.CO] (cit. on pp. 22, 24).
McQuinn, M. et al. (2009), *He II Reionization and its Effect on the Intergalactic Medium*, ApJ **694** 842, arXiv: 0807.2799 [astro-ph] (cit. on p. 21).
Miralda-Escudé, J., M. Haehnelt, and M. J. Rees (2000), *Reionization of the Inhomogeneous Universe*, ApJ **530** 1, arXiv: astro-ph/9812306 [astro-ph] (cit. on p. 24).
Muñoz, J. B. and A. Loeb (2018), *Finding the missing baryons with fast radio bursts and Sunyaev-Zeldovich maps*, Phys. Rev. D **98**, 103518 103518, arXiv: 1809.04074 [astro-ph.CO] (cit. on p. 28).
Muñoz, J. B. et al. (2016), *Lensing of Fast Radio Bursts as a Probe of Compact Dark Matter*, Phys. Rev. Lett. **117**, 091301 091301, arXiv: 1605.00008 [astro-ph.CO] (cit. on p. 26).
Nicastro, F. et al. (2018), *Observations of the missing baryons in the warm-hot intergalactic medium*, Nature **558** 406, arXiv: 1806.08395 [astro-ph.GA] (cit. on p. 22).
Niu, C. .-. et al. (2022), *A repeating fast radio burst associated with a persistent radio source*, Nature **606** 873, arXiv: 2110.07418 [astro-ph.HE] (cit. on p. 21).
Oguri, M. (2019), *Strong gravitational lensing of explosive transients*, Reports on Progress in Physics **82**, 126901 126901, arXiv: 1907.06830 [astro-ph.CO] (cit. on p. 26).
Pagano, M. and H. Fronenberg (2021), *Constraining the epoch of reionization with highly dispersed fast radio bursts*, MNRAS **505** 2195, arXiv: 2103.03252 [astro-ph.CO] (cit. on p. 27).
Palmer, D. M. (1993), *Radio Dispersion as a Diagnostic of Gamma-Ray Burst Distances*, ApJ **417** L25 (cit. on p. 19).
Peacock, J. A. (1999), *Cosmological Physics* (cit. on p. 21).
Pearson, N., C. Trendafilova, and J. Meyers (2021), *Searching for gravitational waves with strongly lensed repeating fast radio bursts*, Phys. Rev. D **103**, 063017 063017, arXiv: 2009.11252 [astro-ph.CO] (cit. on p. 28).
Persic, M. and P. Salucci (1992), *The baryon content of the universe*, MNRAS **258** 14P, arXiv: astro-ph/0502178 [astro-ph] (cit. on p. 22).
Planck Collaboration et al. (2016), *Planck 2015 results. XIII. Cosmological parameters*, A&A **594**, A13 A13, arXiv: 1502.01589 [astro-ph.CO] (cit. on p. 22).
Price, D. C., C. Flynn, and A. Deller (2021), *A comparison of Galactic electron density models using PyGEDM*, PASA **38**, e038 e038, arXiv: 2106.15816 [astro-ph.GA] (cit. on p. 21).
Prochaska, J. X. and M. Neeleman (2018), *The astrophysical consequences of intervening galaxy gas on fast radio bursts*, MNRAS **474** 318, arXiv: 1711.00323 [astro-ph.GA] (cit. on p. 24).
Prochaska, J. X. and Y. Zheng (2019), *Probing Galactic haloes with fast radio bursts*, MNRAS **485** 648, arXiv: 1901.11051 [astro-ph.GA] (cit. on pp. 24, 25).

Qiang, D.-C. and H. Wei (2020), *Reconstructing the fraction of baryons in the intergalactic medium with fast radio bursts via Gaussian processes*, J. Cosmology Astropart. Phys. **2020**, 023 023, arXiv: 2002.10189 [astro-ph.CO] (cit. on p. 28).

Rafiei-Ravandi, M., K. M. Smith, and K. W. Masui (2020), *Characterizing fast radio bursts through statistical cross-correlations*, Phys. Rev. D **102**, 023528 023528, arXiv: 1912.09520 [astro-ph.CO] (cit. on p. 24).

Rafiei-Ravandi, M. et al. (2021), *CHIME/FRB Catalog 1 Results: Statistical Cross-correlations with Large-scale Structure*, ApJ **922**, 42 42, arXiv: 2106.04354 [astro-ph.CO] (cit. on p. 24).

Rauch, M. (1998), *The Lyman Alpha Forest in the Spectra of QSOs*, ARA&A **36** 267, arXiv: astro-ph/9806286 [astro-ph] (cit. on p. 22).

Ravi, V. et al. (2019), *A fast radio burst localized to a massive galaxy*, Nature **572** 352, arXiv: 1907.01542 [astro-ph.HE] (cit. on p. 24).

Ravi, V. et al. (2023), *Deep Synoptic Array science: a 50 Mpc fast radio burst constrains the mass of the Milky Way circumgalactic medium*, arXiv e-prints, arXiv:2301.01000 arXiv:2301.01000, arXiv: 2301.01000 [astro-ph.GA] (cit. on p. 25).

Reischke, R. and S. Hagstotz (2023), *Cosmological covariance of fast radio burst dispersions*, MNRAS **524** 2237, arXiv: 2301.03527 [astro-ph.CO] (cit. on p. 28).

Reischke, R., S. Hagstotz, and R. Lilow (2021), *Probing primordial non-Gaussianity with fast radio bursts*, Phys. Rev. D **103**, 023517 023517, arXiv: 2007.04054 [astro-ph.CO] (cit. on p. 28).

– (2022), *Consistent equivalence principle tests with fast radio bursts*, MNRAS **512** 285, arXiv: 2102.11554 [astro-ph.CO] (cit. on p. 28).

Riess, A. G. et al. (2022), *A Comprehensive Measurement of the Local Value of the Hubble Constant with 1 km s^{-1} Mpc^{-1} Uncertainty from the Hubble Space Telescope and the SH0ES Team*, ApJ **934**, L7 L7, arXiv: 2112.04510 [astro-ph.CO] (cit. on p. 25).

Sammons, M. W. et al. (2020), *First Constraints on Compact Dark Matter from Fast Radio Burst Microstructure*, ApJ **900**, 122 122, arXiv: 2002.12533 [astro-ph.CO] (cit. on pp. 23, 26).

Schneider, P. (2006), *Extragalactic Astronomy and Cosmology* (cit. on p. 20).

Sholomitsky, G. B. (1965), *Variability of the Radio Source CTA-102*, Information Bulletin on Variable Stars **83** 1 (cit. on p. 19).

Simard, D. and V. Ravi (2021), *Measuring interstellar turbulence in fast radio burst host galaxies*, arXiv e-prints, arXiv:2107.11334 arXiv:2107.11334, arXiv: 2107.11334 [astro-ph.GA] (cit. on p. 28).

Simha, S. et al. (2020), *Disentangling the Cosmic Web toward FRB 190608*, ApJ **901**, 134 134, arXiv: 2005.13157 [astro-ph.GA] (cit. on p. 24).

Simha, S. et al. (2023), *Searching for the Sources of Excess Extragalactic Dispersion of FRBs*, ApJ **954**, 71 71, arXiv: 2303.07387 [astro-ph.GA] (cit. on p. 24).

Tytler, D., X.-M. Fan, and S. Burles (1996), *Cosmological baryon density derived from the deuterium abundance at redshift $z = 3.57$*, Nature **381** 207, arXiv: astro-ph/9603069 [astro-ph] (cit. on p. 22).

Vazza, F. et al. (2017), *Simulations of extragalactic magnetic fields and of their observables*, Classical and Quantum Gravity **34**, 234001 234001, arXiv: 1711.02669 [astro-ph.CO] (cit. on p. 27).

Vazza, F. et al. (2018), *Probing the origin of extragalactic magnetic fields with Fast Radio Bursts*, MNRAS **480** 3907, arXiv: 1805.11113 [astro-ph.CO] (cit. on p. 27).

Wagner, J., J. Liesenborgs, and D. Eichler (2019), *Multiply imaged time-varying sources behind galaxy clusters. Comparing fast radio bursts to QSOs, SNe, and GRBs*, A&A **621**, A91 A91, arXiv: 1811.10618 [astro-ph.CO] (cit. on p. 26).

Wang, D., Z. Li, and J. Zhang (2020), *Weak equivalence principle, swampland and H_0 tension with fast single radio bursts FRB 180924 and FRB 190523*, Physics of the Dark Universe **29**, 100571 100571, arXiv: 1907.02838 [astro-ph.CO] (cit. on p. 28).

Wang, Y. K. and F. Y. Wang (2018), *Lensing of fast radio bursts by binaries to probe compact dark matter*, A&A **614**, A50 A50, arXiv: 1801.07360 [astro-ph.CO] (cit. on p. 26).

Wei, J.-J. and X.-F. Wu (2021), *Testing fundamental physics with astrophysical transients*, Frontiers of Physics **16**, 44300 44300, arXiv: 2102.03724 [astro-ph.HE] (cit. on p. 27).

Weinberg, S. (1972), *Gravitation and Cosmology: Principles and Applications of the General Theory of Relativity* (cit. on pp. 19, 25).

Workman, R. L. et al. (2022), *Review of Particle Physics*, Progress of Theoretical and Experimental Physics **2022**, 083C01 083C01 (cit. on p. 20).

Wu, X.-F. et al. (2016), *Constraints on the Photon Mass with Fast Radio Bursts*, ApJ **822**, L15 L15, arXiv: 1602.07835 [astro-ph.HE] (cit. on p. 27).

Wucknitz, O., L. G. Spitler, and U. .-. Pen (2021), *Cosmology with gravitationally lensed repeating fast radio bursts*, A&A **645**, A44 A44, arXiv: 2004.11643 [astro-ph.CO] (cit. on p. 26).

Xiao, H., L. Dai, and M. McQuinn (2022), *Detecting cosmic strings with lensed fast radio bursts*, Phys. Rev. D **106**, 103033 103033, arXiv: 2206.13534 [astro-ph.CO] (cit. on p. 28).

Xu, S. and B. Zhang (2020), *Probing the Intergalactic Turbulence with Fast Radio Bursts*, ApJ **898**, L48 L48, arXiv: 2007.04089 [astro-ph.HE] (cit. on p. 28).

Yamasaki, S. and T. Totani (2020), *The Galactic Halo Contribution to the Dispersion Measure of Extragalactic Fast Radio Bursts*, ApJ **888**, 105 105, arXiv: 1909.00849 [astro-ph.HE] (cit. on p. 25).

Yoshiura, S. and K. Takahashi (2018), *The variance of dispersion measure of high-redshift transient objects as a probe of ionized bubble size during reionization*, MNRAS **473** 1570, arXiv: 1709.08012 [astro-ph.CO] (cit. on p. 27).

Yu, H. and F. Y. Wang (2017), *Measuring the cosmic proper distance from fast radio bursts*, A&A **606**, A3 A3, arXiv: 1708.06905 [astro-ph.CO] (cit. on p. 28).

Zhang, Z. J. et al. (2021), *Intergalactic Medium Dispersion Measures of Fast Radio Bursts Estimated from IllustrisTNG Simulation and Their Cosmological Applications*, ApJ **906**, 49 49, arXiv: 2011.14494 [astro-ph.CO] (cit. on p. 27).

Zheng, Z. et al. (2014), *Probing the Intergalactic Medium with Fast Radio Bursts*, ApJ **797**, 71 71, arXiv: 1409.3244 [astro-ph.HE] (cit. on p. 27).

Zhou, B. et al. (2014), *Fast radio bursts as a cosmic probe?* Phys. Rev. D **89**, 107303 107303, arXiv: 1401.2927 [astro-ph.CO] (cit. on p. 26).

Zitrin, A. and D. Eichler (2018), *Observing Cosmological Processes in Real Time with Repeating Fast Radio Bursts*, ApJ **866**, 101 101, arXiv: 1807.03287 [astro-ph.CO] (cit. on p. 26).

CHAPTER 3

The FRB 20121102A November rain in 2018 observed with the Arecibo Telescope

J. N. Jahns, L. G. Spitler, K. Nimmo, D. M. Hewitt, M. P. Snelders, A. Seymour, J. W. T. Hessels, K. Gourdji, D. Michilli, and G. H. Hilmarsson (2023), *The FRB 20121102A November rain in 2018 observed with the Arecibo Telescope*, MNRAS **519**.1 666, doi:10.1093/mnras/stac3446

Summary

Observing repeaters with large, sensitive telescopes is one of the most effective approaches for studying FRBs, as it allows for more frequent burst detections compared to untargeted searches. By comparing the detected bursts to model predictions, we can constrain emission and progenitor models. The publication in hand is part of a large observing campaign targeted at FRB 121102 with the Arecibo Telescope under the name P3054 (principal investigator Laura Spitler). The campaign goal was to observe the source over several years to monitor burst activity, *DM*, *RM*, and other principle FRB properties. Previous results of the campaign have been published in several papers, including Michilli et al. (2018), Hessels et al. (2019), Gourdji et al. (2019), Hilmarsson et al. (2021), and Hewitt et al. (2022).

The campaign was conducted once or twice a week from November 2015, with intermittent interruptions, such as after Hurricane Maria, until a cable holding the receiver broke in August 2020, leading to the collapse of the telescope in December. Typically, observations lasted about 2 hours and were split into two observing bands, half in L-band with the L-Wide receiver at 1.15–1.73 GHz and the other half in C-band at 4.1–4.9 GHz. Knowledge of the source *DM* allows us to coherently dedisperse the signal at a $DM = 557\,\mathrm{cm}^{-3}$ pc to minimize intra-channel dispersive smearing (coherent dedispersion means that the data is dedispersed before it is channelized, avoiding smearing of the burst over several adjacent time bins within a channel due to the high *DM*). The data were recorded and merged into a PSRFITS file with a time resolution of 10.24 µs and a frequency resolution of 1.5625 MHz.

Before we could search the data, we needed to carry out a few preparational steps. To ensure quick and consistent reduction of the observational data, we developed several pipelines and tools. To all of these tools, I have either made significant improvements or developed large parts. We summarize the whole process enumerating all the steps.

1. We only searched the total intensity data, which we calculated from the four saved polarizations. To

further shrink the data size, we downsampled the data, averaging every 8 time samples. We saved the resulting smaller file to a new location.

2. Then we cleaned the data from technical artifacts and radio frequency interference, which originates, for example, from radars or satellites.

3. We averaged over frequencies to search only the time series. Even though we know the FRB's *DM*, we searched for a number of trial *DM*s around the expected *DM* to ensure picking up bursts in case the *DM* changes and to use them in the classification.

4. For each trial *DM*, we computed the time series and searched for peaks that reach more than 5 times the standard deviation of the noise.

In the pipeline that does these four steps, I completely rewrote step 2 to account for technical artifacts and adapt the RFI exclusion to our data. The technical artifacts were caused by 'GPU node dropouts' and manifested as $1/8$th of the frequency band writing 0s for a fraction of a second, causing a lot of false candidates at their start and end. To account for these dropouts and take the specific statistical properties of our data into account, I also wrote a new RFI excision code. In the substantially cleaner file, I found many fewer false candidates than before, which let me recover many real bursts in the candidate inspection, and even allowed me to decrease the threshold for candidate inspection from 6 to 5 times the standard deviation.

5. We manually inspected all the bursts and classified them whether they are real or not.

6. We cut out real bursts from the raw data for further analysis and to ensure that the full data quality is saved for potential future reanalyses.

Here, I added additional functionality to the inspection tool, such as allowing to revert to the previous candidate. I further implemented a way to extract bursts that extend over different files in the raw data, which were split into several large files.

7. We extracted burst parameters by computing the burst energies and fitting two-dimensional Gaussians.

8. Finally, we did a statistical analysis of all extracted parameters and looked for correlations among them and for changes in time.

I wrote most of the pipeline that extracts the burst properties and carried out the statistical analysis.

I developed a new mathematical model for analyzing the dynamic spectra of bursts. It is a two-dimensional Gaussian with a linear drift, which is fit to each burst component, or *sub-burst*. Compared to previously used models (e.g. Rajabi et al., 2020), my model does not diverge when bursts are straight and, moreover, provides direct interpretation in emission models.

In the publication, we present the results of 10 L-band observations, totaling about 9 hours, in a very active period around November 2018. With the improved pipeline, we found 849 new bursts reaching rates as high as 218 ± 16 bursts per hour. This is the highest rate that has been observed from this FRB. Our analysis of burst arrival times showed that there is no short-term periodicity, even with our high observed rate. Yet, we found bursts to sometimes arrive in packs on timescales of $\lesssim 100$ ms causing a bimodal distribution of the times between consecutive bursts. Otherwise, we found that the bursts do not follow

any pattern, i.e., their arrival times can be described as a Poisson point process with a constant rate within observations.

The energy distribution can give clues on the emission mechanism and can be compared to proposed progenitors like magnetars. We found that the energy distribution is not well described by a simple power law, even within a single observation. Instead, a broken power law provided a better fit for this time period, in contrast to the later activity period observed by FAST (Li et al., 2021). We excluded biases from observations or from the distinction between bursts and sub-bursts as the origins of the form of the energy distribution.

From the fits of the dynamic spectra, we observed a linear correlation between the durations of sub-bursts and their drifts. This correlation is likely related to the sad-trombone effect, meaning the effect involves not only a drift of the sub-burst centers but also a drift of the emission within sub-bursts. However, the linear correlation does not conform to the interpretation within the sad-trombone effect or any other models, posing a challenge for emission models.

References

Gourdji, K. et al. (2019), *A Sample of Low-energy Bursts from FRB 121102*, ApJ **877**, L19 L19, arXiv: 1903.02249 [astro-ph.HE] (cit. on p. 35).

Hessels, J. W. T. et al. (2019), *FRB 121102 Bursts Show Complex Time-Frequency Structure*, ApJ **876**, L23 L23, arXiv: 1811.10748 [astro-ph.HE] (cit. on p. 35).

Hewitt, D. M. et al. (2022), *Arecibo observations of a burst storm from FRB 20121102A in 2016*, MNRAS **515** 3577, arXiv: 2111.11282 [astro-ph.HE] (cit. on p. 35).

Hilmarsson, G. H. et al. (2021), *Rotation Measure Evolution of the Repeating Fast Radio Burst Source FRB 121102*, ApJ **908**, L10 L10, arXiv: 2009.12135 [astro-ph.HE] (cit. on p. 35).

Jahns, J. N. et al. (2023), *The FRB 20121102A November rain in 2018 observed with the Arecibo Telescope*, MNRAS **519** 666, arXiv: 2202.05705 [astro-ph.HE] (cit. on p. 35).

Li, D. et al. (2021), *A bimodal burst energy distribution of a repeating fast radio burst source*, Nature **598** 267, arXiv: 2107.08205 [astro-ph.HE] (cit. on p. 37).

Michilli, D. et al. (2018), *An extreme magneto-ionic environment associated with the fast radio burst source FRB 121102*, Nature **553** 182, arXiv: 1801.03965 [astro-ph.HE] (cit. on p. 35).

Rajabi, F. et al. (2020), *A simple relationship for the spectro-temporal structure of bursts from FRB 121102*, MNRAS **498** 4936, arXiv: 2008.02395 [astro-ph.HE] (cit. on p. 36).

CHAPTER 4

How limiting is optical follow-up for fast radio burst applications? Forecasts for radio and optical surveys

J. N. Jahns-Schindler, L. G. Spitler, C. R. H. Walker, and C. M. Baugh (2023), *How limiting is optical follow-up for fast radio burst applications? Forecasts for radio and optical surveys*, MNRAS **523**.4 5006, doi:10.1093/mnras/stad1659

Summary

FRBs are the first radio sources from cosmological distances that have sub-second durations. As such, they provide a unique chance for astronomers to study aspects of the Universe that were previously inaccessible. We discussed many of these astrophysical and cosmological applications in Chapter 2. Among the most promising applications, FRBs allow us to study the baryons and their distribution in the intergalactic medium and around galaxies, as well as measure cosmological parameters. These and several other applications require the FRB's redshift as an additional measurement to indicate the distance. The redshift can only be obtained in follow-up observations of the FRB host galaxies. First, this requires a precise localization of FRBs, which, for one-offs, can only be obtained upon discovery. Afterward, the location needs to be followed-up with optical and/or infrared telescopes to identify the host galaxy and obtain its redshift. This step bears the difficulty that such telescopes are often highly oversubscribed, and hence it is difficult to get a lot of observing time. Currently, it is possible because the number of precisely localized FRBs is about a dozen per year. However, in the near future, telescope upgrades will provide hundreds of precise localizations every year. For example, the CHIME outrigger stations (Vanderlinde et al., 2019), which are currently under construction, will allow the localization of most FRBs detected by CHIME with sub-arcsecond precision. Thus, CHIME alone will yield about 500 localized bursts per year. Because of this substantial increase in FRB localizations, follow-up observations of the host galaxy will become the bottleneck for FRB applications in the next years.

The problem of obtaining redshifts for large numbers of FRB host galaxies in practice had not been addressed in the literature. The goal of this work was to fill this gap. I used simulations of FRBs and of their host galaxies in various surveys to estimate the fractions of host galaxies that are already observed in optical surveys. I studied the impact of FRB applications when only these cataloged galaxies are used. For this purpose, I applied a Bayesian inference method, previously used to find the missing baryons (Macquart et al., 2020), on my simulated populations. With the realistic data and method, I investigated

the influence of primarily low-z FRBs and the evolution of constraints with observed FRB numbers. From the simulated magnitudes of host galaxies, I calculated the observing time required for the identification in a hypothetical 10-m class telescope. This yields limits on the redshifts at which galaxies can be observed realistically. To find ways to optimize follow-up strategies, I considered that more distant FRBs carry more cosmological signal because the *DM* contribution of the host galaxy gets suppressed. Combining these and other theoretical considerations with the simulations, I develop an optimized observing strategy that builds on existing surveys. I published all these methods and derivations in a PYTHON package named MOCKFRBHOSTS[1], accompanying the paper.

In this work, we confirmed the suspicion that optical follow-up will be the bottleneck of future FRB applications. We found that deeper surveys like the DECam Local Volume Exploration survey (DELVE Drlica-Wagner et al., 2022) can detect 63–85 % of the hosts of ASKAP's FRBs. Yet, in the case of CHIME, which will discover the majority of FRBs in the near future, the community will have to largely rely on the older Sloan Digital Sky Survey (SDSS Abazajian et al., 2009). SDSS will only detect 20–40 % of CHIME's FRBs and limits them to $z < 0.5$. In the slightly farther future, the first stage of the Square Kilometer Array (SKA) will detect FRBs out to $z \sim 5$, but the optical counterpart detection in the Legacy Survey of Space and Time (LSST Ivezić et al., 2019) will be limited to $z \lesssim 1.5$ with a considerable 71–85 % overall fraction.

The inference from the simulated data revealed two key insights. 124 CHIME–SDSS FRB–galaxy pairs yielded 2.6 times weaker constraints on $\Omega_{\rm b}H_0$ than 124 randomly drawn CHIME FRBs, i.e., the same number of FRBs but with higher average redshifts. This shows the importance of considering realistic redshift distributions in forecasts. Applying existing methods to constrain the missing baryons, we showed that even if just 524 of 1000 ASKAP FRB hosts have measured redshifts, $\Omega_{\rm b}H_0$ can be constrained to 10 % (with 95 % credibility). This would represent a significant advancement compared to current constraints from O VII absorption line studies at X-rays, which reach 60 percent uncertainty (Kovács et al., 2019). Uncertainties in theoretical predictions are 2.3 percent from big bang nucleosynthesis and 1.3 percent from big bang nucleosynthesis combined with cosmic microwave background measurements by Planck (Pitrou et al., 2018; Driver, 2021).

Our predictions of the required observation times on our 10-m optical telescope showed that ground based follow-up can only provide secure associations at $z \lesssim 1.5$ and spectra of galaxies at $z \lesssim 0.7$. This discloses a serious challenge for FRB applications that require large redshift FRBs, like studies of the epochs of H and He II reionization.

References

Abazajian, K. N. et al. (2009), *The Seventh Data Release of the Sloan Digital Sky Survey*, ApJS **182** 543, arXiv: 0812.0649 [astro-ph] (cit. on p. 40).

Driver, S. (2021), *The challenge of measuring and mapping the missing baryons*, Nature Astronomy **5** 852, arXiv: 2203.08541 [astro-ph.CO] (cit. on p. 40).

Drlica-Wagner, A. et al. (2022), *The DECam Local Volume Exploration Survey Data Release 2*, ApJS **261**, 38 38, arXiv: 2203.16565 [astro-ph.IM] (cit. on p. 40).

Ivezić, Ž. et al. (2019), *LSST: From Science Drivers to Reference Design and Anticipated Data Products*, ApJ **873**, 111 111, arXiv: 0805.2366 [astro-ph] (cit. on p. 40).

[1] The MOCKFRBHOSTS package is available at https://github.com/JoschaJ/mockFRBhosts.

Jahns-Schindler, J. N. et al. (2023), *How limiting is optical follow-up for fast radio burst applications? Forecasts for radio and optical surveys*, MNRAS **523** 5006, arXiv: 2306.00084 [astro-ph.HE] (cit. on p. 39).

Kovács, O. E. et al. (2019), *Detection of the Missing Baryons toward the Sightline of H1821+643*, ApJ **872**, 83 83, arXiv: 1812.04625 [astro-ph.CO] (cit. on p. 40).

Macquart, J. .-. et al. (2020), *A census of baryons in the Universe from localized fast radio bursts*, Nature **581** 391, arXiv: 2005.13161 [astro-ph.CO] (cit. on p. 39).

Pitrou, C. et al. (2018), *Precision big bang nucleosynthesis with improved Helium-4 predictions*, Phys. Rep. **754** 1, arXiv: 1801.08023 [astro-ph.CO] (cit. on p. 40).

Vanderlinde, K. et al. (2019), "The Canadian Hydrogen Observatory and Radio-transient Detector (CHORD)," *Canadian Long Range Plan for Astronomy and Astrophysics White Papers*, vol. 2020 28 28, arXiv: 1911.01777 [astro-ph.IM] (cit. on p. 39).

CHAPTER 5

Breaking the $\Omega_{\rm b} f_{\rm IGM}$-$H_0$ degeneracy with GW-FRB associations

Motivated by the potential association between GW190425 and FRB 190425A (Moroianu et al., 2023), I have developed a method to resolve the degeneracy between $\Omega_{\rm b} f_{\rm IGM}$ and H_0 using associated GW-FRB events. Despite the uncertain connection between GW190425 and FRB 190425A, the emission of FRBs during the coalescence of two neutron stars and post merger, via the various models described in Section 1.6, appears plausible. Although they can only produce a fraction of the observed FRB rate, the high impact of the studies of GW170817 and its counterparts (e.g. Abbott et al., 2017b; Abbott et al., 2017a) makes the search for FRBs as GW counterparts a worthwhile venture. The campaign around GW170817 benefited from the fortunate circumstance that the event happened at a relatively close distance of only 40 Mpc ($z = 0.01$). Gradual improvements of GW experiments and eventually the third-generation detectors, Einstein Telescope and Cosmic Explorer (Punturo et al., 2010; Evans et al., 2021), will detect GWs to greater distances. This will pose challenges for optical follow-up campaigns similar to those conducted to find GW170817. It comes as a convenient advantage that most telescopes used for FRB searches come with a large field of view. ASKAP for example has a 30 deg^2 field-of-view and could almost cover the 31-deg^2 initial LIGO-Virgo localization region of GW170817 in a single pointing. Should neutron star mergers emit FRBs, these could lead future multi-messenger follow-ups.

As the distances of FRBs increase, identifying a host and subsequently measuring its redshift becomes challenging, as demonstrated in Jahns-Schindler et al. (2023) (Chapter 4). This, together with the 80 % probable host associated with FRB 190425A (Panther et al., 2023), inspired us to develop a method to use GW-FRB associations that does not require a redshift. Although I derive it in the context of a GW-FRB association, this method only requires a luminosity distance measurement of any kind in combination with the *DM* of an FRB.

We will begin with the derivation of the underlying equations in Section 5.1, and then introduce the Bayesian framework in Section 5.2. In Section 5.3, we test the framework on simulated data and forecast its capabilities. In Section 5.4, we present the results of the application to the real data of GW190425 and FRB 190425A under the assumption that they are from the same source, before we discuss the implications in Section 5.5.

5.1 The DM–D_L relation

The method I propose is based on the measurement of DM from the FRB and the luminosity distance D_L derived from the GW. We therefore derive the sightline-averaged $\langle DM_{IGM}\rangle(D_L)$. We assume a flat Λ-cold-dark-matter universe where the redshift-dependent Hubble parameter is given by the Friedmann equation (e.g. Peacock, 1999) in the form

$$H(z) \equiv \frac{\dot{a}}{a} = H_0\sqrt{\Omega_m(1+z)^3 + \Omega_\Lambda}\,, \tag{5.1}$$

where $a = \frac{1}{1+z}$ is the scale factor, H_0 the Hubble constant, $\Omega_m = \frac{\rho_m}{\rho_0}$ the present-day matter density in terms of the critical density $\rho_0 = \frac{3H_0^2}{8\pi G}$ with the gravitational constant G, and $\Omega_\Lambda = \frac{\rho_\Lambda}{\rho_0}$ the dark energy density. The critical density is defined as the density where the universe is flat, which implies $\Omega_m + \Omega_\Lambda = 1$ for our assumed flat universe. The luminosity distance for a source at redshift z follows as

$$D_L(z) = (1+z)\int_0^z \frac{c}{H(z)}\,\mathrm{d}z = (1+z)\frac{c}{H_0}\int_0^z \frac{1}{\sqrt{\Omega_m(1+z)^3 + \Omega_\Lambda}}\,\mathrm{d}z\,. \tag{5.2}$$

The dispersion is a composite of contributions from host galaxy, IGM, and Milky Way. It was already formulated in Chapter 2, but is repeated for the reader's convenience:

$$DM = DM_{MW} + DM_{IGM} + \frac{DM_{host}}{1+z}\,. \tag{5.3}$$

Similarly, the average of DM_{IGM} over many sight lines was given in Eq. (2.10) as

$$\langle DM_{IGM}\rangle(z) = \frac{3c}{8\pi G m_p}\Omega_b H_0 \int_0^z \frac{(1+z) f_{IGM}(z)\left[\frac{3}{4}\chi_H(z) + \frac{1}{8}\chi_{He}(z)\right]}{\sqrt{\Omega_m(1+z)^3 + \Omega_\Lambda}}\,\mathrm{d}z\,. \tag{5.4}$$

In this work, we will consider only low-z FRBs, so we assume hydrogen and helium to be fully ionized, i.e., $\chi_H(z) = \chi_{He}(z) = 1$, and we assume f_{IGM} is constant. Eq. (5.4) then becomes

$$\langle DM_{IGM}\rangle(z) = \frac{3c}{8\pi G m_p}\frac{7}{8}\Omega_b f_{IGM} H_0 \int_0^z \frac{1+z}{\sqrt{\Omega_m(1+z)^3 + \Omega_\Lambda}}\,\mathrm{d}z\,. \tag{5.5}$$

This famous DM–z relation depends on the product $\Omega_b f_{IGM} H_0$, such that these quantities can not be inferred individually. This degeneracy can only be broken with additional constraints, e.g., from measurements of the cosmic microwave background.

If only DM and D_L are available while z is not directly measurable, we can invert $D_L(z)$ to obtain $\langle DM_{IGM}\rangle(D_L)$. The inversion of $D_L(z)$ can only be done numerically, but this does not hinder us from using the relationship. We will refer to the inverted function as $z(D_L)$ and write $\langle DM_{IGM}\rangle(D_L) = \langle DM_{IGM}\rangle(z(D_L))$. The Taylor approximation can be done analytically; the first-order term is

$$\langle DM_{IGM}\rangle(D_L) = \frac{3c}{8\pi G m_p}\frac{7}{8}\Omega_b f_{IGM} H_0 \frac{H_0}{c} D_L + \mathcal{O}(D_L^2) \approx \frac{3}{8\pi G m_p}\frac{7}{8}\Omega_b f_{IGM} H_0^2\, D_L\,. \tag{5.6}$$

Interestingly, this equation is proportional to $\Omega_b f_{IGM} H_0^2$ while the classic DM–z relation has a proportionality to $\Omega_b f_{IGM} H_0$. Combining the DM–D_L relation with the DM–z relation, i.e., GW-FRB associations

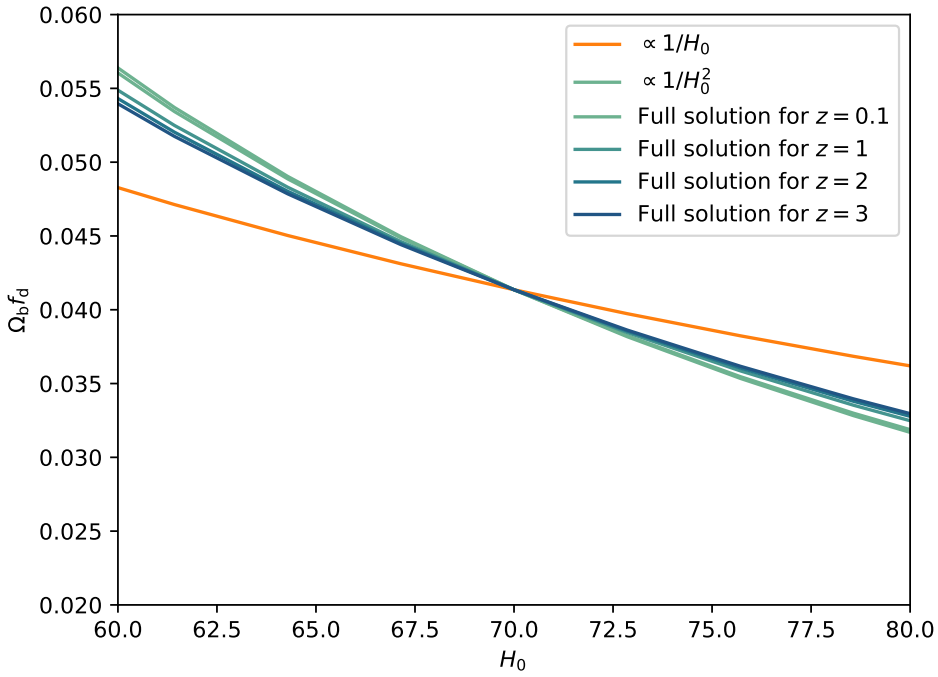

Figure 5.1: The functions along which the different methods are degenerate. The *DM*–z relation is proportional to $\Omega_b f_{IGM} H_0$, hence, degenerate with $\Omega_b f_{IGM} \propto 1/H_0$. The *DM*–$D_L$ relation is approximately proportional to $\Omega_b f_{IGM} H_0^2$, and therefore degenerate with $\Omega_b f_{IGM} \propto 1/H_0^2$. The deviation from this law at higher redshifts is visible in plots of the full solution. Measuring both relations breaks the degeneracy by allowing only the intersection of the two curves.

and independent FRBs that have a measured redshift, we can break the degeneracy between $\Omega_b f_{IGM}$ and H_0.

As we assumed a flat cosmology, we speed up our numerical calculations by using the analytic solutions of the two integrals in Eqs. (5.2) and (5.5). These integrals can be calculated as

$$\int_0^z \frac{1}{\sqrt{\Omega_m (z+z)^3 + \Omega_\Lambda}} \mathrm{d}z = \frac{z+1}{\sqrt{\Omega_\Lambda}} {}_2F_1\left(\frac{1}{3}, \frac{1}{2}; \frac{4}{3}; -\frac{\Omega_m (1+z)^3}{\Omega_\Lambda}\right)\Bigg|_0^z \quad \text{and} \tag{5.7}$$

$$\int_0^z \frac{1+z}{\sqrt{\Omega_m (z+z)^3 + \Omega_\Lambda}} \mathrm{d}z = \frac{(z+1)^2}{2\sqrt{\Omega_\Lambda}} {}_2F_1\left(\frac{1}{2}, \frac{2}{3}; \frac{5}{3}; -\frac{\Omega_m (1+z)^3}{\Omega_\Lambda}\right)\Bigg|_0^z, \tag{5.8}$$

where ${}_2F_1$ is the Gaussian hypergeometric function.

5.2 Bayesian framework

To utilize the derived relation and combine it with other FRB data, we use a Bayesian framework. From Bayes rule (see e.g. Jaynes and Bretthorst, 2003, for an introduction), the posterior probability distribution

is proportional to the product of the likelihood and the prior probability:

$$p(\Omega_b f_{IGM}, H_0 \mid DM, D_L) \propto p(DM, D_L \mid \Omega_b f_{IGM}, H_0)\, p(\Omega_b f_{IGM}, H_0)\,. \tag{5.9}$$

In this exploratory work, we will restrict ourselves to the two free parameters $\Omega_b f_{IGM}$ and H_0, but additional parameters should be left free in further studies. We assume that the Milky Way contribution can be subtracted from the measured DM with sufficient precision, such that we can use the resulting excess $DM_{exc} = DM - DM_{MW} = DM_{IGM} + DM_{host}$. We follow Macquart et al. (2020) in the likelihood definitions of DM_{IGM} and DM_{host}. We describe DM_{host} by a log-normal probability distribution function (PDF) in the formulation of Jahns-Schindler et al. (2023) with median DM_0 and the standard deviation σ_{host} of the DM's base 10 logarithm, i.e.:

$$p_{host}(DM_{host} \mid DM_0, \sigma_{host}) = \frac{\log_{10}(e)}{DM_{host}\sigma_{host}\sqrt{2\pi}} \times \exp\left(-\frac{(\log_{10} DM_{host} - \log_{10} DM_0)^2}{2\sigma_{host}^2}\right). \tag{5.10}$$

We describe the PDF of DM_{IGM} for a given D_L in terms of $\Delta = \frac{DM_{IGM}}{\langle DM_{IGM}\rangle(z(D_L))}$ and with the fluctuation parameter F as

$$p_{cosmic}(DM_{IGM} \mid D_L, \Omega_b f_{IGM}, H_0, F) = A\Delta^{-3} \exp\left(-\frac{(\Delta^{-3} - C_0)^2}{18\,\sigma^2}\right), \quad \sigma = \frac{F}{\sqrt{z(D_L)}}, \tag{5.11}$$

where A is the normalization constant and C_0 is fixed by the condition $\langle\Delta\rangle = 1$. The normalization can be calculated analytically as

$$A = \frac{3(12\sigma)^{1/3}}{3\,\Gamma\left(\frac{1}{3}\right)\,\sigma\,{}_1F_1\left(\frac{1}{6}, \frac{1}{2}, -\frac{1}{2}\,(C_0/3\sigma)^2\right) + \sqrt{2}\,\Gamma\left(\frac{5}{6}\right)\,C_0\,{}_1F_1\left(\frac{2}{3}, \frac{3}{2}, -\frac{1}{2}\,(C_0/3\sigma)^2\right)}, \tag{5.12}$$

where Γ is the gamma function, and ${}_1F_1$ is the generalized hypergeometric function.

Because $DM_{host} = DM_{exc} - DM_{IGM}$, the above equations still leave some freedom for either DM_{IGM} or DM_{host}. We, therefore, use a flat prior for DM_{IGM} between 0 and DM_{exc} and marginalize over it. Additionally, D_L is not an exact measurement but described by a posterior distribution resulting from the GW analysis. When using the real event, we use this posterior as our prior and marginalize over it. When simulating data, we assume that the uncertainty of D_L follows a normal distribution. Finally, we incorporate the results of James et al. (2022), who inferred H_0 from mostly localized FRBs, as a prior in the form $p_J(\Omega_b f_{IGM}, H_0)$ and otherwise put flat prior distributions for $\Omega_b f_{IGM}$ and H_0. Collecting everything in Eq. (5.9) and integrating over D_L and DM_{exc}, yields

$$\begin{aligned} p(\Omega_b f_{IGM}, H_0) &\propto \int \mathrm{d}D_L \int_0^{DM_{exc}} \mathrm{d}DM_{IGM}\, p(DM_{exc}, D_L \mid \Omega_b f_{IGM}, H_0)\, p(\Omega_b f_{IGM}, H_0) && (5.13)\\ &= \int \mathrm{d}D_L \int_0^{DM_{exc}} \mathrm{d}DM_{IGM}\, p_{cosmic}(DM_{IGM} \mid D_L, \Omega_b f_{IGM}, H_0, F) \\ &\quad \times p_{host}(DM_{exc} - DM_{IGM} \mid DM_0, \sigma_{host})\, p_J(\Omega_b f_{IGM}, H_0)\, p(D_L) && (5.14) \end{aligned}$$

where F, DM_0, and σ_{host} are fixed but can be marginalized over in future work.

5.3 Data and simulations

Now that the mathematical framework is set and we obtained the posterior distribution, we will first apply real data and explore the posterior distribution using Markov chain Monte Carlo (MCMC) simulations. Afterward, we will simulate a population of GW-FRB events to forecast the future potential of this method.

5.3.1 Observational data

We use the luminosity distance that was measured for GW190425 (Abbott et al., 2020). To analyze a GW event, the observed time series of the detectors are jointly fit in a Bayesian framework. The parameters include, among the component masses, the position, and others, also the inclination angle of the system. This inclination angle is degenerate with D_L causing large uncertainties, especially in an (almost) single instrument detection. The resulting distance is $D_L = 150^{+80}_{-60}$ Mpc (90 % credible interval). In the analysis, we use the posterior samples reported in the updated analysis of The LIGO Scientific Collaboration et al. (2021)[1]. Specifically, we use the data with a low-spin prior coming from Galactic binary neutron star systems.

For DM, we use the value of $DM_{\mathrm{exc}} = 79.4\,\mathrm{cm}^{-3}\,\mathrm{pc}$ reported by CHIME/FRB Collaboration et al. (2021)[2], where they used the NE2001 model (Cordes and Lazio, 2002) to subtract the Milky Way DM.

We use the constraints on $\Omega_{\mathrm{b}} f_{\mathrm{IGM}} H_0$ from mostly localized FRBs from James et al. (2022). Since they used priors on $\Omega_{\mathrm{b}} f_{\mathrm{IGM}}$ to constrain H_0 but we want the constrains on $\Omega_{\mathrm{b}} f_{\mathrm{IGM}} H_0$, we have to exclude the prior again. We read the PDF of H_0 from their fig. 6 using the WebPlotDigitizer (Rohatgi, 2022), as the data are not published. James et al. (2022) fix $\Omega_{\mathrm{b}}(H_0/100)^2 = 0.02242$, using big bang nucleosynthesis theory and cosmic microwave background measurements (Planck Collaboration et al., 2020). They further use $f_{\mathrm{IGM}}(z=0) = 0.844$ with an evolving $f_{\mathrm{IGM}}(z)$. As there is no possibility to account for the evolution, we have to assume it did not have a big influence on their result, which is reasonable given the mostly low-z FRBs. Hence, we fix $f_{\mathrm{IGM}} = 0.844$ and obtain a constant C that allows us to reverse their assumptions:

$$C = \Omega_{\mathrm{b}} \left(\frac{H_0}{100}\right)^2 100^2 f_{\mathrm{IGM}} = 0.02242 \cdot 100^2 \cdot 0.844 \left(\mathrm{km\,s^{-1}\,Mpc^{-1}}\right)^2 . \tag{5.15}$$

We then transform the PDF reported for H_0, which we label as $p_{H_0}(H_0)$, to account for the change of variables

$$p_{\mathrm{J}}(\Omega_{\mathrm{b}} f_{\mathrm{IGM}}, H_0) = p_{H_0}\left(\frac{C}{\Omega_{\mathrm{b}} f_{\mathrm{IGM}} H_0}\right) . \tag{5.16}$$

After obtaining all the required PDFs, we carry out the MCMC simulation using the emcee package (Foreman-Mackey et al., 2013).

5.3.2 Simulated data set

We simulated a data set of FRBs and associated GWs to test the inference models and estimate future capabilities. To keep it simple, we place all sources at a fixed redshift z_0. We assume a 1-σ Gaussian D_L uncertainty of 10 %, which is a bit less than the lowest uncertainties of 15 % of current detected GW events.[3] With this uncertainty, we draw the D_L 'measurement' around the real value, and later we consider

[1] The data can be obtained from https://doi.org/10.5281/zenodo.5117702.
[2] It can be viewed at https://www.chime-frb.ca/catalog/FRB20190425A.
[3] https://gwosc.org

Table 5.1: Parameters and distributions used in our simulations. Brackets denote the limits of flat distributions, $\mathcal{N}(\mu, \sigma)$ denotes the normal distribution.

Parameter	Value
DM_{exc}	$79.4\,\mathrm{cm}^{-3}\,\mathrm{pc}$
F	0.32
DM_0	2.23
σ_{host}	0.57
z	0.1, 1
Cosmology	Flat ΛCDM
H_0	$70\,\mathrm{km\,s^{-1}\,Mpc^{-1}}$
Ω_m	0.3
	Prior
H_0	$[10, 150]\,\mathrm{km\,s^{-1}\,Mpc^{-1}}$
$\Omega_b f_{IGM}$	$[0, 0.2]$
DM_{IGM}	$[0, DM_{exc}]$
D_L	$\mathcal{N}(D_L(z), D_L(z)/10)$

it in the form of a normal likelihood for D_L. To draw DM, we use Equations (5.10), (5.11), (5.3). We summarize all parameters in Table 5.1. In the described way, we simulate two runs with 10 and 100 FRBs, respectively.

5.4 Results

We applied the Bayesian inference described above to the three data sets: one real FRB, 10 simulated FRBs, and 100 Simulated FRBs. The results are shown in Figures 5.2, 5.3, and 5.4, respectively. The inference with the single association does not give any meaningful constraints, as one might have suspected already. The posterior distribution is essentially the same as the prior that comes from the results of James et al. (2022), which means it is almost completely determined by this prior. This result is likely mostly suffering from low number statistics.

The 10 simulated FRB–GW events at $z = 0.1$ can still not constrain the parameter space beyond the prior distribution. Yet, we can see the posterior that ignores the prior (orange distribution) get smaller. The final posterior is still dominated by the priors. The reason is likely the large scatter in DM. While we lowered the uncertainty in D_L compared with the real event to 10 %, the PDFs that describe DM still allow a large amount of scatter in the data. Particularly at such low redshifts of only $z = 0.1$, DM_{host} can easily dominate over DM_{IGM}.

The 100 simulated FRB–GW events at $z = 1$ finally show meaningful constraints. The resulting parameters are $H_0 = 77^{+18}_{-16}\,\mathrm{km\,s^{-1}\,Mpc^{-1}}$ and $\Omega_b f_{IGM} = 0.034 \pm 0.013$ with 90 % credibility, a 24 and 31 % relative uncertainty, respectively.

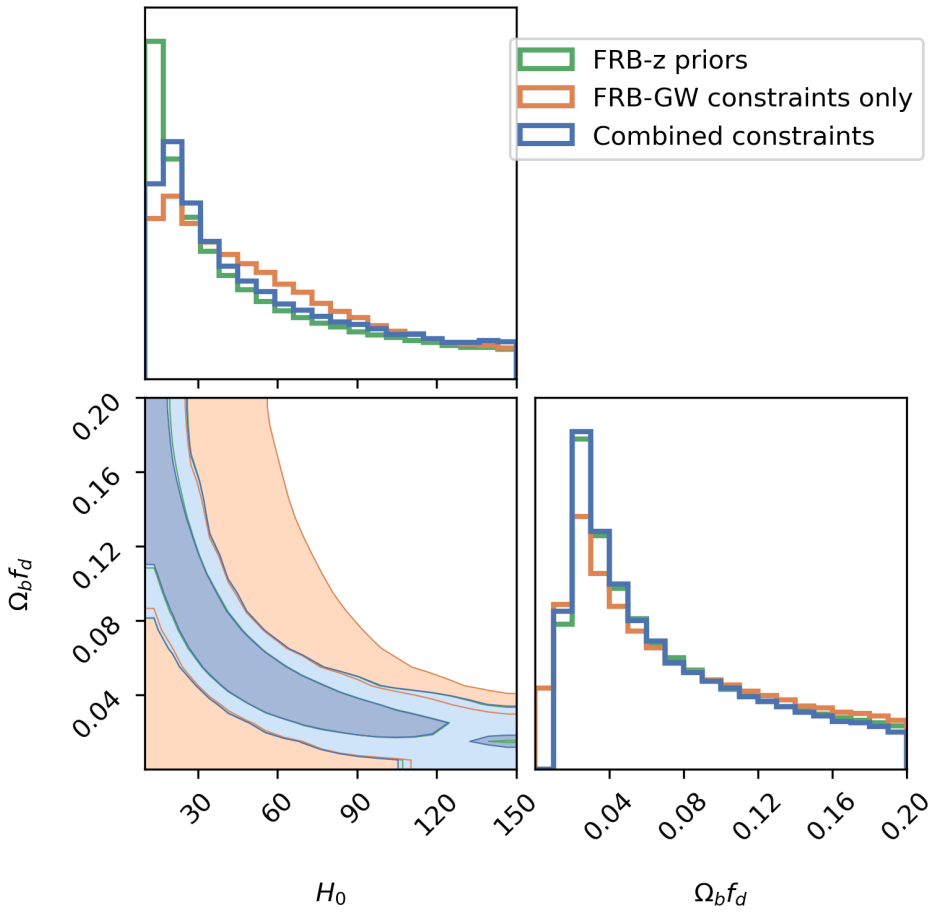

Figure 5.2: Posterior distribution inferred from the real FRB 190425A–GW190425 event. The prior distribution $p_{\mathrm{J}}(\Omega_{\mathrm{b}} f_{\mathrm{IGM}}, H_0)$ derived from the *DM*–*z* relation (James et al., 2022) is also shown, as well as the posterior distribution without using this prior. Panels above and right of the plot show the posteriors when marginalizing over one of the variables.

5.5 Discussion

The constraints on H_0 we forecast for 100 events have the same range as the constraints from FRB *DM*–*z* measurements with CMB priors on Ω_{b}, which are $H_0 = 73^{+22}_{-12}\,\mathrm{km\,s^{-1}\,Mpc^{-1}}$ at 90 % (James et al., 2022). However, our constraints have the advantage that only *DM*, z, and D_L measurements are used without any external priors. This is a promising result, but we want to revisit some of the assumptions that could influence this result.

5.5.1 Uncertain association

The fields of FRBs and GW are both rapidly growing fields with a lot of potential. As mentioned in Chapter 4, CHIME alone is detecting over 500 bursts every year and further telescopes are coming online (e.g. the Deep Synoptic Array, Law et al., 2023). On the other side, GW experiments are also constantly upgraded, and the third generation of GW detectors is currently being planned (Punturo et al., 2010;

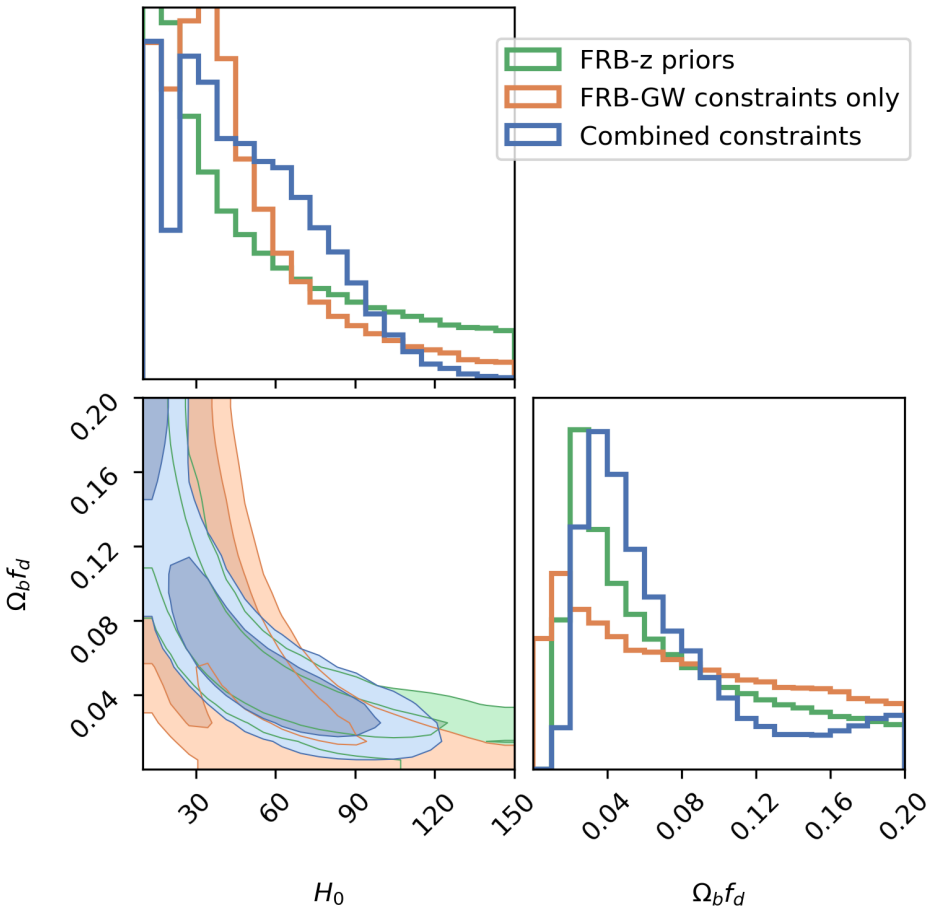

Figure 5.3: Posterior distribution when using 10 simulated FRB–GW events. Similar to Fig. 5.2.

Maggiore et al., 2020; Evans et al., 2021). Predicted rates are in the ranges 910–160 000 per year for the Einstein Telescope and 3 800–650 000 per year for the combination of Einstein Telescope and the Cosmic Explorer (Iacovelli et al., 2022). However, it is still very uncertain if these GW and FRB events will be related via their source.

Our only observational clue is one tentative association, which we discussed in Section 1.6. As a result, the possibilities from no connection to several bursts per GW are all plausible. The case of multiple bursts of GW 190425 has been discarded by Moroianu et al. (2023) based on the FRB morphology. Yet, the probability for the detection would be much higher if FRB 190425A was not the only emitted burst. In this scenario, the emission would not originate from the collapse of the neutron star into a black hole (Falcke and Rezzolla, 2014) but from the magnetosphere of the neutron star before the collapse or from interactions of the jet with the surrounding medium (Usov and Katz, 2000; Rowlinson and Anderson, 2019). From the standpoint of applications, a repeating nature of GW sources would be desirable. It would greatly increase the chances for successful follow-up and GW localizations from FRB detections. Of course, nature is not concerned with the desires of a few astronomers.

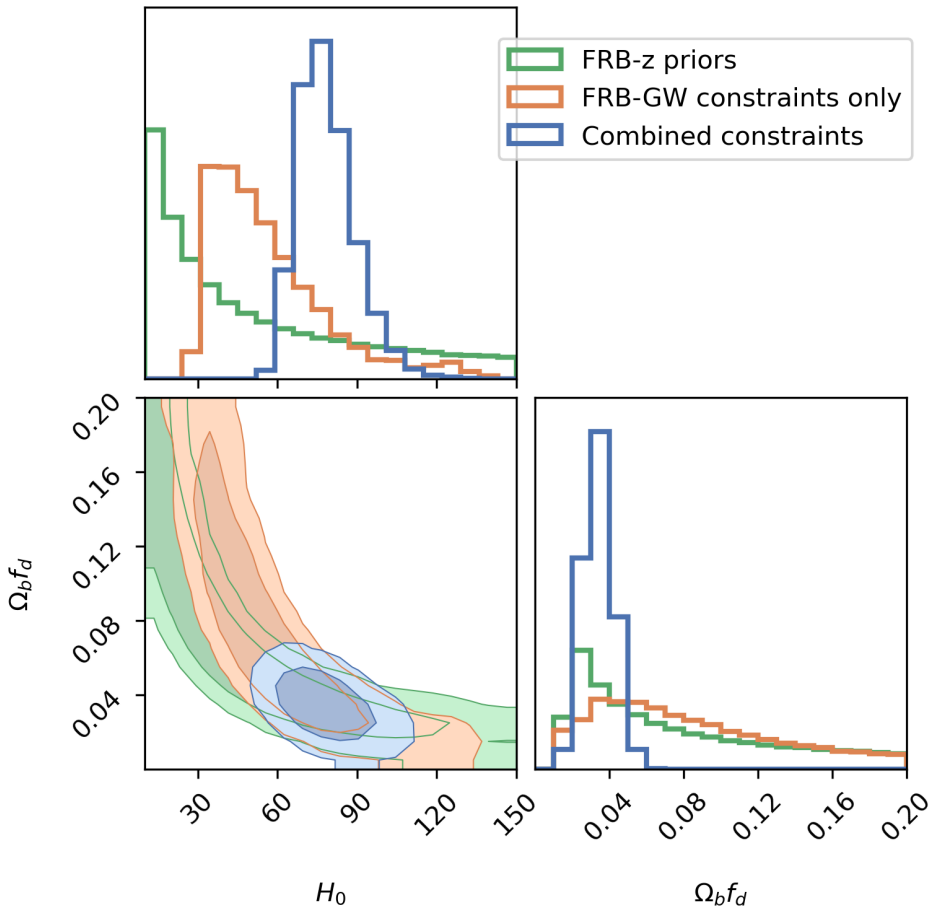

Figure 5.4: Same as Fig. 5.3 but for 100 simulated FRB–GW events. Something is wrong with the code, this needs to be redone.

5.5.2 Chosen redshift distributions

For the purpose of this study, we chose the FRB–GW events to be at a single redshift. We want to compare these with the forecasts for GW detectors. The redshift of the 10 simulated events ($z = 0.1$) is high compared to current GW detectors. This includes planned upgrades for the 5th observing run of LIGO, Virgo, and the Kamioka Gravitational Wave Detector (KAGRA), which is expected to start in 2027. The highest expected distance is 330 Mpc or $z = 0.073$ (Abbott et al., 2018). The distance of $z = 1$ assumed for the 100 simulated events is where the Einstein Telescope will detect most neutron star mergers (Iacovelli et al., 2022).

5.5.3 Mergers with redshift measurement

In this work, we explicitly assumed events that do not have measured redshifts. Some events will have redshift measurements, and FRBs could even provide the necessary localization precision. The additional information would be very valuable. Essentially, the D_L–z relation would provide the H_0 measurement to directly break the degeneracy in the DM–z relation. Wei, Wu, and Gao (2018) provided a framework to

use this via the product $D_L \cdot DM_{\rm IGM}$. It would be straightforward to extend our Bayesian framework to take the additional z measurement into account. The big methodical difference between our approach and the one of Wei, Wu, and Gao (2018) is that they use frequentist inference. Moreover, taking the product of the measurements $D_L \cdot DM_{\rm IGM}$ discards information from the individual values. Therefore using our Bayesian framework should always be advantageous.

5.6 Conclusion

In this Chapter, I developed a new method to use FRBs with an associated luminosity distance measurement as a cosmological tool. This luminosity distance could, e.g., come from a GW counterpart if FRBs arise during a double neutron star merger. The *DM*–D_L measurements allow inferring $\Omega_{\rm b} f_{\rm IGM}$ and H_0 when combined with independent *DM*–z measurements from localized FRBs. The combination of measurements breaks the degeneracy between $\Omega_{\rm b} f_{\rm IGM}$ and H_0 that each measurement would have individually, without using external priors from cosmic microwave background or supernovae measurements. I developed a Bayesian framework to use the *DM* and D_L measurements and combine them with the existing *DM*–z measurements. With a relatively low number of 100 simulated events, it would be possible to constrain $\Omega_{\rm b} f_{\rm IGM}$ and H_0 within 24 % and 31 % (90 % credibility). However, competitive constraints require larger amounts of data, which will be obtained by third-generation GW detectors like the Einstein Telescope and the Cosmic Explorer.

References

Abbott, B. P. et al. (2017a), *Gravitational Waves and Gamma-Rays from a Binary Neutron Star Merger: GW170817 and GRB 170817A*, ApJ **848**, L13 L13, arXiv: 1710.05834 [astro-ph.HE] (cit. on p. 43).

– (2017b), *GW170817: Observation of Gravitational Waves from a Binary Neutron Star Inspiral*, Phys. Rev. Lett. **119**, 161101 161101, arXiv: 1710.05832 [gr-qc] (cit. on p. 43).

Abbott, B. P. et al. (2018), *Prospects for observing and localizing gravitational-wave transients with Advanced LIGO, Advanced Virgo and KAGRA*, Living Reviews in Relativity **21**, 3 3, arXiv: 1304.0670 [gr-qc] (cit. on p. 51).

Abbott, B. P. et al. (2020), *GW190425: Observation of a Compact Binary Coalescence with Total Mass ~ 3.4 $M_\odot$*, ApJ **892**, L3 L3, arXiv: 2001.01761 [astro-ph.HE] (cit. on p. 47).

CHIME/FRB Collaboration et al. (2021), *The First CHIME/FRB Fast Radio Burst Catalog*, ApJS **257**, 59 59, arXiv: 2106.04352 [astro-ph.HE] (cit. on p. 47).

Cordes, J. M. and T. J. W. Lazio (2002), *NE2001.I. A New Model for the Galactic Distribution of Free Electrons and its Fluctuations*, arXiv e-prints, astro-ph/0207156 astro, arXiv: astro-ph/0207156 [astro-ph] (cit. on p. 47).

Evans, M. et al. (2021), *A Horizon Study for Cosmic Explorer: Science, Observatories, and Community*, arXiv e-prints, arXiv:2109.09882 arXiv:2109.09882, arXiv: 2109.09882 [astro-ph.IM] (cit. on pp. 43, 50).

Falcke, H. and L. Rezzolla (2014), *Fast radio bursts: the last sign of supramassive neutron stars*, A&A **562**, A137 A137, arXiv: 1307.1409 [astro-ph.HE] (cit. on p. 50).

Foreman-Mackey, D. et al. (2013), *emcee: The MCMC Hammer*, PASP **125** 306, arXiv: 1202.3665 [astro-ph.IM] (cit. on p. 47).

Iacovelli, F. et al. (2022), *Forecasting the Detection Capabilities of Third-generation Gravitational-wave Detectors Using GWFAST*, ApJ **941**, 208 208, arXiv: 2207.02771 [gr-qc] (cit. on pp. 50, 51).

Jahns-Schindler, J. N. et al. (2023), *How limiting is optical follow-up for fast radio burst applications? Forecasts for radio and optical surveys*, MNRAS **523** 5006, arXiv: 2306.00084 [astro-ph.HE] (cit. on pp. 43, 46).

James, C. W. et al. (2022), *A measurement of Hubble's Constant using Fast Radio Bursts*, MNRAS **516** 4862, arXiv: 2208.00819 [astro-ph.CO] (cit. on pp. 46–49).

Jaynes, E. T. and G. L. Bretthorst (2003), *Probability Theory* (cit. on p. 45).

Law, C. J. et al. (2023), *Deep Synoptic Array Science: First FRB and Host Galaxy Catalog*, arXiv e-prints, arXiv:2307.03344 arXiv:2307.03344, arXiv: 2307.03344 [astro-ph.HE] (cit. on p. 49).

Macquart, J. .-. et al. (2020), *A census of baryons in the Universe from localized fast radio bursts*, Nature **581** 391, arXiv: 2005.13161 [astro-ph.CO] (cit. on p. 46).

Maggiore, M. et al. (2020), *Science case for the Einstein telescope*, J. Cosmology Astropart. Phys. **2020**, 050 050, arXiv: 1912.02622 [astro-ph.CO] (cit. on p. 50).

Moroianu, A. et al. (2023), *An assessment of the association between a fast radio burst and binary neutron star merger*, Nature Astronomy **7** 579, arXiv: 2212.00201 [astro-ph.HE] (cit. on pp. 43, 50).

Panther, F. H. et al. (2023), *The most probable host of CHIME FRB 190425A, associated with binary neutron star merger GW190425, and a late-time transient search*, MNRAS **519** 2235, arXiv: 2212.00954 [astro-ph.HE] (cit. on p. 43).

Peacock, J. A. (1999), *Cosmological Physics* (cit. on p. 44).

Planck Collaboration et al. (2020), *Planck 2018 results. VI. Cosmological parameters*, A&A **641**, A6 A6, arXiv: 1807.06209 [astro-ph.CO] (cit. on p. 47).

Punturo, M. et al. (2010), *The Einstein Telescope: a third-generation gravitational wave observatory*, Classical and Quantum Gravity **27**, 194002 194002 (cit. on pp. 43, 49).

Rohatgi, A. (2022), *Webplotdigitizer: Version 4.6* (cit. on p. 47).

Rowlinson, A. and G. E. Anderson (2019), *Constraining coherent low-frequency radio flares from compact binary mergers*, MNRAS **489** 3316, arXiv: 1905.02509 [astro-ph.HE] (cit. on p. 50).

The LIGO Scientific Collaboration et al. (2021), *GWTC-2.1: Deep Extended Catalog of Compact Binary Coalescences Observed by LIGO and Virgo During the First Half of the Third Observing Run*, arXiv e-prints, arXiv:2108.01045 arXiv:2108.01045, arXiv: 2108.01045 [gr-qc] (cit. on p. 47).

Usov, V. V. and J. I. Katz (2000), *Low frequency radio pulses from gamma-ray bursts?* A&A **364** 655, arXiv: astro-ph/0002278 [astro-ph] (cit. on p. 50).

Wei, J.-J., X.-F. Wu, and H. Gao (2018), *Cosmology with Gravitational Wave/Fast Radio Burst Associations*, ApJ **860**, L7 L7, arXiv: 1805.12265 [astro-ph.CO] (cit. on pp. 51, 52).

CHAPTER 6

Conclusions

FRBs are a new phenomenon with a rapidly evolving field. The quickly changing body of knowledge and new mathematical, statistical, and computational tools offer opportunities and pose challenges. In this thesis, I addressed a broad range of topics around FRBs, from observations, their origins, to their use as astrophysical tools. Here, we will summarize our results, draw conclusions, and outline future routes that the thesis opens.

Chapter 3 described our observations and analysis conducted for studying FRBs and their origins. Using the World's second-biggest radio telescope at the time, I detected one of the largest FRB samples with the highest rate observed thus far for FRB 121102. The large set made properties appear clearly that were previously hidden or in doubt. The analysis has consequences beyond the specific FRB source, particularly for our interpretations of burst arrival times, energies, and spectra.

The wait times between consecutive repeater bursts are sometimes too short for their rate if described as randomly, i.e., by a Poisson process. The Weibull distribution was one suggested solution and thus frequently fitted to FRB wait times (Oppermann, Yu, and Pen, 2018; Oostrum et al., 2020; Cruces et al., 2021; G. Q. Zhang et al., 2021; Niu et al., 2022; Nimmo et al., 2023). For FRB 121102, I found the wait time distribution to be bimodal. This revealed that the Weibull distribution cannot explain any of the characteristics of FRB 121102. It can neither reproduce the change in rate nor the clustering on small timescales. Instead, I found a simple Poisson process with a varying rate, along with bursts sometimes arriving in packs, to be a good description. The timescale of the packs showed to be a characteristic time for FRB 121102 as it was constant over time. Several other FRBs have since shown similar behavior but on different timescales (Xu et al., 2022; Y.-K. Zhang et al., 2023).

The energy distributions of FRBs are difficult to interpret, often hampered by low available burst numbers. The sample of FRB 121102 bursts showed that a simple power-law cannot catch the full energy distribution. Variations between observations and the large differences in the burst rate suggest a joint interpretation of the two quantities might be required.

Statistical analysis of the burst structure uncovered a clear correlation between drift and duration of sub-bursts. The correlation occurred previously under a different parameterization and a specifically developed model (Rajabi et al., 2020). Appearing in two different sources, it was put forward as a law, shared between FRBs (Chamma et al., 2021). In contrast to these claims, I interpreted it as a secondary result of the commonly seen downward drift in frequency. The shared law between FRBs then becomes the known characteristic sad-trombone effect. This interpretation yields a new baseline, deviations from which can be investigated. The first deviation is the linear correlation, which is expected to be quadratic.

This deviation needs to be further investigated with simulations and direct fits of the model to the data.

The drift in structure also affects the measured dispersion, because it is obtained by maximizing the structure. Accounting for the effect, the dispersion in all eight observations is consistent with the same value. Thus, previously reported dispersion variations on short timescales (Aggarwal et al., 2021a; Li et al., 2021) can be entirely explained by the drifting structure.

Chapter 2 focused on applications of FRBs to astrophysical and cosmological problems. It gave a broad summary the ten identified topics as the result of an extended literature research. The most promising application is the study of baryons in the IGM and in the circumgalactic medium of other galaxies, and in particular the Milky Way. FRBs provide a completely unique probe for these plasmas, as the first signal completely independent of the medium temperature. The Hubble constant will be challenging to measure at percent level accuracy. The independent measurement with FRBs is valuable, but it will be difficult for FRBs to compete with other future high precision measurements. Missing external constraints on the baryon fraction in the IGM, f_{IGM}, are the main reason. Studies of other cosmological parameters will be even more challenging and need to be disentangled from the redshift dependencies of f_{IGM} and the host galaxy dispersion. Repeating FRBs lensed by galaxies or galaxy clusters are particularly interesting for cosmology, once they are found. The short durations of FRBs and their large abundance make them unique among transients. Likely for microlensing events, FRBs cover an important mass window yielding either increasing constraints on the abundance of black holes and other compact objects, with every discovered FRB, or eventual detections. FRBs also constrain the hypothetical photon mass. Yet, this application does not scale well with the number of discovered FRBs, but is dominated by individual events. It gives valuable constraints, but they will not improve by orders of magnitude in the future.

FRB application forecasts largely ignore that redshifts will not be a given for every FRB. The work presented in Chapter 4 closed this gap in the scientific body and pointed out practical limits of several applications. It made clear that obtaining telescope time for redshift measurements will be the bottleneck for at least six out of the ten topics discussed in Chapter 2. The significance of methods that study baryons or cosmological parameters greatly depends on the available optical time.

Several applications could be delayed by years or decades because they require redshifts beyond what is observable from the ground. These include studying the epochs of reionization of H and He II, measuring cosmic magnetic fields, and measurements of the optical depth of the cosmic microwave background. To attain time on space based telescopes and conduct these measurements, we require a good understanding of the FRB population and of systematic uncertainties to do realistic forecasts. My simulations provide the source populations for conducting these forecasts. Additionally, they already allow optimizing the use of available observing time.

In Chapter 5, I developed a novel method of using FRBs that are associated with GWs. The biggest caveat is that the connection is still highly uncertain, with only one ambiguous observed event. Should the connection solidify, the joint events could present an important complementary probe to the common DM–z relation, which does not rely on additional redshift measurements. Moreover, the DM–z relation is inherently degenerate with respect to the Hubble constant and the baryons in the IGM. The developed method grants the first way of breaking this degeneracy without external measurements. This indicates considerable synergy potential between FRBs and GWs in the era of third-generation GW detectors.

6.1 Future work

The work opens up several routes for extending the studies and gain a deeper understanding of FRBs and their applications. Two interesting possibilities follow in a more detailed discussion.

6.1.1 Extended spectro-temporal analysis

The detection of the sad-trombone drift within sub-bursts is of further interest in several ways. Our method that led to the detection of the drift in sub-bursts needs to be modified under the new interpretation. The parameters of this interpretation were calculated from the old model, but it would be advantageous to directly include the sad-trombone drift in the model. Combined with Monte Carlo simulations, this will yield more accurate drift rates with most realistic uncertainties.

Previously, only bright bursts with sufficient substructure allowed a fit for drift rates. This method will enable obtaining drift rates for every single burst. Three variations of the fit will allow testing different aspects of the model. These variations are: (I) Fit a drift for each individual sub-burst. (II) For complex bursts, constrain the drift to be the same in each burst. (III) Jointly fit the drift rate of the burst peaks and the sub-bursts. If the *DM* is not known, (II) and (III) can include the *DM* as a free parameter.

These algorithms allow reaching three goals. First, analysis of the frequency dependence can discern different FRB emission models that predict the sad-trombone effect. Second, drift rates of each burst allow the search for temporal variations and correlations with other burst parameters. Third, the algorithms can measure the *DM* to higher accuracies than even the current structure optimizing codes. It will perform particularly better in the case where no structure on very short timescales is present.

6.1.2 Galaxy association probabilities

The mock catalogs of FRBs and galaxies that we generated in Chapter 4 have further potential uses not yet harvested. FRB host galaxy associations are not always unambiguous. Tools exist to assign association probabilities to every galaxy in the vicinity of an FRBs sight line (Aggarwal et al., 2021b). The probability inference must consider the prior probability of the host galaxy being visible at all. This is typically just set to 1. The results in Chapter 4 show that this is not appropriate, and indeed a well localized FRB without a detected host galaxy has recently been reported (Marnoch et al., 2023). Our simulations could provide a correct prior probability. A further problem that is not addressed in the literature are false associations and their effects on FRB applications. This could be addressed by combining our simulations with ray tracing simulations.

CHAPTER 7

Acknowledgments

I had a lot of fun during the time of my PhD, this is most important to me, and I thank everyone who was part of it.

First, I would like to thank Laura for her advice through every stage of this thesis. I have the feeling that I have grown so much during the years of my PhD, and a large part of that is due to your guidance. You were always available for discussions, always with some good advice, whether it was about some small detail in the manuscript or about the grant scheme of the PhD. In the last project, you encouraged me to pursue my own idea, which was a great experience. Thank you so much for everything.

I would like to thank Michael for always giving me the feeling that he will be there if I need him and for having us FRBlers in the Fundi group. Thanks also to all my other TACos, Cristiano, Jason, and Olaf, for providing helpful advice.

Thanks to everyone who has read parts of my thesis for their helpful comments. This includes Ferdinand, Marlon, Surya, Tim, Sachin, Marilyn, Gina, and especially Laura and Michael. I would like to further thank Professor Brock for the LaTeXtemplate, Jakob for his submission guide, and Tim, Jompoj and Cosima for answering my remaining questions.

I would like to thank my office mates for the great time. Tim and Ferdinand, we have been in the same office almost the whole time. Thank you for always being happy to have a quick discussion or playing a prank on someone, and for everything else. Joey, thank you for making the start so easy. Jaswanth with some distance, I hope I can some day forgive you. Livia, I really enjoyed our trip to Effelsberg. Jacob, you have magic cactus hands.

I would like to thank the FRB group for all the inspiring discussions. I love our journal clubs. Mari, thank you so much for the advice you gave me, even before I started. For always having the time to share some stories and for all the fun you bring to every table. Charlie, thank you for jumping in as an advisor when Laura was on leave. Surya, you have such a great vibe. I had a great time in Korea thanks to you. Henning, thanks for introducing me to the FRB tools and for being my idol. Marlon, I admire your actionism and I will leave the institutes' sustainability in your hands.

I would like to thank all Fundis for the great atmosphere in the group. Jaswanth, thanks for being the floor's mother and for all the One Piece nerd discussions. Jonah, I wanted to put a quote from you as a chapter quote, but I did not include them in the end, so here it is: "What matters in the end are the plots we made along the way" (Wagenveld, 2022).

Ein besonderer Dank geht an meine Familie, insbesondere an meine Mutter, die mich mein ganzes Leben ermutigten und mir die Freiheit gaben, meinen eigenen Weg zu gehen. Danke für Eure Unterstützung.

Ich möchte außerdem meinen Freunden danken, die mich jetzt schon so lange begleiten. Für den Ansporn einen Doktor zu machen nochmal besonderer Dank an Carlo und Felix. Es ist bald so weit.

Ganz besonders danken möchte ich meiner Frau Gina für ihre permanente Unterstützung. Danke, dass Du so viel von der mentalen Last getragen hast. Ich freue mich auf unsere Zukunft.

I would like to thank the Blazing Suns for the great time on the court. It was fun improving together. We are the champions.

APPENDIX A

The FRB 20121102A November rain in 2018 observed with the Arecibo Telescope

Monthly Notices of the ROYAL ASTRONOMICAL SOCIETY

MNRAS **519,** 666–687 (2023) https://doi.org/10.1093/mnras/stac3446
Advance Access publication 2022 November 25

The FRB 20121102A November rain in 2018 observed with the Arecibo Telescope

J. N. Jahns [1★] L. G. Spitler [1] K. Nimmo [2,3] D. M. Hewitt [3] M. P. Snelders,[3] A. Seymour,[4] J. W. T. Hessels,[2,3] K. Gourdji [3,5] D. Michilli [6,7] and G. H. Hilmarsson [1]

[1]*Max-Planck-Institut für Radioastronomie, Auf dem Hügel 69, D-53121 Bonn, Germany*
[2]*ASTRON, Netherlands Institute for Radio Astronomy, Oude Hoogeveensedijk 4, NL-7991 PD Dwingeloo, the Netherlands*
[3]*Anton Pannekoek Institute for Astronomy, University of Amsterdam, Science Park 904, NL-1098 XH Amsterdam, the Netherlands*
[4]*Green Bank Observatory, PO Box 2, Green Bank, WV 24944, USA*
[5]*Centre for Astrophysics and Supercomputing, Swinburne University of Technology, Hawthorn, VIC 3122, Australia*
[6]*MIT Kavli Institute for Astrophysics and Space Research, Massachusetts Institute of Technology, 77 Massachusetts Ave, Cambridge, MA 02139, USA*
[7]*Department of Physics, Massachusetts Institute of Technology, 77 Massachusetts Ave, Cambridge, MA 02139, USA*

Accepted 2022 November 22. Received 2022 November 22; in original form 2022 February 11

ABSTRACT

We present 849 new bursts from FRB 20121102A detected with the 305-m Arecibo Telescope. Observations were conducted as part of our regular campaign to monitor activity and evolution of burst properties. The 10 reported observations were carried out between 1150 and 1730 MHz and fall in the active period around 2018 November. All bursts were dedispersed at the same dispersion measure and are consistent with a single value of (562.4 ± 0.1) pc cm^{-3}. The rate varies between 0 bursts and 218 ± 16 bursts per hour, the highest rate observed to date. The times between consecutive bursts show a bimodal distribution. We find that a Poisson process with varying rate best describes arrival times with separations >0.1 s. Clustering on time-scales of 22 ms reflects a characteristic time-scale of the source and possibly the emission mechanism. We analyse the spectro-temporal structure of the bursts by fitting 2D Gaussians with a temporal drift to each sub-burst in the dynamic spectra. We find a linear relationship between the sub-burst's drift and its duration. At the same time, the drifts are consistent with coming from the sad-trombone effect. This has not been predicted by current models. The energy distribution shows an excess of high-energy bursts and is insufficiently modelled by a single power law even within single observations. We find long-term changes in the energy distribution, the average spectrum, and the sad-trombone drift, compared to earlier and later published observations. Despite the large burst rate, we find no strict short-term periodicity.

Key words: methods: data analysis – methods: observational – radio continuum: transients – fast radio bursts.

1 INTRODUCTION

Fast radio bursts (FRBs) are millisecond-duration flashes of radio waves that are of extragalactic origin (Lorimer et al. 2007). The sources of FRBs and their emission mechanisms are still uncertain (see Lyubarsky 2021; Petroff, Hessels & Lorimer 2022, for recent reviews), but growing numbers of FRBs (CHIME/FRB Collaboration 2021) and localizations within host galaxies (e.g. Bannister et al. 2019; Bhandari et al. 2022) recently boosted our understanding of their statistical properties.

Observationally, FRBs are divided into repeaters and FRBs that have so far only been detected once. CHIME/FRB Collaboration (2021) found that these two populations indeed have different statistical properties, with repeaters having narrower bandwidths and longer durations on average (Pleunis et al. 2021). Moreover, the tendency of sub-bursts to drift to lower frequencies within a burst (Hessels et al. 2019) – now called *sad-trombone effect* – is characteristic for repeaters, while being very rare in (apparent) non-repeaters. This suggests that the presence of two distinct populations is due to different underlying source classes or emission mechanisms, even if it turns out that all FRBs will repeat eventually.

FRB 20121102A (hereafter FRB 121102) is the first discovered (Spitler et al. 2014) and most studied repeater. It was observed to repeat by Spitler et al. (2016), which allowed interferometric follow-up observations that localized it to a low-metallicity, star-forming dwarf galaxy at redshift $z = 0.193$ (Bassa et al. 2017; Chatterjee et al. 2017; Tendulkar et al. 2017). The source is colocated with a compact, persistent radio source within 40 pc projected distance (Marcote et al. 2017). Observations between 4 and 8 GHz revealed nearly 100 per cent linear polarization with an extremely high rotation measure of $\sim 10^5$ rad m^{-2} (Gajjar et al. 2018; Michilli et al. 2018b). The rotation measure decreases by an average of 15 per cent per year, with per cent level fluctuations between weeks (Hilmarsson et al. 2021). Together these findings are interpreted as the FRB being in the magneto-ionic environment of a massive black hole, a supernova remnant, or perhaps the wind nebula (plerion) of a young neutron star; the observations are also consistent with a

★ E-mail: jjahns@mpifr-bonn.mpg.de

binary model, if there is a massive stellar companion (e.g. Tendulkar et al. 2021). Several years of observations with different telescopes have also revealed periodic activity with a period of ∼160 d and a duty cycle of about 60 per cent (Rajwade et al. 2020; Cruces et al. 2021). Reasons for this could either be that the source is in a binary system with a corresponding period (e.g. Gu, Yi & Liu 2020; Ioka & Zhang 2020; Lyutikov, Barkov & Giannios 2020; Du et al. 2021; Wada, Ioka & Zhang 2021; Kurban et al. 2022), it is precessing (e.g. Levin, Beloborodov & Bransgrove 2020; Sob'yanin 2020; Zanazzi & Lai 2020; Sridhar et al. 2021), or that it has a thus far unobserved slow period (Beniamini, Wadiasingh & Metzger 2020).

To further understand the source and its emission mechanism, it is crucial to study the burst properties and statistics of large burst samples. Such studies have shown clear spectro-temporal structures in the bursts of FRB 121102 and the sad-trombone effect (see e.g. Hessels et al. 2019). Searches have been most fruitful at 1.4 GHz, where the source shows high activity. The largest numbers of bursts were found with the Arecibo Telescope and the Five-hundred-meter Aperture Spherical radio Telescope (FAST). Hewitt et al. (2022) reported a total of 478 bursts in 59 h of observations with the Arecibo Telescope through 2016 and an activity peak in September [a subset of which was previously found by Gourdji et al. (2019) and Aggarwal et al. (2021)]. Li et al. (2021b) reported 1652 bursts in 59.5 observing hours with FAST in 2019 September and October, triggered when the source was known to be active. Further studies were conducted with the Effelsberg Telescope (Hardy et al. 2017; Houben et al. 2019; Cruces et al. 2021), APERture Tile In Focus (APERTIF; Oostrum et al. 2020), the Lovell Telescope (Rajwade et al. 2020), as well as the MeerKAT and Nançay telescopes (Platts et al. 2019; Caleb et al. 2020).

From the properties that a large burst sample permits to study the energy distribution, the wait times, and the spectro-temporal structure are among the most interesting. The energy distribution can give important insight into the emission mechanism and allows direct comparison to rotation-powered pulsars and magnetically powered magnetars, which are well-studied candidate progenitor classes. Normal pulses of some pulsars form a lognormal energy distribution (see e.g. Burke-Spolaor et al. 2012), whereas energies of giant pulses follow a power law (see e.g. Bera & Chengalur 2019; Abbate et al. 2020). Similarly, burst energies of magnetars also show lognormal distributions with a tail at high energies (Lynch et al. 2015) and power laws in X-rays (Göğüş et al. 1999, 2000). The bursts of FRB 121102 were found to have different power-law indices in different studies; for example Gourdji et al. (2019) reported $\gamma = -1.8$, while Cruces et al. (2021) found $\gamma = -1.1$. Li et al. (2021b) found a bimodal energy distribution, which notably evolved during their observing campaign. Hewitt et al. (2022) reported a separation of bursts into two groups in the parameter space of energy, width, and bandwidth. It now becomes evident that most of these differences come from actual temporal changes in the emission energies and properties, rather than selection effects.

Analysis of the wait times (the time between consecutive (sub-) bursts) can reveal characteristic time-scales or changes in the activity of a repeater. The discovery of the ∼160 d periodicity has explained some of the clustering previously observed (Oppermann, Yu & Pen 2018), yet changes in the rate on time-scales of hours to days still persist. Furthermore, short wait times (first discussed in Katz 2018; Zhang et al. 2018; Gourdji et al. 2019) have appeared in several studies of high-rate observations as a second peak in the wait-time distribution (Li et al. 2019, 2021b; Aggarwal et al. 2021; Hewitt et al. 2022). Cruces et al. (2021) have shown that bursts within single observations still follow Poisson statistics if one excludes wait times of <1 s. However, the rate is not constant and has been seen to change on time-scales of minutes at 6 GHz (Gajjar et al. 2018).

Apart from the sad-trombone effect, a second more subtle, possibly related spectro-temporal effect has been reported by Rajabi et al. (2020) and Chamma et al. (2021). Here, within one sub-burst lower frequencies arrive later than higher frequencies depending on the burst width and frequency. This *intraburst drift* is so far only explained by a family of models where the FRB's emission region moves with relativistic speed and where the emission process has a time delay between a trigger and the emission. It was particularly discussed in the framework of Dicke's superradiance (Dicke 1954; Houde et al. 2019). Studying this effect requires bursts with high signal-to-noise ratios (S/N) and consistent dispersion measure (DM). Therefore, large numbers of bursts, which are close in time, are necessary to get a consistent picture of the effect.

In this paper, we present our statistical analysis of 849 new bursts from FRB 121102 observed with the Arecibo Telescope. We found these bursts in 10 observations during the *November rain*, a burst storm in 2018 October and November, where Cruces et al. (2021) already found high activity in one observation with the Effelsberg Telescope. The sample was collected using new radio frequency interference (RFI) excision techniques and an improved search pipeline. Apart from the general statistical properties, we do an in-depth analysis of the wait times, energies, and intraburst drifts.

We describe our observational campaign, the details of our observing system, and our FRB search pipeline in Section 2. In Section 3, we describe the extraction of burst properties, our two-dimensional Gaussian fits, and the energy calculation. Section 4 presents our analyses and results, which we discuss further in Section 5. In Section 6, we summarize and conclude.

2 OBSERVATIONS AND SEARCH

We observed FRB 121102 with the 305-m William E. Gordon Radio Telescope at the Arecibo Observatory as part of our regular monitoring campaign at 1.4 and 4.5 GHz (project P3054; PI: L. Spitler). The 10 observations presented here were all carried out with the L-Wide receiver with a nominal frequency range of 1150–1730 MHz, dual linear polarizations, a gain of $\sim$10.5 K Jy^{-1}, and a system temperature of about 30 K.[1] The observations were scheduled based on the telescope availability and not on prior knowledge of the source's activity. They include all L-band observations of our campaign between 2018 August 26 and 2019 February 21. We used the pulsar backend Puerto Rico Ultimate Pulsar Processing Instrument (PUPPI)[2] to record our filter bank data coherently dedispersed to DM = 557.0 pc cm^{-3}. The dedispersion is done on 8 GPU nodes, each dedispersing a frequency band of 100 MHz with 64 channels[3] (DuPlain et al. 2008). The bands are then merged together and stored as PSRFITS files. Occasionally, one of the GPU nodes was overloaded and wrote 0s for a short time; we refer to this as *dropouts*. This affected 0.68–3.82 per cent of the data in each of the 10 observations presented here. The data are recorded in the resulting 1.5625 MHz channel width, in 8 bit, and with a sampling time of 10.24 µs. Albeit we record the full Stokes data, we only use the total intensity, as the linear polarization is not measurable. The reasons are that the

[1] http://www.naic.edu/∼astro/RXstatus/Lwide/Lwide.shtml
[2] http://www.naic.edu/puppi-observing/
[3] The backend frequency band extends beyond the receiver band causing the mismatch between the bandwidths.

source's high rotation measure causes intrachannel Faraday rotation smearing for the given channel widths and frequencies (Michilli et al. 2018b), and additionally that the source is less polarized at L-band (Plavin et al. 2022).

We made major changes to the pipeline that was used for previous searches (Gourdji et al. 2019; Hewitt et al. 2022) and which has been described in detail in Michilli et al. (2018a). To save disc space and speed up the search, the data were converted to total intensity and downsampled in time by a factor of 8 to a resolution of 81.92 μs using `psrfits_subband`.[4] In contrast to previous searches, the frequency resolution was kept at 1.5625 MHz per channel to allow for later masking of channels. DM smearing within a channel is caused by the difference ΔDM between the real DM and the DM used for coherent dedispersion. For our channel width $\delta\nu$ it can be approximated as

$$\Delta t \approx a\, 2\,\delta\nu \frac{\Delta\mathrm{DM}}{\nu^3} = 13\,\mu\mathrm{s}\frac{\Delta\mathrm{DM}}{\mathrm{pc\,cm^{-3}}}\frac{\nu^{-3}}{\mathrm{GHz^{-}}}, \quad (1)$$

where ν is the frequency and $a = 4.1488064239(11)\,\mathrm{GHz^2\,cm^{-3}\,pc^{-1}}$ the dispersion constant (Kulkarni 2020). With $\Delta\mathrm{DM} \sim 6\,\mathrm{pc\,cm^{-3}}$ (see Section 3) it varies between 15 μs at the top and 51 μs at the bottom of the band. It is therefore always smaller than the resolution used in the search.

We wrote our own program FIX_GPU_DROPOUTS to identify GPU node dropouts and replace them by random data. These dropouts manifest as 1/8th of the band going to 0 for typically <1 s, often multiple times in a row. In previous searches, the dropouts were treated in the same way as external RFI. This has caused many false candidates in previous versions of the pipeline, rendering parts of the data unusable. The same program was used to flag channels that were affected by narrow-band RFI.

FIX_GPU_DROPOUTS works in three steps. Throughout the program, only the 384 channels from 1150 to 1750 MHz are considered. Other channels are set to 0, this completely includes the lowest GPU band. (i) The program first identifies timestamps where all the samples across a GPU are 0 at the same time and adds 8 ms (100 samples) before and 24 ms (300 samples) after this time to account for *dropping* and *ramping-up* of GPU nodes. The data around the dropouts are scaled back to the mean of 96 (the 8 bit data allow values from 0 to 255) and standard deviation of 32 that is also given to `psrfits_subband` in the downsampling. The dropout is replaced by random Gaussian data with those same mean and standard deviation. (ii) The RFI exclusion is based on the number of outliers, which we define as samples that are five times the standard deviation above the median. To identify channels often affected by RFI, we count the outliers in each channel and block of 0.3 s length. We ignore times with dropouts or where many channels have outliers due to broad-band RFI. For the remaining time, we calculate the median number of outliers in a channel and the interquantile range. We set channels to 0 that have more outliers than the median plus 0.13 times the difference between the 7 per cent quantile and the median (as an unbiased measure of the scatter in the data); the factor was determined empirically. (iii) Ignoring RFI channels, we search for shorter dropouts, where the data values drop in a GPU node, but do not go down to 0. For each timestamp, we take the mean in frequency across a GPU and identify short dropouts where this mean drops below its median minus six times its standard deviation. We again replace these short dropouts by Gaussian random data. The cleaned data are stored as a new PSRFITS file. In our 10 observations, we replace 0.68–3.82 per cent of the data and mask 69–130 channels out of 384 in the receiver band, yielding an effective bandwidth of 492.1875–396.875 MHz.

We searched the data using PRESTO's `single_pulse_search.py`[5] (Ransom 2001) in a DM interval from 461 to 661 $\mathrm{pc\,cm^{-3}}$ in steps of 1 $\mathrm{pc\,cm^{-3}}$ and with an S/N limit of 5 (compared to 6 used in earlier studies). We grouped together events within 20 ms and 5 $\mathrm{pc\,cm^{-3}}$. We set liberal conditions on candidates to be visually inspected: one of the events must have a DM between 551 and 581 $\mathrm{pc\,cm^{-3}}$, and either one of the events must have an S/N > 6 (including single event groups) or the group must consist of at least three events. These liberal conditions are enabled by the earlier rigorous dropout and RFI excision. This is unlike in previous pipeline versions, where much of the RFI exclusion was done right before candidate inspection.

We visually inspect the spectra of candidates in three windows with different time spans and resolutions to classify them as real, RFI, or ambiguous. For later analysis, we cut out real and ambiguous bursts from the full resolution data, although for the analysis in this paper we use only bursts classified as real. Our experience with the data suggests that we are able to detect the majority of bursts above an S/N of about 6.

For future applications of our pipeline, we compare our classification with the one from the machine learning classifier FETCH (Agarwal et al. 2020). We apply FETCH on the observations with MJD 58435, 58439, and 58450. We find that of the 11 available models, model H misses the least amount of bursts. None the less, when we use model H and a probability threshold of 50 per cent, we find that 19 per cent of the bursts in those data sets are missed. Of the bursts that are missed, 90 per cent have an S/N below 8.0 – the minimum S/N of simulated FRBs on which FETCH was trained (Agarwal et al. 2020). For the bursts that have S/N < 8, 34 per cent have a probability less than 50 per cent (model H). FETCH finds 96 per cent of the bursts that have S/N ≥ 8 and the ones that are missed are bursts that are strongly affected by (broad-band) RFI. The fact that FETCH otherwise agreed with our classification for S/N ≥ 8 affirms that the manual inspection is reliable. We therefore continue with our manual visual inspection for the classification and do not use the classification as provided by FETCH. We note that it would be possible to retrain FETCH using data from the Arecibo Telescope, which could improve the performance of the classification. That, however, is beyond the scope of this paper.

3 BURST PROPERTIES

To analyse the bursts, we dedispersed all of them at a common DM. This is to be preferred because the majority of bursts do not have sufficiently resolved structure to determine an accurate DM. Moreover, 844 of the 849 bursts are observed within 18 d and Hessels et al. (2019) have found that the DM of FRB 121102 varies by only 0.07 $\mathrm{pc\,cm^{-3}}$ (standard deviation) on time-scales of weeks. To determine the DM, we used `DM_phase`[6] (Seymour, Michilli & Pleunis 2019), a code that maximizes the temporal structure in a burst rather than the peak S/N. The latter is not reliable, as it can be greatly affected by the sad-trombone effect. We used eight bursts that had temporal structure and high S/N, such that `DM_phase` yields small uncertainties in DM. The mean (weighted by the squared uncertainties) of $(563.02 \pm 0.22)\,\mathrm{pc\,cm^{-3}}$

[4] https://github.com/demorest/psrfits_utils

[5] http://www.cv.nrao.edu/~sransom/presto/

[6] https://github.com/danielemichilli/DM_phase

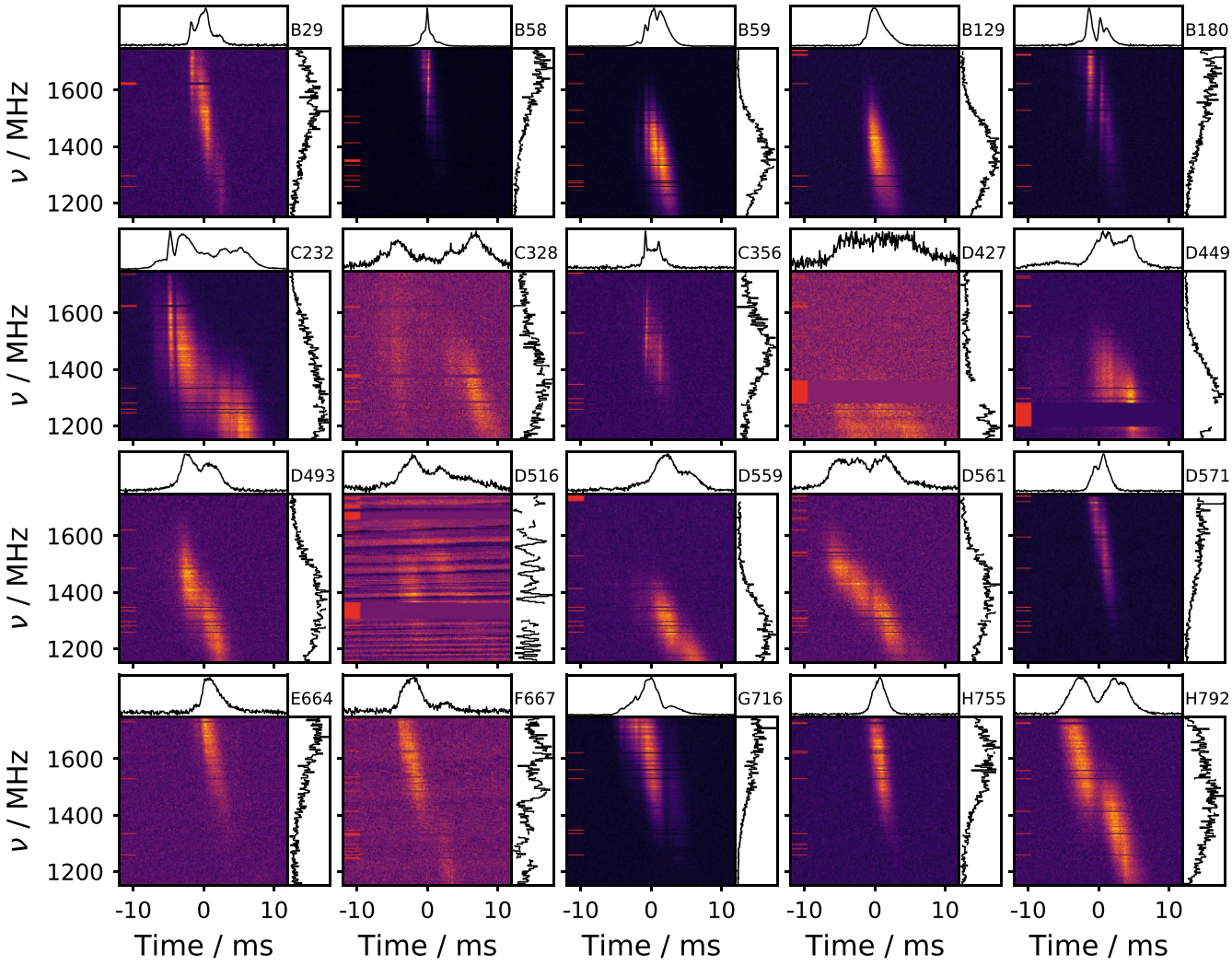

Figure 1. The 20 most energetic bursts. For each burst, the dynamic spectrum is shown with the time series (averaged over the full observing band; top panel) and the spectrum (averaged over the plotted 24 ms window; right-hand panel). The burst IDs are shown in the top right-hand corner; bursts are numbered by the order of occurrence, and letters indicate the observation. All bursts have been dedispersed to a DM of 563.02 pc cm^{-3}. Red bars on the left of the dynamic spectra mark channels that have been excluded because of RFI or GPU node dropouts. The native resolution has been reduced by a factor of 8 in time and 2 in frequency (to 81.92 ms and 3.125 MHz) for visualization purposes. Almost all bursts show temporal structure and the sad-trombone effect.

was used to dedisperse all bursts. The eight bursts used are B29, B58, B59, B129, B180, D493, D561, and G716, which are all shown in Fig. 1 as part of the collection of the 20 brightest bursts. The DM of bursts C232 and C356 could only be obtained at a later stage and would have changed the DM slightly to (562.97 ± 0.18) pc cm^{-3}. To be consistent, we continued using DM = 563.02 pc cm^{-3}. The DM values that were used are shown in the top panel of Fig. 2. The sharpest bursts B58 and C356 are visually overdedispersed, and we will show later that it is better to only consider the sharpest bursts to find the best DM for dedispersion.

For each burst, we masked channels by eye that were contaminated by RFI and selected a time window that fully contains the burst. The on-burst region was used for fitting, while the off-burst region was used to determine the noise to normalize channels. We located the centre of each component of a burst by eye and used it as the initial value for the following fits.

We fit two-dimensional, elliptical Gaussians to each sub-burst in the burst spectra. The exact form that we fit depending on time t and radio frequency ν is

$$\mathcal{G}_{\mathrm{2D}}(t,\nu) = A \exp\left(-\frac{(t - t_0 - d_t(\nu-\nu_0))^2}{2\sigma_t^2} - \frac{(\nu-\nu_0)^2}{2\sigma_\nu^2}\right), \quad (2)$$

with the six free parameters: amplitude A, time of arrival t_0, linear temporal drift d_t, σ_t: duration at ν_0, central frequency ν_0, and bandwidth σ_ν. This is different from the commonly used form where a Gaussian is rotated by an angle. This parametrization has the advantage that σ_t and σ_ν are independent of the DM, while d_t is closely related to it. The formerly used angles α (see e.g. the definition in appendix A of Chamma et al. 2021, although named θ there) can be converted into a drift rate with a small angle approximation $d_t = -\alpha$ ms MHz^{-1} if the time and frequency units ms and MHz were used to obtain α. A second parametrization and interpretations of both are discussed in Section 4.3 and further in Section 5. Additional forms of the elliptical Gaussian, illustrations and explanations, as well as the full conversion equations can be found in Appendix A.

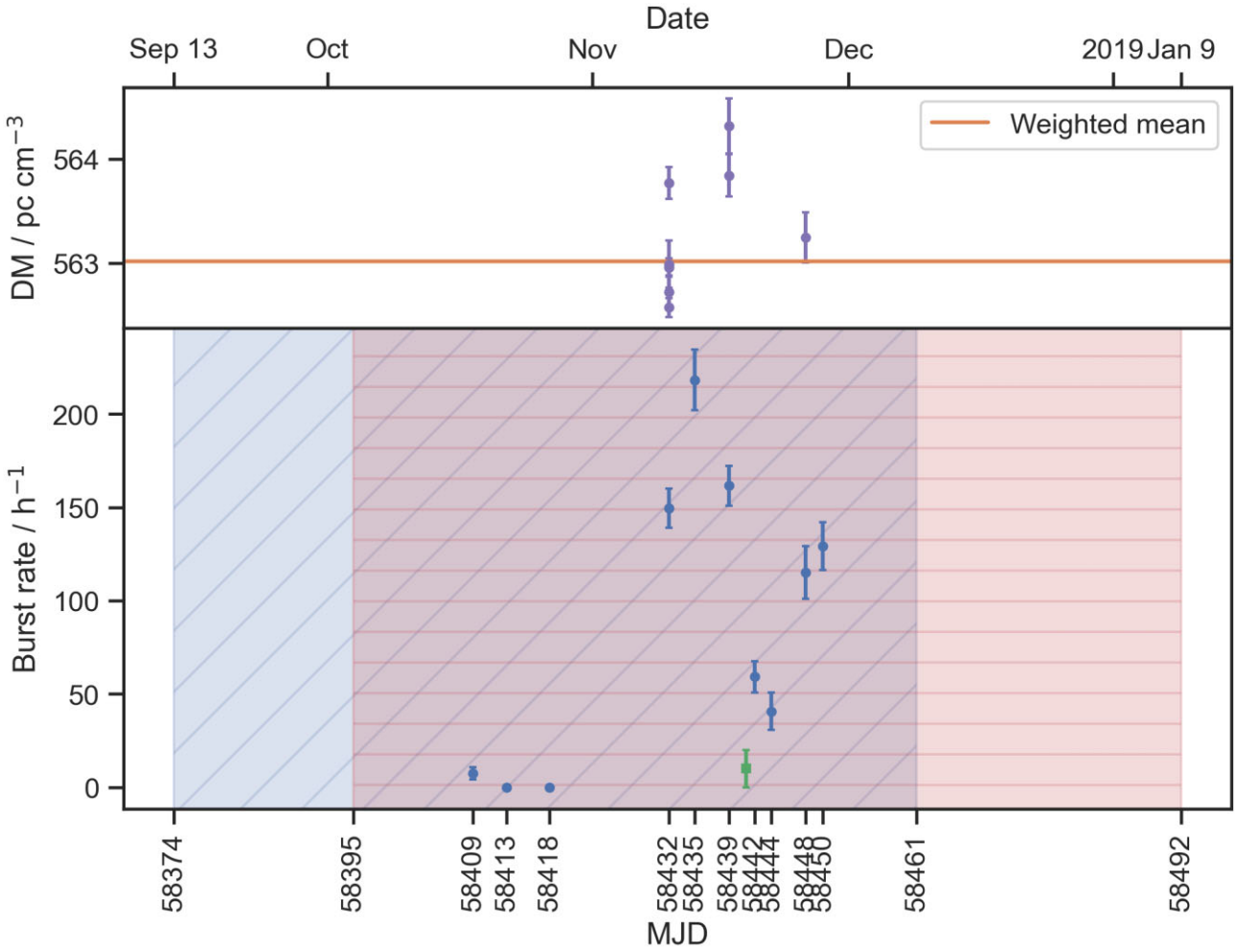

Figure 2. Lower panel: the burst rate in each observation (see also Table 1). Blue, vertically hatched and red, horizontally hatched regions mark the active cycles reported by Rajwade et al. (2020) and Cruces et al. (2021), respectively. A green square marks the only detection by the Canadian Hydrogen Intensity Mapping Experiment Fast Radio Burst (CHIME/FRB) until now (Josephy et al. 2019). Upper panel: the DMs whose mean was used for dedispersion. It is shown later that the seeming DM variation is due to an emission effect.

For the fits we used least-square fitting with the Levenberg–Marquardt algorithm.[7] The number of sub-bursts was decided by eye and from correlations in the free parameters if sub-bursts were too close in time–frequency space. A few sub-bursts were marked as *diffuse* (e.g. the diffuse background component in C356) and excluded from the analysis in Section 4.3. 234 sub-bursts from 183 bursts were fit reasonably well, e.g. the amplitude was larger than its uncertainty. These were generally the high S/N or single-component bursts. For the rest we fit the time series and the spectrum with one-dimensional Gaussians to obtain arrival times, central frequencies, durations, and bandwidths. Here the spectrum was computed from the $2\sigma_{t,1\mathrm{D}}$ before and after the arrival time, where $\sigma_{t,1\mathrm{D}}$ is the 1σ width of the Gaussian in the time series.

We computed fluence and energy with the radiometer equation (see e.g. Lorimer & Kramer 2004) using a system equivalent flux density (SEFD) that depends on frequency and zenith angle θ. The radiometer equation for the flux density $\mathcal{S}$ takes the form

$$\mathcal{S} = \left\langle \frac{(\mathrm{S/N})_{\mathrm{chan}}\,\mathrm{SEFD}(\nu,\theta)}{\sqrt{n_{\mathrm{p}}\,\delta t\,\delta\nu_{\mathrm{chan}}}} \right\rangle_{\nu}, \tag{3}$$

with the signal-to-noise ratio in a time sample and channel $(\mathrm{S/N})_{\mathrm{chan}}$, the number of polarizations n_{p}, the sample time δt, and the frequency width of a channel $\delta\nu_{\mathrm{chan}}$; the average over ν goes over the full observing band. The frequency and zenith angle-dependent SEFD was calculated from system performance measurements.[8] We obtained seven different θ dependent polynomials for seven different frequency bands. Generally, the observing system is less sensitive at lower frequencies and larger zenith angles. A detailed description can be found in Hewitt et al. (2022). To get the fluence $\mathcal{F}$ we integrated $\mathcal{S}$ over the time window that was also used for fitting; in other words, we sum over the time samples $\mathcal{F} = \sum_{\mathrm{samp}} \mathcal{S}\,\delta t$. The energy was obtained from the known redshift $z = 0.193$ (Tendulkar et al. 2017), the resulting luminosity distance $D_{\mathrm{L}} = 949$ Mpc (based on

[7] https://docs.scipy.org/doc/scipy/reference/generated/scipy.optimize.least_squares.html

[8] http://www.naic.edu/~phil/sysperf/sysperfbymon.html

Table 1. The 10 reported observations. The ID is used in the burst names to indicate the observation. k and r are the parameters of a Weibull fit to the wait times in Section 4.1. The measured ks are consistent with $k = 1$ for which the Weibull distribution reduces to a Poisson model.

Date	ID	Start MJD (topocentric)	Duration (s)	Bursts	Rate (h)	k	r (h)
2018-10-18	A	58409.346424	2466	5	7 (3)	$5.11^{+3.11}_{-1.92}$	$6.2^{+0.8}_{-0.7}$
2018-10-22		58413.336181	3056	0	0	–	–
2018-10-27		58418.291134	5002	0	0	–	–
2018-11-10	B	58432.259086	4881	203	150 (11)	$0.97^{+0.06}_{-0.05}$	$126.1^{+9.3}_{-10.1}$
2018-11-13	C	58435.273426	2969	180	218 (16)	$1.05^{+0.06}_{-0.06}$	$193.0^{+15.4}_{-14.4}$
2018-11-17	D	58439.236887	5058	227	162 (11)	$0.96^{+0.05}_{-0.05}$	$154.5^{+10.9}_{-10.5}$
2018-11-20	E	58442.252477	2980	49	59 (8)	$0.85^{+0.11}_{-0.10}$	$50.5^{+10.3}_{-8.5}$
2018-11-22	F	58444.24022	1503	17	41 (10)	$1.43^{+0.33}_{-0.27}$	$37.2^{+7.5}_{-5.8}$
2018-11-26	G	58448.241505	2095	67	115 (14)	$0.89^{+0.09}_{-0.08}$	$110.3^{+17.0}_{-13.9}$
2018-11-28	H	58450.232199	2815	101	129 (13)	$1.06^{+0.09}_{-0.08}$	$121.8^{+11.5}_{-11.0}$

the parameters obtained by Planck Collaboration XIII 2016), and the observing bandwidth $\Delta\nu_{\rm band}$ as

$$E = 4\pi D_{\rm L}^2 \frac{\mathcal{F}\,\Delta\nu_{\rm band}}{1+z}, \tag{4}$$

where the factor $1 + z$ accounts for the redshifted burst duration (Zhang 2018).

Some studies (e.g. Gourdji et al. 2019) use the burst bandwidth instead of the observing bandwidth, and Aggarwal (2021) argued that this is the only correct way. Yet, both methods are correct (and equivalent) if and only if the same bandwidth is used that is also used to calculate the flux density (equation 3). If one makes assumptions about the spectrum and that the observing band is small compared to the central frequency, one can use the observing frequency instead of the bandwidth (Li et al. 2021b). This does not seem well motivated given that the bursts of FRB 121102 are band limited. We therefore use the observing bandwidth as described above.

The energy obtained from equation (4) incorporates only the energy inside the band. The band-limited nature of bursts allows us to scale the energies – computed via equation (4) – with the fitted Gaussians as suggested by Aggarwal (2021). To minimize other effects coming from the limited observing bandwidth, we excluded sub-bursts with ν_0 close to the edges or beyond, i.e. we require $1200 < \nu_0 < 1700$ MHz. This and the exclusion of bursts that were not well fit leave us with 746 of the 849 bursts. We infer the full energy of a burst from the measured energy and the fitted Gaussians. The volume under a Gaussian is given by $V = 2\pi A\sigma_t\sigma_\nu$. The volume in the band can be calculated as

$$V_{\rm band} = \sqrt{2\pi}A\sigma_t \int_{\nu_{\rm bot}}^{\nu_{\rm top}} {\rm e}^{-\frac{(\nu-\nu_0)^2}{2\sigma_\nu^2}}\,{\rm d}\nu \tag{5}$$

$$= 2\pi A\sigma_t\sigma_\nu \frac{1}{2}\left({\rm erf}\left(\frac{\nu_{\rm top}-\nu_0}{\sqrt{2}\sigma_\nu}\right) - {\rm erf}\left(\frac{\nu_{\rm bot}-\nu_0}{\sqrt{2}\sigma_\nu}\right)\right), \tag{6}$$

where $\nu_{\rm bot}$ and $\nu_{\rm top}$ denote the bottom and top frequency of the band and erf is the error function. Indexing the sub-bursts of a burst with i we get the total energy of a burst:

$$E_{\rm tot} = E\frac{\sum_i V_i}{\sum_i V_{{\rm band},i}} \equiv Es, \tag{7}$$

where we introduced the scale factor s. In the 746 bursts, on average 92 per cent of $E_{\rm tot}$ were inside the band ($\langle s^{-1}\rangle = 0.92$). The lowest fraction in the band was 60 per cent.

This method is more accurate than directly using the measured energies, but it has a few caveats that we will mention here, along with the numbers of bursts that were affected. For 52 complex bursts that could only be fit in 1D, we made the approximation that d_t is small and used $\sigma_{t,\rm 1D}$ instead of σ_t. To not mix 1D and 2D fits in one burst, we used 2D fits of weak sub-bursts in 22 bursts, even though the uncertainties were high. We confirmed by eye that these were fit reasonably well, i.e. the fits were in the same location as the visible sub-burst and had flat residuals. Lastly, complex bursts that have single sub-bursts whose centres are outside the band are biased slightly low because their energy was attributed to the other sub-bursts, i.e. their energy in the band is considered, but not scaled adequately.

4 RESULTS

4.1 Rates and wait times

The burst rate of each observation is listed in Table 1 and plotted in Fig. 2. The plotted uncertainties of the rate r, in an observation with burst number $N_{\rm b}$ and length $t_{\rm obs}$ are calculated as $\sigma(r) = \sqrt{N_{\rm b}}/t_{\rm obs}$, i.e. assuming it is a Poisson process (justified by the findings of Cruces et al. 2021). Here and henceforth we show 68 per cent uncertainties unless otherwise stated. The observed rate of detected bursts varies significantly between observations even though the observations are in the same active window, calculated from the periods reported by Rajwade et al. (2020) and Cruces et al. (2021). It ranges from 0 bursts during the 1.4 h observation on MJD 58418 to 180 bursts in the ∼50 min observation on MJD 58435 yielding a rate of 218 bursts per hour. This demonstrates that on time-scales larger than the observations of 1–2 h the times of arrival can no longer be described by a *stationary* Poisson point process, but possibly still by a Poisson point process with a varying rate (see also Nimmo et al. 2022). Notably, the high-rate observations are all in the middle of the activity window reported by Cruces et al. (2021) from Effelsberg monitoring, while the three observations with a low rate are more towards the beginning. However, the sparse sampling does not allow a definite interpretation.

We obtain wait times between consecutive bursts – including sub-bursts – by taking the differences between the barycentre corrected arrival times. The joint histogram of all observations is shown in the upper panel of Fig. 3. One can see two peaks and to analyse them separately we divide the wait times into two groups, one including wait times $\delta < 0.1$ s and one with $\delta > 0.1$ s, where the value 0.1 s was chosen by eye and will be further justified below. With this division,

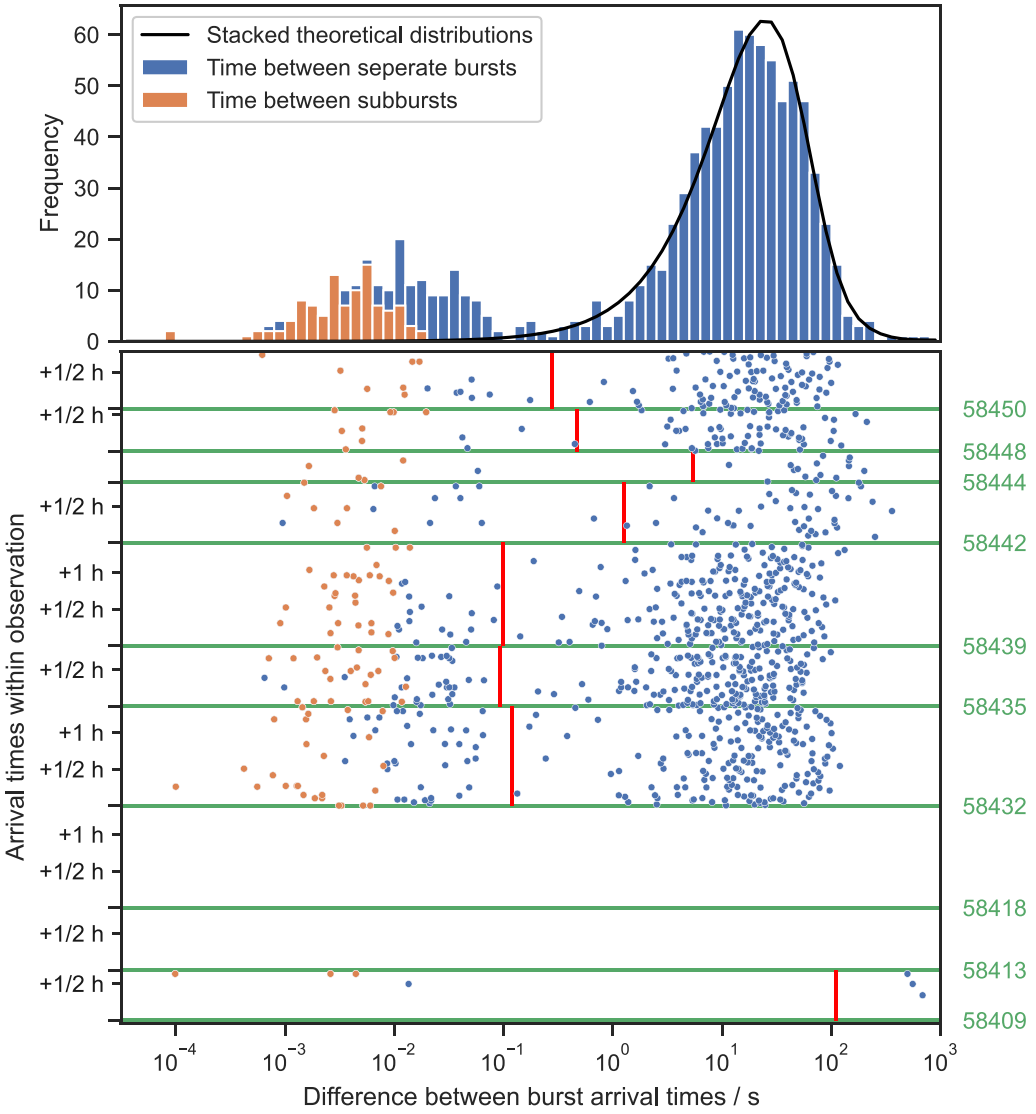

Figure 3. The wait times between bursts and sub-bursts. Times between sub-bursts that are visually part of one burst are plotted in orange, others in blue. The lower panel has time on the y-axis but is broken at green lines, such that it only includes times when observations took place. The observation days are indicated at the start of the observations by their MJD (in green). Red lines mark the time below which only one burst is expected from Poisson statistics, given the number of bursts and observation lengths (see text for details). The upper panel shows a stacked histogram of wait times in all observations. The black line shows the expected distribution for the right-hand peak, assuming Poisson statistics with a different rate in each observation.

the left-hand peak has a median of 9.7 ms and the right-hand peak a median of 17.5 s. Excluding the wait times between sub-bursts, the median of the left-hand peak becomes 22 ms. When including only sub-bursts, the median is 4.3 ms.

The time-scale of the left-hand peak is stable over observations that have very different rates, as can be seen in the lower panel of Fig. 3, where the wait times are plotted against the arrival time within their observation. This means that the left-hand peak must reflect a characteristic time-scale of the emission process.

Furthermore, only half of the left-hand peak consists of sub-bursts that visually belong to the same burst, while the other half consists of bursts between which the signal goes down to the noise or that were even picked up as separate bursts by the pipeline. This confirms that there is a higher chance to get bursts in close proximity but up to ∼0.1 s apart. This suggests that these burst packs are part of the same physical 'event', happening in (the vicinity of) the potential neutron star or other FRB central engine.

In contrast, the peak at higher wait times in Fig. 3 reflects the inverse rate, i.e. it shifts to longer wait times in observations with lower rates as one expects if burst arrival times follow a Poisson point process within observations. In a Poisson point process, bursts occur independently of one another and are solely described by their rate r. The wait times δ follow an exponential probability density function $\mathcal{P}(\delta|r) = r\,\mathrm{e}^{-r\delta}$, with mean $\langle\delta\rangle = r^{-1}$. Since the rate varies between observations, the right-hand peak in Fig. 3 can be described by the joint distribution as $\sum_i n_i \mathcal{P}(\delta|r_i)$, where i goes over all observations, n_i is the number of arrival times $\delta > 0.1$ s, and $r_i = n_i/t_{\mathrm{obs},i}$. It is plotted as a black line in the upper panel of Fig. 3 for the same bins that were used for the histogram. We can also calculate the separation δ, below which we expect to find only one burst pair in an observation

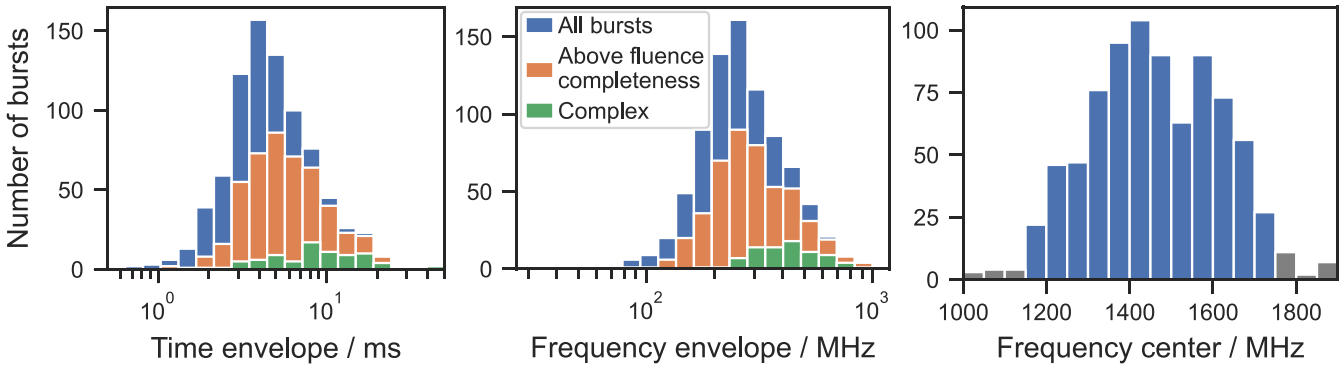

Figure 4. The distributions of burst full width at half-maximum (FWHM) durations (left), bandwidth (middle), and the central frequencies (right) of the 820 bursts that were well fit. For complex bursts we took the time difference between the later half-maximum of the latest sub-burst and the early half-maximum of the first sub-burst and analogously for the bandwidths. The central frequencies show no clearly preferred frequency range.

with N_b bursts. It follows from the cumulative distribution function as

$$\mathrm{CDF}(\delta|r) = 1 - \mathrm{e}^{-r\delta} = 1/N_\mathrm{b} \qquad \text{and therefore} \tag{8}$$

$$\delta = -1/r \log(1 - 1/N_\mathrm{b})\,. \tag{9}$$

It is shown as red lines in Fig. 3 for the number of bursts in each observation (including ones with $\delta < 0.1$ s). This provides a quantitative separator between the peaks of short and long wait times and justifies the choice of 0.1 s as the approximate peak separation.

To confirm that the arrival times are distributed according to Poisson statistics, we used the Bayesian analysis with a Weibull distribution developed by Oppermann et al. (2018). In the past, the Weibull distribution was used to explain the highly non-Poisson nature of the burst arrival times. The source was seen to be highly variable on time-scales of weeks to months, which is now explained by the ∼160-d periodicity. On shorter time-scales, Cruces et al. (2021) have shown that arrival times within an observation are consistent with Poisson statistics if short burst separations are excluded. Here we repeat their analysis with a larger number of bursts, providing better constrains. The Weibull distribution is a generalization of the Poissonian model with a second parameter k but includes the latter as a special case. Here, we use it to test if the resulting parameters are consistent with this special case of Poisson statistics. For wait times δ the Weibull distribution can be written as $\mathcal{W}(\delta|k,r) = k\delta^{-1}[\delta r\Gamma(1+1/k)]^k\,\mathrm{e}^{-[\delta r\Gamma(1+1/k)]^k}$, where $\Gamma(x)$ is the gamma function, r is the rate, and k is the parameter that is >1 for periodic arrival times, <1 for clustered bursts, and 1 for bursts following Poisson statistics. We used the arrival time of burst packs by taking the mean arrival time of bursts that were separated by <0.1 s. We inferred the parameters of the Weibull distribution separately for each observation and obtained the posterior distributions with the formalism described in Oppermann et al. (2018). The resulting k and r parameters are listed in Table 1 and are all consistent with the Poisson model. As an example, we show the posterior distribution of the highest rate observation (MJD 58435) in Fig. C1. For comparison, we also show the posterior distributions for the arrival times of all bursts (i.e. without averaging over arrival times with $\delta < 0.1$ s).

4.2 General properties

A small sample of the detected bursts can be seen in Fig. 1. Like previously discovered bursts, they exhibit a variety of morphologies. Most of the bright bursts show spectro-temporal structures including multiple sub-bursts and the sad-trombone effect. Like in previous observations, no clear upward drifting bursts were found. All bursts are band limited, although the sub-bursts of some drift over the full band. While most burst durations are of the order of ∼5 ms, the sharpest sub-bursts can be shorter than 0.2 ms. We show the fit parameters and additional info of the first 10 sub-bursts in Table C1, the full list is provided as supplementary material.

We first report the general properties of the full bursts (rather than of individual sub-bursts). This includes the distributions of duration, bandwidth, and central frequencies. We report the burst durations in terms of the full width at half-maximum (FWHM) for simple bursts that were fit with a single component. For complex bursts with several sub-bursts, we compute for each sub-burst the earlier half-maximum $t_0 - \sigma_{t,1\mathrm{D}}\sqrt{2\ln 2}$ and the later half-maximum $t_0 + \sigma_{t,1\mathrm{D}}\sqrt{2\ln 2}$ and report the difference between the first and the last half-maximum in the burst. To be consistent between bursts fit in 1D and 2D, we calculate $\sigma_{t,1\mathrm{D}}$ from the 2D fit parameters as $\sigma^2_{t,1\mathrm{D}} = \sigma_t^2 + (d_t\sigma_\nu)^2$. Similarly, we report the burst bandwidth as the FWHM, or for complex bursts the difference between the highest frequency half-maximum and the lowest frequency half-maximum (the parameters in 1D and 2D are equivalent here). The resulting distributions are plotted in Fig. 4 for the full sample and with bursts above the fluence completeness threshold that we will calculate in Section 4.4. The resulting median duration of all bursts is 4.41 ms and for the bandwidth it is 217 MHz. The more physically meaningful medians for the bursts above the completeness threshold are 5.15 ms and 240 MHz and the first and last deciles are $\mathrm{FWHM}_{t,10\,\%} = 2.74$ ms, $\mathrm{FWHM}_{t,90\,\%} = 12.54$ ms, $\mathrm{FWHM}_{\nu,10\,\%} = 150$ MHz, and $\mathrm{FWHM}_{\nu,90\,\%} = 439$ MHz.

The central frequencies of bursts shown in Fig. 4 are subject to several biases. Only the 818 bursts whose fits gave reasonable results are shown, and for complex bursts we took the mean of the obtained ν_0s. The number of burst centres falls off at the edges because of two biases. First, bursts that are not fully in the band are less likely to be detected, and second, these bursts are more likely to have larger errors and therefore be excluded from the analysis. Additional biases come from the frequency-dependent receiver sensitivity, which is overall lower at lower frequencies (see fig. 7 in Hewitt et al. 2022), from RFI, and from GPU node dropouts. Without mitigating for all these effects in detail, we can say that the distribution and the median within the band of 1456 MHz (the central frequency is 1440 MHz) show no clearly preferred frequency band. It could be that the preferred

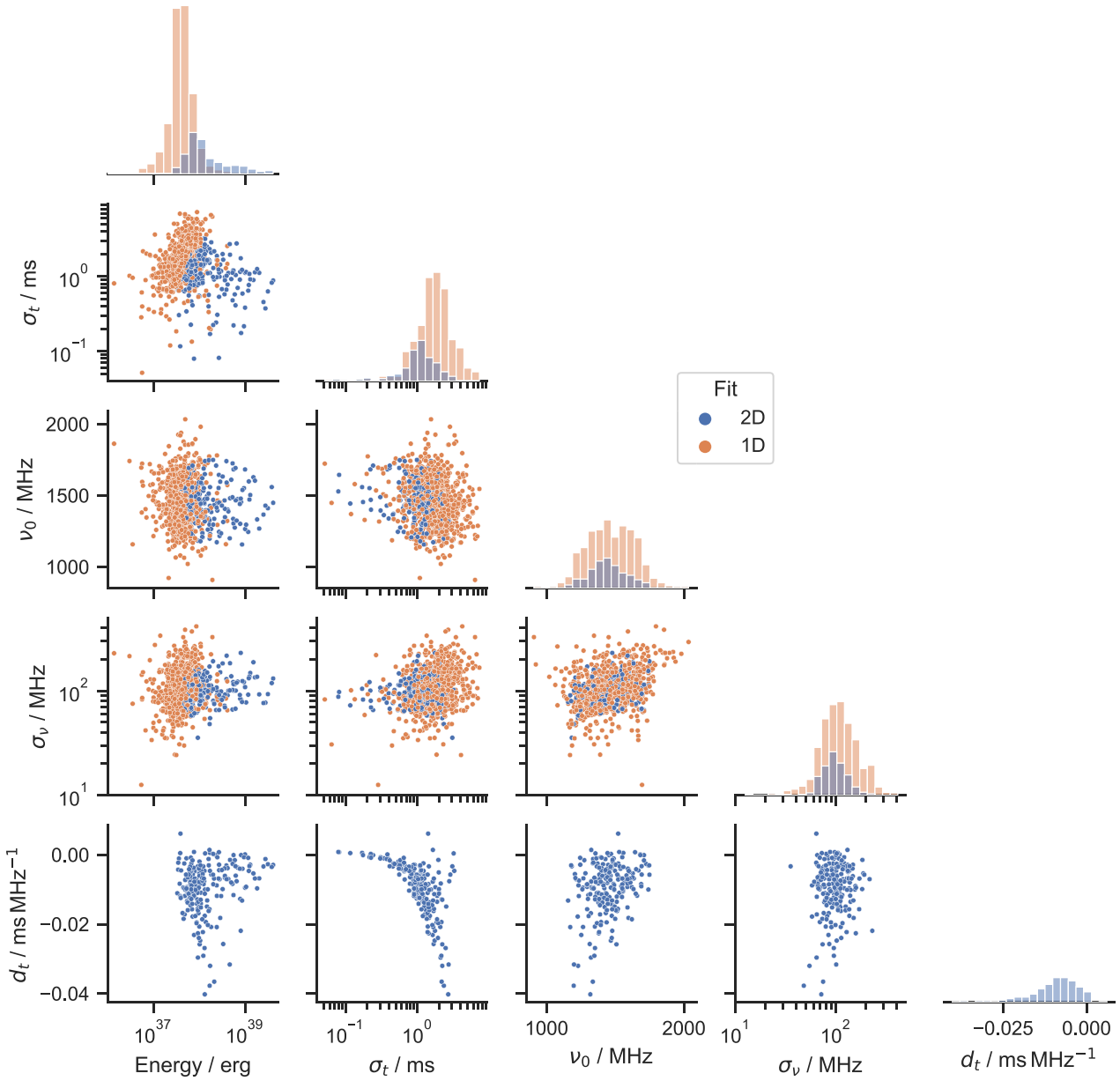

Figure 5. Corner plot of the relations between different fitted parameters and the energy. Note that d_t was not fitted in the 1D model. The strongest correlation is in the d_t–σ_t plot.

frequency is ∼1450 MHz, and that the burst rate is so high because the preferred frequency is so close to the central frequency, but verifying this would require a detailed analysis of the listed biases, which is beyond the scope of this work.

In addition to the burst envelopes, we also looked at the properties of sub-bursts. We explored the full space of quantities obtained from sub-bursts to look for unexpected correlations. Fig. 5 shows a corner plot of the relevant fitted parameters and the isotropic-equivalent energy. For sub-bursts, the energy that was measured for the full bursts had to be calculated from the sub-burst parameters. We did this by distributing the measured energy among the sub-bursts through weighting by the volume under the fitted Gaussians. The tilt d_t is only plotted for bursts or sub-bursts that were fit in 2D because it is not obtainable from the 1D fits. The σ_t parameter for 1D and 2D fits are plotted in the same panels but are mathematically different because σ_t in equation (2) is the width at the central frequency while $\sigma_{t,1D}$ is the width in the time series. The two are related by the tilt as $\sigma^2_{t,1D} = \sigma_t^2 + (d_t\sigma_\nu)^2$.

The most striking relationship can be seen between d_t and σ_t. We want to stress again that in the parametrization that we use in equation (2) d_t and σ_t are mathematically independent. We will further investigate this relationship in Section 4.3.

Apart from this, we find weaker correlations in d_t–ν_0 and σ_ν–ν_0. We looked for temporal trends or systematic changes in the distributions of ν_0, σ_t, and energy with time but did not find any. Bursts also showed no significant correlation between their energy and wait times, before or after a burst. Bursts of the same pack showed a weak tendency that later arriving bursts are at lower frequency. 63 out of 103 bursts that arrived within 0.1 s after another burst had

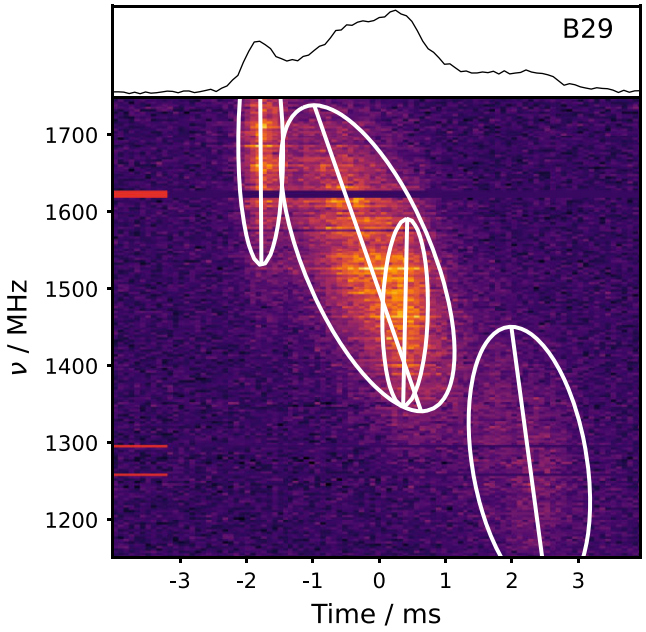

Figure 6. Example of the temporal drift d_t and the d_t–σ_t relationship. White ellipses show the 32 per cent contour for each sub-burst, individually computed from the Gaussian fits. A white line shows the fitted d_t, i.e. the line along which t_0 drifts with frequency. It is visible that the two shorter sub-bursts drift much less than the broader components.

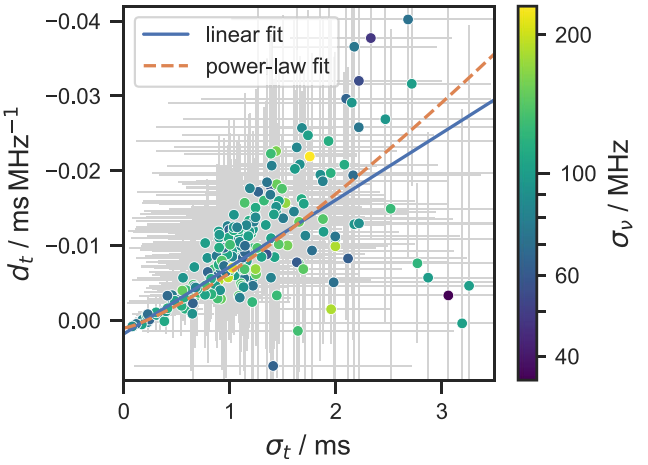

Figure 7. The intraburst drift d_t plotted against σ_t. Similar to the second panel in the bottom row of Fig. 5, but with a linear σ_t-axis and the colour representing σ_ν on a logarithmic scale. Uncertainties are shown in grey. The fitted linear- and power-law models are similar by eye, but not consistent with each other.

a lower frequency than their predecessor, which is 2.26σ from the mean.

A positive correlation between wait times and energy could indicate a build-up of energy that is released with the burst. The observed lack of a correlation, however, can have several reasons. Beaming effects could wash out the correlation. The energy budget of FRBs is small compared to high-frequency bursts from magnetars and a built-up might not be needed. The missing wait time–energy correlation therefore provides no clear insight into the emission mechanism.

4.3 The time–frequency drift

Among the diverse spectro-temporal effects observed in FRBs, two can be well quantified: the drift between sub-bursts (i.e. the 'sad-trombone effect') and the intraburst drift. To avoid confusion, we will refer to the first as sad-trombone drift. The sad-trombone effect is the effect that within bursts with multiple sub-bursts, the central frequencies drift to lower frequencies with time. This effect can be seen in most of the bright bursts in Fig. 1, good examples are bursts B29, B180, and D516. It is commonly quantified in the units MHz ms^{-1} (e.g. in Hessels et al. 2019). The intraburst drift, on the other hand, is the drift of the emission within a sub-burst, it is possibly – but not necessarily – related to the sad-trombone drift. In the form that we fit to the bursts (equation 2) lower frequencies arrive later and hence it drifts in time with frequency with (inverse) units of ms MHz^{-1}. This effect is illustrated in Fig. 6. In the context of our Gaussian models, the sad-trombone drift can be described as the central frequencies ν_0 decreasing for later arriving sub-bursts. The intraburst drift is quantified by the fit parameter d_t.

Instead of letting a sub-burst drift in time (i.e. t_0 drifts) as in equation (2) one can equivalently let the frequency ν_0 drift. Both alternatives can yield a perfectly (elliptical) Gaussian burst, such that it cannot be decided whether a sub-burst is drifting in time or in frequency. Likewise, the way we interpret the sad-trombone effect as a frequency drift is not unambiguous, in many bursts it could also be interpreted as a delay of lower frequencies. The likely reason it is perceived as the first is due to the visible substructure. Specifically, if the substructure in bright bursts were not vertical but horizontal we would interpret it as a drift in time, where bursts at lower frequencies arrive later (here ignoring the potential difficulty in DM determination). Since no clear substructure is visible in sub-bursts, we will discuss both interpretations of the intraburst drift and the sad-trombone drift in this section. When needed, we distinguish them as 'temporal drift' (in ms MHz^{-1}) and 'frequency drift' (in MHz ms^{-1}). The frequency drift will show its worth as the interpretation that is closer to the sad-trombone drift, but the temporal drift can often be measured more precisely and allows us to measure and correct the DM.

In Fig. 7, we show again d_t plotted against σ_t where we already saw a correlation in the previous section. The low scatter in the points compared to the error bars indicates that the 2D Gaussian fit to the bursts likely overestimates the uncertainties. A trend is visible between d_t and σ_t with sharper bursts having very small d_t, while it gets larger with longer burst durations. Above the points that follow the trend, a sharp edge is visible, which means that there is a limit on how much a sub-burst can drift for a given σ_t. Below the trend, the edge is less sharp and a few outliers with positive d_t exist that are all weak single-component bursts whose measurement is likely affected by unresolved sub-bursts.

A change in the intraburst drift could be wrongly ascribed to a varying DM, but the close relationship with σ_t strongly suggests that it must be an effect intrinsic to the emission mechanism, as a variation in the DM would add to d_t independent of σ_t. Furthermore, a relation between d_t and the duration measured in the time series ($\sigma_{t,1D}$) would be expected naturally, but we want to stress again that it is not the origin of the correlation here because σ_t in equation (2) is instead the width of a sub-burst at the central frequency ν_0.

From the illustration in Fig. 6 we can already partly understand the d_t–σ_t relationship. If we imagine that the second sub-burst consisted of several unresolved smaller sub-bursts with low intraburst drift (like the first and third), the sad-trombone drift of their central frequencies

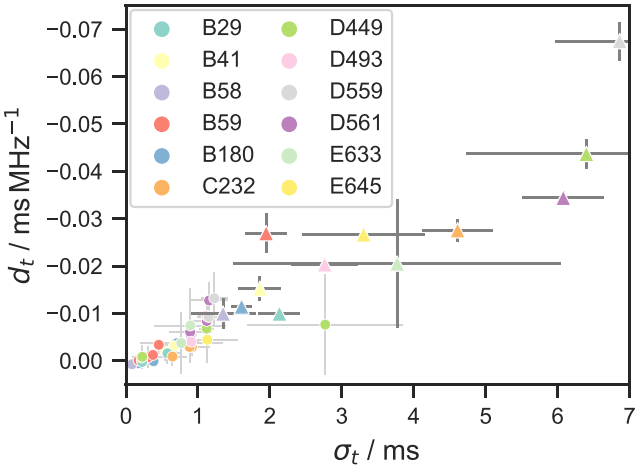

Figure 8. Comparison of the temporal drift from the sad-trombone effect (triangles) to the intraburst drift (circles) for the 12 bursts with three or more sub-bursts. Full bursts have larger drifts, but are in the same regime as broader sub-bursts in Fig. 7.

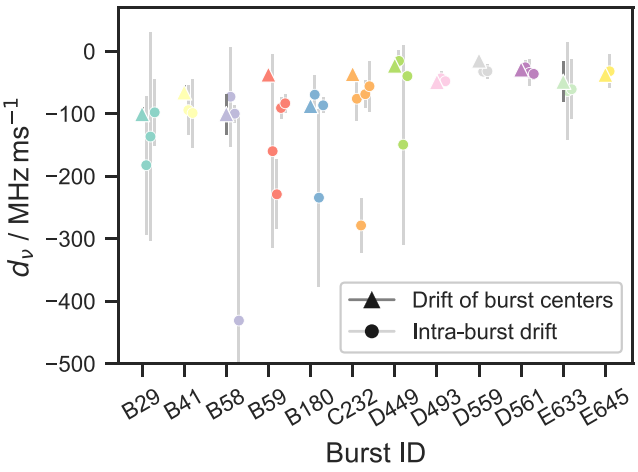

Figure 9. An alternative interpretation of the sub-burst drifts, in terms of a drift of the frequencies instead of the time centre (note the inverse units). The frequency drift of sub-burst centres due to the sad-trombone effect is mostly compatible with the intraburst drift for the same sub-bursts. The colours are the same as in Fig. 8.

causes the larger d_t in the wider (larger σ_t) observed sub-burst. We will see after the following quantitative analysis that this simple picture cannot completely explain the relationship.

To quantify the d_t–σ_t trend in absence of a theoretical model, we fit a power law and a straight line to the data. The power law is of the form $d_t(\sigma_t) = -(b\,\sigma_t)^k\,\mathrm{ms\,MHz^{-1}} + c$. We use the Levenberg–Marquardt algorithm to minimize the sum of the squared residuals and weight by the squared uncertainty of d_t. We find $k = 1.28 \pm 0.08$, $b = ((0.022 \pm 0.005)\,\mathrm{ms^{-1}}$, and $c = (0.0010 \pm 0.0001)\,\mathrm{ms\,MHz^{-1}}$. When fitting a linear $d_t(\sigma_t) = b\,\sigma_t + c$, we get $b = -0.00862(37)\,\mathrm{MHz^{-1}}$ and $c = 0.00171(30)\,\mathrm{ms\,MHz^{-1}}$. The power-law fit does not agree with a linear law, but visually it does not describe the data much better, because of the large scatter in the data. For the following analysis, we will therefore use the simpler linear model.

We want to compare the intraburst drift to the sad-trombone drift. To do this, we calculate the sad-trombone drift for the 12 bursts that have three or more sub-bursts by fitting a line to the sub-burst centres. One can choose to interpret the resulting slope as a temporal drift in frequency in units of $\mathrm{ms\,MHz^{-1}}$ or inversely as frequency centres drifting with time in $\mathrm{MHz\,ms^{-1}}$. We first compare the temporal drifts to see if there is a difference in magnitudes between the sad-trombone drift and the intraburst drift. The sad-trombone drifts of the 12 bursts are shown in Fig. 8 along with the d_t of the sub-bursts of the same bursts. The FWHM calculated in Section 4.2 has been divided by $2\sqrt{2\ln 2} \approx 2.355$ to get a quantity that is comparable to σ_t. We can see that the sad-trombone drifts are generally higher than the intraburst drifts, which is not surprising as the sub-bursts already appear straighter in their spectra in Fig. 1. Moreover, the bursts seem to continue the same trend without a gap between the drifts of sub-bursts and full bursts. Rather, the sad-trombone drifts fall in the same regime as broader sub-bursts in Fig. 7. This is also not unexpected, as we know that weaker bursts sometimes consist of several unresolved sub-bursts.

A more suitable comparison can be done by comparing the drift of frequency centres to the drift of the emission frequency in individual sub-bursts. To do this, we first need to convert the d_t to a comparable quantity. For that, the drift of the emission frequency can be obtained by converting to a different parametrization of the 2D Gaussians, where – in contrast to equation (2) – the frequencies drift linearly with slope d_ν in units of $\mathrm{MHz\,ms^{-1}}$,

$$\mathcal{G}_{\mathrm{2D},\nu}(t,\nu) = A\exp\left(-\frac{(t-t_0)^2}{2w_t^2} - \frac{(\nu-\nu_0-d_\nu(t-t_0))^2}{2w_\nu^2}\right). \quad (10)$$

Here w_t reflects the full duration in the time series (i.e. is equivalent to $\sigma_{t,\mathrm{1D}}$), and w_ν is the bandwidth at t_0. All parameters can be calculated from the fitted parameters as done in Appendix A; for d_ν one gets

$$d_\nu = \frac{d_t}{d_t^2 + \frac{\sigma_t^2}{\sigma_\nu^2}}\,. \quad (11)$$

For the sharpest bursts, for which $|d_t| \ll \sigma_t/\sigma_\nu$ still holds, equation (11) can be approximated as $d_\nu \approx d_t\sigma_\nu^2/\sigma_t^2$, and uncertainties in d_t coming from the DM that are greater than d_t itself can cause variations in d_ν of the order of several $100\,\mathrm{MHz\,ms^{-1}}$. This causes large uncertainties in d_ν for the ∼5 sharpest bursts and requires us to correct for the small overdedispersion δDM (visible in bursts B58 and C356). We do this by subtracting each d_t by a small $d_t(\nu_0)$, which is derived below in equation (12). In Fig. 9, we show the drifts of frequency centres and the drifts of the emission frequency within sub-bursts d_ν for the same 12 bursts as in Fig. 8. The strong susceptibility to small offsets in DM of some bursts is reflected in their large error bars. For many bursts, the sad-trombone drifts and the intraburst drifts are very similar and within the uncertainties. Exceptions from this are bursts B59 and C232. In burst C232 in Fig. 1 it is visible that the later sub-bursts stop drifting, which might cause the lower sad-trombone drift.

Even though most bursts agree with the sad-trombone drift, we have to note that the majority of error bars on the d_ν are relatively large. Moreover, the linear d_t–σ_t relation does not agree with equal sad-trombone and intraburst drifts in the following simple picture. Let us hypothesize a toy burst that has frequency drift d_ν and a Gaussian frequency envelope with width w_ν at any point in time. If it is then modulated in time into sub-bursts using Gaussians with varying widths, we can calculate the resulting d_t from equations (A2) and (A3). The resulting equality $d_t = \sigma_t^2 d_\nu/w_\nu^2$ is a square-law and in conflict with the observation of a linear relation.

We mentioned in Section 3 that d_t is closely related to the DM that is used for dedispersion. The reason is that if we overdedisperse the

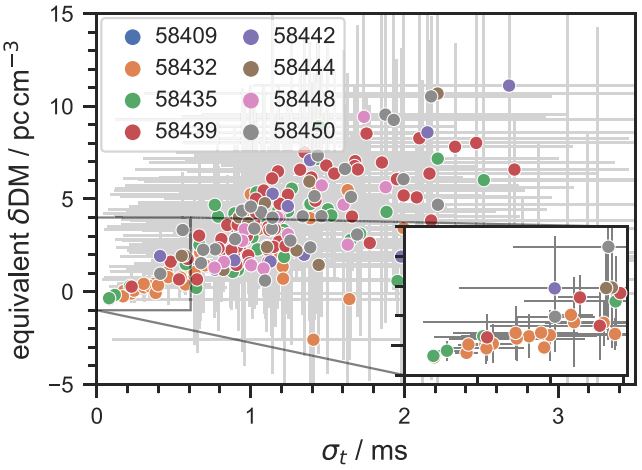

Figure 10. The apparent DM difference from the dedispersion DM caused by the intrinsic tilt of the sub-bursts. Main panel: the 234 sub-bursts that were well fit in 2D with error bars. The intrinsic intraburst drift can cause a burst to be found at a DM that appears to be $\lesssim$12 pc cm^{-3} higher than the real DM. Inset: zoom in on bursts with $\sigma_t < 0.6$ ms. Considering the linear trend, the difference in the real DM within and between observations is much less than 1 pc cm^{-3}.

bursts it will add a positive intraburst drift to all of them, while underdedispersion causes the opposite. Since we dedispersed all bursts at the same DM, this does not affect the slope b but only c. In fact, the small positive intraburst drift d_t of the sharpest bursts in Fig. 7 suggests that we used a slightly too high DM. Under the assumption that the linear law extends to very sharp bursts ($\sigma_t \to 0$) and for these bursts d_t becomes 0, we can estimate the real DM from c as follows.

If the real DM is $\mathrm{DM_{real}} = \mathrm{DM_{applied}} + \delta\mathrm{DM}$, i.e. it is higher than the applied dispersion by a small δDM, it will cause a small shift Δt with respect to a central frequency ν (in our case δDM will be negative because we overdedispersed). The apparent intraburst drift caused by the wrong DM can then be approximated with the tangent at ν by

$$d_t(\nu) = \frac{\Delta t}{\Delta \nu} \approx \frac{\mathrm{d}}{\mathrm{d}\nu} a\,\delta\mathrm{DM}\left(\frac{1}{\nu^2} - \frac{1}{\nu_{\mathrm{ref}}^2}\right) = -2a\,\delta\mathrm{DM}\frac{1}{\nu^3}. \tag{12}$$

A more rigorous derivation is given in Appendix B. Solving for δDM we obtain

$$\delta\mathrm{DM} = -\frac{1}{2}\frac{\nu^3}{a} d_t. \tag{13}$$

And finally putting in $d_t = c$, and the frequency at the centre of the band $\nu = 1440$ MHz we get $\delta\mathrm{DM} = -0.61(11)$ pc cm^{-3} and therefore

$$\mathrm{DM_{real}} = 563.02\,\mathrm{pc\,cm^{-3}} + \delta\mathrm{DM} = 562.41(11)\,\mathrm{pc\,cm^{-3}}. \tag{14}$$

It is very unlikely that the physical reason for the intraburst drift is a different DM in each burst, because of its tight relationship with the burst width and the small separation in time of many bursts. But given that the intraburst drift is an intrinsic property, it is still useful to look how it changes the DM that one would measure if one were to observe only a single burst or sub-burst of FRB 121102. To calculate this we can again use equation (13) with the central frequency ν_0 and the tilt d_t of each burst. The δDM that we obtain is now the apparent DM difference from the DM that was used for dedispersion.

The resulting apparent δDM is shown in Fig. 10. The left-hand panel demonstrates that the intrinsic tilt can make a burst appear to have a DM that is higher by up to $\sim$12 pc cm^{-3}. This illustrates why DMs obtained by maximizing S/N vary a lot. It can even affect structure maximized DMs in the absence of sharp sub-bursts, although differences are likely to be less than $\sim$1 pc cm^{-3}. Note that the values shown here are from sub-bursts, and a structure maximizing code is used for bursts with several sub-bursts. The measured DM therefore depends on the width of each sub-burst, the amplitudes, and how those are weighted within the code.

The inset in Fig. 10 allows us to compare differences in the apparent DM between bursts with $\sigma_t < 0.6$ ms between different observations. A change in the real DM between bursts in the same observation would result in a scatter in δDM independent of σ_t, whereas a significant change between observations would cause bursts to be offset by that DM. From this consideration, we can put tentative upper limits on these changes of 0.5 pc cm^{-3}.

4.4 Burst energy distribution

In this section, we present the scaled burst energies as we calculated them in Section 3. However, the term burst is not clearly defined, and what we used as bursts and sub-bursts are only practical, empirical differentiations that lack theoretical justification. We therefore carry out the analysis in this section for three different interpretations of burst energy: (1) the scaled energy of bursts as they were used in the fitting process; (2) the energy of burst packs as we defined them in Section 4.1, where we summed up the energies of bursts that are separated by less than 0.1 s; and (3) the energy split between individual sub-bursts according to their volume V_i. For all three versions, we use the scaled energies.

We exclude bursts that are close to the edge of the observing band, to ensure that the fit to the spectrum fully includes the burst centres. This also takes care of biases from narrow-band bursts having a higher chance to emit their full energy in the band (given that the burst centre is in the band), and biases from wide-band bursts that are more likely to be detected than narrow-band bursts if their centre is outside the band. A smaller observational bias could come from bursts with small bandwidths being less affected by DM smearing, therefore detectable over a larger DM range and more easily classified as real bursts (bursts detected at a single DM are classified as RFI by most pipelines).

The dominating observational effect is that bursts with energies close to the detection limit may or may not be detected depending on other properties, primarily burst width and zenith angle. Modelling these detection effects can be complicated and ultimately requires injections into the search pipeline. The common, simple solution is to exclude bursts below a threshold, above which the majority of bursts are being detected. The completeness threshold of the fluence depends primarily on the burst width, as $\mathcal{F}_{\mathrm{thres}} \propto \sigma_t^{1/2}$ (since $\mathcal{S}_{\mathrm{thres}} \propto \sigma_t^{-1/2}$). We compute the fluence completeness threshold from equation (3) as

$$\mathcal{F}_{\mathrm{thres}} \approx \frac{(\mathrm{S/N})_{\mathrm{thres}}\,\mathrm{SEFD}_{95\,\%}\sqrt{\mathrm{FWHM}_{t,95\,\%}}}{\sqrt{n_{\mathrm{p}}\,\Delta\nu_{\mathrm{band}}}} \tag{15}$$

$$= \frac{6 \times 4.8\,\mathrm{Jy} \times \sqrt{12.5\,\mathrm{ms}}}{\sqrt{2 \times 580\,\mathrm{MHz}}} = 0.095\,\mathrm{Jy\,ms}, \tag{16}$$

where a subscript 95 per cent denotes the quantile, and $\Delta\nu_{\mathrm{band}}$ the observing bandwidth. The energy threshold follows from equations (4) and (7) as

$$E_{\mathrm{thres}} = 4\pi D_{\mathrm{L}}^2 \frac{\mathcal{F}\,\Delta\nu_{\mathrm{band}}}{1+z} s_{95\,\%} = 7 \times 10^{37}\,\mathrm{erg}. \tag{17}$$

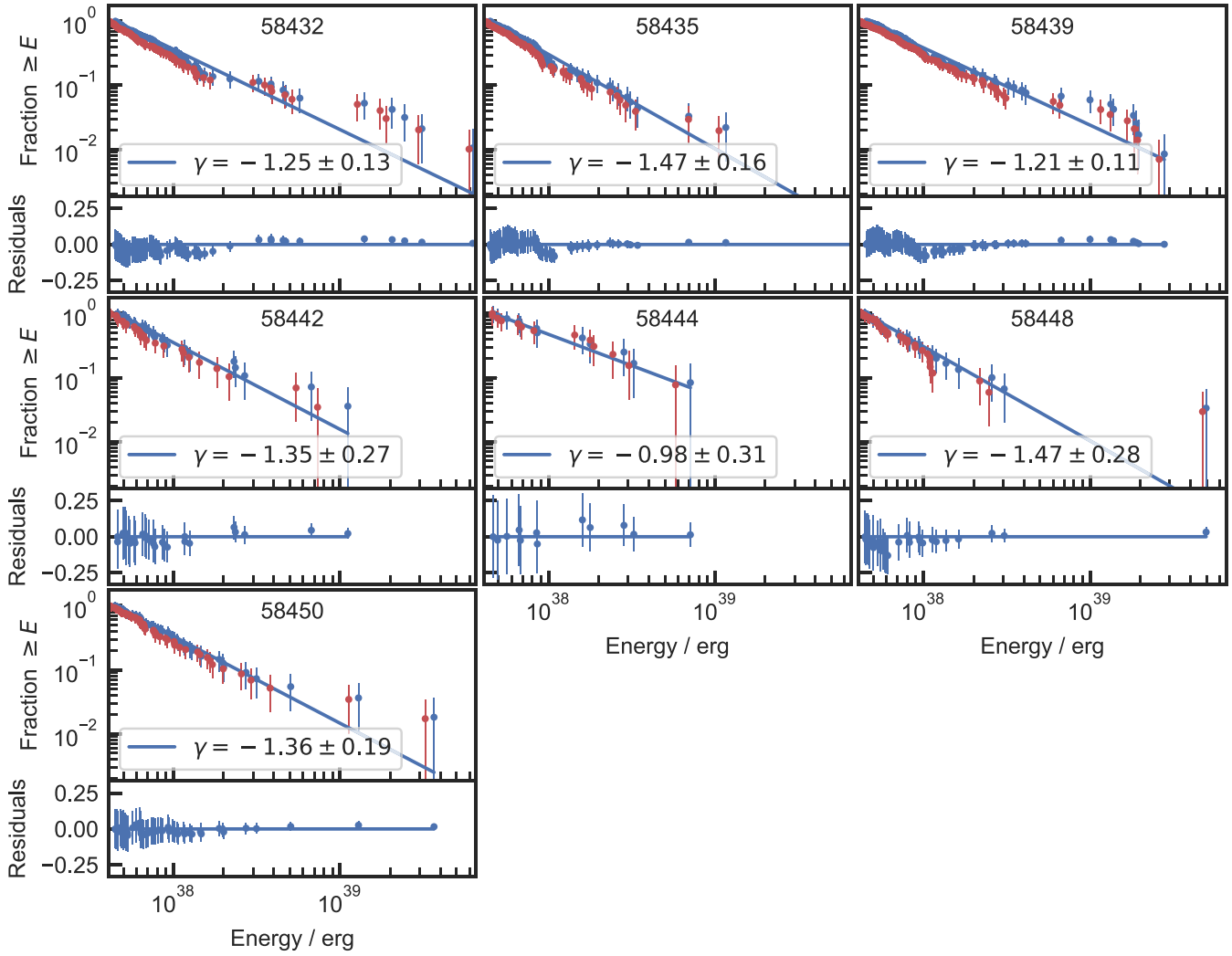

Figure 11. Cumulative burst fraction higher than a given energy, for each observation. Red markers show the measured isotropic-equivalent energies. Blue markers show isotropic-equivalent energies that have been calculated from the measured energy in the band and using the Gaussian fits to extrapolate beyond the band edges. Lower panels show residuals for each observation. Fitted power-law indices are given in the legend. The observation on MJD 58409 is not shown due to insufficient number of bursts.

We show the cumulative energy distribution function above the completeness limit for each observation in Fig. 11, excluding the observation on MJD 58409, with only two bursts. For comparison, we show the measured in-band energies in red and the scaled energies $E_{\rm tot}$ in blue. The errors of the cumulative number N are calculated assuming Poisson statistics via $\sigma(N) = \sqrt{N}$. We fit a power law of the form $N(>E) = kE^{\gamma}$ to the distribution, where k is some constant and γ is the power-law index. We use the maximum likelihood method presented in James et al. (2019; based on Crawford, Jauncey & Murdoch 1970), with the unbiased estimate for γ and its uncertainty given by

$$\frac{1}{\gamma} = -\frac{1}{(N-1)} \sum_i \log \frac{E_i}{E_{\rm thres}} \quad \text{and} \quad \sigma(\gamma) = \frac{\gamma}{\sqrt{N-2}}. \tag{18}$$

The resulting fits are overplotted in Fig. 11 and the residuals are shown in separate panels. The power-law indices vary between observations, but the uncertainties indicate that the difference is not statistically significant. The later observations from MJD 58442 onwards seem to be well described by a single power law, while the three earlier observations (top row) show deviations. The three earlier observations also have the highest burst numbers. Hence, the effect may be subtle and requires a sufficient number of bursts (as opposed to being a time-variable effect). All three show a dip in the burst numbers around an energy of $E \sim 1 \times 10^{38}$ erg that is not visible in the later observations. Observations 58432 and 58439 have significantly more bursts at $E \gtrsim 10^{39}$ erg than one would expect from the power-law fit.

We want to explore how the energy distribution depends on the definition of a burst. We show the histogram and the cumulative distribution for three different definitions in the left-hand panel of Fig. 12. The results show that the different definitions yield similar shapes for the energy distribution. It is so rare (8 per cent) that several bursts occur close to each other that the blue and orange points are almost identical. The incompleteness at energies below the completeness threshold can be seen as a smooth drop in the number density. The sub-burst energies in green do not extend as far to high energies, and the overabundance that was around $E \sim 10^{39}$ erg is shifted to the left. This is because the most energetic bursts all have several sub-bursts among which the energy gets distributed. The dip that was already visible in Fig. 11 is even more pronounced.

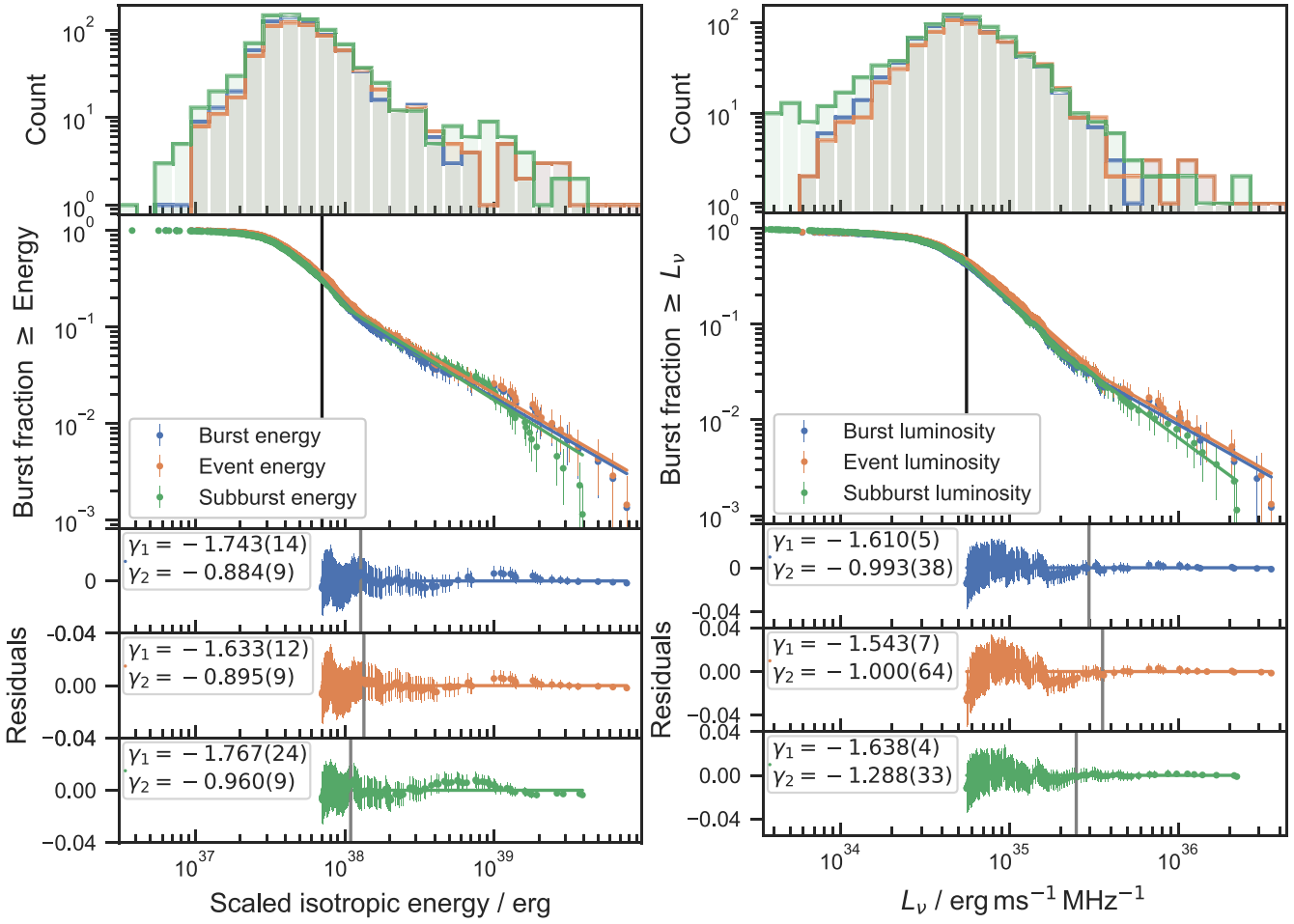

Figure 12. Cumulative burst fraction higher than a given isotropic-equivalent energy (left) and average specific luminosity (right), summing the bursts from all observations. The differential distribution is shown in the top panel for the three variations. All burst energies (luminosities) are limited to bursts where the burst centres are well within the observing band; and they are scaled up to account for the energy outside the band using the fitted Gaussians. In blue, we plot each burst; in orange, we summed up the energies (luminosities) of bursts that occur within 0.1 s; in green, the energies (luminosities) are distributed among the sub-bursts. Lines mark the broken power laws that were fit. The three lower panels show the residuals for each fit, with a grey line at the fit break. A black line shows the completeness threshold.

It is visible that a single power law would not fit the cumulative distributions well. We therefore fit broken power laws to the three variations that have the form

$$N(>E) = \begin{cases} k(E/E_{\rm break})^{\gamma_1}, & E < E_{\rm break}, \\ k(E/E_{\rm break})^{\gamma_2}, & E \geq E_{\rm break}. \end{cases} \tag{19}$$

We simultaneously fit the four parameters γ_1, γ_2, k, and $E_{\rm break}$ to minimize the squares of the residuals. The resulting indices are given in Fig. 12. The residuals below $E_{\rm break}$ show the dip around 1×10^{38} erg that we saw in some observations and a bump below it. They indicate that a power law might not be a good model for the data below $E_{\rm break}$.

Previous studies have placed their focus on the energy distribution; here we want to extend our analysis to the specific luminosity distribution. The isotropic-equivalent specific luminosity can be used as the source intrinsic quantity related to the flux, while the energy is related to the fluence. One reason why the specific luminosity has not received much attention is that the peak flux – a useful measure for Gaussian-shaped bursts – does not have much value for complex bursts with several peaks. We therefore use the specific isotropic-equivalent luminosity averaged over burst duration and bandwidth, calculated from the scaled energies via $L_\nu = E_{\rm tot}/{\rm FWHM}_t/{\rm FWHM}_\nu$. We calculate the specific luminosity completeness threshold analogously to the energy threshold as

$$L_{\rm thres} = 4\pi D_{\rm L}^2 \frac{({\rm S/N})_{\rm thres}\,{\rm SEFD}_{95\,\%}\,\Delta\nu_{\rm band}}{\sqrt{n_{\rm p}\,\Delta\nu_{\rm band}\,{\rm FWHM}_{t,5\,\%}}} \frac{s_{95\,\%}}{{\rm FWHM}_{\nu,\rm median}} \tag{20}$$

$$= 4\pi(949\,{\rm Mpc})^2 \frac{6 \times 4.8\,{\rm Jy} \times 580\,{\rm MHz}}{\sqrt{2 \times 580\,{\rm MHz} \times 1.9\,{\rm ms}}} \frac{1.4}{259\,{\rm MHz}} \tag{21}$$

$$= 6.6 \times 10^{31}\,{\rm erg\,s^{-1}\,Hz^{-1}}, \tag{22}$$

with the main difference that the 5th percentile instead of the 95th percentile of burst widths has to be used. The specific luminosity distributions are shown in the right-hand panel of Fig. 12, again for the three variations described above. There is no principle difference in the shapes of the energy and specific luminosity distribution, but some of the features are more pronounced in the luminosity distribution, like the dip around a specific luminosity of 2×10^{35} erg ms^{-1} MHz^{-1}. The overabundance of bursts at luminosities $>3 \times 10^{35}$ erg ms^{-1} MHz^{-1} is less pronounced, resulting in smaller differences between the power-law indices. This difference is smallest when the specific luminosity of sub-bursts (green) is used, this version is therefore most consistent with a single power law.

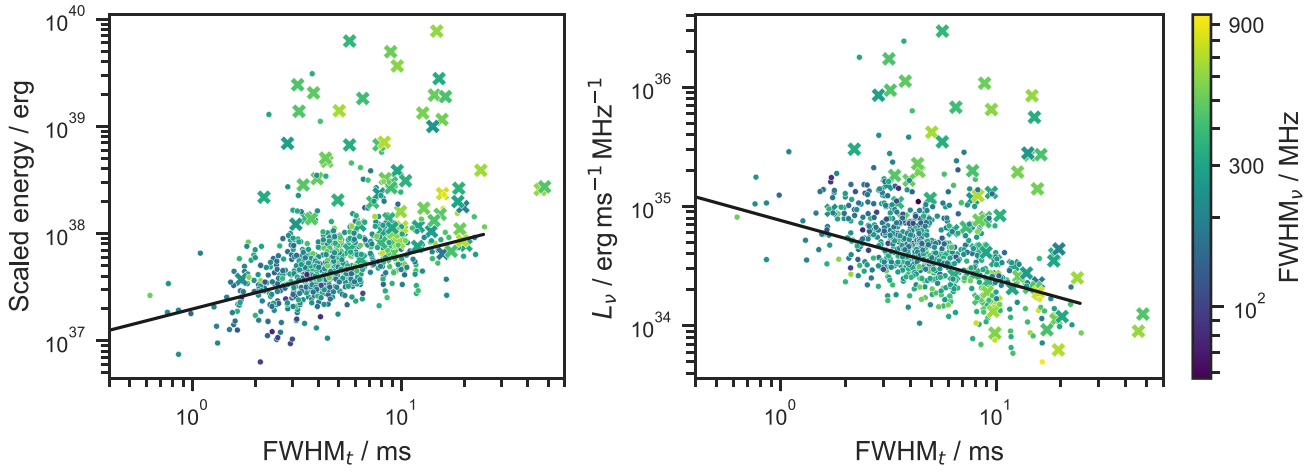

Figure 13. Scaled energies (left) and luminosities (right) plotted against burst duration and bandwidth as colour. Points mark bursts with a single component, while crosses mark bursts with substructure or several sub-bursts. This has the caveat that it is often not possible to identify structure in bursts below a certain S/N. A black line marks the completeness threshold.

To further compare the energy and specific luminosity distributions, we show both plotted against the burst width and bandwidth in Fig. 13. Point and cross markers represent single-component and multicomponent bursts, respectively, as classified by eye. An important caveat is that it is often not possible to identify structure in bursts below a certain S/N (as illustrated in fig. 7 of Gourdji et al. 2019). The completeness threshold can be seen as a black line. Around the energy of 10^{38} erg in the left-hand panel, we can see a steep drop in number density towards higher energies. Interestingly, this drop does not seem to be at the same energy for different widths, but rather seems to follow a similar slope as the completeness. Arguably, this is still – although less – visible in the right-hand panel.

Complex bursts dominate the distribution at high energies, and the break energies in the broken power-law fits roughly correspond to the energy above which the majority of bursts are complex. It is difficult to tell if this is an observational or a physical effect, because there is a certain energy below which the complex structure of bursts gets buried in noise. This could just coincidentally be similar to the break energy.

We tested if the overabundance of high-energy bursts is due to more sub-bursts being identified by looking at the distribution of only the brightest sub-bursts of each burst, but the energy distribution still showed the same features. The larger bandwidth of complex bursts is most likely also an observational effect, with weaker sub-bursts emerging out of the noise.

4.5 Periodicity

The search for short-term periodicity focused on the detections on MJD 58435 and MJD 58439, which had the highest detection rate (218 burst per hour) and highest number of detections (227), respectively. Two detection algorithms were applied: the Pearson χ^2 test and the Lomb–Scargle periodogram. For both search methods, the range of trial periods searched was 10 ms to 100 s. These values are just below and just above the two peaks in the wait-time distribution given in Fig. 3. In the case of bursts with multiple sub-bursts, a single arrival time was calculated by taking the weighted mean of the temporal centres of each fitted Gaussian component. For the Pearson χ^2 test, the detections were folded with a set of trial logarithmically spaced periods and grouped into eight profile bins. No statistically significant periods were found in either observation. The Lomb–Scargle periodogram was calculated using the ASTROPY Lomb–Scargle function. No significant peaks were identified in either observation.

5 DISCUSSION

5.1 Rates and wait times

Like previous studies of FRB 121102 (Katz 2018; Zhang et al. 2018; Gourdji et al. 2019; Li et al. 2019, 2021b; Aggarwal et al. 2021; Hewitt et al. 2022) we found a bimodal distribution of wait times (Fig. 3). We showed that the peak on time-scales of tens of seconds can be well described by a Poisson process, i.e. randomly arriving bursts, with the rate – that varies between observations – as the only parameter. We confirmed the results of Cruces et al. (2021) that the two-parameter Weibull model is not needed to explain the wait-time distribution within a single observation. Expanding on their conclusion, the Weibull model would also require a varying rate and cannot explain the peak at <0.1 s. It therefore has no advantage over the simpler Poisson model. We also see no advantage in the (two parameter) lognormal distribution that is usually used as an approximation to the Poisson model. Variations in the peak position (Aggarwal et al. 2021) contain no information other than the varying rate and different sensitivities of telescopes. Zhang (2018) found a rapidly changing rate in a 5-h observation at 4–8 GHz with 45 out of 93 bursts arriving in the first 30 min. Nimmo et al. (2022) found a rapidly changing rate for FRB 20200120E at 1.4 GHz. It remains to be seen if these quick changes can also occur for FRB 121102 below 4 GHz, or if changes are slower, as in the presented observations.

In contrast, the wait-time peak at <0.1 s shows that the bursts sometimes come in packs. Its position is stable over observations with very different rates, and it is therefore reflecting a time-scale of the emission process. The wait times reported by different groups are subject to the different – sometimes unclear – distinction between bursts and sub-bursts. The nine wait times reported by Li et al. (2019), which are dominated by data from Gajjar et al. (2018) and Zhang (2018) at frequencies 4–8 GHz, yield a median of 5.2 ms. Li et al. (2021b) report their lognormal fit to peak at (3.4 ± 1.0) ms, which is

dominated by the wait times between sub-burst. Hewitt et al. (2022) report 24 ms, whereas they did not use wait times between sub-bursts. The different fitting methods and better sensitivity of FAST – likely resolving more sub-bursts – dominate the differences in numbers and can explain the difference between the (3.4 ± 1.0) ms and our median of 9.7 ms. Our median of 22 ms, when we exclude wait times of sub-bursts, is close to the 24 ms of Hewitt et al. (2022), implying no significant change over the ∼2 yr between the studied observations. The ambiguity in the definition of sub-bursts also dominates the difference between Li et al. (2021b) and the higher value of 39 ms that Xu et al. (2022) find for FRB 20201124A without using wait times between sub-bursts. Still, compared to our 22 ms, the 39 ms in FRB 20201124A is almost twice as high (at rest frame they translate to ∼18 and 34.5 ms, respectively) and show that the peak time-scale is different for different sources.

In summary, we see one peak in the wait times that reflects the occurrence time-scale and one that reflects an emission time-scale. They have to be interpreted in the light of proposed emission mechanisms, keeping in mind the lack of a strict short-term periodicity. The most popular FRB models involve a neutron star as the central engine of the FRB source (Platts et al. 2019; Petroff et al. 2022). Direct observational evidence came from bursts of the magnetar SGR 1935+2154 that would have been observable from an extragalactic distance. They were simultaneously observed in radio (Bochenek et al. 2020; CHIME/FRB Collaboration 2020) and hard X-rays (Mereghetti et al. 2020; Li et al. 2021a; Ridnaia et al. 2021; Tavani et al. 2021). Magnetars in X-rays often show several sub-bursts within a rotational phase (see e.g. Huppenkothen et al. 2015), while the arrival of normal pulses follows Poisson statistics (Göğüş et al. 1999, 2000; Kondratyev & Korovina 2018). The counterpart in radio to what is seen as sub-bursts in X-rays, can be visible as separate bursts, as was seen in the simultaneous bursts of SGR 1935+2154 (see e.g. fig. 1 in Mereghetti et al. 2020). The clustering in SGR 1935+2154 radio bursts has also been seen by Kirsten et al. (2021), who detected two bursts in several hundred hours of observations. These two bursts were only ∼1.4 s apart and within the same rotation. Other magnetars (Pearlman et al. 2018; Wharton et al. 2019) and pulsar giant pulses (see e.g. Karuppusamy, Stappers & van Straten 2010; Geyer et al. 2021) can as well occur multiple times within a rotational period, which produces bimodality in the wait times, similar to the one we see in FRB 121102. Apart from these similarities, magnetars emit in radio only in parts of their rotational phase (Pearlman et al. 2018), while no such rotational period has been found in FRB 121102 (and in Section 4.5; Zhang 2018; Aggarwal et al. 2021; Cruces et al. 2021; Li et al. 2021b; Hewitt et al. 2022). The Galactic Centre magnetar J1745−2900 can, however, emit radio pulses in ∼70 per cent of its rotational phase, although they are clustered in smaller windows (Wharton et al. 2019). In the context of a rotating magnetar with stable emission regions, we can constrain the rotational period to be between the two observed peaks, but several scenarios could make the period unobservable. One possibility is that the emission cone of the source is larger than the angular difference between the rotational axis and our line of sight. This way, bursts would be observable in every part of the rotational phase. Another possibility is that – unlike in magnetars – the emission region is not restricted by the magnetic axis and hence the rotational phase.

The stable wait-time peak at <0.1 s is also in accordance with sub-bursts coming from oscillations in a magnetar crust and core, as proposed by Wadiasingh & Chirenti (2020). This model is used to explain quasi-periodic oscillations seen in magnetar X-rays that are at similar time-scales as sub-bursts of FRB 121102. In the framework of the synchrotron maser mechanism (Metzger, Margalit & Sironi 2019; Margalit et al. 2020), the observed emission time-scale could be the time-scale over which the maser is stable or at least can emit in our observing band in a stable manner. Li et al. (2019) have argued that the presence of the short wait-time peak would favour models where a neutron star travels through an asteroid belt and FRBs are caused by the collisions between asteroids and the neutron star. This hypothesis is ruled out by the fact that the <0.1 s wait-time peak is stable on time-scales of years (compare our results here with those of Hewitt et al. 2022). We can think of no reason for asteroids to consistently cluster such that they would collide with the neutron star on subsecond time-scales.

5.2 General properties

Earlier observations of FRB 121102 reported in Gourdji et al. (2019) observed a lack of bursts below 1350 MHz, with all 41 bursts being higher than this frequency. Hewitt et al. (2022) confirmed the tendency in a larger set of observations around the same time in 2016 September, although they found some bursts below 1350 MHz. We showed that there is no such clear, preferred frequency range in the time window that we reported here. The change in emission frequency must be due to the difference in time of about 2 yr (five activity cycles). Future observations are needed to investigate if this is a long-term trend to lower frequencies or random variations of the emission band.

Hessels et al. (2019) showed that the DM of bursts is stable on weekly time-scales by analysing bright, structured bursts. They also measured the scintillation bandwidth and estimated from it that scattering is negligible at L-band. Nevertheless, some studies have interpreted the sad-trombone effect in unresolved bursts as short term DM variations (Li et al. 2021b) and intrinsic burst shapes as scattering tails (Aggarwal et al. 2021). We confirmed the conclusions from Hessels et al. (2019) by showing that there is a relationship between burst durations and the intraburst drift. This relationship must be intrinsic because DM variations would affect all bursts regardless of their temporal width. However, intraburst drifts by themselves can look like DM variations of several pc cm^{-3}. These apparent DM variations do not change the conclusion of other studies on the long-term trend in the DM of FRB 121102 that is of the order of ∼10 pc cm^{-3} since its discovery (Spitler et al. 2014). It has been investigated by Hessels et al. (2019), Oostrum et al. (2020), and Li et al. (2021b) using structure optimized DMs, thereby largely mitigating the effect of intrinsic burst drifts. Cosmological applications of FRBs are also not significantly affected by these higher appearing DMs because the uncertainties in the DMs of host galaxies, which are of the order 50 pc cm^{-3}, are much higher. Interestingly, burst C232 has not only sub-bursts that follow the law of the intraburst drift, but also structure in the last component that is instead straight at the inferred DM. The reason could either be that the drift rate changes in the middle of the burst, or the structure could be a propagation effect that happened shortly after emission.

The temporal width distribution is consistent with the literature on FRB 121102 and shows no long-term temporal variations. In Fig. 4 complex bursts have systematically larger widths and bandwidths, this is likely a bias and a hint that we are systematically missing additional sub-bursts in weaker bursts.

5.3 The time–frequency drift

We have introduced a new way of fitting bursts from repeating FRBs. Previous studies have used various methods. Hessels et al.

(2019) used 2D Gaussians (without drift or rotation) to measure the drift of burst centres and compared it to their second method, where a 2D elliptical Gaussian rotated by an angle θ is fitted it to the 2D autocorrelation function of bursts. Rajabi et al. (2020) applied the latter technique to sub-bursts to measure the intraburst drift. Aggarwal et al. (2021) have fitted the bursts dynamic spectra with a more complex function, including a burst-dependent DM and scattering. In this work, we fitted the dynamic spectra with 2D elliptical Gaussians that include a linear shift of the arrival time t_0 with frequency. This form has several mathematical and practical advantages. Mathematically it describes the same function as a rotated Gaussian, but a rotation in a space with different dimensions (here time and frequency) makes the parameters lose their physical meaning. On the other hand, σ_t and σ_ν in our definition have a clearly defined meaning for all d_t. The rotation angle θ itself is only meaningful as an approximation to our d_t.

The sad-trombone drift has previously been measured by several studies (Hessels et al. 2019; Josephy et al. 2019; Caleb et al. 2020) and Hessels et al. (2019) find much stronger drifts than the ones presented here. Only three of their 13 analysed bursts, which were observed with the same observing system, have a drift above $-100\,\mathrm{MHz\,ms^{-1}}$ and the strongest drift is $(-286.89 \pm 0.03)\,\mathrm{MHz\,ms^{-1}}$. In contrast, the strongest drift in our 12 analysed bursts is $-100.6\,\mathrm{MHz\,ms^{-1}}$ and our range agrees with the bursts that Caleb et al. (2020) found at similar frequencies, although using a different method and a small sample. The large differences show a significant temporal change in the sad-trombone drifts between 2016 September (Hessels et al. 2019) and 2018 November.

In Section 4.3, we found that within bursts, the intraburst drift and sad-trombone drift are equal within the uncertainties. Yet, d_t and σ_t were seen to be in a nearly linear relationship. This excludes the following two simple models. The simplest model would be that in the sad-trombone effect only the frequency centres of sub-bursts drift while sub-bursts are not affected. This would mean only statistical fluctuations of d_t around 0 and no relation between d_t and σ_t. The second model was described earlier as bursts drifting constantly with drift d_ν and a Gaussian frequency envelope w_ν that is superimposed by temporal modulation. For this model, one obtains a quadratic relationship for the measured quantities as $d_t = \sigma_t^2 d_\nu / w_\nu^2$. These two simple yet plausible possibilities are in conflict with the nearly linear relationship found.

Radius-to-frequency mapping is the common explanation for the sad-trombone drift in models where the emission originates in the magnetosphere of a neutron star (Lyutikov 2020; Tong et al. 2022). A close relation between the sad-trombone drift and the intraburst drift can be expected in this model, but it does not predict the way in which a burst is modulated in time. The linear d_t–σ_t therefore does not contradict the radius-to-frequency mapping, but it sets constrains for the way that the temporal structure is created. To our knowledge, there are no predictions for this structure from the emission models.

The toy model of Metzger et al. (2022) describes the spectro-temporal structure as a Gaussian in frequency, whose central frequency, bandwidth, and flux evolve as power laws. It can describe the emission in the framework of several physical models like the synchrotron maser model (e.g. Metzger et al. 2019), or radius-to-frequency mapping (Lyutikov 2020). The toy model can reproduce many properties of FRB 121102 very well, like the sad-trombone effect and shorter bursts with stronger drifts at high frequencies. On the other hand, the model predicts a dependency of duration on bandwidth and frequency, which we do not see in our data. Yet, it might be obscured by the strong d_t–σ_t correlation. Another feature that the model does not reproduce well is the variety of sub-bursts that we see. Bursts like B29, B180, or C232 show a variety of sub-burst widths and fluxes that require adding individual parameters per sub-burst. Finally, some d_t–σ_t relationship is expected for the model, but the exact shape has not yet been investigated and requires simulations with realistic parameters.

So far, the d_t–σ_t relation is only explained by Rajabi et al. (2020) for a family of models where a relativistically moving FRB source is triggered and only after a delay time τ'_D emits radiation at a narrow frequency ν'_0 with a width τ'_W in the source's rest frame. The radiation is then observed at a frequency ν_obs changed by the relativistic Doppler shift. The delay time and width are equally Doppler shifted and therefore observed as

$$t_\mathrm{D} = \tau'_\mathrm{D} \frac{\nu'_0}{\nu_\mathrm{obs}} \quad \text{and} \quad t_\mathrm{W} = \tau'_\mathrm{W} \frac{\nu'_0}{\nu_\mathrm{obs}}. \tag{23}$$

A slightly faster part of the emission region will be observed with slightly less delay and at a higher frequency with the ratio given by

$$d_t \equiv \frac{\mathrm{d}t_\mathrm{D}}{\mathrm{d}\nu_\mathrm{obs}} = -\tau'_\mathrm{D} \frac{\nu'_0}{\nu^2_\mathrm{obs}} = -\frac{\tau'_\mathrm{D}}{\tau'_\mathrm{W}} \frac{t_\mathrm{W}}{\nu_\mathrm{obs}}. \tag{24}$$

The ratio $\tau'_\mathrm{D}/\tau'_\mathrm{W}$ is a constant that depends on the emission mechanism; t_W is equivalent to our σ_t. This quick reformulation of the model by Rajabi et al. (2020) showed that the linear d_t–σ_t is the same that is predicted, and also that the formulation we used is a good description of their model. Apart from this success, the model does currently not predict a relationship between the sad-trombone drift and the intraburst drift. It furthermore does not give a reason for the sad-trombone drift to always be negative.

In summary, none of the current models can explain both observational aspects that we discussed. Additional theoretical and observational studies are needed to understand our findings – and the spectro-temporal structure of FRBs in general – in the context of the various proposed models. Bursts detected at various frequency bands but within the same activity window could be used to extend our analysis to the relationships between d_ν, d_t, σ_ν, and ν_0. This has the potential to further test the theory of Rajabi et al. (2020), the results of Chamma et al. (2021), the model of Tuntsov, Pen & Walker (2021), as well as the model by Metzger et al. (2019) in different theoretical contexts.

5.4 Burst energy distribution

The high burst rate in our observations allowed us to probe and compare the energy distribution on individual days. We found that a single power law is an insufficient fit even in single observations due to an excess of high-energy bursts. These bright bursts also tend to have more complex morphologies. It is unclear whether this represents different emission mechanisms or regions, or if this is simply a result of complex morphologies being easier to see in brighter bursts.

Past studies have focused entirely on the analysis of the energy distribution. We showed that instead it is the power or specific luminosity that is dictating the energy distribution, while the distribution of burst width and bandwidth do not vary significantly between low- and high-energy bursts. However, we found no features in the specific luminosity distribution that were not already visible in the energy distribution.

Past studies of the energy distribution (Gourdji et al. 2019; Lin & Sang 2020; Aggarwal et al. 2021; Cruces et al. 2021; Hewitt et al. 2022) have found different power-law indices, but low numbers and different energy-dependent completeness thresholds have complicated the comparisons. Li et al. (2021b) found a bimodal energy

distribution and that the higher energy bursts were only detectable in their earlier observations so that not only the rate changes but also the form of the energy distribution. We see weak evidence for such a change, e.g. comparing observations 58439 and 58448. The dip in three consecutive observations is around the same energy of 1×10^{38} erg, where Li et al. (2021b) report a deficiency of bursts. We also see a similar, yet weaker bimodality in the top panel of Fig. 12. In our data this appears only when the energies of individual sub-bursts are used, but we confirmed with the available data of Li et al. (2021b) that the bimodality persists when bursts close in time are summed together. To sum up, we therefore cannot conclusively confirm these important results, but our data suggest that they are not due to a detection bias and that the emission mechanism is indeed time variable. This is also visible in the difference between the energy–width relation of Hewitt et al. (2022) and our data (Fig. 13). The clear distinction between high- and low-energy bursts is not present any more in our data. Furthermore, our value of $\gamma_1 = -1.74$ in the broken power law in Fig. 12 is much steeper than the $\gamma_1 = -1.38$ of Hewitt et al. (2022). The other values of $\gamma_2 = -0.88$ above $E_{\rm break} = 1.28 \times 10^{38}$ erg agree roughly with the ones of Hewitt et al. (2022), which are $\gamma_2 = -1.04$ above $E_{\rm break} = 1.15 \times 10^{38}$ erg. Our values also agree with other previously reported values. The value of $\gamma = -1.8 \pm 0.3$ by Gourdji et al. (2019), which was dominated by low-energy bursts, was close to our γ_1. Cruces et al. (2021) reported $\gamma = -0.8 \pm 0.1$ for predominantly high-energy bursts, in agreement with our γ_2. We showed that the uncertainties are dominantly systematic and come from different burst definitions – i.e. the unclear distinction between sub-bursts, bursts, and packs – and from the estimated completeness threshold.

In the absence of concrete theoretical predictions for the slope of the energy distribution, it is most interesting to compare our findings to the energy distributions of known sources that are related to proposed FRB models. Normal pulses from pulsars tend to follow a lognormal energy distribution (see e.g. Burke-Spolaor et al. 2012), whereas cumulative energies of giant pulses follow a power law with index $\gamma = -2$ for the Crab Pulsar (Popov & Stappers 2007; Bera & Chengalur 2019) and -2.63 ± 0.02 for J1823−3021A (Knight 2007; Abbate et al. 2020). For magnetars a γ of -0.7 t0-0.6 was found in X-rays (Göğüş et al. 1999, 2000). In radio, the magnetar J1745−2900 shows a lognormal distribution with a high-energy tail (Lynch et al. 2015). Our value of -0.85 only agrees with the values of magnetar X-ray bursts, but this could also indicate similar underlying statistics rather than a common emission mechanism. For example, this underlying statistics could possibly be described by self-organized criticality (see Aschwanden et al. 2016, for a review), as discussed for magnetars by Huppenkothen et al. (2015).

6 CONCLUSIONS

With our improved search pipeline, we found 849 bursts in eight observations during the active period in 2018 November. The large number of bursts and the high rate of up to 218 ± 16 bursts per hour allowed us to probe several statistical properties to new precisions and to compare them with burst properties measured at other epochs.

(i) The new form of Gaussians that was fit to the dynamic spectra showed several advantages, and we recommend future studies to adopt it. On the other hand, error estimates in the fitting process could be improved by using Bayesian fits, as was done by Aggarwal et al. (2021).

(ii) The event rates vary strongly between observations of the same active cycle, separated by only a few days.

(iii) As in previous studies, a bimodal wait-time distribution is clearly visible. We confirm the results of Cruces et al. (2021) with high precision that the peak on time-scales of tens of seconds is well fit by Poisson statistics. Therefore, burst arrival times with separation >0.1 s are best described by a non-stationary Poisson process. The peak at <0.1 s is stable and reflective of a source and emission mechanism time-scale. It is consistent with the time-scales of magnetar bursts.

(iv) The (temporal) intraburst drift and σ_t (the width at ν_0) are related linearly. For 10 out of 12 bursts we find it to be consistent with the sad-trombone drift if not only the burst centres drift but also the emission within sub-bursts. None of the current models can explain both of these findings.

(v) The intraburst drift is the cause of the apparent short-term variations in DM that have been reported. We recommend future studies to use the smallest DM (from the sharpest sub-bursts) to dedisperse bursts at the same DM if the separation is on the order of weeks.

(vi) The energy distribution is not well fit by a single power law, as it shows an overabundance of high-energy bursts and a dip around 1×10^{38} erg that persist over three consecutive observations. A broken power law fits the high-energy bursts better and yields $\gamma_1 = -1.74 \pm 0.01$ below $E_{\rm break} = 1.28 \times 10^{38}$ erg and $\gamma_2 = -0.88 \pm 0.01$ above. The quoted error includes only statistical uncertainties.

(vii) With the given burst numbers, systematic uncertainties can dominate over statistical uncertainties. The distinction between bursts and sub-bursts influences the location of the wait-time peak at <0.1 s, as well as the energy power-law slope.

(viii) The specific luminosity is a more fundamental quantity for FRBs than the energy, but has the disadvantage in complex bursts that the peak luminosity is not well measurable. We encourage further exploration of the burst averaged specific luminosity.

ACKNOWLEDGEMENTS

We thank M. Cruces for her help with the Weibull fit and Arun Venkataraman for regularly swapping the hard drives at the Arecibo Observatory according to our needs. We thank Fronefield Crawford for refereeing the manuscript and for his helpful comments, and also Zorawar Wadiasingh and Navin Sridhar for useful hints. The Arecibo Observatory is a facility of the National Science Foundation operated under cooperative agreement by the University of Central Florida and in alliance with Universidad Ana G. Mendez, and Yang Enterprises, Inc. LGS is a Lise Meitner Max Planck independent research group leader and acknowledges funding from the Max Planck Society. Research by the AstroFlash group at University of Amsterdam, ASTRON, and JIVE is supported in part by an NWO Vici grant (PI Hessels; VI.C.192.045).

DATA AVAILABILITY

The results of the burst fits and some of the derived properties are available as supplementary material. The first 10 lines of both tables are in Tables C1 and C2. The program FIX_GPU_DROPOUTS is available at https://github.com/JoschaJ/fix_gpu_dropouts. The raw data are available upon reasonable request.

REFERENCES

Abbate F. et al., 2020, MNRAS, 498, 875
Agarwal D., Aggarwal K., Burke-Spolaor S., Lorimer D. R., Garver-Daniels N., 2020, MNRAS, 497, 1661

Aggarwal K., 2021, ApJ, 920, L18
Aggarwal K., Agarwal D., Lewis E. F., Anna-Thomas R., Tremblay J. C., Burke-Spolaor S., McLaughlin M. A., Lorimer D. R., 2021, ApJ, 922, 115
Aschwanden M. J. et al., 2016, Space Sci. Rev., 198, 47
Bannister K. W. et al., 2019, Science, 365, 565
Bassa C. G. et al., 2017, ApJ, 843, L8
Beniamini P., Wadiasingh Z., Metzger B. D., 2020, MNRAS, 496, 3390
Bera A., Chengalur J. N., 2019, MNRAS, 490, L12
Bhandari S. et al., 2022, AJ, 163, 69
Bochenek C. D., Ravi V., Belov K. V., Hallinan G., Kocz J., Kulkarni S. R., McKenna D. L., 2020, Nature, 587, 59
Burke-Spolaor S. et al., 2012, MNRAS, 423, 1351
Caleb M. et al., 2020, MNRAS, 496, 4565
Chamma M. A., Rajabi F., Wyenberg C. M., Mathews A., Houde M., 2021, MNRAS, 507, 246
Chatterjee S. et al., 2017, Nature, 541, 58
CHIME/FRB Collaboration, 2020, Nature, 587, 54
CHIME/FRB Collaboration, 2021, ApJS, 257, 59
Crawford D. F., Jauncey D. L., Murdoch H. S., 1970, ApJ, 162, 405
Cruces M. et al., 2021, MNRAS, 500, 448
Dicke R. H., 1954, Phys. Rev., 93, 99
Du S., Wang W., Wu X., Xu R., 2021, MNRAS, 500, 4678
DuPlain R., Ransom S., Demorest P., Brandt P., Ford J., Shelton A. L., 2008, in Bridger A., Radziwill N. M., eds, Proc. SPIE Vol. 7019, Advanced Software and Control for Astronomy II. SPIE, Bellingham, p. 70191D
Gajjar V. et al., 2018, ApJ, 863, 2
Geyer M. et al., 2021, MNRAS, 505, 4468
Göğüş E., Woods P. M., Kouveliotou C., van Paradijs J., Briggs M. S., Duncan R. C., Thompson C., 1999, ApJ, 526, L93
Göğüş E., Woods P. M., Kouveliotou C., van Paradijs J., Briggs M. S., Duncan R. C., Thompson C., 2000, ApJ, 532, L121
Gourdji K., Michilli D., Spitler L. G., Hessels J. W. T., Seymour A., Cordes J. M., Chatterjee S., 2019, ApJ, 877, L19
Gu W.-M., Yi T., Liu T., 2020, MNRAS, 497, 1543
Hardy L. K. et al., 2017, MNRAS, 472, 2800
Hessels J. W. T. et al., 2019, ApJ, 876, L23
Hewitt D. M. et al., 2022, MNRAS, 515, 3577
Hilmarsson G. H. et al., 2021, ApJ, 908, L10
Houben L. J. M., Spitler L. G., ter Veen S., Rachen J. P., Falcke H., Kramer M., 2019, A&A, 623, A42
Houde M., Rajabi F., Gaensler B. M., Mathews A., Tranchant V., 2019, MNRAS, 482, 5492
Huppenkothen D. et al., 2015, ApJ, 810, 66
Ioka K., Zhang B., 2020, ApJ, 893, L26
James C. W., Ekers R. D., Macquart J. P., Bannister K. W., Shannon R. M., 2019, MNRAS, 483, 1342
Josephy A. et al., 2019, ApJ, 882, L18
Karuppusamy R., Stappers B. W., van Straten W., 2010, A&A, 515, A36
Katz J. I., 2018, MNRAS, 476, 1849
Kirsten F., Snelders M. P., Jenkins M., Nimmo K., van den Eijnden J., Hessels J. W. T., Gawroński M. P., Yang J., 2021, Nat. Astron., 5, 414
Knight H. S., 2007, MNRAS, 378, 723
Kondratyev V. N., Korovina Y. V., 2018, Phys. Part. Nucl., 49, 105
Kulkarni S. R., 2020, preprint (arXiv:2007.02886)
Kurban A. et al., 2022, ApJ, 928, 94
Levin Y., Beloborodov A. M., Bransgrove A., 2020, ApJ, 895, L30
Li B., Li L.-B., Zhang Z.-B., Geng J.-J., Song L.-M., Huang Y.-F., Yang Y.-P., 2019, preprint (arXiv:1901.03484)
Li C. K. et al., 2021a, Nat. Astron., 5, 378
Li D. et al., 2021b, Nature, 598, 267
Lin H.-N., Sang Y., 2020, MNRAS, 491, 2156
Lorimer D. R., Kramer M., 2004, Handbook of Pulsar Astronomy. Cambridge Univ. Press, Cambridge
Lorimer D. R., Bailes M., McLaughlin M. A., Narkevic D. J., Crawford F., 2007, Science, 318, 777
Lynch R. S., Archibald R. F., Kaspi V. M., Scholz P., 2015, ApJ, 806, 266
Lyubarsky Y., 2021, Universe, 7, 56
Lyutikov M., 2020, ApJ, 889, 135
Lyutikov M., Barkov M. V., Giannios D., 2020, ApJ, 893, L39
Marcote B. et al., 2017, ApJ, 834, L8
Margalit B., Beniamini P., Sridhar N., Metzger B. D., 2020, ApJ, 899, L27
Mereghetti S. et al., 2020, ApJ, 898, L29
Metzger B. D., Margalit B., Sironi L., 2019, MNRAS, 485, 4091
Metzger B. D., Sridhar N., Margalit B., Beniamini P., Sironi L., 2022, ApJ, 925, 135
Michilli D. et al., 2018a, MNRAS, 480, 3457
Michilli D. et al., 2018b, Nature, 553, 182
Nimmo K. et al., 2022, preprint (arXiv:2206.03759)
Oostrum L. C. et al., 2020, A&A, 635, A61
Oppermann N., Yu H.-R., Pen U.-L., 2018, MNRAS, 475, 5109
Pearlman A. B., Majid W. A., Prince T. A., Kocz J., Horiuchi S., 2018, ApJ, 866, 160
Petroff E., Hessels J. W. T., Lorimer D. R., 2022, A&AR, 30, 2
Planck Collaboration XIII, 2016, A&A, 594, A13
Platts E., Weltman A., Walters A., Tendulkar S. P., Gordin J. E. B., Kandhai S., 2019, Phys. Rep., 821, 1
Plavin A., Paragi Z., Marcote B., Keimpema A., Hessels J. W. T., Nimmo K., Vedantham H. K., Spitler L. G., 2022, MNRAS, 511, 6033
Pleunis Z. et al., 2021, ApJ, 923, 1
Popov M. V., Stappers B., 2007, A&A, 470, 1003
Rajabi F., Chamma M. A., Wyenberg C. M., Mathews A., Houde M., 2020, MNRAS, 498, 4936
Rajwade K. M. et al., 2020, MNRAS, 495, 3551
Ransom S. M., 2001, PhD thesis, Harvard University, Cambridge, MA
Ridnaia A. et al., 2021, Nat. Astron., 5, 372
Seymour A., Michilli D., Pleunis Z., 2019, Astrophysics Source Code Library, record ascl:1910.004
Sob'yanin D. N., 2020, MNRAS, 497, 1001
Spitler L. G. et al., 2014, ApJ, 790, 101
Spitler L. G. et al., 2016, Nature, 531, 202
Sridhar N., Metzger B. D., Beniamini P., Margalit B., Renzo M., Sironi L., Kovlakas K., 2021, ApJ, 917, 13
Tavani M. et al., 2021, Nat. Astron., 5, 401
Tendulkar S. P. et al., 2017, ApJ, 834, L7
Tendulkar S. P. et al., 2021, ApJ, 908, L12
Tong H., Liu J., Wang H. G., Yan Z., 2022, MNRAS, 509, 5679
Tuntsov A., Pen U.-L., Walker M., 2021, preprint (arXiv:2107.13549)
Wada T., Ioka K., Zhang B., 2021, ApJ, 920, 54
Wadiasingh Z., Chirenti C., 2020, ApJ, 903, L38
Wharton R. S. et al., 2019, ApJ, 875, 143
Xu H. et al., 2022, Nature, 609, 685
Zanazzi J. J., Lai D., 2020, ApJ, 892, L15
Zhang B., 2018, ApJ, 867, L21
Zhang Y. G., Gajjar V., Foster G., Siemion A., Cordes J., Law C., Wang Y., 2018, ApJ, 866, 149

SUPPORTING INFORMATION

Supplementary data are available at *MNRAS* online.

Table C1. The times of arrival are barycentre corrected and dispersion corrected to infinite frequency using the dispersion constant $a = 4.1488064239(11)$ GHz^2 cm^3 pc^{-1} ms (Kulkarni 2020).
Table C2. Some of the burst properties derived throughout the paper.

Please note: Oxford University Press is not responsible for the content or functionality of any supporting materials supplied by the authors. Any queries (other than missing material) should be directed to the corresponding author for the article.

APPENDIX A: DIFFERENT PARAMETRIZATIONS FOR AN ELLIPTICAL GAUSSIAN

Throughout the study, we use two parametrizations for elliptical two-dimensional Gaussians. Here we want to provide additional illustrations to familiarize the reader with the different parameters, in particular the drift rates d_t and d_ν. Further, we will provide the equations to compute one from the other and two additional parametrizations that were not used in the paper.

Both are illustrated in Fig. A1, the properties can be summarized as follows. In the first ($\mathcal{G}_{\mathrm{2D},t}$, equation 2), the central time of arrival t_0 drifts linearly in frequency with rate d_t in ms MHz^{-1}, the width σ_t is given at ν_0, while σ_ν is the bandwidth of the whole emission, which is equivalent to the bandwidth in a 1D fit to the spectrum. The advantages are that this form is closely related to the DM (see equation 13 and the surrounding discussion), it is therefore also useful for fitting because small DM offsets can be corrected. Lastly, this form is a good description of the FRB model by Rajabi et al. (2020) better yet than the rotated Gaussian in the original description. A disadvantage is that this form is difficult to compare to the sad-trombone drift.

In the second parametrization ($\mathcal{G}_{\mathrm{2D},\nu}$, equation 10) it is the central frequency ν_0 that drifts with rate d_ν in MHz ms^{-1}. Contrary to the first form, the width w_t is the overall width equivalent to the burst width in the time series, while w_ν is the bandwidth at t_0. The advantage of this form is that it is close to our interpretation of the sad-trombone effect, where we believe that the frequency centres drift with time. A disadvantage in fitting is that the drifts of sharp bursts are strongly susceptible to small DM changes, but this can possibly be used as an advantage in the future to measure the DM with high precision once we fully understand the underlying relations (e.g. by not optimizing the structure but instead requiring equality of d_ν and the sad-trombone drift).

To find the conversion between the two forms, we look at the general form of an elliptical two-dimensional Gaussian function. It can generally be expressed as

$$\mathcal{G}(x, y) = A \exp[-(a(x - x_0)^2 + 2b(x - x_0)(y - y_0) + c(y - y_0)^2)]. \tag{A1}$$

The Gaussians that we defined in equations (2) and (10) are also elliptical Gaussians as they can be rewritten in the above form

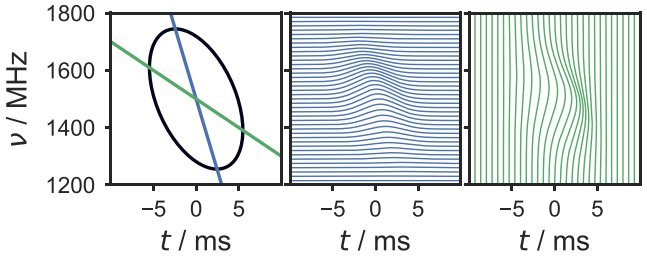

Figure A1. Illustration of the two Gaussian parametrizations. The tree panels show the same elliptical Gaussian. Left-hand panel: a single contour of the Gaussian and the lines along which the Gaussians drift in the temporal and frequency versions, i.e. $t_0 - d_t(\nu - \nu_0)$ in blue and $\nu_0 - d_\nu(t - t_0)$ in green. Middle panel: parametrization that drifts in time ($\mathcal{G}_{\mathrm{2D},t}$), each line can be thought of as one frequency channel. Right-hand panel: parametrization that drifts in frequency ($\mathcal{G}_{\mathrm{2D},\nu}$), each line represents the spectrum at one point in time.

(replacing x by t and y by ν) with

$$a = \frac{1}{2\sigma_t^2}, \qquad b = -\frac{d_t}{2\sigma_t^2}, \qquad c = \frac{d_t^2}{2\sigma_t^2} + \frac{1}{2\sigma_\nu^2} \tag{A2}$$

for $\mathcal{G}_{\mathrm{2D},t}$ and

$$a = \frac{1}{2w_t^2} + \frac{d_\nu^2}{2w_\nu^2}, \qquad b = -\frac{d_\nu}{2w_\nu^2}, \qquad c = \frac{1}{2w_\nu^2} \tag{A3}$$

for $\mathcal{G}_{\mathrm{2D},\nu}$. For a given burst the two functions have to be equal and one obtains the conversion relations

$$w_\nu = \frac{\sigma_\nu}{\sqrt{1 + \left(\frac{d_t \sigma_\nu}{\sigma_t}\right)^2}}, \quad d_\nu = \frac{d_t}{d_t^2 + \frac{\sigma_t^2}{\sigma_\nu^2}}, \quad w_t = \sqrt{\sigma_t^2 + (d_t \sigma_\nu)^2}. \tag{A4}$$

The reverse relation can simply be obtained from the symmetry by swapping $w \leftrightarrow \sigma$ and $\nu \leftrightarrow t$.

A third form that was not used in this study but is commonly used in statistics and referred to as bivariate normal distribution takes the form

$$\mathcal{G}(t, \nu) = A \exp\left[-\frac{1}{(1-\rho^2)}\left(\frac{(t-t_0)^2}{2w_t^2} - \rho\frac{(t-t_0)(\nu-\nu_0)}{w_t \sigma_\nu} + \frac{(\nu-\nu_0)^2}{2\sigma_\nu^2}\right)\right], \tag{A5}$$

with $-1 < \rho < 1$. It is related to the other forms via

$$\rho = d_t \frac{\sigma_\nu}{w_t}, \quad \rho = d_\nu \frac{w_t}{\sigma_\nu} \tag{A6}$$

and equation (A4). ρ describes the tilt of the Gaussian in units of w_t and σ_ν, which seems to have no useful physical interpretation in the case of FRBs. However, it might be useful for fitting as the parameters could be less correlated.

A fourth form is the Gaussian that is rotated by an angle θ and was used in earlier studies. Its parameters have no physical meaning, and we recommend using one of the other three forms instead. Results from previous studies that used the rotated form can be converted as follows. The rotated Gaussian is given with respect to the general form by

$$a = \frac{\cos^2\theta}{2\sigma_x^2} + \frac{\sin^2\theta}{2\sigma_y^2}, \tag{A7}$$

$$2b = -\frac{\sin(2\theta)}{2\sigma_x^2} + \frac{\sin(2\theta)}{2\sigma_y^2}, \quad \text{and} \tag{A8}$$

$$c = \frac{\sin^2\theta}{2\sigma_x^2} + \frac{\cos^2\theta}{2\sigma_y^2}. \tag{A9}$$

Note how these equations are already in conflict with σ_x and σ_y having different units. Ignoring these violations of mathematical rules this form can be set equal to equation (A5) and after some time one can obtain

$$\rho = \frac{k \sin(2\theta)/2}{\sqrt{1 + (k \sin(2\theta)/2)^2}}, \quad \text{with} \quad k = \frac{\sigma_x}{\sigma_y} - \frac{\sigma_y}{\sigma_x}, \tag{A10}$$

$$w_t = \sigma_x \sigma_y \sqrt{\frac{1 + (k \sin(2\theta)/2)^2}{\sigma_x^2 \sin^2\theta + \sigma_y^2 \cos^2\theta}}, \tag{A11}$$

$$\sigma_\nu = \sigma_x \sigma_y \sqrt{\frac{1 + (k \sin(2\theta)/2)^2}{\sigma_x^2 \cos^2\theta + \sigma_y^2 \sin^2\theta}}, \tag{A12}$$

or reversely

$$\tan(2\theta) = \frac{2\rho}{w_t \sigma_v (\sigma_v^{-2} - w_t^{-2})} \quad \text{and} \tag{A13}$$

$$\sigma_x^2 = \frac{2(1-\rho^2) w_t \sigma_v}{\frac{\sigma_v}{w_t} + \frac{w_t}{\sigma_v} + \mathrm{sgn}(w_t^{-2} - \sigma_v^{-2})(w_t^2 \sigma_v^{-2} + w_t^{-2} \sigma_v^2 - 2 + 4\rho^2)^{1/2}}. \tag{A14}$$

APPENDIX B: DERIVATION OF δDM

Doing the full Taylor expansion of Δt yields

$$\Delta t = \sum_{n=0}^{\infty} \left. \frac{\Delta t^{(n)}(\nu)}{n!} \right|_{\nu=\nu_0} (\nu - \nu_0)^n \tag{B1}$$

$$= \Delta t(\nu_0) + \left. \frac{\mathrm{d}\Delta t}{\mathrm{d}\nu} \right|_{\nu=\nu_0} (\nu - \nu_0) + \mathcal{O}(\nu^2) \tag{B2}$$

$$= a\,\delta\mathrm{DM} \left(\frac{1}{\nu_0^2} - \frac{1}{\nu_{\mathrm{ref}}^2} \right) - 2a\,\delta\mathrm{DM} \frac{1}{\nu_0^3} (\nu - \nu_0) + \mathcal{O}(\nu^2). \tag{B3}$$

Dropping the first term as we only care about the shift with respect to ν_0 we get

$$\Delta t \approx -2a\,\delta\mathrm{DM} \frac{1}{\nu_0^3} (\nu - \nu_0). \tag{B4}$$

APPENDIX C: SUPPLEMENTARY MATERIAL

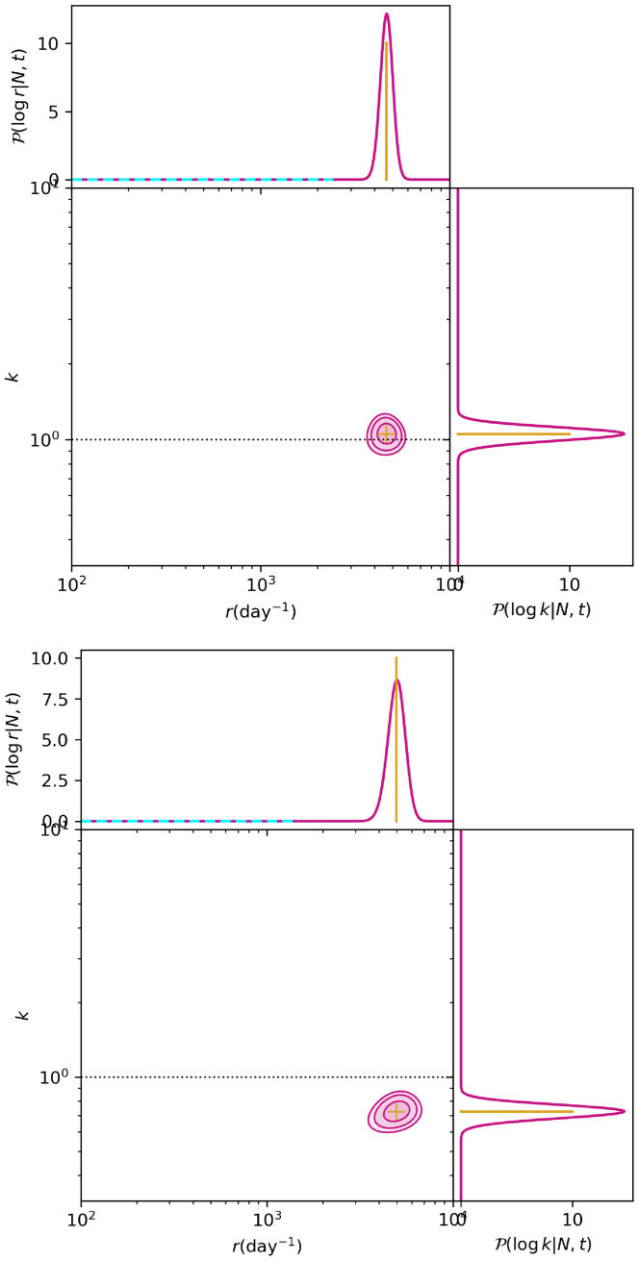

Figure C1. Posterior distribution for the Weibull parameters in the observation on MJD 58435 for all bursts (bottom plot) and for burst packs where we averaged over the arrival times of bursts that arrived within $\delta < 0.1$ s (top plot). In the latter case where wait times $\delta < 0.1$ s are excluded the arrival times are consistent with a Poisson distribution ($k = 1$).

Table C1. The first 10 lines of the data table that is available as supplementary material. The times of arrival are barycentre corrected and dispersion corrected to infinite frequency using the dispersion constant $a = 4.1488064239(11)$ GHz^2 cm^3 pc^{-1} ms (Kulkarni 2020).

ID	Sub-burst	TOA/MJD	A	d (ms MHz^{-1})	t_0 (s)	σ_t (ms)	ν_0 (MHz)	σ_ν (MHz)	Scaled energy (erg)
A1	sb1	58409.3564972816	0.64(30)	− 0.0048(34)	548.9640(4)	0.66(30)	1430(63)	132(65)	7.76×10^{37}
A2	sb1	58409.3643956201	0.56(38)	− 0.0053(82)	1231.3234(11)	0.63(44)	1700(185)	107(151)	3.90×10^{37}
A3	sb1	58409.3708097451	0.15(31)	− 0.0044(103)	1785.4575(21)	0.52(104)	1577(416)	162(470)	2.37×10^{37}
A4	sb1	58409.3708099014	0.17(28)	0.0125(465)	1785.4710(38)	1.26(212)	1687(244)	82(235)	2.55×10^{37}
A5	sb1	58409.3765544552	0.63(80)	− 0.0007(90)	2281.7590(10)	0.64(68)	1741(548)	146(344)	8.56×10^{35}
A5	sb2	58409.3765544853	0.54(102)	− 0.0008(97)	2281.7616(18)	0.86(120)	1778(961)	200(520)	1.37×10^{36}
A5	sb3	58409.3765544864	82.55(1558104)	− 0.0016(76)	2281.7617(846)	0.47(64)	3061(52502)	436(7972)	2.47×10^{38}
A5	sb4	58409.3765545378	1.06(161)	− 0.0045(37)	2281.7662(39)	0.76(35)	1828(845)	250(411)	2.96×10^{36}
B6	sb1	58432.2646080422	0.14(40)	0.0074(676)	13.7812(114)	1.71(506)	1187(1319)	148(960)	4.49×10^{37}
B6	sb2	58432.2646081021	0.18(57)	0.0015(145)	13.7863(21)	0.56(191)	1317(764)	183(805)	2.39×10^{37}

$\mathrm{TOA_{1D}}$ (MJD)	A_{1D}	$t_{0,1D}$ (s)	$\sigma_{t,1D}$ (ms)	$\nu_{0,1D}$ (MHz)	$\sigma_{\nu,1D}$ (MHz)
58409.356497281	4.54(27)	548.96394(6)	0.912(64)	1429(7)	122(7)
58409.3643956236	2.76(29)	1231.32370(9)	0.752(90)	1688(14)	90(13)
58409.3708097508	0.96(27)	1785.45799(39)	1.217(394)	1972(964)	369(409)
58409.3708099035	1.10(21)	1785.47119(33)	1.543(335)	2237(2297)	477(774)
58409.3765544568	3.99(33)	2281.75916(7)	0.637(75)	1763(52)	158(29)
58409.3765544868	3.82(32)	2281.76175(9)	0.809(127)	1863(128)	229(55)
58409.3765545116	3.42(38)	2281.76389(8)	0.501(84)		
58409.3765545488	6.07(26)	2281.76711(5)	1.020(54)	1741(38)	215(23)
58432.2646080413				1059(308)	227(142)
58432.2646081035				1310(16)	157(18)

Class	Diffuse/tail	Dropouts	Fluence (Jy ms)	Downsampling	t_{fit} (ms)
Default	False	False	0.1412	8	5
Default	False	False	0.0709	8	5
Default	False		0.0432	8	5
Default	False	False	0.0465	8	5
Multi	False	False	0.4578	8	5
Multi	False	False	0.4578	8	5
Multi	False	False	0.4578	8	5
Multi	False	False	0.4578	8	5
Multi	False	False	0.6717	8	5
Multi	False	False	0.6717	8	5

Table C2. Some of the burst properties derived throughout the paper. The full table is available as supplementary material. The TOA is averaged over sub-burst TOAs. Time and frequency envelopes and ν_{cent} are explained in Section 4.2 and shown in Fig. 4, values are missing if the fits were not successful. The fluence was measured using a frequency and zenith-angle-dependent SEFD, as described in Section 3. The scaled energy is the isotropic equivalent energy that is scaled from the fluence and the 2D Gaussian fits via equation (7), it is only present for bursts where the 2D fits had reasonable uncertainties. The average specific luminosity is derived in Section 4.4.

Observation	ID	TOA (MJD)	Time envelope (ms)	Frequency envelope (MHz)	ν_{cent} (MHz)	Fluence (Jy ms)	Scaled energy (erg)	Specific luminosity (erg ms^{-1} MHz^{-1})	Search ID
58409	A1	58409.3564972816	2.13	310	1430	0.141	7.58×10^{37}	1.37×10^{35}	2798
58409	A2	58409.3643956201	1.77	213	1688	0.071	4.93×10^{37}	1.56×10^{35}	2857
58409	A3	58409.3708097451				0.043			3995-1
58409	A4	58409.3708099014				0.046			3995
58409	A5	58409.3765545122	9.90	644	1789	0.458			57
58432	B6	58432.2646081847	9.51	309	1304	0.672	3.86×10^{38}	1.56×10^{35}	5095
58432	B7	58432.2647338737	2.56	182	1704	0.043			7732
58432	B8	58432.2650200047	3.12	272	1417	0.050	2.64×10^{37}	3.72×10^{34}	8343
58432	B9	58432.2652493147	18.97	517	1500	0.198	1.10×10^{38}	1.34×10^{34}	7500
58432	B10	58432.2652784695	2.11	636	1448	0.051	3.63×10^{37}	3.22×10^{34}	7963

This paper has been typeset from a TEX/LATEX file prepared by the author.

APPENDIX B

How limiting is optical follow-up for fast radio burst applications? Forecasts for radio and optical surveys

Monthly Notices of the ROYAL ASTRONOMICAL SOCIETY

MNRAS **523,** 5006–5023 (2023) https://doi.org/10.1093/mnras/stad1659
Advance Access publication 2023 June 13

How limiting is optical follow-up for fast radio burst applications? Forecasts for radio and optical surveys

Joscha N. Jahns-Schindler [1]★ Laura G. Spitler [1] Charles R. H. Walker[1] and Carlton M. Baugh [2]

[1]*Max-Planck-Institut für Radioastronomie, Auf dem Hügel 69, D-53121 Bonn, Germany*
[2]*Institute for Computational Cosmology, Department of Physics, Science Laboratories, Durham University, South Road, Durham, DH1 3LE, UK*

Accepted 2023 May 28. Received 2023 May 24; in original form 2023 March 3

ABSTRACT

Fast radio bursts (FRBs) are the first cosmological radio sources that vary on millisecond time-scales, which makes them a unique probe of the Universe. Many proposed applications of FRBs require associated redshifts. These can only be obtained by localizing FRBs to their host galaxies and subsequently measuring their redshifts. Upcoming FRB surveys will provide arcsecond localization for many FRBs, not all of which can be followed up with dedicated optical observations. We aim to estimate the fraction of FRB hosts that will be catalogued with redshifts by existing and future optical surveys. We use the population synthesis code FRBPOPPY to simulate several FRB surveys, and the semi-analytical galaxy formation code GALFORM to simulate their host galaxies. We obtain redshift distributions for the simulated FRBs and the fraction with host galaxies in a survey. Depending on whether FRBs follow the cosmic star formation rate or stellar mass, 20–40 per cent of CHIME FRB hosts will be observed in an SDSS-like survey, all at $z < 0.5$. The deeper DELVE survey will detect 63–85 per cent of ASKAP FRBs found in its coherent search mode. CHIME FRBs will reach $z \sim 3$, SKA1-Mid FRBs $z \sim 5$, but ground based follow-up is limited to $z \lesssim 1.5$. We discuss the consequences for several FRB applications. If ∼1/2 of ASKAP FRBs have measured redshifts, 1000 detected FRBs can be used to constrain $\Omega_b h_{70}$ to within ∼10 per cent at 95 per cent credibility. We provide strategies for optimized follow-up, when building on data from existing surveys. Data and codes are made available.

Key words: cosmological parameters – large-scale structure of Universe – software: simulations – fast radio bursts.

1 INTRODUCTION

Fast Radio Bursts (FRBs) are flashes of radio light coming from distant galaxies. They are a relatively new class of transients (Lorimer et al. 2007) that have so far been observed at frequencies between 110 MHz (Pleunis et al. 2021a) and 8 GHz (Gajjar et al. 2018). Currently, 4 per cent of FRBs have been observed to emit more than once and are therefore classified as repeaters (Spitler et al. 2016; CHIME/FRB Collaboration et al. 2019). The larger sample of CHIME/FRB Collaboration et al. (2021) at 600 MHz suggest that repeaters and non-repeaters do indeed have different statistical properties (Pleunis et al. 2021b). Nevertheless, the source and emission mechanisms are still puzzling (see Lyubarsky 2021; Petroff, Hessels & Lorimer 2022, for recent reviews), although the recent detections of an FRB-like burst from the galactic source SGR 1935+2154 (Bochenek et al. 2020; Chime/Frb Collaboration et al. 2020; Dong & Chime/Frb Collaboration 2022) support a connection to magnetars.

Even if their origins remain unclear, FRBs can be used as astrophysical tools in numerous ways. For many applications, the most important quantity that can be measured is the dispersion measure (DM). It is caused by all the free (non-relativistic) electrons along the path between source and observer and manifests as a frequency dependent dispersive delay ($\Delta t \propto \mathrm{DM}\,\nu^{-2}$). As a result, FRBs have been proposed as tools for finding the 'missing' baryons (McQuinn 2014; Prochaska & Zheng 2019; Walters et al. 2019); locating the baryonic matter in the intergalactic medium (IGM), around galaxies, and specifically the Milky Way (Keating & Pen 2020; Platts, Prochaska & Law 2020); measuring cosmological parameters (Gao, Li & Zhang 2014; Zhou et al. 2014); observing the reionization epochs of H and He II (Deng & Zhang 2014; Zheng et al. 2014; Bhattacharya, Kumar & Linder 2021); measuring intergalactic magnetic fields (Akahori, Ryu & Gaensler 2016; Vazza et al. 2018; Hackstein et al. 2019); constraining the abundance of massive compact halo objects (Zheng et al. 2014; Muñoz et al. 2016; Kader et al. 2022; Leung et al. 2022); testing Einstein's equivalence principle (Wei et al. 2015; Nusser 2016; Minazzoli et al. 2019; Reischke et al. 2022); constraining the photon mass (Bonetti et al. 2016; Wu et al. 2016); and others, in particular various applications in the case of strongly lensed (repeating) FRBs (Li et al. 2018; Zitrin & Eichler 2018; Wagner, Liesenborgs & Eichler 2019; Wucknitz, Spitler & Pen 2021).

Many of these applications require or benefit from knowledge of the FRBs' redshifts. For example, the baryons in the IGM are detected via their contribution to the DM ($\mathrm{DM_{IGM}}$) (Ginzburg 1973). On average, it increases with distance, which means that the redshift z is needed as a second distance estimate to determine the baryon density (McQuinn 2014). Likewise, a hypothetical photon mass produces a delay that increases with light-travel-time and therefore redshift (see e.g. Wei & Wu 2020). Cosmological parameters influence the shape of $\langle \mathrm{DM_{IGM}} \rangle(z)$, again requiring z to be measured, although the large

★ E-mail: jjahns@mpifr-bonn.mpg.de

DM scatter makes it difficult for this application to compete with other cosmological probes (Walters et al. 2018; Jaroszynski 2019). The epoch of H reionization is expected to cause $\langle \mathrm{DM_{IGM}} \rangle(z)$ to plateau around $z \sim 6$. The real redshift location can most directly be found through the DM and redshift of high-z FRBs (e.g. Beniamini et al. 2021). In addition to these direct applications, localized FRBs also help to learn more about their local environments, and thus, their potential progenitors (Heintz et al. 2020; Bhandari et al. 2022). In summary, localizations and redshift measurements of FRBs are crucial for unpacking the full potential of FRBs.

To *localize* an FRB, its location needs to be known with arcsecond precision (Eftekhari & Berger 2017). Only then can the host galaxy be identified in optical or infrared images below per cent level chance coincidence. Once the host galaxy is known, its redshift can be measured using spectroscopy. A localization via interferometric follow-up observations is possible for FRBs that repeat frequently (e.g. Chatterjee et al. 2017; Marcote et al. 2020). Most FRBs, however, have not yet been seen to repeat. These can only be localized upon discovery, and only if the discovering instrument is an interferometer (and if the FRB has sufficient signal to noise). Current instruments that localize FRBs on a regular basis are the Australian SKA Pathfinder (ASKAP), Deep Synoptic Array-110 (DSA-110), and MeerKAT.

Upcoming surveys will – possibly as soon as 2023 – yield more than a 100 localizations per year. At the time of publication, there are only 27 localized FRBs (see e.g. Bhandari et al. 2022). These localizations were obtained over the last 3 years, and are dominated by ASKAP. However, this number will grow rapidly in the near future as several instrumental updates are currently carried out. DSA-110 (Kocz et al. 2019) is currently under commission and already located a few FRBs (Ravi et al. 2023). ASKAP's CRAFT coherent upgrade (CRACO; James et al. 2022c) is being carried out, which will allow searching in the image plane to yield a boost to ∼100 FRBs per year from ASKAP alone. It is expected to be operational within 2023. The Canadian Hydrogen Intensity Mapping Experiment (CHIME) outriggers are under construction and will provide very-long-baseline interferometry localization of nearly all the ∼500 FRBs per year that CHIME detects (CHIME/FRB Collaboration et al. 2021). These outriggers will likely become operational within 2023 (Vanderlinde et al. 2019). On time-scales of a few years, additional instruments will be built that are capable of localizing similar numbers of FRBs upon discovery. Among these are HIRAX (Crichton et al. 2022), GReX (Connor et al. 2021), BURSTT (Lin et al. 2022), CHORD (Vanderlinde et al. 2019), DSA-2000 (Hallinan et al. 2019), PUMA (Cosmic Visions 21-cm Collaboration et al. 2018), the square kilometre array (SKA Dewdney et al. 2009), and ngVLA (Law et al. 2018).

With this many FRBs with arcsecond positions available, the most likely bottleneck to comprehensive cosmological analyses will be optical follow-up observations that provide host galaxy identification and redshift measurements. It will be impossible to dedicate the same amount of observing time for each FRB as is currently allocated (Simha et al. 2020; Chittidi et al. 2021, e.g. together invested 4.4 h of optical follow-up on one FRB). The available time and the follow-up strategy will influence the number of FRBs with known redshift and their redshift distribution. Taking the effect of limited observing time into account in a forecast is difficult, as the available telescope time is unknown. Therefore, previous forecasts of FRB applications have only considered a localized FRB population with simplified redshift distributions. These included FRBs at a fixed redshift, following cosmic distributions like the star formation history, or observed distributions of other sources like supernovae or gamma-ray bursts, and recently the simulation of a realistic distribution for ASKAP/CRACO (James et al. 2022c). In this work, we want to, for the first time, consider the effects of limited optical follow-up. Thus, we estimate the fraction of future FRBs whose host galaxies will already be contained in optical catalogues and, conversely, the fraction that will need dedicated follow-up observations with optical telescopes.

We first describe the simulations and parameters used to create our synthetic FRB population in Section 2. In Section 3, we present the resulting redshift distributions for our simulated FRBs, comparing different underlying radio surveys and simulating the effects of redshift distributions on FRB constraints of the cosmic baryon budget. In Section 5, we develop an optimized follow-up strategy, before we discuss limitations of and prospects for our approach in Section 6. We conclude in Section 7.

2 SURVEY SIMULATIONS

The goal in this section is to generate realistic redshift distributions for future observed FRBs and to compute the fraction of them that have identified host galaxies. We do this in two steps, which we summarize here. In the first step, we simulate FRBs using the population synthesis code FRBPOPPY.[1] It applies telescope and survey selection criteria to a cosmic FRB population and returns the properties of any observed FRBs. In this way, we generate mock catalogues for ASKAP, CHIME, and SKA1-Mid. In the second step, we draw a host galaxy for each FRB from a data base of simulated galaxies created using the GALFORM semi-analytical galaxy formation code. This data base contains the magnitudes of galaxies in the passbands for a number of relevant optical surveys. We use these magnitudes to ascertain whether the host galaxies could be observed in the following four large surveys: the Sloan Digital Sky Survey (SDSS), the DECam Local Volume Exploration survey (DELVE), the Euclid-wide survey, or the Vera C. Rubin Observatory's Legacy Survey of Space and Time (LSST). We repeat this process for each of our selected radio telescopes and for different cosmic FRB distributions. For each radio telescope and distribution, we simulate 1000 observed FRBs. Different telescope detection rates could be used to scale the numbers relative to each other to generate realistic detection ratios between telescopes, but this is left for more application specific forecasts. In this section, we describe the above codes in more detail and discuss the chosen cosmic probability distributions.

2.1 Simulation of FRBs with FRBPOPPY

The FRBPOPPY PYTHON package is designed to synthesize FRB populations (Gardenier et al. 2019; Gardenier et al. 2021). It is meant to be used to infer the intrinsic FRB properties, but it is also well suited for our forecasts. The software synthesizes an FRB population in two steps. First, a cosmic population of FRBs is created from intrinsic properties specified by the user, such as the cosmological number density of sources and their luminosity distribution, spectral index, emission range, and pulse widths. Second, a telescope and survey is modelled and used to 'observe' the FRBs. This step requires accurate modelling of telescope parameters, including gain, system temperature, beam pattern, and more. Below, we describe and justify our choices of parameters. For the reader's convenience, values that are used for all surveys are collected in Table 1, and values that

[1] https://github.com/davidgardenier/frbpoppy

Table 1. Parameters used in FRBPOPPY.

Parameter	Value	Reference
$\nu_{\rm low}$	100 MHz	non-restrictive
$\nu_{\rm high}$	50 GHz	"
α	−0.65	James et al. (2022b)
$L_{\rm bol,max}$	3.89×10^{44} erg s^{-1}	"
$L_{\rm bol,index}$	−1.05	"
μ_w	5.49 ms	James et al. (2022a)
σ_w	2.46	"

change between our chosen telescopes, or redshift distributions, are contained in Table 2.

We adopt the cosmological parameters from Planck Collaboration et al. (2020). For the cosmological FRB number density, we use all three of the models provided by FRBPOPPY. These models are as follows: in the first, the number density follows the redshift evolution of the star formation rate (SFR), in the second, it follows the stellar mass density (SMD), and the third is a toy model, where the number density is constant in the comoving coordinate system. Which of the first two models above is correct (or if it is a mix) is still under debate. Zhang & Zhang (2022), Qiang, Li & Wei (2022), and Hashimoto et al. (2022) use different statistical tests and find that the SMD is favoured. However, James et al. (2022b) are the only ones that allow for a frequency dependent rate, and they find that the distribution is still consistent with following the SFR. For the FRB luminosity function, we use the power law provided by FRBPOPPY but the index ($L_{\rm bol,index}$) and range that was found by James et al. (2022b). We adopt the log-normal model for the pulse widths from the default population in Gardenier et al. (2019), with median $\mu_{\rm w} = 5.49$ ms and $\sigma_{\rm w} = 2.46$ (James et al. 2022a).

The spectral index is one of the most uncertain properties of FRBs. James et al. (2022b) and Shin et al. (2023) both infer FRB population parameters under the two interpretations that α is a spectral index, or it expresses how the cosmic rate changes with frequency. From the many bursts with limited bandwidth found by CHIME/FRB Collaboration et al. (2021), it appears that narrow-band FRBs dominate the population; thus, we lean towards the rate interpretation. We use the index $\alpha = -0.65$ that James et al. (2022b) derived under this interpretation from the results of Macquart et al. (2019). This value is also well within the uncertainties of α derived by Shin et al. (2023) for both interpretations ($-1.39^{+0.86}_{-1.19}$ and $-1.10^{+0.67}_{-0.99}$ for the spectral index and the rate interpretation, respectively).

To calculate the luminosity distribution of our FRB population, we convert the maximum energies inferred by James et al. (2022b) and Shin et al. (2023). The two studies give the maximum energy $E_{\rm max}$ in a 1 GHz band at 1.3 GHz and 600 MHz, respectively. From the data at 1.3 GHz, one can calculate the specific luminosity at frequency ν,

$$L_\nu = \frac{E_{\rm max}}{\Delta\nu\,\Delta t}\left(\frac{\nu}{1.3\,{\rm GHz}}\right)^{\alpha}, \tag{1}$$

where $\Delta\nu = 1$ GHz is the frequency bandwidth, and Δt is a characteristic width of the burst sample. For the ASKAP and Parkes FRB sample of James et al. (2022b), we use the median width $\Delta t = 2.67$ ms reported by Arcus et al. (2021), and subsequently obtain $L_{1.3\,\rm GHz} = 10^{35.45^{+0.24}_{-0.48}}$ erg s^{-1} Hz^{-1}. This is in agreement with Shin et al. (2023), whose result is equivalent to $L_{1.3\,\rm GHz} = 10^{35.07^{+0.47}_{-0.46}}$ erg s^{-1} Hz^{-1} (68 per cent confidence limits in both cases). Finally, we calculate the bolometric luminosity

$$L_{\rm bol} = \left(\frac{\nu_{\rm high}}{1.3\,{\rm GHz}}^{1+\alpha} - \frac{\nu_{\rm low}}{1.3\,{\rm GHz}}^{1+\alpha}\right) L_{1.3\,\rm GHz}, \tag{2}$$

where we use $\nu_{\rm low} = 100$ MHz and $\nu_{\rm high} = 50$ GHz, to ensure that the emission frequency is not a limiting factor for any of the telescopes.

There are a number of parameters that we do not use here because we simulate a fixed number of FRBs for each survey. These include the sky position and absolute rates. We simulate the DM separately in Section 4. We neglect scattering in this study for two reasons. First, scattering from the host galaxy and Milky Way depends only weakly on the redshift (through a redshift dependent SFR). Second, the probability that an FRB will intersect a galaxy is very low (Prochaska & Neeleman 2018), while the contribution from intervening galaxy haloes to scattering is very uncertain (see e.g. the discussion in Ocker et al. 2022).

We generally use telescope parameters as tabulated in FRBPOPPY (table 2 of Gardenier et al. 2021), with the exception of ASKAP/CRACO. The ASKAP FRB sample will be dominated by the CRACO upgrade as soon as operations begin. As it is not yet implemented in FRBPOPPY, we use the incoherent survey parameters, but multiply the gain by 4.4 and decrease the bandwidth to 288 MHz, as anticipated by James et al. (2022c). Fig. 1 shows the intrinsic and observed distributions of several parameters for ASKAP/CRACO, as an example.

Table 2. Parameters used in FRBPOPPY that differ by survey. $z_{\rm max}$ and $L_{\rm bol,\,min}$ are chosen as large and as low as possible, respectively, while still having an observable number of FRBs.

Survey	Survey model	Beam model	z model	$z_{\rm max}$	$L_{\rm bol,min}$
ASKAP/ICS	`askap-incoh`	Gaussian	SFR	1.2	2×10^{40}
			SMD	1.2	8×10^{39}
			$V_{\rm C}$	1.2	5×10^{39}
ASKAP/CRACO	`askap-incoh`[a]	Gaussian	SFR	2.5	8×10^{39}
			SMD	1.8	2×10^{39}
			$V_{\rm C}$	2.0	3×10^{39}
CHIME/FRB	`chime-frb`	`chime-frb`	SFR	3.5	1×10^{41}
			SMD	2.2	1×10^{40}
			$V_{\rm C}$	2.8	3×10^{40}
SKA-Mid	`ska-mid`	Gaussian	SFR	6.0	3×10^{37}
			SMD	5.0	4×10^{36}
			$V_{\rm C}$	6.0	3×10^{37}

Note. [a]The gain was multiplied by 4.4 and the bandwidth reduced to 288 MHz.

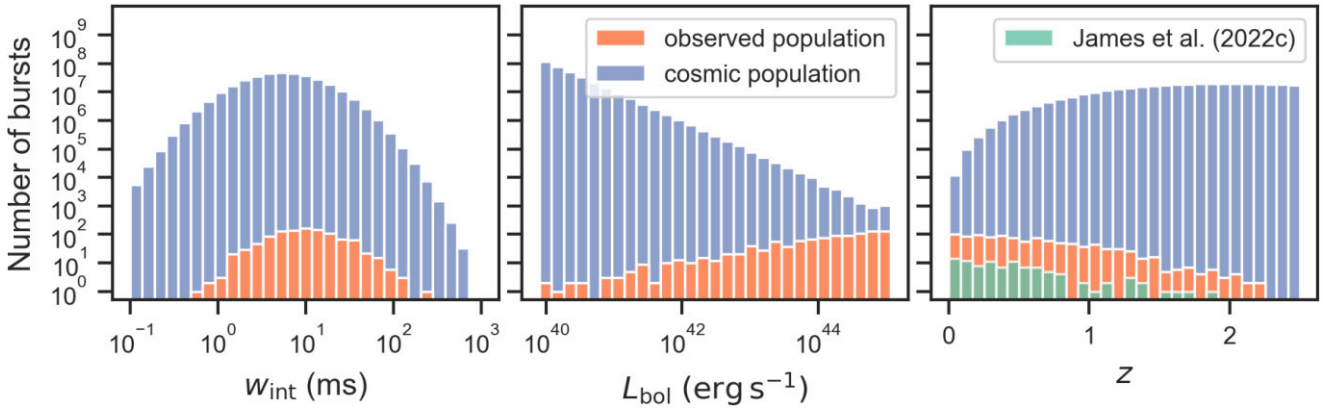

Figure 1. The intrinsic and observed distributions of burst width, luminosity, and redshift that we simulated for ASKAP with the CRACO pipeline. In this example, the FRB population followed the comic star formation rate (SFR). The FRBs simulated in James et al. (2022c) for the same pipeline are shown for comparison. It is apparent in the middle panel how important the maximum luminosity is for the redshift distribution. Even if the luminosity follows a power law that goes down towards high luminosities, the observed distribution does the opposite, and a large fraction of high-luminosity FRBs in the field of view are observed.

2.2 Host galaxies generated with GALFORM

GALFORM is a semi-analytic model of galaxy formation (Cole et al. 2000). The goal of semi-analytic models is to understand the physical processes that govern galaxy formation and evolution. The modelling includes 14 different physical processes, such as feedback from supernovae and active galactic nuclei (Lacey et al. 2016). The gravitational conditions are given by the halo merger tree, in which the baryonic physics is implemented. This is taken from dark matter only N-body simulations; in the case of the GALFORM version used here, the P-Millennium simulation was used (Baugh et al. 2019). The main advantage of semi-analytical models over full hydrodynamical simulations is their speed, which allows the comparison of model galaxies drawn from large numbers of halo merger histories over a wide dynamic range in mass to observed galaxies.

Here, we use the GALFORM version from Lacey et al. (2016), as recalibrated in Baugh et al. (2019). This model includes a detailed treatment of dust absorption, which allows it to produce realistic predictions for the flux from model galaxies in the optical and near infrared. Most importantly for us, the optical filters of several telescopes (e.g. SDSS, DECam, Euclid) are applied to generate the model galaxy magnitudes in different bands. These magnitudes include the effects of extinction in the host galaxy and are in the observer's reference frame, i.e. they consider the redshifting of the spectrum relative to the filter. GALFORM tracks quiescent star formation in galactic discs and bursts of star formation triggered by mergers or the motion of gas in dynamically unstable discs. In the model used here, bursts are assumed to take place with a top-heavy stellar initial mass function (IMF), whereas a solar neighbourhood IMF is adopted for star formation in discs. The model tracks the star formation and mass assembly in a disc and bulge component for each galaxy. Different bulge-to-disc ratios can be associated with different morphological types. Apart from the magnitudes, we only need the stellar mass and SFR to randomly draw host galaxies from the population, consistent with their cosmic number density.

Twelve snapshots from the simulation were used between redshifts 0 and 6.011. The P-Millennium is a $540/h$ Mpc box. The model output we used corresponds to a random sampling of merger trees from this volume at the rate of 1/1024. The snapshot redshifts and the number of galaxies contained in them are listed in Table 3.

Table 3. GALFORM snapshots that the host galaxies are drawn from.

Snapshot	Redshift	Number of galaxies
0	0.0	182 711
1	0.249	192 040
2	0.496	201 698
3	0.757	212 338
4	1.007	221 551
5	1.496	238 861
6	2.002	254 227
7	2.51	251 020
8	3.046	233 644
9	3.534	212 626
10	4.008	190 478
11	6.011	95 180

We draw a host galaxy for each FRB from the snapshot that is closest to the FRB in redshift space. We draw these galaxies weighted either by their stellar mass or SFR, choosing the same model that was used for the redshift distribution of FRBs. For the redshift distribution following $V_{\rm C}$, we chose the stellar mass.

2.3 Detections in optical surveys

We wish to assess what fraction of our simulated observed FRBs will have a host galaxy catalogued in one of the surveys: SDSS, DELVE, Euclid wide, or LSST. The reason is that this is the fraction of FRBs for which we will get the photometric redshift (photo-z) 'for free' without needing dedicated follow-up. In this analysis, we will concentrate on photo-zs. This is because the more precise spectroscopic redshifts require much more observation time, resulting in spectroscopic surveys that are usually too shallow or too narrow to cover a significant fraction of FRB hosts. Furthermore, a dedicated spectroscopic measurement requires previous detection and identification of the host galaxy. Hence, if one requires spectroscopic redshifts for a given method, photometric detection is still the necessary first step.

Table 4. Optical surveys and their overlaps with FRB surveys.

Survey	Filter	Magnitude limits [f]	Sky area (deg^2)	Restrictions [g]	Sky overlap with ASKAP/SKA ($\delta < 48°$) (per cent)	Sky overlap with CHIME ($\delta > -10°$) (per cent)
SDSS [a]	u, g, r, i, z	22.0, 22.2, 22.2, 21.3, 20.5	14555		$\lesssim$30	∼50
LSST [b]	u, g, r, i, z, y	26.1, 27.4, 27.5, 26.8, 26.1, 24.9	18000	$5° > \delta > -65°$	>50	∼5.5
Euclid wide survey [c]	I, Y, J, H	26.2, 24.5, 24.5, 24.5	15000	$\lvert\beta\rvert > 10°$, $\lvert b\rvert > 23°$	>35	$\lesssim$35
DELVE (DR2) [d]	g, r, i, z	24.3, 23.9, 23.5, 22.8	17000	$\lvert b\rvert > 10°$, $\delta < 30°$	∼50	<25
Pan-STARRS1 survey [e]	g, r, i, z, y	23.3, 23.2, 23.1, 22.3, 21.3	31000	$\delta > -30°$	<70	100

Notes. [a]Abazajian et al. (2009), Alam et al. (2015), https://www.sdss4.org/dr17/scope
[b]Ivezić et al. (2019), https://www.lsst.org/scientists/keynumbers
[c]Euclid Collaboration et al. (2022), https://sci.esa.int/web/euclid/-/euclid-nisp-instrument
[d]DECam Local Volume Exploration survey; Drlica-Wagner et al. (2022).
[e]The Panoramic Survey Telescope and Rapid Response System (Pan-STARRS) is not included in our simulations; Chambers et al. (2016).
[f]SDSS: 95 per cent completeness for point sources. LSST: 5σ point source depth for stationary sources after 10 years. Euclid: 5σ point source depth. The DELVE and Pan-STARRS1 survey have inhomogeneous coverage, thus denoted magnitudes are the median and mean 5σ point-source depth, respectively.
[g]δ denotes the declination, b the Galactic latitude, and β the ecliptic latitude.

Photo-zs are only an estimate of the true redshift. For LSST, the target photo-z precision[2] is $\sigma_z < 0.02(1+z)$. The uncertainty is generally redshift dependent (see e.g. Graham et al. 2020), and catastrophic outliers – substantially inaccurate redshift estimates – are also possible. Such catastrophic outliers could possibly be identified by a mismatch between photo-z and DM, although, care has to be taken to not bias the science that is done with the exact same relation. For simplicity, we will assume in this analysis that the uncertainty can be absorbed into other larger uncertainties, like the uncertain host galaxy DM ($\mathrm{DM_{host}}$), and the scatter in $\mathrm{DM_{IGM}}$ that comes from the large-scale structure and intervening galaxy haloes. In a way, we regard spectroscopic redshifts as a bonus that would improve precision. As a motivation, we can compare σ_z to the scatter in $\mathrm{DM_{host}}$. If we assume $\mathrm{DM_{host}}$ has a log-normal probability with a median of $\mathrm{DM_0} = 100\,\mathrm{cm^{-3}\,pc}$ and width parameter $\sigma_{\mathrm{host}} = 1$, the relative uncertainty of σ_z would be 40 per cent of $\mathrm{DM_{host}}$ at $z = 1$ and equal to the standard deviation of $\mathrm{DM_{host}}$ around $z = 2$. Here, we approximated $\langle \mathrm{DM_{IGM}} \rangle \approx 1000\,\mathrm{cm^{-3}\,pc} \cdot z$ and used the standard deviation of the log-normal distribution $\mathrm{DM_0}\sqrt{\exp\left(2\sigma^2_{\mathrm{host}}\right) - \exp\left(\sigma^2_{\mathrm{host}}\right)}$.

In order to assess the visibility in optical surveys, the absolute magnitudes $M_{\mathrm{G}} = M - 5\log(h)$ that GALFORM provides (in the observer frame and including extinction) need to be converted to the apparent magnitudes m, as would be observed from Earth. This is done via

$$m = M_{\mathrm{G}} + 5\log(h) - 2.5\log(1+z) + 5\log(D_L(z)/10\,\mathrm{pc}), \qquad (3)$$

where h is the dimensionless Hubble constant and D_{L} the luminosity distance. Note that M is already in the observer frame, and the $-2.5\log(1+z)$ term is a band shift term from the magnitude definition used in GALFORM. The apparent magnitudes are then compared to the survey limits of the numerous bands listed in Table 4.

We assume that a redshift can be obtained if a galaxy is visible in all bands. We confirmed this simple approach for SDSS by comparing it to the more sophisticated requirements of Beck et al. (2016). We found that almost no galaxies are excluded by the additional requirements. Another reason to refrain from using a specific algorithm to compute photo-zs from the simulated magnitudes is the large number of available algorithms that have been developed for LSST (see e.g. Schmidt et al. 2020).

[2]LSST Science Requirements Document available at https://docushare.lsstcorp.org/docushare/dsweb/Get/LPM-17

2.4 Survey overlaps

We chose the four optical surveys by availability in GALFORM and relevance to FRB surveys. SDSS represents a well-established survey with significant legacy data. Situated in the Northern Hemisphere, it is most relevant to CHIME. The Pan-STARRS1 survey, which covers almost the entire Northern Sky, was not available in the simulation. Its depth is reported as the mean depth, differently from SDSS, and it has one filter that is different, but taking these differences into account, the depth is roughly similar to SDSS. The SDSS results are therefore also applicable to Pan-STARRS1, and we refrain from simulating the Pan-STARRS bands additionally to the SDSS bands.

DELVE represents a newer, ongoing survey that is slightly deeper. It covers large parts of the Southern Hemisphere and is therefore most relevant to telescopes like ASKAP and MeerKAT. With LSST, we consider a wide and deep survey that represents the best that will be available in the foreseeable future. As the full survey will only be complete in 10 years (although with yearly data releases), we mainly present LSST with our future radio survey, SKA1-Mid.

In the following, we describe how we estimate the overlap between our FRB-searching radio surveys and host galaxy-identifying optical surveys, which we tabulate in Table 4. Optical surveys observe to equal depths within most of their footprint. Therefore, we frame our question as: what fraction of time will our FRB surveys spend within the footprints of our optical surveys?

Most FRB surveys piggyback on other radio surveys. These surveys are numerous in the case of ASKAP (and MeerKAT) and will only dictate their observing schedules in the near future. Our limited knowledge is best described by assuming isotropic coverage of the visible sky for ASKAP and SKA1-Mid. Following this assumption, we estimate the FRBs that will be within an optical survey by the fractional overlaps of the visible sky with the optical survey footprints.

The ASKAP telescope is located at a latitude of $-26.7°$ and can observe sources from declination $-90°$ to $48°$ (Hotan et al. 2021). Similarly, MeerKAT (and therefore the future SKA1-Mid), which is situated at latitude $-30.7°$, can observe up to declination $44°$ (Kapp 2016). DELVE is the combination of data from several surveys that were conducted with the Dark Energy Camera (DECam). The goal of

DELVE is to image the entire Southern Sky, except for the Galactic plane, in four bands, which would eventually yield ∼26 000 deg^2 coverage. The Vera C. Rubin Observatory is located at latitude −30.2°. Its main survey, the LSST, will cover about 18 000 deg^2 (Marshall et al. 2017) from −65° to about 5°, excluding the Galactic plane.

The CHIME telescope in the Northern Sky is a transit telescope with a declination dependent beam (CHIME/FRB Collaboration et al. 2021; Josephy et al. 2021). Since SDSS is also not homogeneous, we do the following estimate. We approximate the CHIME detection rate to be constant in declination at $\delta > 0°$ in rough agreement with the results of Josephy et al. (2021). For SDSS, we estimate the coverage from the footprint (Aihara et al. 2011) to be 3/4 at $\delta = 0°$–$40°$, 1/2 at $\delta = 40°$–$70°$, and 0 otherwise. We estimate about half of CHIME's FRBs to land in the SDSS footprint, yet, we note again that the other half is completely covered by Pan-STARRS1, which is of similar depth.

Euclid's survey area is equally distributed between Northern and Southern Sky, covering ∼35 per cent of the entire sky. It is therefore of interest to all FRB surveys. However, it targets $z \sim 1$ galaxies using one broad optical band (the *I*-band) and three infrared bands (Y, J, H). Spectral features that are important for photo-z determination remain in the same band over the full expected redshift range up to $z \sim 2$. The 4000 Å break, for example, will be in the *I*-band for all galaxies (see e.g. Section 5.5 of Euclid Collaboration et al. 2022). Euclid will therefore rely on photo-zs from optical, ground-based telescopes. Keeping this in mind, Euclid can still be interesting for identifying host galaxies as it is the second-deepest survey considered here, after the LSST.

After outlining the survey situation, we want to gauge if the coverage or depth of optical surveys is the limiting factor. Thus, we need to estimate what fraction of the sky is not covered by any optical survey. CHIME's visible sky is completely covered by SDSS and Pan-STARRS1, albeit to a lower depth in the Galactic plane. ASKAP's sky is covered to 50 per cent by the DELVE survey, but SDSS and Pan-STARRS1 cover everything else that is above $\delta = -30°$. This leaves only the Milky Way at $\delta < -30°$ uncovered, which is about 10 per cent of the total field of view of ASKAP. Altogether, the depth of the surveys will be the limiting factor for all radio telescopes.

Throughout the remainder of the paper, we only consider FRBs within the optical survey footprints. We leave the absolute number open of how many FRBs will be in which optical survey.

2.5 Milky Way extinction

In the previous section and in this work overall, we do not consider extinction from the Milky Way. This simplification is mostly to keep our results independent of the sky direction, except for being either inside or outside of an optical survey. This simplification is not always justified (Schlegel, Finkbeiner & Davis 1998),[3] particularly in the galactic plane, where extinction often exceeds 1 mag; for example in the cases of FRB 20180916B (CHIME/FRB Collaboration et al. 2019; Marcote et al. 2020) and FRB 20210407E (Shannon 2023) at galactic latitudes $b = 3.72°$ and $-6.71°$, respectively. Enhanced scattering of FRBs in the Galactic disc does not significantly affect the FRB detection rates (Josephy et al. 2021) and therefore does not reduce the importance of Milky Way extinction. However, the Milky Way DM contribution is much higher in the Galactic plane, resulting in much higher DM uncertainties (see e.g. Price, Flynn & Deller 2021). It might therefore be beneficial to exclude FRBs that are in the Galactic plane to avoid potential biases. By ignoring Milky Way extinction, we therefore make the hidden assumption that only FRBs outside the Milky Way plane will be used for cosmological applications. Considering this, the estimated survey overlaps in Section 2.4 are somewhat conservative, because we did not exclude the Galactic plane in the estimates.

[3]A tool to estimate extinction is available at https://irsa.ipac.caltech.edu/applications/DUST/

3 RESULTS

From the simulations described in Section 2, we obtained observed populations of FRBs and their host galaxies. The quantities we collect for FRB populations include their redshifts, and host galaxy quantities include their magnitudes in several optical surveys, which informs us which FRBs would have a measured redshift. These data provide us with an observed redshift distribution, from which we can directly forecast constraints on cosmological FRB applications. We present these results in the following section.

The simulated parameter space of different survey combinations is too large to be fully discussed here, so we limit ourselves to a selection of the results. We present the combinations ASKAP/CRACO with DELVE, CHIME with SDSS, and SKA1-Mid with LSST. Additional combinations of FRB and optical/infrared surveys, in particular with the Euclid survey, are presented in Appendix A.

3.1 ASKAP

The ASKAP telescope is located in the Southern Hemisphere and has a large 30 deg^2 field of view thanks to its phased array feeds (Bannister et al. 2019). In incoherent sum mode (ICS) its FRB survey (CRAFT) is relatively shallow with all FRBs at $z \lesssim 1$. The upcoming CRACO mode will be significantly deeper according to our simulations, as is shown in Fig. 2. It will detect FRBs up to $z \sim 2$ if FRBs follow the SFR, or to $z \sim 1.5$ in the two other simulated distance models.

Many host galaxies of ASKAP/CRACO FRBs will be visible in the DELVE survey. The numbers that were visible in all bands of the DELVE survey are 634, 847, and 819 out of 1000, for the distance models SFR, SMD, and V_C, respectively. This is also shown in the left-hand panel in Fig. 2. Furthermore, only 7.6–25 per cent would not be detected in any of the bands, such that the FRBs would have a completely unidentified host.

The FRB population in the right-hand panel of Fig. 2 that follow the SFR are clearly distinct from the ones that follow SMD and V_C. The cosmic SFR increases towards its peak around $z \sim 2$. The effect of this is visible as the FRBs are detected in higher numbers at about $z > 0.5$ compared to the populations that follow SMD or V_C. They also reach a higher maximum redshift, but are much less abundant at $z < 0.2$. The same can also be seen for other surveys (see next sections).

It can be difficult to unambiguously identify higher z FRB hosts because of chance coincidence rates, even when their host galaxy is visible. Calculating the chance coincidence, e.g. via PATH (Aggarwal et al. 2021), requires the probability that a galaxy is visible, prior to consulting optical images at the sky position. The distribution in Fig. 2 can be interpreted as this prior probability distribution for a given redshift. Around $z \sim 0.7$, the probability drops below 0.5 for ASKAP/CRACO. This low prior probability can become an issue, in particular for ASKAP FRBs, because ASKAP's localization precision is sometimes on the order of several arcseconds (see e.g.

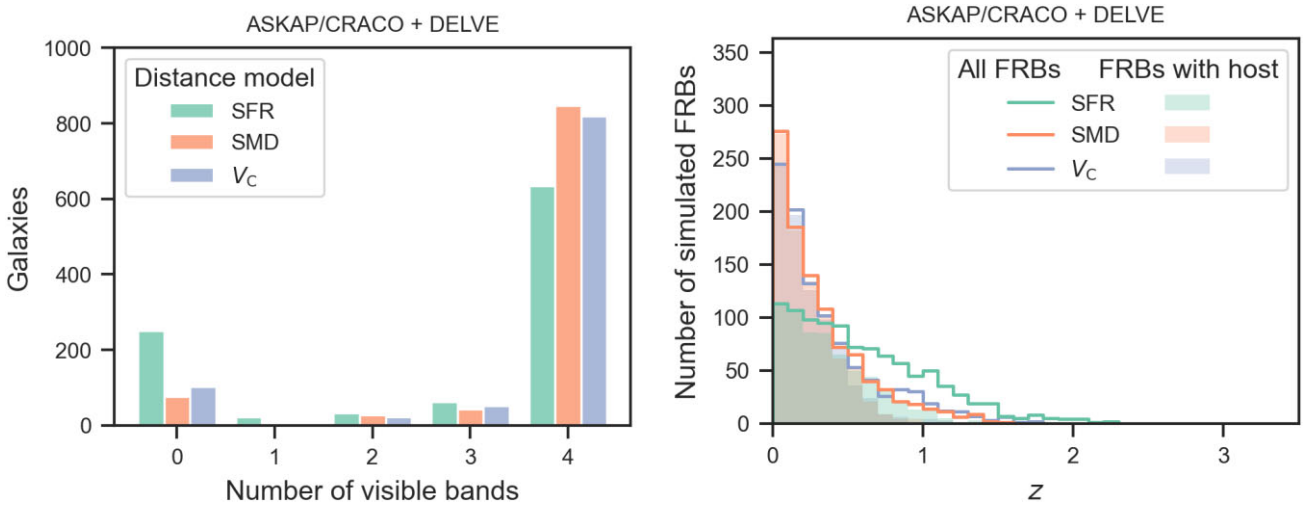

Figure 2. *Left:* Forecast of the number of DELVE bands in which FRB host galaxies will be visible for 1000 FRBs detected by ASKAP with the CRACO update. Shown are three different models where the intrinsic FRB distance distribution follows the SFR, the stellar mass density (SMD), or the comoving volume (V_C). DELVE will detect ∼63–85 per cent of ASKAP host galaxies in all bands, depending on the true cosmic FRB distance distribution. *Right:* The redshift distributions of FRBs (lines) and of FRBs whose host was detected in all bands (shaded regions). If FRBs follow the SFR, more are detected at high redshifts, and it will reach up to $z \sim 2$. The larger distances result in less detections in all bands compared to other distance models.

Macquart et al. 2020). With the resulting high chance coincidence probabilities, secure associations will be difficult for distant FRBs. Since it would require ray-tracing simulations, we do not further consider these effects in this study.

3.2 CHIME

For CHIME, once it can localize FRBs, the situation will be very different. The results of our simulations are shown in Fig. 3. CHIME is more sensitive than ASKAP and detects FRBs up to $z \sim 3$ if FRBs follow SFR, and up to $z \sim 2$ if they follow SMD. At the same time, the SDSS is shallower than DELVE. This results in only 20–40 per cent of CHIME FRBs having their host galaxies detected in all bands of SDSS, while for 26–65 per cent no host can be identified.

Compared to ASKAP, CHIME will detect FRBs to higher redshifts. The host galaxies predicted to be seen in SDSS are not only a small fraction of the total, but also all fall below $z = 0.5$. We will explore the impact of having only low-z FRBs in Section 4. The coverage gets worse if we consider that a significant fraction of FRBs will be outside the SDSS footprint. Although, the Pan-STARRS1 survey, which we did not simulate, covers the entire CHIME sky and its mean sensitivity lies between the SDSS and DELVE surveys. Either way, we can only harvest the signal in CHIME's high-redshift FRBs for cosmological analysis, if we follow them up with dedicated optical observations.

The low prior probability of higher-z FRBs to have a visible host is less problematic for CHIME. With its long baseline outrigger stations, it will have a very precise localization precision. Yet, some FRBs in the outskirts of their host galaxies will still be difficult to associate with their host. A visible galaxy therefore does not guarantee a host identification.

3.3 SKA1-Mid

The results for SKA1-Mid are shown in Fig. 4. SKA1-Mid will be at a similar latitude as ASKAP, but ∼25 times more sensitive (Dewdney et al. 2009). The larger FRB distances result in about 71–85 per cent of hosts being visible in all LSST bands in the final data release that will be published after 10 years of observation. The visible fraction of host galaxies is decreasing towards $z \sim 2$. The FRB redshifts observed reach a maximum of ∼5 if FRBs follow SFR or V_C, but only $z \sim 3$ if they follow SMD.

3.4 Euclid

The Euclid results are relevant to all radio surveys, although as we discussed in Section 2.4, Euclid alone cannot obtain photo-zs. The figures that include Euclid are most interesting in direct comparison to the other optical telescopes therefore we only present them in Figures A1 and A2.

As the limiting magnitudes suggest, the results show that Euclid is more sensitive than DELVE. Surprisingly, in the cases where FRBs follow the SMD or the V_C Euclid also detects a higher number of host galaxies in all bands than LSST. An investigation of the visible LSST bands shows that it is almost always the LSST u-band where galaxies are no more visible at higher distances. The number of galaxies that are not visible in any band is very similar for Euclid and LSST. Another similarity to LSST is that galaxies that are visible in all bands are limited to $z \lesssim 1.5$.

4 CONSTRAINING MISSING BARYONS

After simulating different FRB populations, we want to use them as mock observations to forecast constraints on the cosmic baryon density. We will do these forecasts for the FRBs simulated for ASKAP/CRACO as these will dominate the FRB population in the next 1–2 years, and for CHIME to illustrate the influence of differently distributed FRBs. We chose the Bayesian MCMC simulations of Macquart et al. (2020) as the method to constrain the cosmic baryon content. For this purpose, we first draw a DM from the same probability distributions that the model of Macquart et al. (2020) assumes. In principle, the DM can be split into different contributions, which are difficult to disentangle observationally. For this analysis, we express it as the DM from the host galaxy $\mathrm{DM_{host}}$, the intergalactic medium $\mathrm{DM_{IGM}}$, and the Milky Way $\mathrm{DM_{MW}}$, which

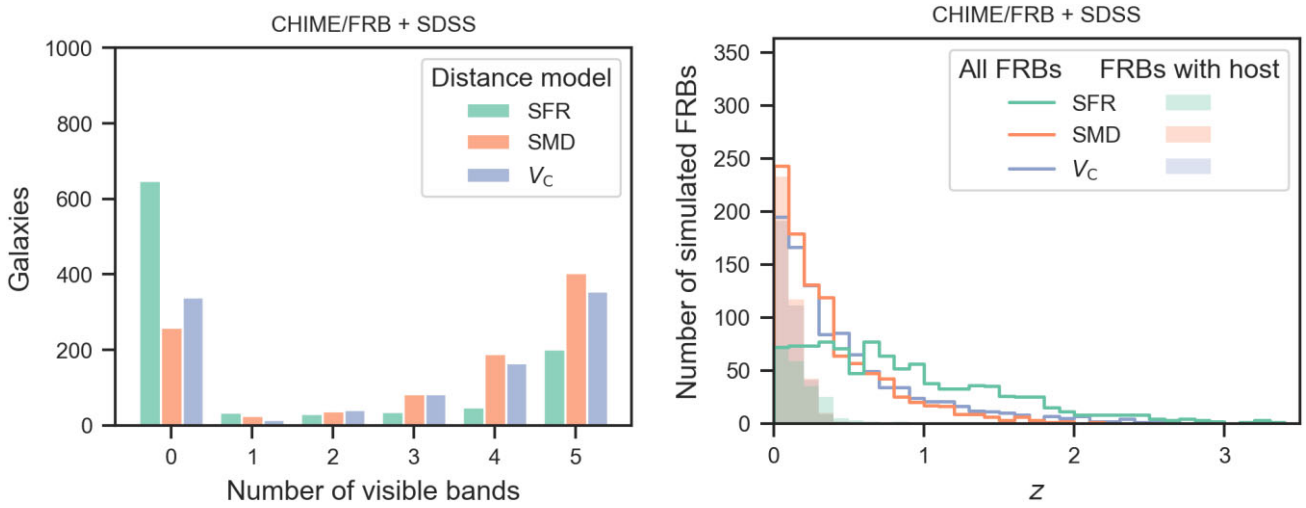

Figure 3. Like Fig. 2, but for the Northern Sky, with CHIME as FRB instrument and SDSS as the optical survey. SDSS only contains the hosts of FRBs at $z \lesssim 0.4$, which only covers 20–40 per cent of the CHIME telescopes FRBs, depending on the distance model. As in Fig. 2, this does not include the FRB fraction that will be outside the SDSS footprint. Although, this fraction will be covered by Pan-STARRS1, which is of similar depth.

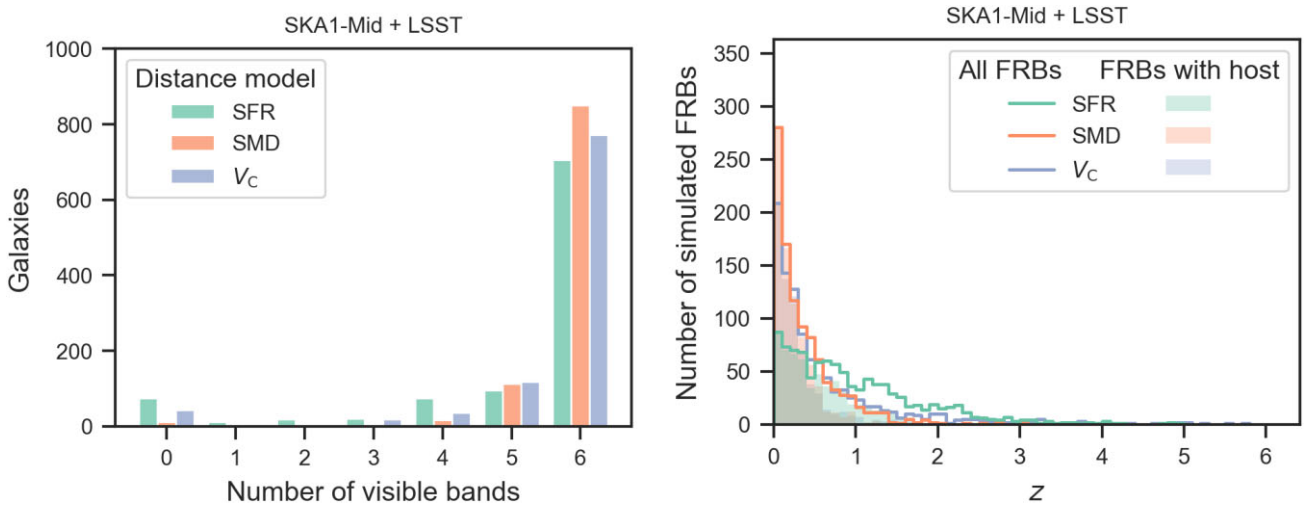

Figure 4. Similar to Fig. 2 for SKA. Despite SKA's sensitivity, still 71–85 per cent – depending on the distance model – will be detected in all bands of the Vera Rubin Observatory. The SKA barely reaches $z \sim 5$ in two models, which is still not sufficient to reach the H reionization epoch at $z \sim 6$.

yields

$$\mathrm{DM} = \mathrm{DM_{MW}} + \mathrm{DM_{IGM}} + \frac{\mathrm{DM_{host}}}{1+z}. \tag{4}$$

In the following, we assumed that contributions from the Milky Way can be sufficiently modelled and therefore only consider DM contributions from the IGM and the host galaxy.

The method of constraining the missing baryons is based on the Macquart relation, which describes the mean DM from the intergalactic medium (Deng & Zhang 2014; Zhou et al. 2014)

$$\langle \mathrm{DM_{IGM}} \rangle (z) = \frac{3c\,\Omega_\mathrm{b} H_0 f_\mathrm{IGM}}{8\pi G m_\mathrm{p}} \int_0^z \frac{(1+z)\left[\frac{3}{4} X_\mathrm{H}(z) + \frac{1}{8} X_\mathrm{He}(z)\right]}{\sqrt{\Omega_\mathrm{m}(1+z)^3 + \Omega_\Lambda}}, \tag{5}$$

where Ω_b is the cosmic baryon density, H_0 the Hubble constant, f_IGM the fraction of baryons residing in the IGM, m_p the proton mass, X_H and X_He the ionization fractions of hydrogen and helium, Ω_m the cosmic matter density, and Ω_Λ the cosmic energy density.

We drew $\mathrm{DM_{host}}$ from a log-normal distribution,

$$p(\mathrm{DM_{host}}|\mathrm{DM_0}, \sigma_\mathrm{host}) = \frac{\log_{10}(e)}{\mathrm{DM_{host}}\sigma_\mathrm{host}\sqrt{2\pi}} \tag{6}$$

$$\times \exp\left(-\frac{(\log_{10}\mathrm{DM_{host}} - \log_{10}\mathrm{DM_0})^2}{2\sigma_\mathrm{host}^2}\right), \tag{7}$$

where we chose a median of $\mathrm{DM_0} = 100\,\mathrm{cm^{-3}}$ pc and $\sigma_\mathrm{host} = 0.43$, in accordance with the values found by James et al. (2022b) and Shin et al. (2023). We drew $\mathrm{DM_{IGM}}$ from

$$p_\mathrm{cosmic}(\Delta) = A\Delta^{-\beta} \exp\left(-\frac{(\Delta^{-\alpha} - C_0)^2}{2\alpha^2\sigma_\mathrm{DM}^2}\right), \quad \Delta = \frac{\mathrm{DM_{IGM}}}{\langle \mathrm{DM_{IGM}} \rangle}, \tag{8}$$

where we chose $\alpha = 3$, $\beta = 3$, and $\sigma_\mathrm{DM} = F/\sqrt{z}$, with $F = 0.2$ (Macquart et al. 2020). A and C_0 are not free parameters, but determined by the condition $\langle \Delta \rangle = 1$ and the normalization. Note that in the method of Macquart et al. (2020) the degeneracy between

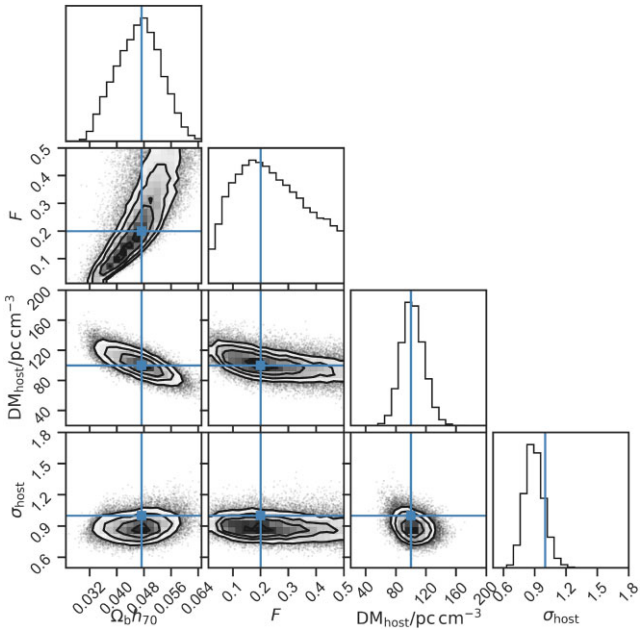

Figure 5. Outcome of an MCMC simulation using the method of Macquart et al. (2020), for the 124 FRBs that are visible in all bands of SDSS out of 1000 simulated CHIME FRBs following the SFR (green shaded region in Fig. 3, right-hand panel). Blue lines mark the input values. Contours are at 20, 40, 60, and 80 per cent confidence.

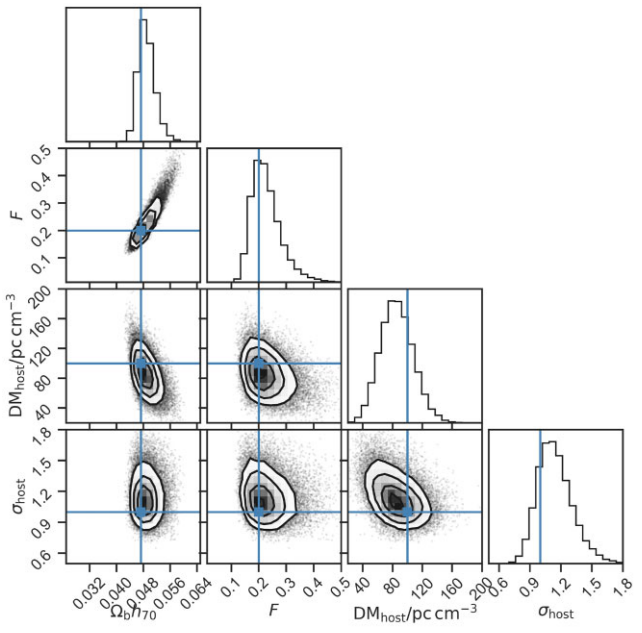

Figure 6. Like Fig. 5, but for comparison 124 FRBs are randomly drawn from the 1000 CHIME FRBs (from the distribution marked by the solid green line in Fig. 3, right-hand panel) and assumed to be localized. The cosmological parameters F and $\Omega_b h_{70}$ are tighter constrained than in Fig. 5, while host galaxy parameters $\mathrm{DM_{host}}$ and σ_{host} are less constrained.

f_{IGM} and $\Omega_b h_{70}$ has been broken, but Ω_b and h_{70} are still degenerate and the product is measured.

4.1 Influence of low-z FRBs

We do this procedure for 124 simulated CHIME FRBs that were visible in all SDSS bands. To see the influence of the low-z limitation that SDSS imposes on the sample, we repeat the simulations for 124 FRBs that are instead randomly drawn from all the simulated 1000 CHIME FRBs.

The outcomes of the two cases are shown in Figs 5 and 6. Compared to the results of Macquart et al. (2020) derived from 5 FRBs, the plot shows big improvements in the constraints of all parameters. Interestingly, there is a large difference between the two cases. Fig. 6 shows much tighter constraints on the cosmological parameters $\Omega_b h_{70}$ and F. This is the effect of FRBs from higher redshifts carrying a stronger cosmological signal compared to scatter from the inhomogeneous IGM. Surprisingly, it is also clear that the low-z FRBs in Fig. 5 constrain the host galaxy parameters $\mathrm{DM_{host}}$ and σ_{host} better than the population in Fig. 6. This must be a combination of $\mathrm{DM_{host}}$ getting lower with $(1+z)^{-1}$ in equation (4), and of less absolute scatter from the IGM at low redshifts. The ratios of the 95 per cent credible intervals of the two runs are 2.6, 2.2, 0.7, and 0.5 for $\Omega_b h_{70}$, F, $\mathrm{DM_{host}}$, and σ_{host}, respectively.

4.2 Evolution of constraints

We want to see how the constraints on different parameters evolve with the number of FRBs. We use the simulated ASKAP/CRACO FRBs that were visible in DELVE, with the distance distribution following the SFR. Starting with five FRBs, we consecutively add more FRBs to our detected total up to the maximum of 524 in this run, and we repeat the Bayesian analysis. Fig. 7 shows how the size of the 95 per cent credible interval for all four parameters evolves with the number of FRBs. The constraints on F only seem to go down linearly, probably due to it still being somewhat degenerate with $\Omega_b h_{70}$. The other parameters seem to follow $1/\sqrt{n_{\mathrm{FRBs}}}$ laws like quantities with Gaussian distributed uncertainties.

The maximum simulated amount of 1000 ASKAP/CRACO FRBs that resulted in 524 hosts in DELVE yields a 95 per cent credible interval of 0.01 for $\Omega_b h_{70}$, which is 21 per cent relative to the input value and roughly equivalent to a 10 per cent 2σ uncertainty.

5 FOLLOW-UP OPTIMIZATION

Dedicated optical follow-up will be needed for galaxies that are either not in survey footprints or too dim. Apart from this, spectroscopic follow-up is needed to get precise redshifts of identified hosts to improve uncertainties. We investigate in this section how to optimize optical follow-up from theoretical considerations and from our simulations.

5.1 Theoretical considerations

The most important quantity that needs to be considered when seeking to optimize FRB follow-up campaigns is the redshift of the FRBs. As different cosmological applications require different FRB redshift populations, sources should be targeted on the basis of these requirements. For example, the detection of the epochs of He II and H reionization requires FRBs at $z \gtrsim 3$ and 6, respectively. For other applications that rely on $\mathrm{DM_{IGM}}$ two effects have to be balanced. On the positive side, FRBs that are further away have a higher $\mathrm{DM_{IGM}}$ signal relative to its variance. This was first shown by McQuinn (2014), the average $\mathrm{DM_{IGM}}$ increases faster with redshift than the variance from large-scale structure or intervening galaxy haloes (see also Prochaska & Zheng 2019). The variance due to $\mathrm{DM_{host}}$ even gets lower. However, this must be considered against the fact that more distant galaxies will, on average, need more observing time.

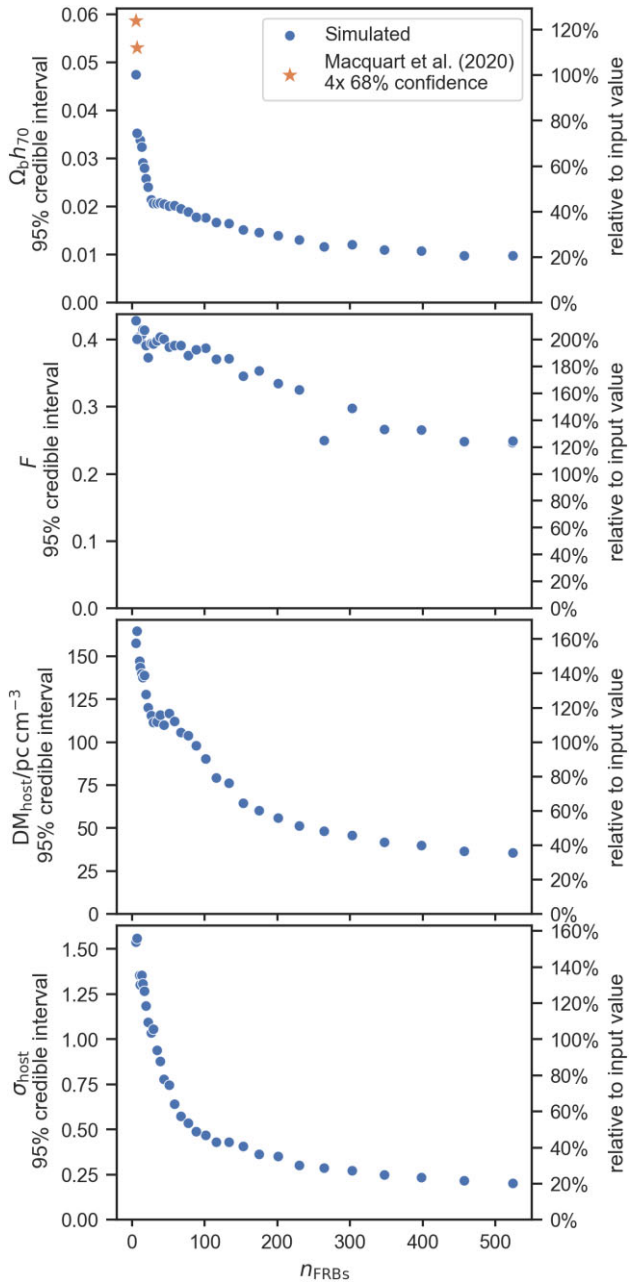

Figure 7. Evolution of the size of the credible interval (specifically the highest density interval) of the four parameters with growing numbers of FRB localizations. This forecast is for ASKAP/CRACO with localizations in the DELVE survey. For a Gaussian probability function, the 95 per cent credible interval is equivalent to $2 \cdot 2\sigma$, so we over plot this value as measured from real data.

The observing time that is needed to get a fixed signal-to-noise ratio (SNR) is $t_{\mathrm{obs}} \propto S^{-2}$, where S is, in our case, the flux of a host galaxy. This flux depends on luminosity L and luminosity distance D_{L}, as $S = L/\left(4\pi D_{\mathrm{L}}^2\right)$. It follows that the expected observation time is

$$t_{\mathrm{obs}} \propto D_{\mathrm{L}}^4, \tag{9}$$

for sources whose mean luminosity is constant with z. This first order estimate suggests that the increasing observing time dominates the effect of a higher cosmological signal, suggesting it may always be preferable to target close FRBs first.

5.2 Photometric observing time

In the following, we will compare this theoretical expectation with our simulations. The CHIME/FRB survey with SDSS is the radio/optical combination that requires the most extra follow-up, as many FRBs have no observed host galaxy. It is therefore well suited to test different follow-up strategies, and we use it in the following version where FRBs follow the SFR. To obtain realistic follow-up times, we assume a 10-m optical telescope with two observing systems, a photometer and a slit spectrometer.

We calculate the follow-up time needed for each galaxy for the example photometric and spectroscopic systems following chapter 17.3 of Schroeder (2000), partly in the notation of Poggiani (2017). The spectrometer will be considered in Section 5.3. Here, we assume that we want to detect each galaxy in a single photometric band of width $\Delta\lambda = 100\,\mathrm{nm}$, with a target SNR of 10. We use the galaxy magnitudes in the simulated SDSS r-band, and the galaxy sizes fixed to about 10 kpc. We assume we are in the background limited regime where the observing time simplifies to

$$t_{\mathrm{obs}} = \mathrm{SNR}^2 \frac{B}{Q\kappa^2 S^2}, \tag{10}$$

where S is the galaxy flux, B the background flux, Q the quantum efficiency of the detector, and κ accounts for losses, not included in the system transmittance. The fluxes are related to the magnitudes by

$$S = N_{\mathrm{p}} \tau \frac{\pi}{4}(1-\varepsilon^2) D^2 \Delta\lambda \cdot 10^{-0.4m} \quad \text{and} \tag{11}$$

$$B = N_{\mathrm{p}} \tau \frac{\pi}{4}(1-\varepsilon^2) D^2 \Delta\lambda \cdot 10^{-0.4 m_B} \phi\phi', \tag{12}$$

where $N_{\mathrm{p}} = 10^4\,\mathrm{photons/(s\,cm^2\,nm)}$ is the magnitude to flux conversion factor, τ the transmission efficiency, ε the obscuration factor, m the galaxy magnitude, m_{B} the sky background magnitude per solid angle, and $\phi\phi'$ the galaxy solid angle. For our example telescope we assume (following Schroeder 2000) $Q = 0.8$, $\kappa = 0.8$, $\tau = 0.3$, $\frac{\pi}{4}(1-\varepsilon^2) = 0.7$, $D = 10\,\mathrm{m}$, $m_{\mathrm{B}} = 22\,\mathrm{mag\,arcsec^{-2}}$, and $\phi\phi' = 4\,\mathrm{arcsec}^2\,(1\,\mathrm{Gpc}/D_{\mathrm{A}})^2$ approximately corresponding to the above-mentioned 10 kpc diameter, with the angular diameter distance D_{A}.

5.3 Spectroscopic observing time

To calculate the observing time needed for spectroscopy, we take an example split spectrometer. The time can be calculated from equations (10) to (12) with two modifications. First, the bandwidth $\Delta\lambda$ is now the width of the line of interest, we assume it to be $\Delta\lambda_{\mathrm{line}} = 1\,\mathrm{nm}$. Second, the slit might not cover the whole galaxy, in that case, the dimensions of the slit and the galaxy's surface brightness will determine S. We assume that the slit is long enough to cover the whole galaxy, but its width is not. The observed flux is then $S_{\mathrm{spec}} \approx S \frac{\Delta\lambda_{\mathrm{line}}}{\Delta\lambda} \frac{\phi_{\mathrm{slit}}}{\phi}$, with ϕ_{slit}, the projected width on the sky, given by $\phi_{\mathrm{slit}} = \frac{w'}{rDF_2}$, where w' is the slit, reimaged on the camera focus, r the anamorphic magnification, and F_2 the ratio of the camera optics' focal length to the diameter of the collimated beam, incident on the disperser. We use again the values from Schroeder (2000): $w' = 30\,\mu\mathrm{m}$, $r = 0.9$, and $F_2 = 1.5$, which yield $\phi_{\mathrm{slit}} = 0.46\,\mathrm{arcsec}$.

We use the photometric magnitudes therefore the calculated time is for the continuum and would be less for specific emission

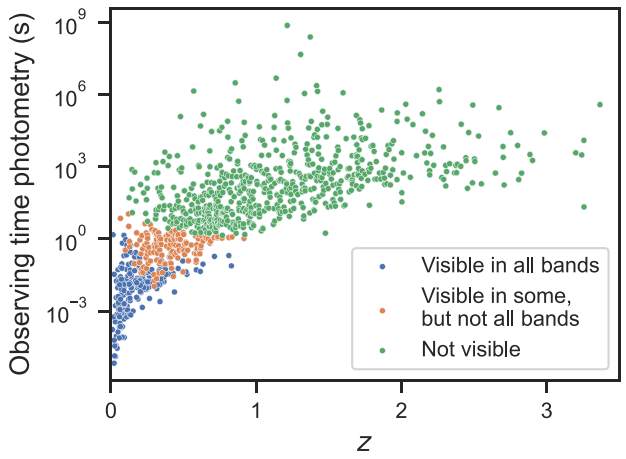

Figure 8. Optical observing time needed for our FRB host galaxies, simulated for CHIME. Photometric observing times are calculated to obtain an SNR of 10 in a single band in a 10-m class telescope, assuming the simulated SDSS *r*-band magnitudes and a fixed galaxy diameter around 10 kpc. Spectroscopic observing times are larger by a factor of 218, which we obtained assuming a slit spectrometer and 1 nm line width (see text for details). Colours represent galaxy visibilities in SDSS. The time varies by 15 orders of magnitude. Blue points have a known photo-z. Follow-up strategies should first target orange points. The fixed magnitude limit produced a horizontal cut therefore the expected observing time for green points is comparable at redshifts where some galaxies are observed (here $z = 0$–0.7).

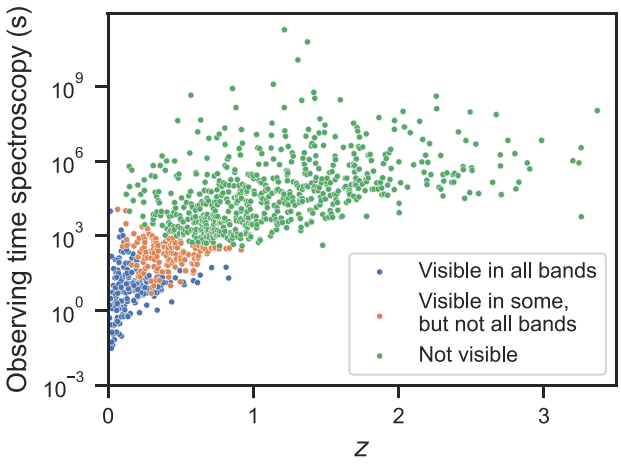

Figure 9. Like Fig. 8, but with spectroscopic observing time.

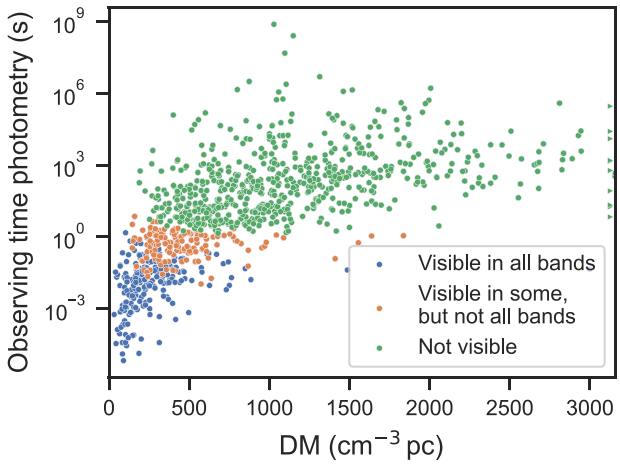

Figure 10. Like Fig. 8, but with the DM on the abscissa. The DM will be the best estimate for the distance, as the redshift is the object of desire and therefore unknown a priori. The limits on the DM axis have been chosen, such that it covers the same range as Fig. 8 in terms of $\langle \mathrm{DM_{IGM}} \rangle(z)$. Triangles indicate points outside the range.

lines. Additionally, the assumed SNR of 10 is higher than needed for a redshift measurement, which only requires line positions. The calculated time is therefore a conservative value. The reader may scale the resulting times with a constant factor for differing assumptions. Variations in intrinsic galaxy sizes, which we assumed to be fixed, might cause some additional scatter in the required observing times.

5.4 Results

The photometric observing time is shown in Fig. 8 against the redshift. The observing time required to detect any given galaxy can vary by over 15 orders of magnitude, demonstrating that a good observing strategy is necessary. The three considered cases – where FRB host galaxies are not visible, visible in some bands, or visible in all bands – are clearly separated in different ranges of observing time and redshift.

Galaxies that are visible in SDSS would be visible within seconds in our 10-m example telescope. Within a few minutes, one could already make secure associations up to $z \sim 1$. The highest expectable observing time is on the order 10^3 s. As a result, already at $z < 1$, a few per cent of FRBs will be without an observable host. Above $z \gtrsim 1.5$, a significant fraction will be undetectable by ground based telescopes, false associations would be problematic and make secure associations difficult.

Fig. 9 shows the observing time needed with our spectrometer. Follow-up of this kind would only be possible for bright galaxies that are already visible in at least some bands of SDSS. Furthermore, it is limited to $z \lesssim 0.7$.

5.5 Follow-up optimization for CHIME

Given the secure detection and lower required observing time of galaxies that are visible in some bands (orange points in Fig. 8), it will be most efficient to follow these up first, at least under the assumption that a high-z population is not required for a given application. After these galaxies have been followed up, there is an almost vertical cut below the not visible galaxies (green points), in our example at redshifts 0–0.7. This cut results in very similar expected observing times at these redshifts. Generally formulated, the expected time is similar for redshifts, where FRB host galaxies have already been found. To maximize the cosmological signal, we therefore expect that the most efficient strategy would be to first target the higher redshift host galaxies within this interval, i.e. around $z = 0.5$–0.7. We will test this hypothesis in Section 5.6.

In practice, the distance of an FRB is not known a priori but needs to be estimated from FRB properties. The DM is already used as a distance estimator on a regular basis (James et al. 2022a). The probability density $p(z|\mathrm{DM})$ has a long tail towards low redshifts, but drops down quickly towards higher redshifts. Therefore, the follow-up will often yield host galaxies that are much closer than expected but not much further way. The tendency that FRB DMs scatter more towards higher DMs can be seen in Fig. 10, where we show the observing time plotted against the DM instead of redshift. This

asymmetry limits the number of cases, where the required follow-up time is much longer than expected. Other distance estimators could be the amount of scatter or the width of a burst, but both have a large intrinsic randomness compared to their distance dependence (see e.g. CHIME/FRB Collaboration et al. 2021; Ocker et al. 2022).

As a final note, the large difference in observing time shows that it will not be uncommon to have single galaxies that need significantly more follow-up time than others, or will not be visible at all. For example, even at $z \sim 0.3$, there are galaxies who need of order 1000 times longer observing times than even the dimmest galaxies visible in SDSS.

5.6 Optimal DM and observing time limit

We want to test the hypothesis that the best target redshift is at the higher end of observed redshifts and investigate which maximum observing time should be spent on one galaxy. We further aim to find the best balance between this maximum observing time and the number of FRBs in a sample in the case of limited observing time, and we consider specific follow-up strategies. To be independent of the cosmological parameter to be constrained (e.g. Ω_m or H_0) and for computational feasibility, we change from the MCMC approach to a simpler approach. We define the 'cosmological signal' of all FRBs with a redshift measurement as

$$\mathrm{SNR_c} \equiv \sqrt{\sum_i \left(\frac{\langle \mathrm{DM_{IGM}} \rangle (z_i)}{\sigma_\mathrm{c}(z_i)} \right)^2}, \tag{13}$$

where $\langle \mathrm{DM_{IGM}} \rangle (z_i)$ is given by equation (5) and

$$\sigma_\mathrm{c}(z_i) = \sqrt{(\sigma_\mathrm{h}/(1+z_i))^2 + \sigma_\mathrm{IGM}(z_i)^2}\,, \text{ with} \tag{14}$$

$$\sigma_\mathrm{h} = \mathrm{DM_0}\sqrt{e^{2\sigma_\mathrm{host}} - e^{\sigma_\mathrm{host}}} \qquad \text{and} \tag{15}$$

$$\sigma_\mathrm{IGM}(z_i) = 0.2\,\langle \mathrm{DM_{IGM}} \rangle (z_i)/\sqrt{z_i}. \tag{16}$$

The estimate for σ_IGM has been derived from simulations by Kumar & Linder (2019) and is valid until $z \sim 3$. In this section, we will consider $\mathrm{SNR_c^2}$ because the data will always build on some previous data set with $\mathrm{SNR_0}$, and therefore yield an improvement

$$\frac{\mathrm{SNR_{tot}}}{\mathrm{SNR_0}} = \frac{\sqrt{\mathrm{SNR_0^2} + \mathrm{SNR_c^2}}}{\mathrm{SNR_0}} \approx 1 + \frac{1}{2}\frac{\mathrm{SNR_c^2}}{\mathrm{SNR_0^2}}, \tag{17}$$

where $\mathrm{SNR_{tot}}$ is the total cosmological signal.

We use the FRB host galaxies that are not visible in any of the bands from the previous section (green points in Fig. 10). To find the best target DM for carrying out the optical follow-up, we pick several DMs and select the 100 FRBs closest to them. Some of the galaxies are too dim to be detected in a reasonable time, so an efficient strategy always has to include some upper limit on the observing time that is spent per galaxy. Since we do not know what the best time limit would be, we start low and increase the limit gradually until we detect all galaxies. For each central DM and time limit, we compute the efficiency $\mathrm{SNR_c^2}/t_\mathrm{tot}$, where t_tot is the total observing time spent on all galaxies.

This efficiency is shown in Fig. 11 against the time limit for a few different central DMs. The highest efficiency is reached at a low time limit, when only a fraction of the FRBs are observed. This can be understood from the distribution in Fig. 10 remembering that the time axis is logarithmic, indicating a distribution dominated by low observing times with a very long tail. To determine the DM centre that can give the highest efficiency, we do smaller DM steps and

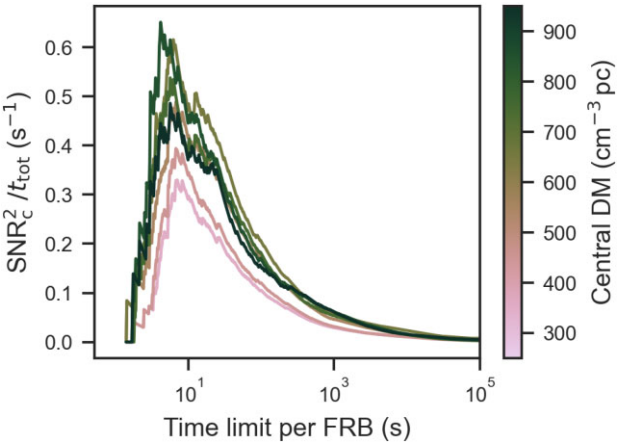

Figure 11. The efficiency as a function of the maximum time spent per host galaxy for different central DMs, each time considering the 100 closest FRBs. The data are the CHIME FRBs, with galaxies not visible in SDSS, i.e. the green dots in Fig. 10.

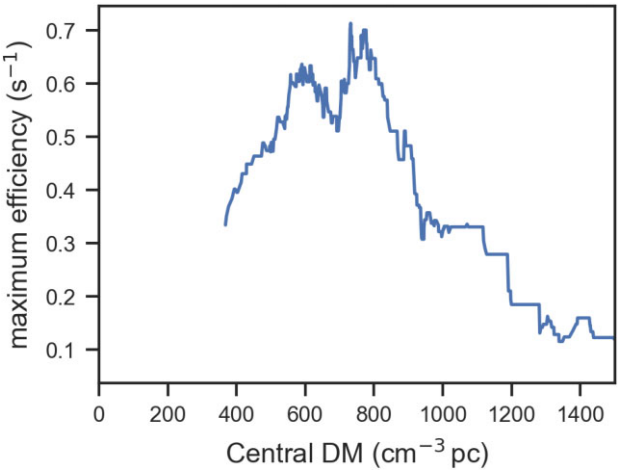

Figure 12. The efficiency at the time limit, where it takes on its maximum value. The highest efficiency can be reached around a DM of 750 $\mathrm{cm^{-3}}$ pc, but it is relatively constant between 500 and 800 $\mathrm{cm^{-3}}$ pc.

compute the maximum efficiency for each DM. The result is shown in Fig. 12. The highest efficiency is reached around a central DM of 750 $\mathrm{cm^{-3}}$ pc in agreement with our predictions in the previous section, but stochastic variations dominate in the range from ∼500 to 800 $\mathrm{cm^{-3}}$ pc.

When observing time is the limiting factor, we need to balance the FRB sample size that we follow up, against the maximum time spent on each source. Since we just found the optimal DM to be around 700 $\mathrm{cm^{-3}}$ pc, we consider this finding, but for simplicity only try to maximize the number of detected host galaxies instead of $\mathrm{SNR_c^2}$. To consider the previous findings, we start at DM = 700 $\mathrm{cm^{-3}}$ pc and increase our number of FRBs N in the sample gradually by whichever FRB's DM is closest to 700 $\mathrm{cm^{-3}}$ pc, but below 1000 $\mathrm{cm^{-3}}$ pc until all FRBs below this limit are included. We show the efficiency of the detected cosmological signal, $\mathrm{SNR_c^2}/t_\mathrm{tot}$, against the total time spent, in Fig. 13 for different N. For a given observing time, one could read the optimal N from the graph. However, if the distribution of galaxies with respect to their required observing time is not known, we propose the following algorithm, which we derive in Appendix B.

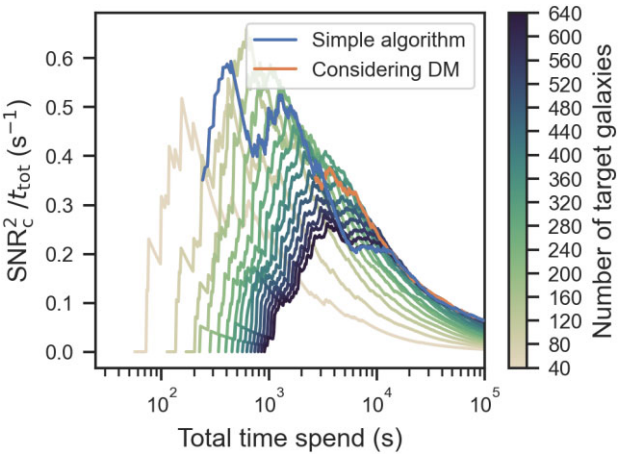

Figure 13. The efficiency in terms of the squared cosmological signal per total observing time. Overplotted lines show the outcomes of our two developed algorithms. The simple algorithm considers the last four detections, the number of total and detected galaxies, and the total observing time. The order in which galaxies are added is based on the FRB DMs. The second algorithm additionally considers the DM to compute the time limit for FRBs with a DM beyond 1000 cm^{-3} pc.

(i) Start with a number of targets that is small compared to the available observing time but large enough to not be affected by low number statistics, and observe 'simultaneously' until the first galaxy is visible.

(ii) If the probability p_{t_l} to find a galaxy in the next Δt at the current observing time limit t_l satisfies

$$p_{t_l} > \frac{n\,(N-n)}{t_{\mathrm{tot}}}, \tag{18}$$

where n is the number of detected galaxies, increase t_l until the next galaxy is detected, otherwise increase the sample of target galaxies N by one. To estimate p_{t_l}, one can take the difference Δt_l between the times needed to discover the last Δn galaxies and obtain $p_{t_l} = \Delta n/\Delta t_l$.

(iii) Repeat this step until the available time runs out.

In this way, the algorithm essentially finds the optimal t_l and subsequently increases N. This simple algorithm works well at first, as can be seen in the blue curve in Fig. 13. However, once the FRBs that are added exceed DM $\sim$ 1000 cm^{-3} pc, the distribution of observing times differs too much towards longer times from the distribution of already observed galaxies. Starting at this DM, we impose a second condition, assuming that the distribution roughly keeps its shape.

(i) If the next FRB is at a DM $>$ 1000 cm^{-3} pc, we require that

$$t_l \geq \frac{D_L(\mathrm{DM})^4}{D_L(1000\,\mathrm{cm}^{-3}\,\mathrm{pc})^4}\, t_{l,700}, \tag{19}$$

where $t_{l,\,1000}$ is the time limit when reaching DM = 1000 cm^{-3} pc, and $D_L(\mathrm{DM})$ is the expected luminosity distance for a given DM, obtained by inverting equation (5) to get $z(\mathrm{DM})$.

The result of the improved algorithm is again shown in Fig. 13, yielding close to optimal results at all times. Deviations from the ideal efficiency come from our assumption that the highest number will also lead to the highest cosmological signal, but also from the unavoidable fact that the algorithm only knows 'past' detections and not the whole population.

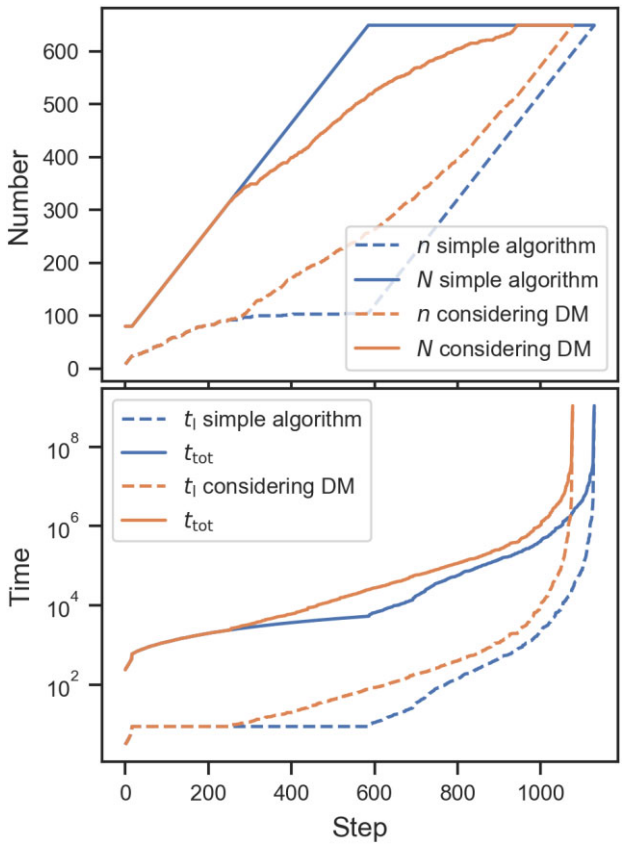

Figure 14. Evolution of the numbers and times in our algorithms. N denotes the FRBs or target galaxy sample size, n the number of detected galaxies, t_l the time limit on each galaxy, and t_{tot} the total observing time spent. In every step, either t_l is increased to detect one more galaxy in the current sample, or one galaxy is added to the sample.

The outcomes of the two algorithms are shown in Fig. 14 in terms of the times and numbers after each step. The curve for t_l in the simple algorithm shows that t_l is independent of N, as it stays constant with growing N after it is found. The theoretical reason is given in Appendix B.

6 DISCUSSION

6.1 Limitations

Our estimates here are limited by knowledge about the FRB population in several ways. The most important uncertainties are the FRB's L_{max} (or E_{max}), spectral index, and distance distribution (if it, e.g. follows SFR or SMD). The strong dependence on L_{max} is visible in the middle panel of Fig. 1, where a larger fraction of high-L FRBs are observed, compared to less luminous FRBs (this also illustrates why constraints on L_{max} are much better than on L_{min} (James et al. 2022b)). The value of L_{max} directly affects the maximum redshift at which FRBs can be observed. The shape of the redshift distribution is rather unaffected by these high-L FRBs, because they are distributed across redshifts.

The spectral index also has a strong influence on the maximum possible observed redshift. For example, a burst at $z = 2$ observed on the Earth between ν = 1.2–1.4 GHz, must have been emitted between ν = 3.6–4.2 GHz. Extrapolating the uncertain value of α

to these high frequencies yields a large uncertainty in the maximum observable redshift.

The effect of our different distance models that follow SFR, SMD, and V_C is evident in Figs 2, 3, and 4, and has already been discussed in Section 3.

6.2 Consequences for FRB applications

The epochs of H and He II reionization are expected to be at $z \sim 6$ and 3, respectively. FRBs need to be detected from these distances, and their redshift must be obtained. The epoch of H reionization cannot be reached by any of our simulated surveys, not even SKA1-Mid. While ASKAP's FRBs are also not distant enough to reach the epoch of He II reionization, CHIME is just reaching it, but only if the cosmic FRB density follows the SFR. SKA1-Mid will reach the epoch of He II reionization in all distance models. However, none of the optical surveys detects galaxies at $z > 2$ in all bands, making dedicated optical follow-up a necessity to detect the He II epoch of reionization. Moreover, we showed in Section 5.4 that this optical follow-up is not feasible with a 10-m ground-based telescope, but likely needs to be carried out from space.

In Section 4, we examined the effects of limited follow-up on cosmological constraints, in particular on $\Omega_b h_{70}$. When only optical surveys are used to obtain FRB redshifts, the usable FRB population is restricted to low redshifts. These low-z FRBs result in lower constraints on $\Omega_b h_{70}$ or in correspondingly more FRBs needed to reach the same constraints. Note, that it is not beneficial to increase the number of low-z FRBs indefinitely, as at some number, several FRBs will probe the same sight lines (Reischke & Hagstotz 2023).

To probe the intergalactic magnetic fields (Akahori et al. 2016), FRBs have to be distant enough that the intergalactic contribution to the rotation measure becomes comparable to the host contribution. Depending on the progenitor of FRBs, this will likely only be the case around $z \gtrsim 3$ (Hackstein et al. 2019). SKA1-Mid FRBs with optical follow-up of space-based telescopes might therefore be needed to reach sufficient numbers for this method.

The signal from a hypothetical photon mass almost plateaus around $z \sim 1$ (see e.g. fig. 1 of Wei & Wu 2020). Therefore, FRBs at $z \lesssim 1$ are best for this application. They can be obtained with any of the radio surveys, but need an optical follow-up that is deeper than SDSS.

FRBs that are gravitationally lensed by an intervening galaxy or galaxy cluster are so rare and valuable (see e.g. Wucknitz et al. 2021) that they should be followed up in any possible way.

6.3 Studying FRB progenitors

Optical follow-up of host galaxies is not only important for FRB applications but also for studies of FRB origins (e.g. Heintz et al. 2020; Bhandari et al. 2022). Photometric studies can localize FRBs within galaxies, for example, to spiral arms or star-forming regions (see e.g. Tendulkar et al. 2021), and allow comparing the morphological types with other transients. Spectroscopy can reveal the history of star formation via stellar population synthesis. These methods mainly require close by FRBs to obtain a uniformly well-studied set of host galaxies and direct environments. To obtain a set that is as unbiased as possible, FRB follow-up should be deep with conservative upper limits on DM to not exclude close by high DM_{host} FRBs.

FRBs at $z > 2$ are interesting to study the evolution with the cosmic SFR and the frequency dependence of the rate. Our simulations show how the possibility of obtaining a complete set depends on the depth of the optical survey. DELVE is already nearly complete at $z \lesssim 0.4$. Dedicated follow-up from ground base telescopes could yield nearly complete sets up to $z \sim 1$, depending on the available time. Larger redshifts might only be accessible with space-based telescopes.

6.4 Outlook

In our models, we made a few assumptions that would lead to biases in the inferred parameters. For example, the expected DM_{host} will likely correlate with the host galaxy's mass and SFR. In turn, brighter galaxies will be biased towards higher DM_{host}, which is not a problem if the properties of the DM_{host} distribution are inferred together with e.g. the missing baryon density. However, the bias has to be taken into account when combining FRBs that have been followed up to different depths or with otherwise different strategies. Other biases can come from misidentified galaxies. The influence of these effects on observed galaxy properties was previously inspected by Seebeck et al. (2021). This study will serve as a basis for the community to investigate biases in FRB applications in the future, but must be complemented by magnetohydrodynamic simulations.

The optimal follow-up time for any given FRB is also affected by these considerations. Deeper follow-up will decrease the number of misidentified host galaxies, as the true host might emerge out of the noise. Additionally, it will increase the number of identified galaxies close to the line of sight whose halo is intersected by an FRB (see e.g. Simha et al. 2020). For the design of an FRB follow-up campaign, these effects need to be considered, to essentially weigh the quantity against the quality of localized FRBs.

A second use case of the model is getting prior probabilities for host galaxies to be observable. The probability of an FRB-host association depends on the prior probability that the true host is below the detection threshold. This prior probability could be calculated from our simulations for given radio and optical telescopes and an FRB's DM.

7 CONCLUSIONS

How limiting is optical follow-up for FRB applications? To answer this question, we have simulated a realistic FRB population, using parameters obtained by recent studies (James et al. 2022b; Shin et al. 2023). We used galaxies from a semi-analytic model as the mock hosts of our FRBs and tested how many would be visible in current and future optical and infrared surveys. As representative radio telescopes, we used ASKAP, CHIME, and SKA1-Mid. As host galaxy surveys, we used SDSS, DELVE, Euclid, and LSST.

(i) We found that all applications that require FRBs with measured redshifts can be severely limited by the number of detected host galaxies, since e.g. only 20–40 per cent of CHIME FRBs within the SDSS footprint are also visible in all of its bands, additionally they are limited to $z < 0.5$. On the other hand, a deeper survey like DELVE will detect 63–85 per cent of ASKAP's FRBs. Although, a detection does not guarantee a secure association.

(ii) The redshift ranges resulting from our simulation suggest that the He II epoch of reionization, expected at $z \sim 3$, will be measurable by several radio telescopes. However, dedicated space based follow-up will be needed to obtain redshifts, as even LSST is not deep enough to detect most FRB host galaxies at $z \gtrsim 1.5$. The same restrictions apply to the use of FRBs as a probe of intergalactic magnetic fields, which also requires FRBs at $z \gtrsim 3$. The H epoch of reionization around $z \sim 6$ can not yet be reached, even with SKA1-Mid.

(iii) Applying existing methods to constrain the missing baryons, we showed that even if just 524 of 1000 FRB hosts have measured

redshifts, $\Omega_b h_{70}$ can be constrained to 10 per cent (with 95 per cent credibility). This would be a great improvement over the constraints of 60 per cent from current O VII absorption line studies in X-rays (Kovács et al. 2019), and one step closer to the uncertainties of theoretical predictions of 2.3 per cent from big bang nucleosynthesis and 1.3 per cent from big bang nucleosynthesis combined with Planck Collaboration et al. (2020) cosmic microwave background measurements (Pitrou et al. 2018; Driver 2021).

(iv) Assuming an optical 10-m class telescope and sufficient FRB localization precision, we showed that follow-up with ground based telescopes can only yield secure associations at $z \lesssim 1.5$ and spectra of galaxies at $z \lesssim 0.7$

(v) In general, to minimize observing time, the first FRBs to be followed up, should be those whose hosts can be identified in some optical bands of the large surveys. Afterwards, galaxies at the higher redshifts at which host galaxies were observed in the optical survey yield the largest cosmological signal per observing time; their shorter required observing time outweighs the larger cosmological signal of high redshift FRBs. DMs of FRBs are well suited as a distance estimate for targeting the optimal redshifts. Although, resulting biases have to be taken into account. We show that the optimal observing time limit is independent of available time or the number of FRBs. However, it increases when observing galaxies at higher distances than the ones of galaxies visible in optical surveys. We provide methods to find the optimal observation time limit.

ACKNOWLEDGEMENTS

We thank Stefan Hackstein for helping shape the project in the beginning, Luiz F. S. Rodrigues for early discussions on GALFORM, Nataliya Porayko for tips on how to test the MCMC simulations, Lachlan Marnoch and Sunil Simha for their input regarding optical surveys, Clancy James for providing details about the ASKAP/CRACO update, David Gardenier as well as Macquart et al. (2020) for making their code available, Olaf Wucknitz for useful comments on the manuscript, and the referee for several useful comments, in particular for suggesting to assume a 10-m telescope instead of arbitrary units.

LGS is a Lise Meitner Max Planck independent research group leader and acknowledges funding from the Max Planck Society.

CMB acknowledges support from the Science Technology Facilites Council (STFC) through ST/T000244/1. This work used the DiRAC@Durham facility managed by the Institute for Computational Cosmology on behalf of the STFC DiRAC HPC Facility (www.dirac.ac.uk). The equipment was funded by BEIS capital funding via STFC capital grants ST/P002293/1, ST/R002371/1 and ST/S002502/1, Durham University and STFC operations grant ST/R000832/1. DiRAC is part of the UK's National e-Infrastructure.

DATA AVAILABILITY

All code used for this paper is available as a PYTHON package, MOCKFRBHOSTS, at https://github.com/JoschaJ/mockFRBhosts. The host galaxies simulated with GALFORM are available at https://doi.org/10.5281/zenodo.7926078.

REFERENCES

Abazajian K. N. et al., 2009, ApJS, 182, 543
Aggarwal K., Budavári T., Deller A. T., Eftekhari T., James C. W., Prochaska J. X., Tendulkar S. P., 2021, ApJ, 911, 95
Aihara H. et al., 2011, ApJS, 193, 29
Akahori T., Ryu D., Gaensler B. M., 2016, ApJ, 824, 105
Alam S. et al., 2015, ApJS, 219, 12
Arcus W. R., Macquart J. P., Sammons M. W., James C. W., Ekers R. D., 2021, MNRAS, 501, 5319
Bannister K. W. et al., 2019, Science, 365, 565
Baugh C. M. et al., 2019, MNRAS, 483, 4922
Beck R., Dobos L., Budavári T., Szalay A. S., Csabai I., 2016, MNRAS, 460, 1371
Beniamini P., Kumar P., Ma X., Quataert E., 2021, MNRAS, 502, 5134
Bhandari S. et al., 2022, AJ, 163, 69
Bhattacharya M., Kumar P., Linder E. V., 2021, Phys. Rev. D, 103, 103526
Bochenek C. D., Ravi V., Belov K. V., Hallinan G., Kocz J., Kulkarni S. R., McKenna D. L., 2020, Nature, 587, 59
Bonetti L., Ellis J., Mavromatos N. E., Sakharov A. S., Sarkisyan-Grinbaum E. K., Spallicci A. D. A. M., 2016, Phys. Lett. B, 757, 548
Chambers K. C. et al., 2016, preprint (arXiv:1612.05560)
Chatterjee S. et al., 2017, Nature, 541, 58
CHIME/FRB Collaboration et al., 2019, ApJ, 885, L24
CHIME/FRB Collaboration et al., 2020, Nature, 582, 351
CHIME/FRB Collaboration et al., 2021, ApJS, 257, 59
Chittidi J. S. et al., 2021, ApJ, 922, 173
Cole S., Lacey C. G., Baugh C. M., Frenk C. S., 2000, MNRAS, 319, 168
Connor L. et al., 2021, PASP, 133, 075001
Cosmic Visions 21 cm Collaboration et al., 2018, preprint (arXiv:1810.09572)
Crichton D. et al., 2022, J. Astron. Tel. Instr. Syst., 8, 011019
Deng W., Zhang B., 2014, ApJ, 783, L35
Dewdney P. E., Hall P. J., Schilizzi R. T., Lazio T. J. L. W., 2009, IEEE Proceedings, 97, 1482
Dong F. A., Chime/Frb Collaboration 2022, ATel, 15681, 1
Driver S., 2021, Nat. Astron., 5, 852
Drlica-Wagner A. et al., 2022, ApJS, 261, 38
Eftekhari T., Berger E., 2017, ApJ, 849, 162
Euclid Collaboration et al., 2022, A&A, 662, A112
Gajjar V. et al., 2018, ApJ, 863, 2
Gao H., Li Z., Zhang B., 2014, ApJ, 788, 189
Gardenier D. W., Connor L., van Leeuwen J., Oostrum L. C., Petroff E., 2021, A&A, 647, A30
Gardenier D. W., van Leeuwen J., Connor L., Petroff E., 2019, A&A, 632, A125
Ginzburg V. L., 1973, Nature, 246, 415
Graham M. L. et al., 2020, AJ, 159, 258
Hackstein S., Brüggen M., Vazza F., Gaensler B. M., Heesen V., 2019, MNRAS, 488, 4220
Hallinan G. et al., 2019, The DSA-2000 — A Radio Survey Camera, in Bulletin of the American Astronomical Society. Vol. 51, Issue 7, preprint (arXiv:1907.07648)
Hashimoto T. et al., 2022, MNRAS, 511, 1961
Heintz K. E. et al., 2020, ApJ, 903, 152
Hotan A. W. et al., 2021, PASA, 38, e009
Ivezić Ž. et al., 2019, ApJ, 873, 111
James C. W. et al., 2022c, MNRAS, 516, 4862
James C. W., Prochaska J. X., Macquart J. P., North-Hickey F. O., Bannister K. W., Dunning A., 2022a, MNRAS, 509, 4775
James C. W., Prochaska J. X., Macquart J. P., North-Hickey F. O., Bannister K. W., Dunning A., 2022b, MNRAS, 510, L18
Jaroszynski M., 2019, MNRAS, 484, 1637
Josephy A. et al., 2021, ApJ, 923, 2
Kader Z. et al., 2022, Phys. Rev. D, 106, 043016
Kapp F., 2016, in SPIE Conf. Ser. Vol. 9911, System engineering and scienceprojects: lessons from MeerKAT. SPIE, Bellingham, p. 99110T
Keating L. C., Pen U.-L., 2020, MNRAS, 496, L106
Kocz J. et al., 2019, MNRAS, 489, 919
Kovács O. E., Bogdán Á., Smith R. K., Kraft R. P., Forman W. R., 2019, ApJ, 872, 83
Kumar P., Linder E. V., 2019, Phys. Rev. D, 100, 083533
Lacey C. G. et al., 2016, MNRAS, 462, 3854
Law C. J., Bower G. C., Burke-Spolaor S., Butler B. J., Demorest P., Lazio T. J. W., Linford J. D., 2018, in Murphy E., ed., ASP Conf. Ser. Vol. 517, Science with a Next Generation Very Large Array. Astron. Soc. Pac., San Francisco, p. 773

Leung C. et al., 2022, Phys. Rev. D, 106, 043017
Li Z.-X., Gao H., Ding X.-H., Wang G.-J., Zhang B., 2018, Nat. Commun., 9, 3833
Lin H.-H. et al., 2022, PASP, 134, 094106
Lorimer D. R., Bailes M., McLaughlin M. A., Narkevic D. J., Crawford F., 2007, Science, 318, 777
Lyubarsky Y., 2021, Universe, 7, 56
Macquart J. P. et al., 2020, Nature, 581, 391
Macquart J. P., Shannon R. M., Bannister K. W., James C. W., Ekers R. D., Bunton J. D., 2019, ApJ, 872, L19
Marcote B. et al., 2020, Nature, 577, 190
Marshall P. et al., 2017, Lsst Science Collaborations Observing Strategy White Paper: 'Science-Driven Optimization Of The Lsst Observing Strategy'. Zenodo
McQuinn M., 2014, ApJ, 780, L33
Minazzoli O., Johnson-McDaniel N. K., Sakellariadou M., 2019, Shortcomings of Shapiro delay-based tests of the equivalence principle on cosmological scales. Phys. Rev. D, 100, 104047
Muñoz J. B., Kovetz E. D., Dai L., Kamionkowski M., 2016, Phys. Rev. Lett., 117, 091301
Nusser A., 2016, ApJ, 821, L2
Ocker S. K., Cordes J. M., Chatterjee S., Gorsuch M. R., 2022, ApJ, 934, 71
Petroff E., Hessels J. W. T., Lorimer D. R., 2022, A&A Rev., 30, 2
Pitrou C., Coc A., Uzan J.-P., Vangioni E., 2018, Phys. Rep., 754, 1
Planck Collaboration et al., 2020, A&A, 641, A6
Platts E., Prochaska J. X., Law C. J., 2020, ApJ, 895, L49
Pleunis Z. et al., 2021a, ApJ, 911, L3
Pleunis Z. et al., 2021b, ApJ, 923, 1
Poggiani R., 2017, Optical, Infrared and Radio Astronomy: From Techniques to Observation. Springer International Publishing, Cham, Switzerland
Price D. C., Flynn C., Deller A., 2021, PASA, 38, e038
Prochaska J. X., Neeleman M., 2018, MNRAS, 474, 318
Prochaska J. X., Zheng Y., 2019, MNRAS, 485, 648
Qiang D.-C., Li S.-L., Wei H., 2022, J. Cosm. Astropart. Phys., 2022, 040
Ravi V. et al. 2023, ApJL, 949, L3
Reischke R., Hagstotz S., 2023, preprint (arXiv:2301.03527)
Reischke R., Hagstotz S., Lilow R., 2022, Consistent equivalence principle tests with fast radio bursts. MNRAS, 512 285
Schlegel D. J., Finkbeiner D. P., Davis M., 1998, ApJ, 500, 525
Schmidt S. J. et al., 2020, MNRAS, 499, 1587
Schroeder D. J., 2000, Astronomical Optics. Academic Press, Cambridge, Massachusetts
Seebeck J., Ravi V., Connor L., Law C., Simard D., Uzgil B., 2021, preprint (arXiv:2112.07639)
Shannon R., 2023, TNS Fast Radio Bursts, 470, 1
Shin K. et al., 2023, ApJ, 944, 105
Simha S. et al., 2020, ApJ, 901, 134
Spitler L. G. et al., 2016, Nature, 531, 202
Tendulkar S. P. et al., 2021, ApJ, 908, L12
Vanderlinde K. et al., 2019, The Canadian Hydrogen Observatory andRadio-transient Detector (CHORD), in Canadian Long Range Plan for Astronomy and Astrophysics White Papers. Zenodo
Vazza F., Brüggen M., Hinz P. M., Wittor D., Locatelli N., Gheller C., 2018, MNRAS, 480, 3907
Wagner J., Liesenborgs J., Eichler D., 2019, A&A, 621, A91
Walters A., Ma Y.-Z., Sievers J., Weltman A., 2019, Phys. Rev. D, 100, 103519
Walters A., Weltman A., Gaensler B. M., Ma Y.-Z., Witzemann A., 2018, ApJ, 856, 65
Wei J.-J., Gao H., Wu X.-F., Mészáros P., 2015, Phys. Rev. Lett., 115, 261101
Wei J.-J., Wu X.-F., 2020, Res. Astron. Astrophys., 20, 206
Wu X.-F. et al., 2016, ApJ, 822, L15
Wucknitz O., Spitler L. G., Pen U. L., 2021, A&A, 645, A44
Zhang R. C., Zhang B., 2022, ApJ, 924, L14
Zheng Z., Ofek E. O., Kulkarni S. R., Neill J. D., Juric M., 2014, ApJ, 797, 71
Zhou B., Li X., Wang T., Fan Y.-Z., Wei D.-M., 2014, Phys. Rev. D, 89, 107303
Zitrin A., Eichler D., 2018, ApJ, 866, 101

APPENDIX A: FIGURES OF ALL TELESCOPE COMBINATIONS

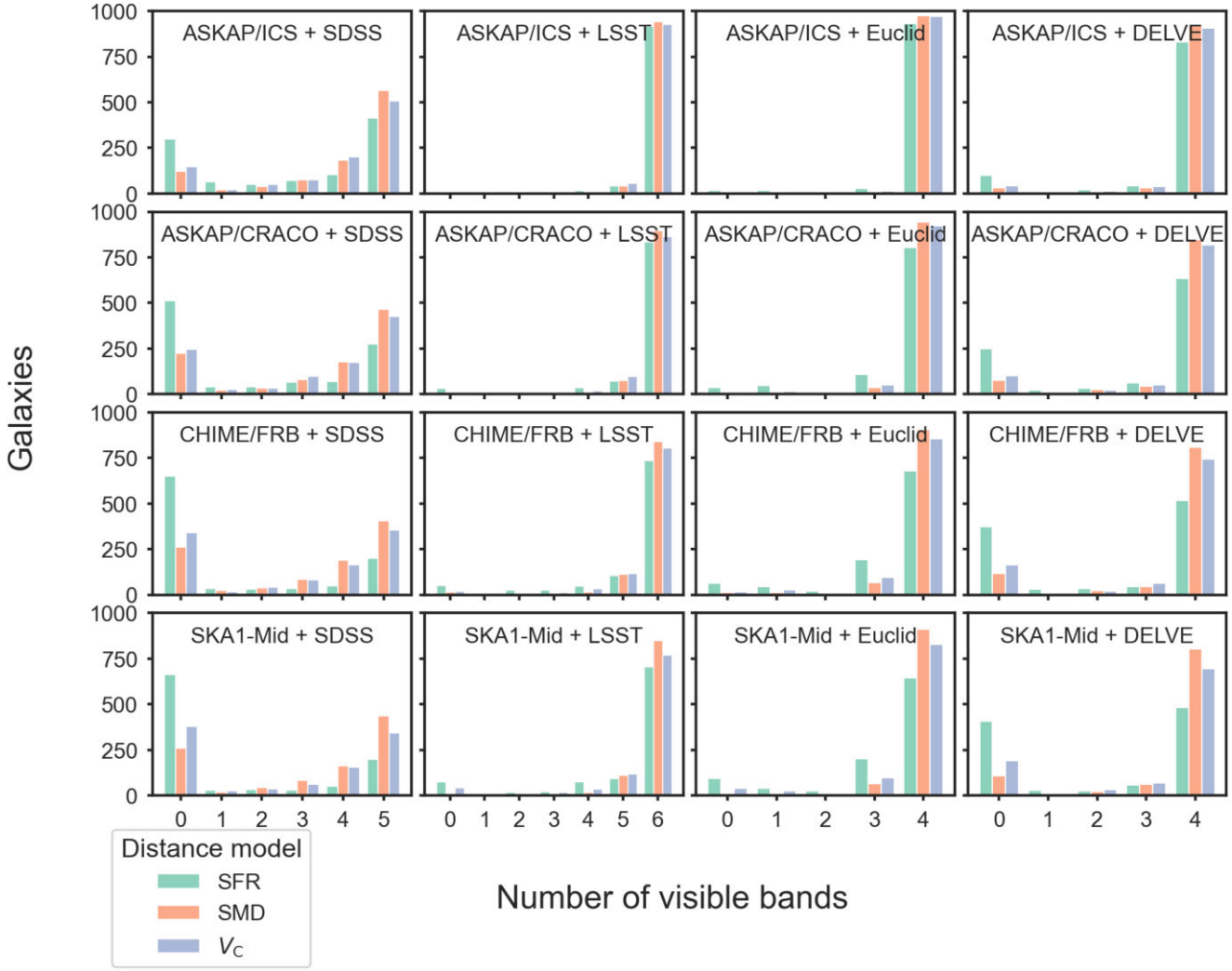

Figure A1. Forecast of the number of pass bands in which FRB host galaxies will be observed for all combinations of radio surveys and optical/infrared surveys that we simulated. Simulations were carried out for three different intrinsic FRB distance distributions, each simulated with 1000 FRBs.

APPENDIX B: DERIVATION OF THE OPTIMAL TIME LIMIT

To derive equation (18), we compare the efficiency of increasing the observation time limit t_l with the efficiency of increasing the galaxy sample N. We have to assume that all follow-up times are drawn from the same probability density function, i.e. we ignore here the dependence on the DM. The gain in detections from increasing t_l by a small Δt_l is given by $\Delta n = p_{t_\mathrm{l}}\,\Delta t_\mathrm{l}$, where p_{t_l} is just the probability at t_l to find a galaxy in the next Δt_l. Simultaneously, the total observing time increases by $\Delta t_\mathrm{tot} \approx (N-n)\,\Delta t_\mathrm{l}$, yielding the efficiency

$$\left(\frac{\Delta n}{\Delta t_\mathrm{tot}}\right)_{t_\mathrm{l}} = \frac{p_{t_\mathrm{l}}}{N-n}. \tag{B1}$$

On the other hand, the gain from increasing the total number is approximately $\Delta n = n/N\,\Delta N$, and the additional time is $\Delta t_\mathrm{tot} \approx t_\mathrm{tot}/N\,\Delta N$, which yields

$$\left(\frac{\Delta n}{\Delta t_\mathrm{tot}}\right)_{N} = \frac{n/N}{t_\mathrm{tot}/N} = \frac{n}{t_\mathrm{tot}}. \tag{B2}$$

Setting the two equations equal yields the point where increasing t_l is just as efficient as increasing N,

$$\frac{p_{t_\mathrm{l}}}{N-n} = \frac{n}{t_\mathrm{tot}}. \tag{B3}$$

This gives equation (18).

In this equation, the optimal t_l is independent of N. To show this, we rearrange the terms and rewrite it as

$$\frac{p_{t_\mathrm{l}}}{N}\frac{t_\mathrm{tot}}{N} = \frac{n}{N}\frac{N-n}{N}. \tag{B4}$$

For any given t_l, each of the fractions is independent of N.

If one wants to compute t_l without applying our algorithm, good knowledge of the distribution of observing times is needed. Expressed in terms of the probability density $p(t)$ of finding a galaxy in the observing time interval $\mathrm{d}t$, the expected observed number n after t_l will be

$$n = N\int_0^{t_\mathrm{l}} p(t)\,\mathrm{d}t, \tag{B5}$$

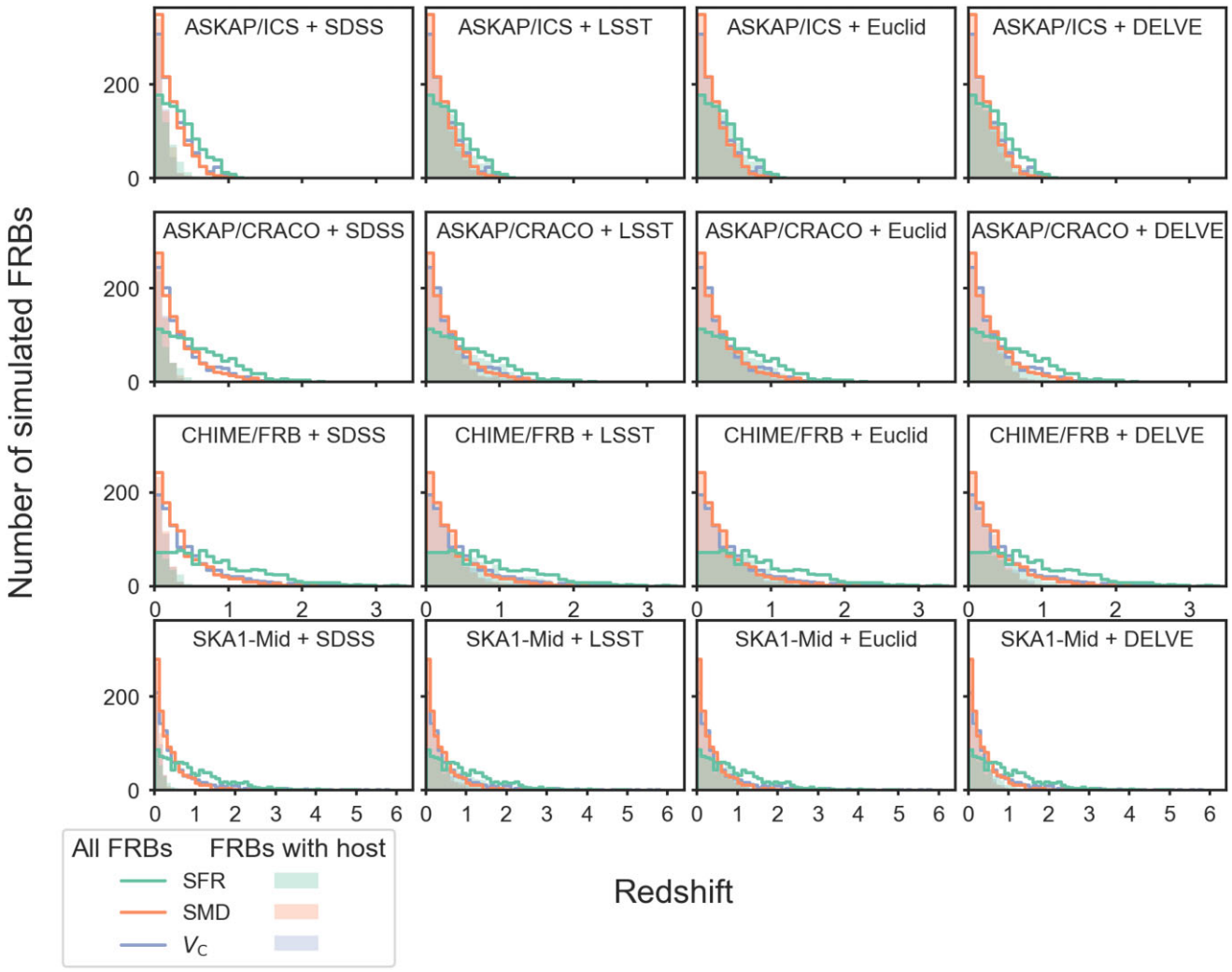

Figure A2. The forecasted redshift distributions of detected FRBs (lines) and of FRBs whose host galaxy was detected in all bands (shaded regions) for all simulated combinations of radio and optical/infrared surveys.

and the observing time will be

$$t_{\rm tot} = N\int_0^{t_{\rm l}} p(t)t\,{\rm d}t + Nt_{\rm l}\int_{t_{\rm l}}^{\infty} p(t)\,{\rm d}t$$
$$= Nt_{\rm l} + N\int_0^{t_{\rm l}} p(t)(t-t_{\rm l})\,{\rm d}t \qquad \text{(B6)}$$

Inserting equations (B5) and (B6) into equation (B4) and using $p(t_{\rm l}) = p_{t_{\rm l}}/N$ (or alternatively taking the derivative of $n/t_{\rm tot}$ with respect to $t_{\rm l}$), we obtain

$$p(t_{\rm l})\left(t_{\rm l} + \int_0^{t_{\rm l}} p(t)(t-t_{\rm l})\,{\rm d}t\right) = \int_0^{t_{\rm l}} p(t)\,{\rm d}t\left(1-\int_0^{t_{\rm l}} p(t)\,{\rm d}t\right). \qquad \text{(B7)}$$

This equation can be inverted numerically to obtain the optimal $t_{\rm l}$. Subsequently, one can calculate the optimal N for a given observing time $t_{\rm tot}$ from equation (B6).

We can generalize this result to maximize $\mathrm{SNR}_{\rm c}^2$ instead of the number and further include the DM dependency. The SNR and time will be given in terms of the expected $\mathrm{SNR}(\mathrm{DM_i})$ at a given DM, where indices go over all FRBs, by

$$\mathrm{SNR}_{\rm c}^2 = \sum_{i=1}^{N}\int_0^{t_{\rm l}} p(t,\mathrm{DM_i})\,\mathrm{SNR}(\mathrm{DM_i})^2\,{\rm d}t, \quad \text{and} \qquad \text{(B8)}$$

$$t_{\rm tot} = \sum_{i=1}^{N}\left[\int_0^{t_{\rm l}} p(t,\mathrm{DM_i})\,t\,{\rm d}t + t_{\rm l}\left(1-\int_0^{t_{\rm l}} p(t,\mathrm{DM_i})\,{\rm d}t\right)\right]. \qquad \text{(B9)}$$

The maximum condition $\frac{\rm d}{{\rm d}t_{\rm l}}\frac{\mathrm{SNR}_{\rm c}^2}{t_{\rm tot}} = 0$ yields

$$t_{\rm tot}\sum_{i=1}^{N} p(t_{\rm l},\mathrm{DM_i})\mathrm{SNR}(\mathrm{DM_i})^2 = \mathrm{SNR}_{\rm c}^2\sum_{i=1}^{N}\left(1-\int_0^{t_{\rm l}} p(t,\mathrm{DM_i})\mathrm{d}t\right). \qquad \text{(B10)}$$

This paper has been typeset from a TEX/LATEX file prepared by the author.

List of Figures

List of Tables